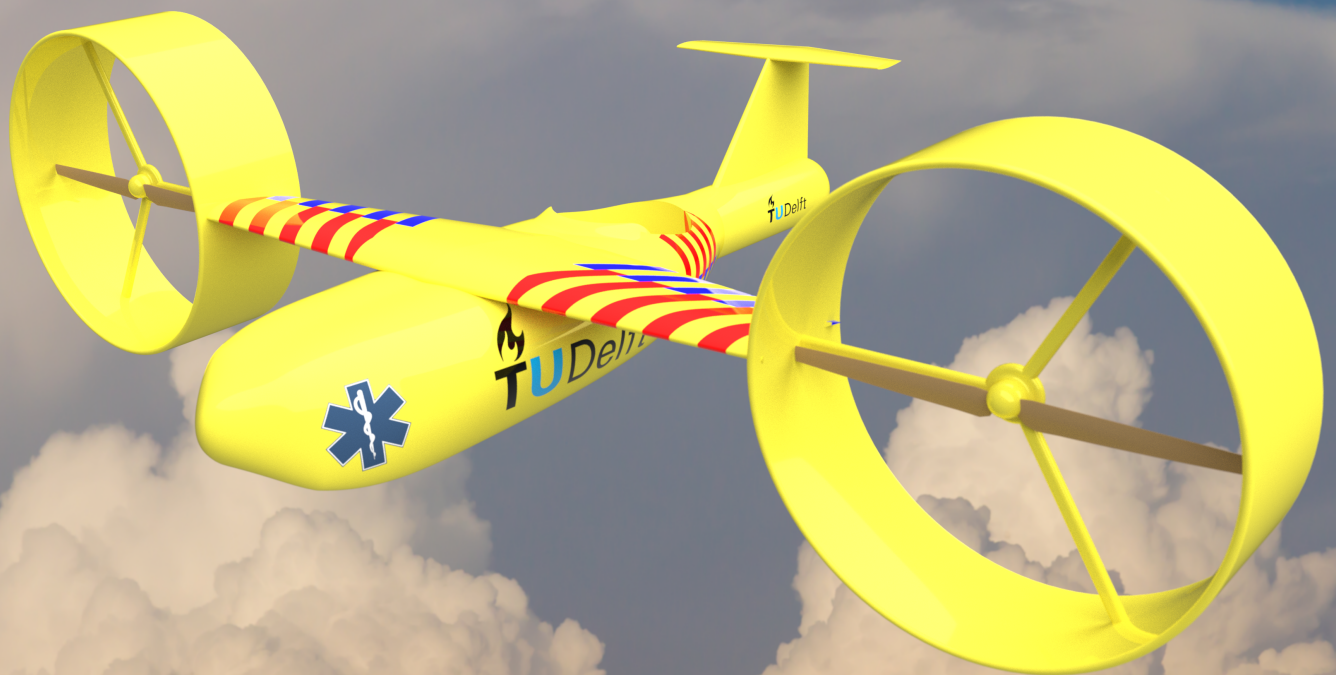# HEALR Drone
Hydrogen-Powered
Emergency All-Weather
Long Range Medical Drone

AE3200 DSE Final Report

Group 17
June 30, 2020

Version 2

TUDelft

[This page is intentionally left blank.]

HEALR Drone
Hydrogen-Powered
Emergency All-Weather
Long Range Medical Drone

AE3200 DSE Final Report

by

Group 17
June 30, 2020

Toon Bloem	4679733
Fenna van den Bogaard	4678745
Maarten Dom	4675126
Mihnea Floriș	4663675
Anish Jadoenathmisier	4572378
Lauren Kaffa	4546792
Floris Kuipers	4668995
Giovanni Lieuw	4550889
Boris Ulyanov	4672798
Thijs Vink	4669614
Malte Wegener	4672194

TUDelft

Preface

This report is the fourth and final technical design report on the design of a hydrogen-powered all-weather medical drone. This project was executed in 11 weeks by 11 students, who all are nearing the obtainment of their Bachelor's degree in Aerospace Engineering at the TU Delft. This final report goes into more detail on the conceptual design that was established in the previous reports.

Group 17
June 30th, 2020

Executive Overview

This report focuses on the detailed design of a hydrogen powered all-weather medical drone. In the previous report [63], multiple concepts were thought of and further developed such that a trade-off could be performed to select the most promising design. This reports continues with a more detailed analysis of the chosen design. Before continuing with the design of this concept, a market analysis and trade-off summary are presented. In the market analysis it is explained where the drone could fit in the market. The trade-off summary shall elaborate on how the tiltrotor concept was chosen. Following this, a requirement overview is presented stating what the drone is required to do and how it's going to function. Next, all subsystems are designed further, starting with a functional and requirement analysis for each subsystem, followed by a design method and analysis. Finally each subsystems ends with a verification and validation chapter paired with a sensitivity analysis and a compliance matrix. Furthermore, each subsystem takes the all weather requirement into account where applicable. After having a more in depth design for each subsystem, the final design is verified and validated. Furthermore an overview of the final design is given. Furthermore this report contains, a technical risk assessment, Operations and logistics concept, production plan, a sustainability development strategy and a preliminary overview of the future of progress of this project. Finally the report is closed with a conclusion and recommendations.

Market Analysis, Trade-Off and Requirements Overview

To start the design phase, background information is needed and conceptual designs are to be made. Also, all requirements need to be set. This is summarized in a market analysis, trade-off of conceptual designs and a requirements overview.

Market Analysis   When analyzing the current market, it was seen that the HEALR Drone has a relatively high payload mass coupled with a large range compared to other drones currently on the market. On top of this, the drone has a higher reliability than other drones in most cases and it is developed with a large focus on sustainability. This gives the drone a competitive advantage with respect to other drones and currently there is nothing quite like it. Overall it is expected to have at least 700 mission per year for this drone.

Trade-off summary   In the Midterm Report [63], a concept was a chosen based on a trade off. The final trade-off was performed by "grading" each concept on the following criteria:

- Stability and control (15%)
- J/km/kg(energy consumption) (10%)
- Manufacturability (15%)
- Cruise speed (30%)
- Reliability (30%)

After having graded each concept on these criteria, a final design was determined. This design was verified using a sensitivity analysis, showing that stability, most likely, will be the relative weakness of the drone whereas the cruise speed and reliability will be a relative strengths.

Requirement Overview   To guide the design process, requirements were determined using the Functional Breakdown Structure and Functional Flow Diagram. The driving requirements and key requirements are the following, indicated in boldface and italicized, respectively:

MD-SYS03:   **The drone shall be able to carry a payload of at least 10 [kg]**
MD-SYS09:   ***The system shall be capable of handling all-weather conditions, reaching a dispatch reliability in 99% or more of the days.***
MD-SYS13:   **The drone shall have a range of at least 100 nautical miles for a return trip.**
MD-SYS17:   **The drone shall comply with the regulations of the specific risk category set by EASA.**
MD-SYS19:   **The drone shall be able to take-off and land vertically.**
MD-SYS21:   **The drone shall have a self-loading and/or self-unloading system of the payload.**
MD-SYS23:   *The unit cost of the drone shall not exceed a value of €100k.*
MD-SYS24:   *The operational cost of the drone shall not exceed 0.05-0.10 [€/kg/km].*
MD-SYS25:   *The drone shall be hydrogen powered.*
MD-SYS30:   **The drone shall have a circular design.**

Subsystem Design

The drone consists of multiple subsystems. These all have their own characteristics and design specifications. The subsystems that are discussed are aerodynamics, hydrogen, propulsion, structures and control, navigation and guidance.

Aerodynamics   The aerodynamics subsystem comprises of lift generation during cruise and minimizing drag of the whole design. Furthermore it is responsible for the aerodynamic design of the proprotors.
During cruise all lift is provided by a single wing that is mounted in a high wing configuration. For the cross section of the wing, a Clark Y airfoil is selected, as this airfoil offers the best performance of the analyzed airfoils. The wing has an Aspect Ratio of 5, and features a span of 1.6 [m]. With this, the wing has an area of 0.53 [m^2] and is designed to work at low Reynolds numbers of circa $1.3 \cdot 10^6$. The wing has a taper ratio of 0.6 in order to provide good aerodynamic performance, while keeping the structural weight low. Furthermore, the fuselage is designed to fit all components of the drone. The fuselage has a length of 1.2 [m] and a maximum width and height of 0.3 [m]. In order to provide all subsystems with enough airflow to function properly, an air inlet and outlet were designed. As a final step, the zero lift drag of the drone is determined by estimating the drag of all exposed elements. This drag coefficient is found to be 0.057 with respect to the area of the main wing. This leads to a cruise lift to drag ratio, or glide ratio, of 16:1. This glide ratio is inline with modern airliners. These analyses were performed using an open source 3D panel method, which was validated using experimental data.

The aerodynamic design of the proprotors has to comply with the requirements that come from the propulsion subsystem design. These include the available power and required thrust for both VTOL and cruise phase and also the blade radius. For VTOL the power available and thrust required for both proprotors is 3.7 [kW] and 310 [N] respectively. Whereas for the back rotors it is 1 [kW] and 42 [N]. The radii for the proprotors and back rotors are 0.37 [m] and 0.135 [m] respectively. The proprotors have two blades and the back rotors have three, as this was found to be the most efficient. The rotors were analyzed using JBLADE.

For the aerodynamic design of the proprotors, the first step was airfoil selection. This selection was dependent on the experienced Reynolds numbers on the blade. Since the blades are spinning, they have different wind speeds along the blade span, thus different Reynolds numbers. The airfoil was selected based on Reynolds numbers up to 300,000, as this was found to be the approximate range. Furthermore, a good airfoil performance includes high C_l/C_D and low $C_{m\alpha}$. The low moment coefficient is required as the blades are not able to withstand the aerodynamic moment. This eliminates the use of thin highly cambered airfoils, which normally do have the better lift performance at low Reynolds numbers. Three different airfoils were analyzed in XFLR5 based on their lift performance at Reynolds numbers of 50,000, 150,000 and 250,000. The best option turned out to be the Boeing-Vertol VR-5 airfoil. There was another airfoil that performed better at the lowest Reynolds number, but it also had low stall angles. As there will be a twist in the blade, the root section experiences the highest angles of attack and will thus need a high stall angle airfoil. Consequently, the Boeing airfoil was used for the entire blade. Taper and twist are introduced in the blade to counteract the uneven lift distribution. The taper reduces the increase of the Reynolds number and makes it more uniform. The optimal taper ratio was found to be 0.45, where the chords at the root and tip section are 0.06 [m] and 0.027 [m] respectively. The twist counteracts the

change in lift by altering the angles of attack along the blade and thus the created lift coefficient. Moreover, the twist in the blade is necessary as the inflow angle changes along the span. The inflow angle is the angle at which the blade segment should be pitched, in order to have an angle of attack of zero. This means that in order to have the entire blade experience the same angle of attack, a certain amount of negative twist is necessary. The twist to reduce the angle of attack is added to this amount. The optimal twist was found to be a linear decrease from 18° at 7.2 [cm] span (from root) till 0° at the tip. Next, the pitch and RPM were changed to match the optimal conditions for VTOL and cruise, while complying with the thrust and power requirements. The found pitch and RPM were 10° and 3,630 for VTOL and 42° and 2,050 for VTOL, with an cruise propulsive efficiency of 0.88.

The back rotors were designed in the same manner, without any taper. Taper is not necessary for the small radius back rotors and would only increase the manufacturing complexity. The RPM is significantly higher for the back rotors due to the small radius. Therefore, the Reynolds numbers are not much smaller as for the proprotors. Hence, the same airfoil was the best choice for the blades. The final values are a linear twist from +18° at 0.013 [m] to 0° at the tip, a RPM of 6,250 and a pitch of 23°.

Hydrogen   Three functions shall be fulfilled by the hydrogen subsystem, to name them briefly: providing power, storing fuel and making safe refueling possible. The first is needed to provide electrical power to the entire system throughout the mission. The latter two are to allow for safe storage and refueling of the liquid hydrogen. At an earlier stage in the design process, it was opted to use a proton exchange membrane fuel cell (PEMFC). These fuel cells are under rapid development, especially when looking at UAV-specific fuel cells. As it would be too complicated to design a new fuel cell that will be better than one that will be on the market in the upcoming three years, it was decided to explore options that are available commercially. After some research, fuel cells from Intelligent Energy and HES Energy Systems were found to be used in various hydrogen-powered UAV prototypes. These fuel cells are able to fulfill all fo the functions required for the current design and do so at relatively high values of specific power. After comparing different models from the above manufacturers, it was decided to use three pairs of 800 [W] fuel cells, each pair consisting of two 800 [W] fuel cells connected to each other by a so-called power path module. Despite the potential increase in complexity for this system, this combination was chosen, as it turned out to be minimizing the required weight and volume. Pieter Lantermans, external expert for this project and leading a similar hydrogen-powered drone project, was also consulted prior to making this design decision.

Several components are needed alongside the fuel cells to make it function properly. These include a humidifier, hydrogen regulator and an intake for oxygen and cooling. Humidifiers are required as the membrane might dry out due to the production of heat during fuel cell operation. However, the chosen fuel cell is made self-humidifying and therefore no extra components are needed. The hydrogen regulator ensures delivery of liquid hydrogen to the fuel cell at the correct pressure and flow rate. It also ensures the pressure is regulated within the fuel tank (adequate amount of evaporation), such that liquid hydrogen can flow to the tank while keeping tank pressure within its allowed limits. Lastly, the oxygen and cooling intake make sure that there is a sufficient supply of oxygen present for the fuel cell to produce power and keeps the fuel cell at the proper temperature. This air intake is done by making a duct in the skin with a filter in front of it. If everything happens properly the cell's efficiency shall be 0.53, of which the remainder is contributed to heat losses.

The six fuel cells together provide a nominal power of 4.8 [kW]. However, the drone should be able to provide a peak power of 6 [kW] during VTOL. Therefore, two batteries are provided, each capable of producing 600 [W] for three minutes maximum. These batteries are standard batteries provided with the fuel cell by Intelligent Energy, hence are easy to connect and combine with the fuel cells.

The designed fuel storage system comprises of two concentric cylinder vessels with hemispherical end caps. They are constructed from the aluminum alloy Al-2219, which has suitable properties overall for the tank design considered: (relatively) low density, high strength and stiffness, and resistant against hydrogen embrittlement and cryogenic temperatures. Also, extensive study was done on its properties for this purpose, for which it was also chosen as tank wall material.

As it was chosen for was double-walled design, the method and material chosen for insulation was a high vacuum in combination with MLI, for which *CRS Wrap 1303B* is used, manufactured by *Lydall*. This was chosen as is lightweight, has a low thermal conductivity and minimizes heat leaks due to radiation. Furthermore, the chosen variant of MLI is more environmental friendly than the average MLI insulation materials, as it made from biosoluble

Table 1: Component weights of a comparable LH_2 fuel storage system, adapted from subsection 6.2.2.

Component	Mass [kg]
LH_2 tube system	1.71
Vapor extraction tube system	0.47
Baffle system	0.30
Supports (G10)	0.03
Inner and outer vessel	3.39
Insulation - MLI	0.24
Other components	1.72
Estimated total	**7.86**

microfiberglass, instead of carcinogenic fiberglass particles. This greatly reduces it environmental footprint, poses less to no measures to be taken during manufacturing and disposal of the material. Furthermore, multiple components are installed onto the tank to regulate tank pressure and fuel flow of LH_2 into the fuel tank during refueling and gaseous hydrogen towards the fuel cells for adequate operation during the mission.

The designed tank forms an integral part of the structure, and connects aft fuselage with the empennage. The horizontal and vertical tailplanes will be attached to the tank bymeans of induction welding. This tank-empennage assembly will be made detachable from the aft fuselage for ease of operations during (routine) maintenance and inspections.

Propulsion   The propulsion subsystem shall provide thrust for VTOL and cruise. Four rotors are used to provide thrust upward. Two of these can tilt forward to provide horizontal thrust for cruise. They are mounted at the tip of the wing. This placement makes it easier to let them tilt than when they are mounted somewhere else. Moreover, the wake of the rotors have less influence on the other systems of the drone here. The other two rotors are co-axial rotors which turn in opposite direction. These are used to improve the stability during VTOL and provide part of the VTOL vertical thrust. The front rotors can thus be smaller since they do not have to provide as much thrust in VTOL as they would have on their own. All rotors use ducts which increases their efficiency, but add structural weight.

Initially, the areas of the rotor disks were picked. These were found using a maximum power of 5 [kW] and the minimum rate of climb at 3 [m/s]. The disk area of the back rotor could be lowered because of using co-axial rotors. These two together deliver more thrust than one for the same disk area. To find the radii of the rotors an area ratio was used. This area ratio is defined as the disk area of the two front rotors divided by the area of all rotors combined. The area ratio was plotted against the front rotor radius and power required. Applying the constraints to this graph the design point was found. Which resulted in a final radii for the back and front rotors of 0.135 and 0.37 [m] respectively.

The transition phase was analysed next. This is the phase in which the front rotors start tilting forward to create horizontal velocity. For the transition phase two constraints were combined to find the thrust levels. First, the altitude lost during transition should be zero. This is of importance because the drone flies in a city, and any height lost means it can come dangerously close to buildings. Next, the moment around the center of gravity should be zero. A slight increase in thrust of the back rotor will give it a pitch angle downward, so the thrust created by the back rotors also has a horizontal component. The velocity of the drone is not large enough here to create a significant amount of drag, but later this pitch angle needs to change back again.

The cruise speed is found by looking at the propulsive efficiency of the propellers, together with the power available and the drag coefficient of the drone. The velocity during cruise is equal to 50 [m/s] for a propulsive efficiency of 0.88. This speed is reached when both front propellers together deliver a thrust of 64 [N]. To pick motors, the turn velocities of the propellers is looked at. The motors should turn at the required cruise turn velocity when given 25 [V], which is the voltage given by the fuel cells. If the motors work on this voltage during cruise, no converter is needed, which saves a lot of power.

Stability and Control   The stability and control subsystem is designed to provide passive and active stability and control during hover, the transition phase and cruise. During cruise passive stability and control is achieved by

designing for a horizontal tail surface area using a 'scissor plot' to ensure passive stability ($\frac{C_M}{d\alpha} < 0$) and being able to achieve trim condition for all c.g. locations. This resulted in $\frac{S_h}{S} = 0.11$, $S_h = 0.06$ [m^2], $x_{wing} = 0.81$ [m] and $x_{tail} = 2.11$ [m]. Then it was checked whether the horizontal thrust from the engines do not introduce any pitching moments that cannot be trimmed with this found surface area. The vertical distance between the c.g. and the horizontal thrust resulted in a moment for which a smaller surface area is needed than calculated from the scissor plot. With this area the incidence angle for the horizontal tail could be found to ensure zero elevator deflection to reduce drag during cruise. The incidence angle is 2.0° downward, thus providing negative lift during cruise. The vertical tail is designed for the condition of maximum crosswind and one engine inoperative. A 24 [m/s] cross wind resulted in a required C_{L_v} of 0.5, hence with no rudder control, the drone is in equilibrium at a side slip angle of 7°. For the one engine inoperative condition, sizing without a rudder resulted in an area of 70% of the main wing due to high thrust force and large moment arm from the engine. An option to decrease this area is to increase the tail arm, but since the fuel tank is used as integral primary load bearing structure, it was decided to include the rudder design to decrease the total area. This resulted in $S_v = 0.15$ [m^2]. Furthermore due to using a symmetrical airfoil, the drone has a tendency to turn its nose into any slip angle disturbance (weather-vane stability') ensuring passive lateral stability. To meet the yaw, pitch and roll requirements the control surfaces are designed accordingly. Results can be found in the table below.

Parameter	Aileron (1 out of 2)	Elevator (1 out of 2)	Rudder
Span length [cm]	24.2	28	54.6
Chord length [cm]	16.4	4	8
Surface area [cm^2]	396.9	112.0	436.8
Hinge moment [N·cm]	92	8	51

For the transition- and hover phase, the required power and corresponding engine rotation angles (the two front engines are capable of rotating forward and backward) are calculated to meet the yaw, pitch and roll requirements during hover. The tables below show the results, in which motor 1 and 2 are the front engines (left and right as seen from the perspective of the drone), and motor 3 & 4 indicate the back engine which cannot rotate (3 and 4 refer to the two co-axial rotors of the back engine). The numbers show the power required for yawing to the left (in the direction of motor 1), rolling to the left (motor 1 going downwards) and pitching down (motor 3 going upwards).

Negative yaw acceleration	Motor 1	Motor 2	Motor 3&4
θ [°]	0	3.0	0
Δ Thrust [N]	0	0.2	0
Power required [W]	0	0.09	0

Negative roll acceleration	Motor 1	Motor 2	Motor 3&4
θ [°]	≈ 0	0	0
Δ Thrust [N]	≈ 0	3.9	1.2
Power required [W]	≈ 0	7.5	3.4

Negative pitch acceleration	Motor 1	Motor 2	Motor 3
θ [°]	0	0	0
Delta Thrust [N]	-2.9	-2.9	5.8
Power required [W]	-4.8	-4.8	38

A general flight controller is designed for the hover phase. It is designed such that for given required states and the actual states determined from sensors, the error is calculated and by tuning PID controllers, the engines are controlled to reach a steady-state condition within a desired time. A simplified controller has been designed for the pitch control in case of a gust wind of 24 [m/s] which is modeled as a pulse input. The change in thrust is around 40 N maximum and arrives at steady state after around 30 seconds. A sensitivity analysis is done by changing the input for the payload mass and the mass moment of inertias. As a result the design does not change too much when adding up to 25% of payload mass. But it is sensitive to an increase of mass moment of inertias with regards to power required for pitch, yaw and roll control during hover. From analysis it could be concluded that the current values used for the inertias and pitch, yaw and roll requirements are very conservative and hence it is not likely that the drone will encounter any problems with regards to power shortage for control during VTOL. However attention should be paid to this strong coupling as either the power available or the design lay-out could have to be changed when entering the next design phase with the current design. Finally the tools used and the results found are subjected to verification methods to ensure obtainment of the expected outputs, and validation to check how well they approximate reality.

Structures   The structures subsystem is responsible for designing load bearing structures for the different parts of the drone, by choosing a material and taking into account different load factors that the drone needs to support. After the work was divided into designing the tail section, the wing section and the fuselage, the first step was finding out what load factor should be applied to the aerodynamic loads. By making use of the Very Light Aircraft EASA regulations (closest category to HEALR) and by taking into account the gust speeds that need to be sustained, a load factor of $n = 3.8$ resulted. After this, an analysis tool was set to iterate the geometry by first determining the reaction forces, then plotting V and M loading diagram, followed by the direct and shear stresses graphs and finally the deflections, based on a chosen material.

The analysis started with a simple cross-section layout for the lifting surfaces in the form of a rectangle with the same thickness of 2 [mm] throughout the chord, height and the span. Going step by step, the basic equilibrium equations were computed and the loading diagrams were verified by checking if the forces and moments were zero at the free end, except for the wing, in which case forces and moments had to correspond with those of the rotor at the tip. With the help of the Macaulay step function and by also checking the critical buckling stress, the stresses were calculated as seen in Table 2. It was concluded that the wing during the cruise phase experiences the highest stresses and so it was taken as a reference when choosing the material.

Table 2: Maximal stresses experienced by the structure

Part	Condition	Maximal normal stress	Maximal shear stress	Maximal von Mises stress
Wing	VTOL	12.6 MPa	17.7 MPa	30.7 MPa
	cruise	23.3 MPa	34.8 MPa	64.6 MPa
Horizontal tail	VTOL	≈ 0.0 MPa	0.1 MPa	0.1 MPa
	cruise	0.4 MPa	4.3 MPa	7.4 MPa
Vertical tail	VTOL	$\approx$ - 0.0 MPa	0 MPa	≈ 0.0 MPa
	cruise	0.1 MPa	3.2 MPa	5.5 MPa

With the stresses now calculated, it was seen that there is no need for a material with very high strength and stiffness properties, and so composites were selected over metals. In particular, a flax fibre composite with cellulose propionate (CP) resin proved to be interesting not only because it could carry the stresses with relative ease, but also because it has a good sustainability score. The plants used to create the material consume more CO_2 while growing than is released when the material is created. Moreover, at EOL, it is biodegradable, leaving behind no waste. The actual material had to be modified by having the directions of the fibres rearranged such that it was also able to carry shear forces better. Its properties are shown in Table 3.

Table 3: Modified flax fibre composite properties

	Density [kg/m3]	Flexural modulus [GPa]	Flexural yield stress [MPa]	Ultimate (tensile) strength [MPa]	Shear modulus [GPa]	Shear strength [MPa]	Poisson ratio [-]	Recyclable?
Modified flax fibre reinforced CP composite	1393	11.7 (parallel) 11.7 (transverse)	136.02 (parallel) 136.02 (transverse)	136.47 (parallel) 136.47 (transverse)	4.5 (parallel) 4.5 (transverse)	81.9 (parallel) 81.9 (transverse)	0.29	Yes

After the material was chosen, it was seen that the maximum deflection along the x axis was almost 7 [cm] which is the equivalent of 8.5% of the span. Following this first analysis, a first set of verification and validation procedures was set in place in order to verify the tool. With comparable results from the verification and validation procedures, an updated shape for the wing-box was proposed for future work. The skin of the wing now becomes a load bearing structure and one of the spars from the rectangular wing-box is removed.

Communication   To make sure the drone gets to and from the hospitals the communication subsystem is used. The drone needs to determine its location, which is done by using the GNSS network. If the satellite signal drops there are also IMU's installed, which can calculate the position from the last known location. Once the location is found this can immediately be compared to the route it should be on. since all of the routes have to pre-approved.

This information combined with data from the other subsystems within the drone needs to be transmitted to the main station. For this the bandwidth of 380 till 385 [MHz] is available. Alternatively 4G and 5G could be used in the future to transmit and receive data.

Final design overview

The final drone has a zero fuel weight of 35.1 [kg] and can store up to 930 [g] of hydrogen in its fuel tank. With a full fuel tank, the drone can transport a 10 [kg] payload up to 100 [nmi] and return to base. The highest weight components are the liquid hydrogen fuel tank and the 6 fuel cells, which provide 4.2 [kW] of continuous power. The drone has a total span of 2.9 [m] and a length of 2 [m], these dimensions comply with the "specific" category of drones set by the regulatory authorities. The cost of production for a single drone is evaluated to be around €83k which complies with the customer requirements. The operational costs are assessed and the cost of transporting 1 [kg] of payload over a single kilometer is found to be €0.097. In order to evaluate the stability and feasibility of the design, a sensitivity analysis was performed. This analysis revealed that the design is sensitive to changes in non-functional weight. This sensitivity mainly originates from the low power density of current fuel cells, however the development of better fuel cells is progressing at a very fast pace and this limitation will vanish with better technology. In order to analyse the operational envelope of the drone for different payloads, a payload range diagram has been generated. The operational range can be improved by 20% by halving the payload, which is very attractive to customers who need to transport lighter payloads. In order to be self loading and unloading, the drone will land on the payload and will be fixed to the drone by 2 redundant connectors. In order to further secure the payload, it will be hold on the side by actuators, which also act as dampeners in the case of strong accelerations.

Product Verification and Validation   There are four product verification techniques: inspection, analysis, demonstration and test. All system requirements have to be verified by one of these techniques. However, most of this verification can only be done in the future. The reason for this is twofold: there is no real life model available yet and there are no analysis tools developed yet that can simulate and analyse the model in representative circumstances. Therefore, complete verification has to be done in the future. Also, validation at this point in the design is fairly hard, as of the same reasons as for verification. The take-off weight of the drone is compared to that of other drones with comparable missions, to see if it is in line. This is the case, which implies that the MTOW of the drone is validated. Other validation procedures, like wing tunnel testing, need to be performed after this design phase.

Technical Risk assessment

The risk analysis was split in two parts. First, the risks expected to be encountered during production of the drone were addressed. These were subdivided into part manufacturing risks and assembly risks. Then, the risks associated to drone operation were covered per subsystem of the drone. Mitigation strategies were developed for each risk, aiming to reduce either its impact or its magnitude. A scenario common to many operational risks even after mitigation was identified, namely an unexpected landing away from the destination. This was deemed undesirable and so an additional mitigation strategy was developed for these cases. It involves sending a team to pick up the drone and bring it to its destination. Two risk maps could then be generated to judge the severity of each risk. Each was assigned one of three categories. There are unacceptable risks which require mitigation, watchlist risks that must also be mitigated, but only if the design allows it, and negligible risks which are benign and need not be mitigated. All risks were reduced to watchlist or negligible status after the first round of mitigations, save for the operational risk of the drone encountering weather conditions that exceed its design envelope. To combat this, the general strategy for unexpected landing was applied. Its use reduced this risk to watchlist status. This means that the manned pick-up protocol is a necessary part of the drone project, as otherwise one of the risks remains unacceptable after mitigation.

Operations and Logistics

The operations and logistics of the drone can be divided into four sections, Operations,Logistics,RAMS analysis and Production Plan.

Operations   The operations of the drone are all based on the use of "drone airports". These central locations take care of the refueling, maintenance and operation of the drone. This method was chosen in order to minimise operational costs. Furthermore, it is unrealistic to have a refueling system installed in all hospitals as well as an operator at each hospital, mainly due to cost. On top of this the current system of transplantation operations can remain the same since there is already a governing body in the form of "Eurotransplant".

Logistics   The flight routes of the drone are all pre-defined and made for each possible mission. In this way, the missions do not need any permission from authorities to start. These flight paths have to avoid populated areas as much as possible due to safety and noise reasons. The regulations regarding drones are renewed by EASA, which means that these new rules were considered for the design. The most important requirements from the new EASA rules follow from the respective risk class a drone is given. The goal of this drone is to be in the 'specific' category, because the category with higher risk involves too strict safety and reliability procedures for the drone

to be worth operating. The requirements that follow are a maximum characteristic dimension of less than 3 [m] and a crash-protected container for dangerous goods. Since the drone is hydrogen powered, an Specific Operations Risk Assessment needs to be performed in future research to validate the placing of the drone in the specific category.

RAMS analysis   A Reliability, Availability, Maintainability and Safety (RAMS) analysis was performed to asses these factors of the design. In most cases each subsystem has a form of redundancy that increases the reliability of the drone. Moreover, each subsystem takes safety into account where applicable. Certain subsystems have more redundancy than they have safety applied and vice versa. In these cases either redundancy or safety are not directly applicable therefore it is made sure that the other factor is as good as possible. Furthermore, the availability and maintainability are analyzed. Since the drone needs to be able to fly at 99% of the time, the drone needs to be highly available. As for the maintainability, the more the drone needs to have maintenance performed on it the less available it will be. The maintenance can be divided in three types: pre-flight, post-flight and periodic checks. pre and post flight checks are mainly part of one mission, whereas the periodic checks are outside the mission. If it is the case that maintenance is necessary this will be done in the "drone airport".

Production plan   The production of the drone is split up into four steps which are done consecutively. The first step is acquiring all components. Components which are specific for this drone need to be manufactured. The fuselage, wing, propeller blades and empennage structures and skin will be made from flax fiber composite. The manufacturing technique that is used with this material is injection moulding. Also, one layer of the fuel tank is made of this material. The other layer of the tank is made of aluminum, which is rubber formed into its desired shape. Finally, polyurethane foam is used in between two flax fiber composite layers in the ducts to decrease the noise. This is manufactured by cutting. All other components are bought and thus not have to be manufactured by this project. This includes the fuel cells, batteries, motors, power control unit and all cabling, valves, regulators that are needed.

After all components have been assembled, the constructing of the wing group, empennage group and fuselage group can be done simultaneously. All of these processes have the same order. First constructing the base construction of the respective group. Then adding the wiring that is needed. Then, adding the control surfaces and their wiring/connections (only for the wing and empennage group). Finally, the skin will then be added.

After all groups are assembled, the third stage of the production can start. This is combining the empennage and the fuselage to each other. This is done before adding the wings, as wings are large and require more space. Finally, the wings are added to the fuselage.

Sustainability Development Strategy
The drone has been analyzed with regards to how it contributes to sustainability, which has been done by identifying strong and weak points. For the identified weak points, improvements are considered. The analysis has been done with the aid of constructing a so-called 'EcoDesign Strategy Wheel'. The dimensions considered include; obtainment and consumption of materials, manufacturing techniques, operations and durability, and end of life. The wheel can be found below.

- *Acquiring and consumption of materials*: strong points include the use of flax fibre composite with cellulose propionate resin which is bio-degradable. The obtainment of the flax fibre requires much lower energy compared to carbon fiber or glass fiber and is a CO_2 negative contributor. Furthermore the composite is easily recycleable and non-toxic. On top of this aluminium is used for the tank which can be recycled and the insulation layer used is bio-degradable and does not require any adhesive or adherent. On the other hand, the use of polyurethane foam and batteries reduce the score dramatically. The production of the foam uses toxic gases and it is hard to recycle. The materials used for batteries require toxic chemicals and come from non renewable sources. Therefore the drone scores below the required score. In order to increase its sustainability, improvements can be made by choosing alternatives for the foam or select a foam that is produced from recyclable parts and do not make use of toxic gases. Furthermore the usage of batteries should be reconsidered, the sustainability could be improved by selecting batteries that are constructed from as many recycled parts and uses as less non renewable sources as possible.

EcoDesign Strategy Wheel
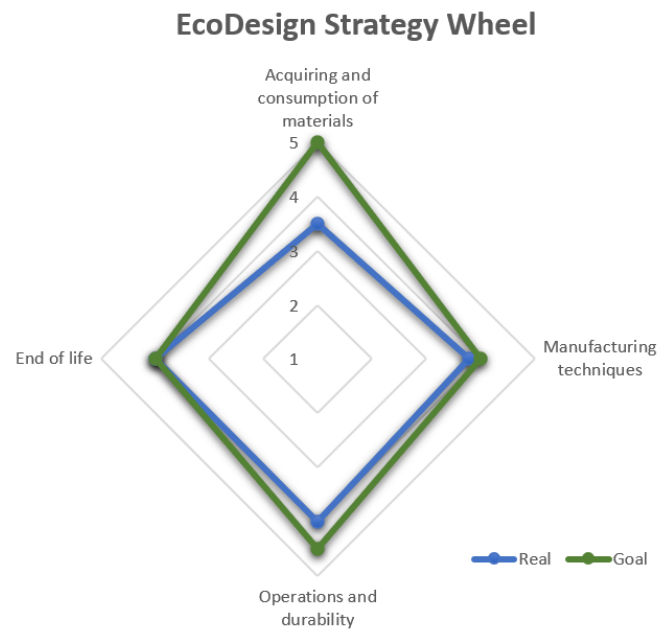
- *Manufacturing techniques*: strong points are the usage of injection moulding and rubber forming which are efficient processes with no waste production. Furthermore the most used assembly method is friction stir welding which is energy efficient and no heating is required. The score is slightly below due to cutting techniques used to cut the polyurethane foam leading to possible non recyclable waste. Thus attention should be paid on the processing of this foam.

- *Operations and durability*: Strong points include no CO_2 emissions during flight, high durability of the flax fibre composite, polyurethane foam and aluminium. The drone scores high for the maintainability of most of the components except for the tilting mechanism of the engines due to low accessibility. Furthermore, the lifetime of the fuel cells are only around 1,000 flight hours, which is significantly lower than the lifespan of all other components. Thus, an improvement on durability would be to increase the accessibility of the tilting mechanisms of the engines and to increase the lifespan of the fuel cells, which is expected to happen in the near future.

- *End of life*: Strong points include the high recyclability of the flax fibre composite (of which the drone mostly consists of) and aluminium, bio-degradable insulation material and recycle possibilities for the batteries. Lacking are, again, the fuel cell and the polyurethane foam. For both the fuel cell and the foam recycling possibilities are being developed, hence improving the end of life score in the future.

Post DSE

After DSE is finished, the drone design could continue. In this case the process of how this would continue is explained. After the DSE, this post DSE design and development logic is divided into four main sections, namely Research and Development, Prototype testing and building, Production and Assembly, and Life Cycle Management. These phases are explained in a flow diagram, showing what is still left to be done. Furthermore, this is also shown using a Gantt chart. The Gantt chart also corresponds with the time frame defined by the development period. Lastly, a post DSE cost breakdown is presented. Here, it can be seen that Research and Development is expected to be the phase with the highest costs.

List of Abbreviations

ADSEE-I   Aerospace Design and Systems Engineering Elements 1
AM   Additive manufacturing
ASM   Aerospace Materials
BVLOS   Behind visual line of sight
CAD   Computer-assisted design
CFRP   Carbon fiber reinforced polymer
c.g.   Centre of gravity
CNG   Communication, navigation and guidance
COTS   Commercial-off-the-shelf
CS-VLA   Certification Specification - Very Light Aircraft
DC   Direct current
DOT   Design option tree
EoL   End of life
FBD   Free Body Diagram
GH_2 Gaseous hydrogen
GNSS   Global Navigation Satellite System
GR   Glide ratio
IMU   Inertial Measurement Unit
INDI   Incremental non-linear dynamic inversion
LCA   Life Cycle Assessment
L/D   Lift to drag ratio
LEMAC   Leading edge mean aerodynamic chord
LH_2 Liquid hydrogen
LiIo   Lithium ion (battery)
LiPo   Lithium polymer (battery)
LOX   Liquid oxygen
MAC   Mean aerodynamic chord
MLI   Multi layer insulation
MNS   Mission Need Statement
MTOW   Maximum take-off weight
NiMH   Nickel metal hydride (battery)
PPM   Power Path Module
PEM   Proton exchange membrane
PEMFC   Proton exchange membrane fuel cell
RAMS   Reliability, availability, maintainability, safety
RPM   Rounds Per Minute
RCS   Reaction Control System
SM   Stability Margin
SPL   Sound Pressure Level
TRL   Technology readiness level
TR   Taper Ratio
UAV   Unmanned aerial vehicle
UAS   Unmanned aerial system
VTOL   Vertical take-off and landing
WBS   Work breakdown structure
WFD   Workflow diagram
W/A   (Rotor) Disk loading
W/P   Power loading
W/S   Wing loading

List of Symbols

A	(Mean) Conductive area	$[m^2]$
A_m	Enclosed cross-section area	$[m^2]$
A_{front}	Area of the front propellers	$[m^2]$
A_{back}	Area of a back propeller	$[m^2]$
AR	Wing aspect ratio	$[-]$
arm_b	Distance from the c.g. to the back propellers	$[m]$
arm_f	Distance from the c.g. to the front propellers	$[m]$
arm_t	Distance from the c.g. to the tail	$[m]$
arm_w	Distance from the c.g. to the main wing	$[m]$
b	Wing span	$[m]$
c	Wing chord	$[m]$
$C_{d,p}$	Parasitic drag coefficient	$[-]$
$C_{d,i}$	Induced drag coefficient	$[-]$
C_d	drag coefficient	$[-]$
C_l	Lift coefficient of a 2D airfoil	$[-]$
$C_{l,max}$	Maximum lift coefficient	$[-]$
C_{L_v}	Lift coefficient vertical tail	$[-]$
C_{L_α}	Lift coefficient gradient	$[radians^{-1}]$
$C_{L_{\alpha_h}}$	Lift coefficient gradient horizontal tail	$[radians^{-1}]$
$C_{L_{\alpha_{A-h}}}$	Lift coefficient gradient of the drone without tail	$[radians^{-1}]$
$C_{m,q/4}$	Quarter chord aerodynamic moment coefficient	$[-]$
C_{mac}	Moment coefficient around MAC of the main wing	$[-]$
$C_{m\alpha}$	Moment coefficient gradient	$[-]$
$C_{N_{\delta_r}}$	Rudder control derivative	$[-]$
d_i	Diameter (of inner tank)	$[m]$
E	Young's Modulus	$[GPa]$
ER	Expansion Ratio	$[-]$
F_T	Thrust force	$[N]$
G	Shear Modulus	$[GPa]$
I_{xx}	Moment of inertia	$[m^4]$
K	limit stress (in operational conditions)	$[MPa]$
K_g	Gust alleviation factor	$[-]$
k_{MLI}	Thermal conductivity of MLI	$[W/(m{\cdot}K)]$
l	(Tank) length	$[m]$
L	Lift	$[N]$
L_{tail}	Lift generated by the horizontal tail	$[N]$
L_{wing}	Lift generated by the main wing	$[N]$
l_h	Tail arm	$[m]$
m	Mass	$[kg]$
$M(H_2)$	Molecular mass of hydrogen	$[kg/mol]$
M_t	tip mach number	$[-]$
N_D	Drag induced yawing moment	$[N{\cdot}m]$
$N_{t_{crit}}$	yawing moment generated by operative engine	$[N{\cdot}m]$
N_p	Number of propellers	$[-]$
P_{br}	Useful propeller power	$[W]$

p_P	(burst or maximum over)pressure	$[bar]$
q	Dynamic pressure	$[Pa]$
$q_{s,0}$	Redundant shear flow	$[N/m]$
q_b	Base shear flow	$[N/m]$
$\dot{Q}_{MLI,cond}$	Heat transfer due to conduction via MLI	$[W]$
r	(Tank) radius	$[m]$
R	Universal gas constant	$[J/(mol \cdot K)]$
Re	Reynolds number	$[-]$
s_{wall_s}	(spherical cap's) wall thickness	$[mm]$
SF	Safety factor	$[-]$
S_h	Horizontal tail area	$[m^2]$
S_v	Vertical tail area	$[m^2]$
S_{wing} or S	Wing area	$[m^2]$
t	Thickness	$[m]$
T	Thrust	$[N]$
T	Temperature	$[K]$
T_b	Total thrust of the back rotors	$[N]$
T_f	Total thrust of the front rotors	$[N]$
T_{rot}	Rotor torque	$[N \cdot m]$
V	Volume	$[m^3]$
V_{cruise}	Cruise speed	$[m/s]$
V_{dive}	Dive speed	$[m/s]$
V_{mcs}	Minimum control speed	$[m/s]$
V_{stall}	Stall speed	$[m/s]$
V_t	(Tank) volume	$[L]$
V_{VTOL}	VTOL speed	$[m/s]$
V_{wall}	Tank-wall volume	$[m^3]$
V_0	Airspeed	$[m/s]$
W_{rot}	Weight of the rotor	$[kg]$
W_{wing}	Weight of the wing	$[kg]$
$\bar{x}_{ac}$	Location of aerodynamic center of the wing with respect to LEMAC	$[m]$
$\bar{x}_{cg}$	Location of c.g. with respect to LEMAC	$[m]$
α	Angle of attack	$[radians]$
α_{gust}	Gust angle of attack	$[radians]$
β	Pitch angle	$[radians]$
δ_r	Rudder deflection	$[radians]$
η_j	Propulsive efficiency	$[-]$
ρ	(Air) density	$[kg/m^3]$
$\sigma_{cr,buckling}$	Critical buckling stress	$[MPa]$
τ_s	Shear stress	$[MPa]$
θ	Twist along the span of the lifting surface	$[deg]$
ν	Weld efficiency	$[-]$
ν_g	Air vehicle mass aspect ratio	$[-]$
$\frac{d\theta}{dy}$	Rate of twist along the span of the lifting surface	$[deg/m]$
$\frac{d\epsilon}{d\alpha}$	Change of down-wash angle with respect to change in angle of attack	$[-]$

Contents

1

Introduction

Throughout the world, medical goods such as organs, tissues or vaccines have to be reliably collected and delivered from one hospital to another, which are often far away from each other. Nowadays, medical payload is delivered by helicopters, cars or even by bike which are for the most part inefficient, pollutant and can be subject to traffic jams or lack of infrastructure in remote areas. In an attempt to introduce sustainable energy sources in more fields, an all weather hydrogen powered drone is proposed to deliver small but critical payloads over long distances. With no waiting time, fast travel speeds and high reliability for all weather conditions, this drone would provide the necessary aid within only a couple of hours from when the order is placed. Moreover, with autonomous operation and by only creating water as a byproduct, the safety and well-being of people would be increased both at an individual and a global scale. The project has the following Mission Need Statement and Project Objective Statement:

Mission Need Statement:
Provide a sustainable, hydrogen-powered, inter-regional transport solution, reliable for transplant organs and critical medical supplies and capable of operating in all weather conditions.

Project Objective Statement:
Design, within ten weeks, an all-weather, hydrogen-powered vertical takeoff and landing drone capable of flying round-trip missions with 100 nm range while carrying 10 kg of medical payload.

This report is the final in a series of reports. The first report, the Project Plan [64], focused on the organization and the workflow of the design. Each team member was assigned roles, the work was broken down in small tasks and organized chronologically. Next, the Baseline Report [62] aimed to improve on the preparations made in the Project Plan and give an overview of the project mission. Lastly, in the midterm report [63] a trade-off was preformed between different concepts and from this trade-off it was concluded that a tilt rotor medical drone would be the best option. In addition to the trade-off, the Midterm report included a technical risk assessment, a sustainable development strategy and a logistical overview of the whole system.

By making use of the preparatory work and the chosen conceptual design coming from the previous reports, this final report aims to detail the design of each of the drone's subsystems, along with methods for verification and validation and also propose actions for future design and implementation. First, a description of the market in which the drone shall operate is given in chapter 2. Following this chapter, a summary of the trade-off preformed in the Midterm Report is found in chapter 3. After which, in chapter 4, a description of the full system is given, including the Mission Need Statement (MNS), requirements, functional breakdown structure (FBS) and several diagrams such as the hardware and software diagrams, a communication diagram and a functional flow diagram. The first subsystem design is given in chapter 5, which describes the aerodynamics of the drone. Next, the hydrogen subsystem is developed in chapter 6. In this chapter the type of fuel cell is explained, but also the method of sizing the tank is elaborated upon. The propulsion subsystem is developed next in chapter 7, this chapter includes the propulsion layout but also the performance during the three flight phases: VTOL, transition and cruise. Stability and control is discussed next in chapter 8, where the sizing of the tail is explained and the flight controller is designed. The analysis of the whole structure of the drone is presented in chapter 9. chapter 10 then discusses the last subsystem: communication, navigation and guidance. The verification and validation of the product as a whole is performed in chapter 11 and an overview of the HEALR drone is given in chapter 12. This includes budget

breakdowns, a sensitivity analysis, a flight envelope and the compliance matrix. Then, chapter 13 performs a risk analysis on all subsystems and the drone as a whole. chapter 14 presents all operations and logistics that come with operating and producing the drone. In chapter 15 the sustainability development strategy is discussed, going into detail on the three different phases in the life of the drone. After the design phase, the post DSE activities were determined and presented in chapter 16. Finally, the conclusion and recommendations are presented in chapter 17.

2

Market Analysis

To gain a better understanding of the market in which the designed drone shall operate, a market overview is given. Another aspect that can be obtained from the market overview are the key stakeholders that will need the drone. Furthermore, the advantages and the way in which drone shall be utilized is explained. Finally, a SWOT analysis is performed.

2.1. Market Overview

Unmanned Aerial Vehicles (UAV) or drones are being utilized for more and more tasks. They can be seen in agriculture, military applications, logistics and much more. The drone industry is steadily growing and an increasing amount of drone technologies are breaking through the traditional barriers set by the industry [33]. The utilization of UAVs lead to increased work efficiency and productivity, while decreasing workload and production cost and as cherry on top, increased accuracy [33]. One of the industries where drone usage is gaining interest, is in the commercial goods sector. More companies are adopting drones to deliver commercial goods to customers. These include the Amazon Prime drone, designed to deliver packages to customers all over the United States [1], as well as fast food chains such as Domino's or Pizza Hut are investigating ways to deliver pizza by drone[2].

"*To give a better idea of where the industry is right now, in early 2020, the total number of projects which were about using drones for transport was 110 [33]. Half of these projects are conducted in Europe, followed by Asia-Pacific and the United States. The drone service market is expected to grow from $4.4 billion in 2018 to $63.6 billion by 2025 and consumer drone shipments are projected to hit around 30 million by 2021 [2]. In Figure 2.1, the distribution of this market around the world is shown.*" (quoted from Baseline Report [62], as reported earlier during this DSE project.)
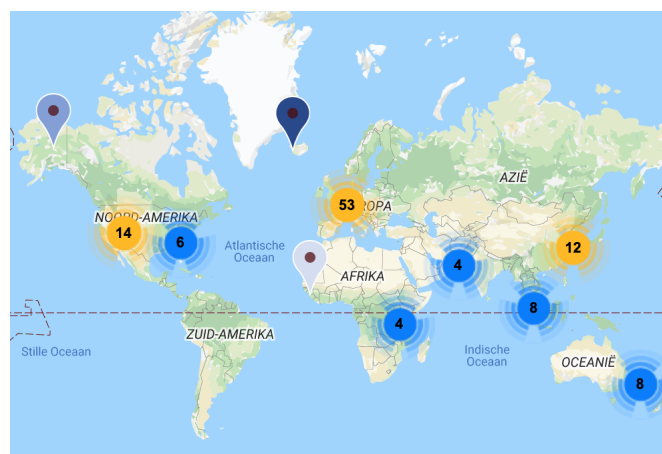
Figure 2.1: Distribution of uprising drone companies around the world (also shown in [62]

---

[1]`https://www.amazon.com/Amazon-Prime-Air/b?ie=UTF8&node=8037720011`
[2]`https://www.cnbc.com/2016/11/16/dominos-has-delivered-the-worlds-first-ever-pizza-by-drone-to-a-new-zealand-couple.html`

Medical goods are also expected to be delivered by drones in the future. Currently, medical goods are being delivered either by land transportation or aircraft. However, due to problems such as traffic jams or flight delays, or even bad road conditions, people are not able to get their medicine on time which could lead to a medical situation growing more critical and in some cases lead to death [31] . This is why faster transportation is needed, to save people those that are now dying due to delays. Drones are one solution of this problem and medical drones are already being utilized in Rwanda, where Zipline [3] (see Figure 2.2) is delivering blood and other essential medical goods to hospitals around the country. Vaccines for example, can be transported to a hospital within 15 minutes, instead of having to wait for hours for a delivery car. This drastic decrease in time has helped save people's lives and due to Zipline's success, the company is expected to deliver medical goods in more countries[4].

Matternet has helped Haiti when disaster struck in the form of delivering essential medicine to those in need in remote and inaccessible areas [5]. Another example of the transport of medical payload by drone is an experiment done by the University of Maryland[6], where a DJI drone was utilized to deliver a kidney to a patient. This was the first time that an organ was transported using a drone, however more companies are looking for ways to increase the amount of payload they can carry such that organ transport by drone could become a regular thing.

Figure 2.2: Zipline drone[3]

2.2. Market for HEALR Drone

The drone developed in this report will first and foremost be
able to carry more payload and reach longer distances than its competitors. The stakeholders identified include: Hospitals, Society, Air Traffic Control,Authorities and the Manufacturers [62]. Furthermore, the drone shall have a high reliability and shall also be developed as a more sustainable product compared to its competitors. To keep the cost of operation as low as possible, the way HEALR Drone shall be utilized is as follows; the drone shall be produced, stored, maintained and operated from a remote hangar. The drone can be rented by blood banks or hospitals to perform services such as, for example, blood delivery. A typical mission would start from the hangar, go to the pick-up location, travel to the drop-off location and then return back to the hangar for checks and refuelling. A more detailed description of this logistical chain can be found in chapter 14. Potentially, a drone could also be stored in the hospitals, but that would imply more operating and maintenance costs.

To get a better overview of the market share the drone would occupy, data on the amount of organ and blood transports was researched. Initially, only the market share of the Netherlands is considered. From the ambulance services [7], it was found that there an average cost of €435 is to be made during each mission. Assuming that organs are usually transported by ambulances, this income can be taken for each flight the drone has. Then, by looking at the operational cost, a profit margin can calculated. From the organ transplant data [8], it was found that there are 750 transplants per year in the Netherlands, out of which 125 are heart and lung transplants, which the drone is unable to carry. This is because surgery for these organs is more complicated than for other organs and it requires equipment much larger than the payload box can fit. This leaves us with 625 possible transports for year. Since the drone also carries blood, a factor of 2 was used for the organ transports to take this into account. Furthermore, some transplants are not going to require any transport since both operations can take place in the same hospital; for this a factor of 0.8 was used. Then, assuming large compliance from governmental agencies, another factor of 0.7 was used to account for the market share the drone would occupy (thus 70% of the remaining needed transports).

All of these factors give an estimated number of 700 of such transports per year. By dividing the Netherlands in 3 regions, a total of 3 drones, one for each region, can be assumed to be in operation at the same time. Then, with some success in the Netherlands, the drone can be introduced and used in neighbouring countries. Therefore, for

---

[3]https://www.cnbc.com/2019/05/17/zipline-medical-delivery-drone-start-up-now-valued-at-1point2-billion.html
[4]https://www.dronesinhealthcare.com/
[5]shorturl.at/nyC09
[6]https://dronelife.com/2019/05/01/university-of-maryland-drone-delivers-kidney-for-successful-transplant/
[7]https://www.ambulancezorg.nl/sectorkompas/facts-figures-2018
[8]https://www.transplantatiestichting.nl/publicaties-en-naslag/cijfers-over-donatie-en-transplantatie/
  organen-jaarcijfers/aantal-orgaantransplantaties

the production cost, the option will be made available that 7 drones can be produced at the same time in the initial post-development phase.

2.3. SWOT Analysis

A SWOT analysis was preformed in the Baseline Report [62], this same analysis is repeated here.

Strenghts
- All weather capabilties
- Very high reliability
- Autonomous/RC capabilities
- Unmanned aircraft
- Verical take-off and landing capabilities
- Can operate where no roads are present
- No CO_2 emissions
- Payload capabilities of up to 10 kg
- Range of up to 100 nm
- The medical sector has lower restrictions

Weaknesses
- EASA regulations not set
- Semi-complex loading and unloading infrastructure
- Need of dedicated personnel at every site
- Refueling infrastructure and storing hydrogen
- Lack of a system architecture in place
- Noise pollution
- In case of transporting organs, they can not be accompanied by the medical staff performing the operation

SWOT

Oppurtunities
- Overcome expiration time for different medical supplies due to poor transport infrastructure
- Introdyce transport of products over long ranges
- Acces to pandemic/calamity areas without endangering people
- Remote location for operations and maintenance, possibly due to a small number of products needed in theory
- Overcome pollution by making this kind of transport sustainable

Threats
- People usually reject novelty ideas at first when the framework is not set in place
- Storing hydrogen at take-off spots may prove hazardous
- Specialized personnel and equipment might have to move from site to site inducing more risks
- People might try to hack or steal the drone due to the expensive payload
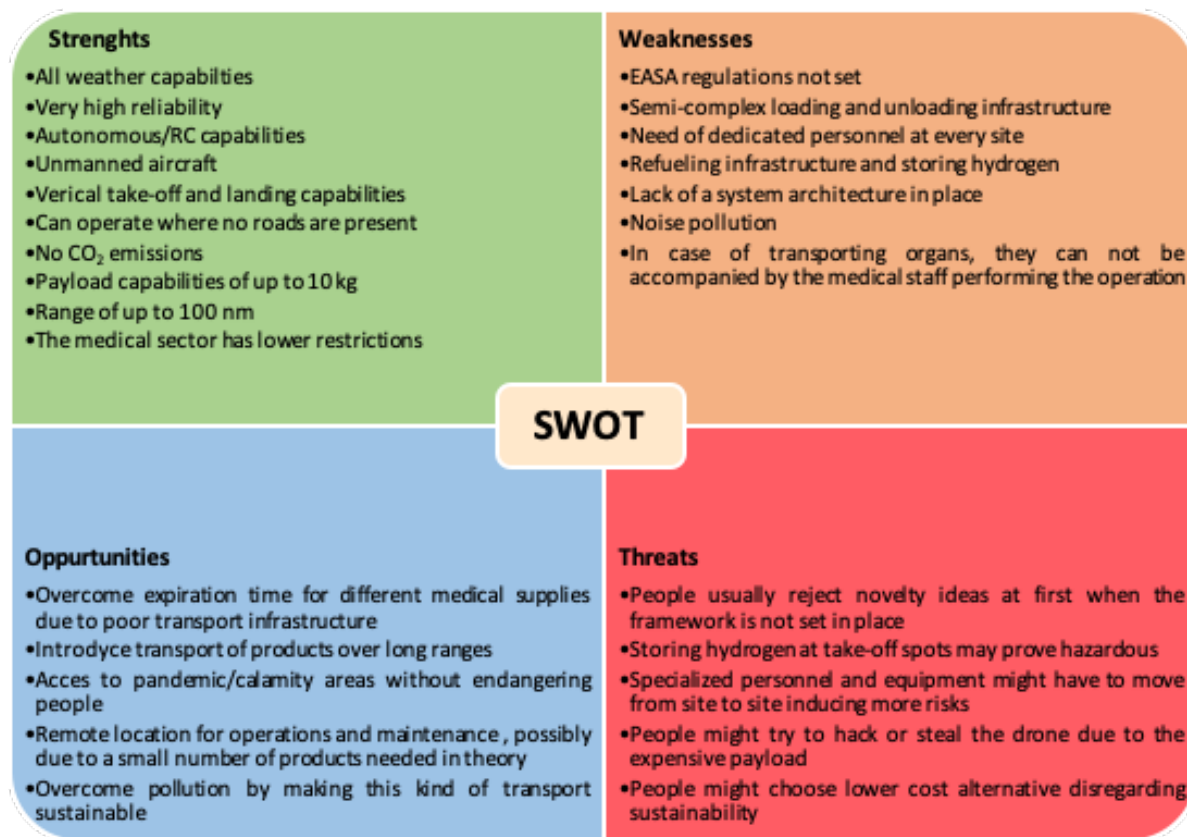- People might choose lower cost alternative disregarding sustainability

Figure 2.3: SWOT analysis of the HEALR Drone

From the SWOT analysis, shown in Figure 2.3, it can be seen that this ambitious project provides many advantages compared to regular options for cargo transportation, but it also has its downsides. For the strengths, an all-weather, high reliability, autonomous aircraft would make the transport of medical supplies safer and faster as it does not have to rely on road infrastructure. Vertical take-off and landing capabilities also allow the drone to reach places where no roads are present. Due to the drone being powered by hydrogen, the negative impact on the environment can be low compared to other aircrafts. The high payload capabilities and the large range also allow more flexibility in possible missions. The project's weaknesses mainly come from its novelty. EASA regulations are still developing in the area of UAV's so there is some uncertainty when it comes to the possible maneuvers the drone can perform. Moreover, the system does not have a standard architecture set in place so operations like loading & unloading the payload and refuelling might be complex at first. Moreover, hydrogen is really hazardous if not handled properly.

3
Trade-Off Summary

During the preliminary design phase, several design options were considered. These design options were combined into five different configurations, which can be seen in Figure 3.1. The different characteristics can be found in Table 3.1.
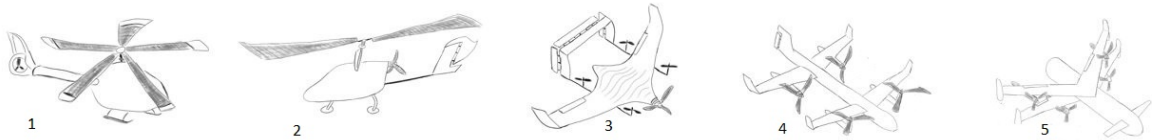

Figure 3.1: Sketches of all five preliminary designs

Table 3.1: Characteristics per design configuration

Design concept	Rotor	Propeller	Wing
1. Helicopter	✓	✓	
2. Autogyro	✓	✓	
3. Fixed thrust	✓	✓	✓
4. Tiltable thrust		✓ ($tiltable$)	✓
5. Tailsitter		✓	✓

In order to decide which of these five designs is the best one to continue with, a trade-off is done. In order to perform the trade-off, first five criteria were determined. These criteria are listed below, together with their weight factors.

- **Stability & Control (15%)**: The all-weather requirement requires the drone to fly even when there are large wind gusts. This means that the drone should both be stable and controllable. This is judged by studying literature on each concept.

- **J/km/kg (energy consumption) (10%)**: A vehicle should always be as efficient as possible. A higher score for a design means that the drone consumes less fuel, which is profitable.

- **Manufacturability (15%)**: A designed drone can be performing excellent and meeting all the requirements, but if it can not be manufactured, this design can not be used in real life. This is graded on the item cost of several components of the drone, the part manufacturing abilities and the complexity of assembly.

- **Cruise speed (30%)**: In some cases, the drone will be performing emergency transport. Therefore, it is important that the drone is flying as fast as possible. The higher the cruise speed of a concept design, the higher the grade.

- **Reliability (30%)**: As this drone will transport medical goods, it might transport life-saving organs, blood or medicines. Therefore, the drone should be very reliable. This is based on a risk assessment on every concept design.

All the designs are graded on each criterion. This can be seen in the summary table in Table 3.2. As one can see, the tiltable thrust concept wins the trade-off. This, of course, has to be verified by a sensitivity analysis. This sensitivity analysis included increasing the weights of certain criteria and removing certain criteria. This analysis showed that the cruise speed and reliability are the relative strengths of the tiltable thrust design. If these are left out, it does not win anymore. Stability is the relative weakness of the tiltable thrust design, hence a close eye should be kept on this during the detailed design.

Table 3.2: Full trade-off summary table

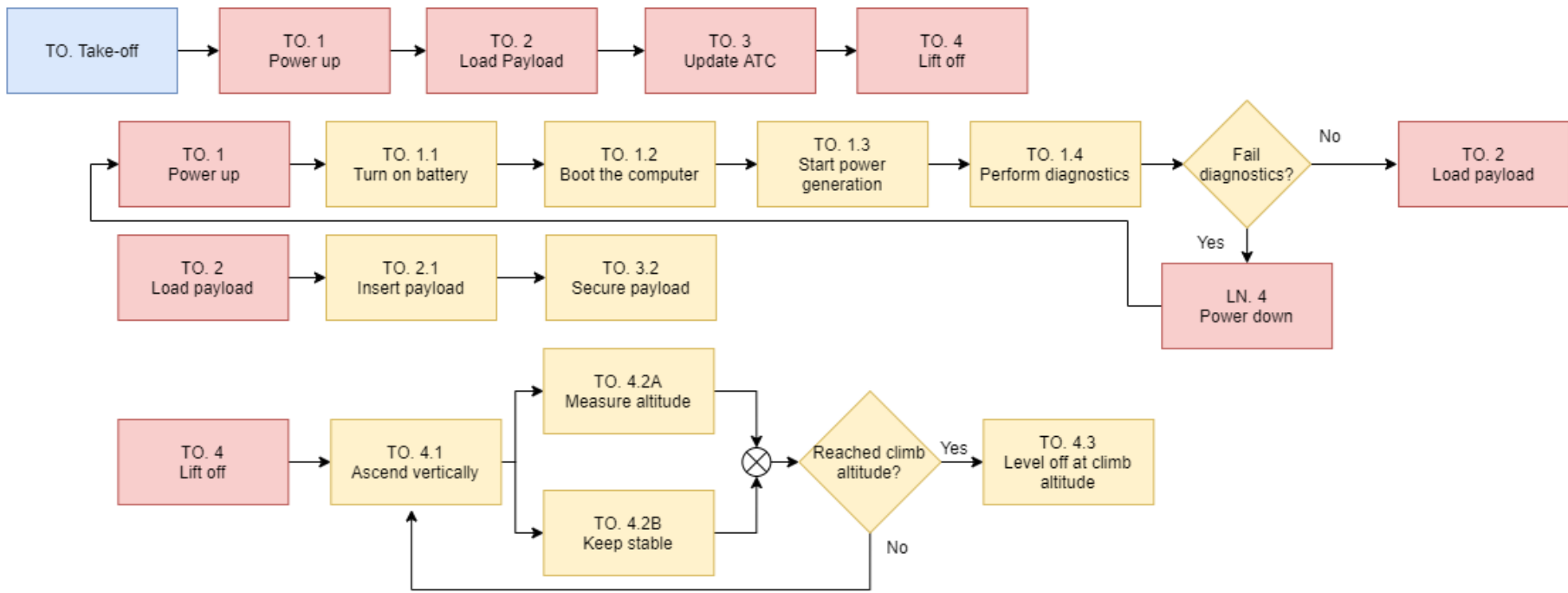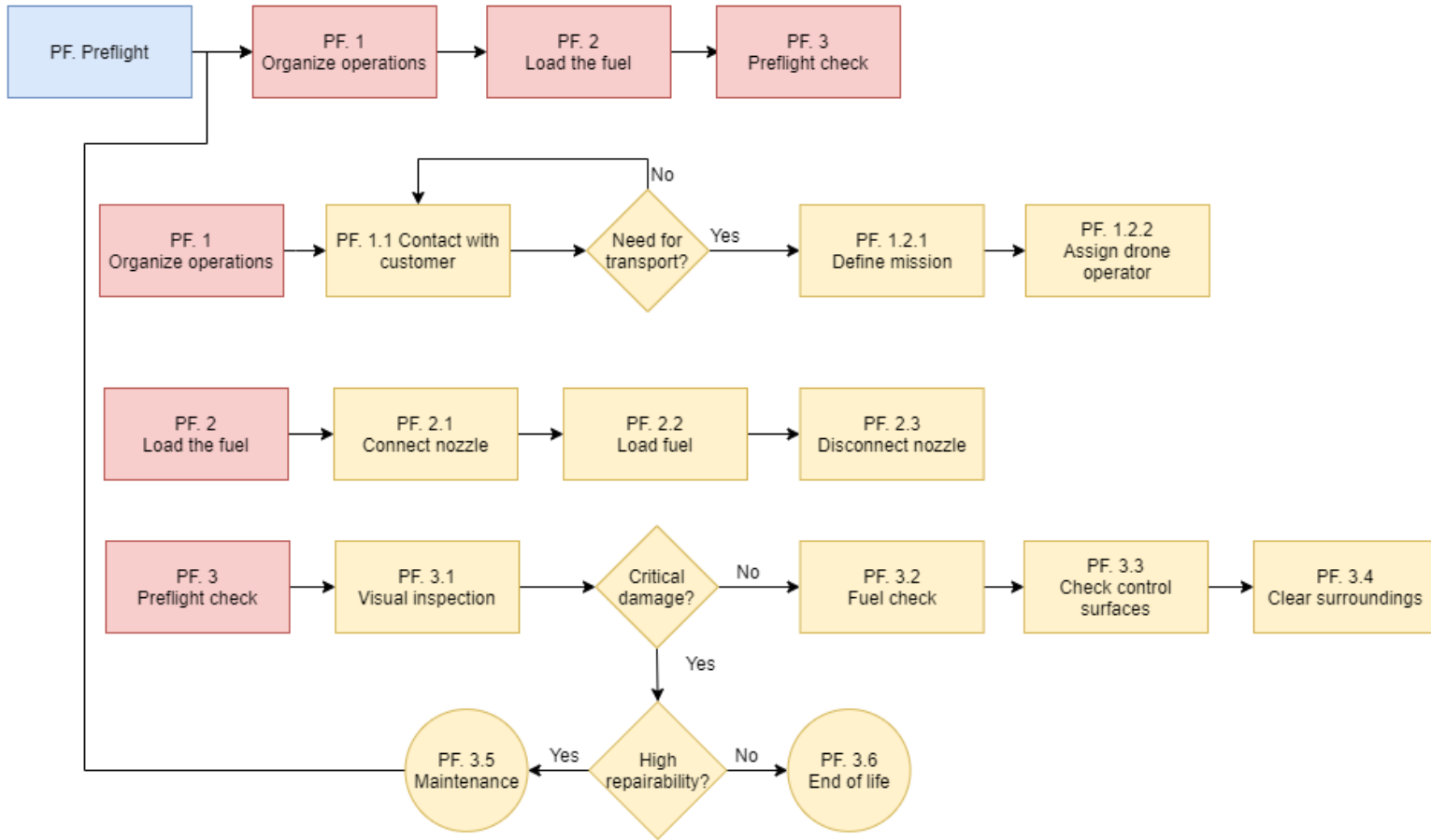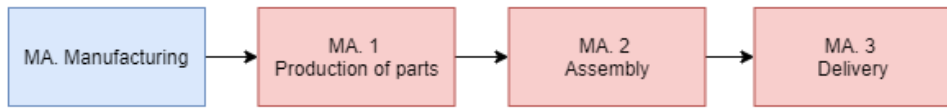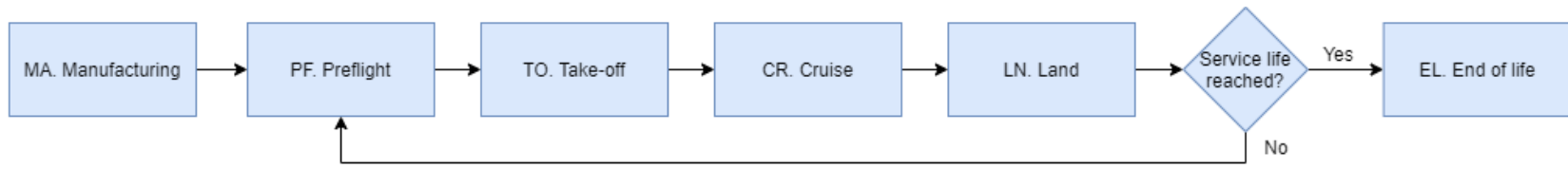|	Stability & Control (15%)	J/km/kg (10%)	Manufacturability (15%)	Cruise speed (30%)	Reliability (30%)	Total
1. Helicopter	Good	Average	Average	Good	Average	2.45
2. Autogyro	Average	Below Average	Good	Below Average	Good	2.05
3. Fixed thrust	Good	Average	Good	Good	Below Average	2.3
4. Tiltable thrust	Average	Good	Below Average	Excellent	Average	**2.55**
5. Tail-sitter	Poor	Below Average	Average	Average	Below Average	1.4

4

Requirements Overview

This chapter is used to give a general overview of the requirements for which the drone shall be designed. To start, the functional flow diagram and the functional breakdown structure are shown in section 4.1. From this, requirements are defined. These can be seen in section 4.2.

4.1. Functional Flow Diagram & Functional Breakdown Structure

The method for finding the requirements was by first analysing the functions that the drone has to preform. This was done utilising a Functional Flow Diagram and Functional Breakdown Structure, in this section both are shown. The Functional Flow Diagram was directly taken from [62]. This is because the functions of the drone at a high level has not changed. The Functional flow diagram can be found in Figure 4.1. Furthermore the requirements have either been derived from the initial mass and power budgets calculated in with the class II estimator, or they have been derived from regulations or literature.

Similarly the functional breakdown structure of the system at a high level has not changed. Although the functional break down at a system level has not changed the functional breakdown of each subsystem had been made, these diagrams can be found in their respective chapters.
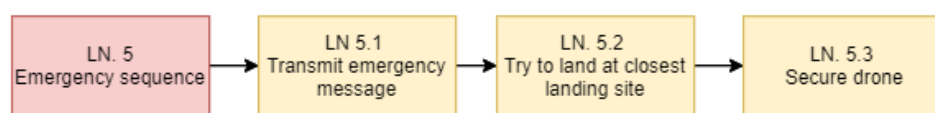
Top level

MA. Manufacturing → PF. Preflight → TO. Take-off → CR. Cruise → LN. Land → Service life reached? —Yes→ EL. End of life
Service life reached? —No→ PF. Preflight

MA. Manufacturing

MA. Manufacturing → MA. 1 Production of parts → MA. 2 Assembly → MA. 3 Delivery

PF. Preflight

PF. Preflight → PF. 1 Organize operations → PF. 2 Load the fuel → PF. 3 Preflight check

PF. 1 Organize operations → PF. 1.1 Contact with customer → Need for transport? —No→ PF. 1.1 Contact with customer
Need for transport? —Yes→ PF. 1.2.1 Define mission → PF. 1.2.2 Assign drone operator

PF. 2 Load the fuel → PF. 2.1 Connect nozzle → PF. 2.2 Load fuel → PF. 2.3 Disconnect nozzle

PF. 3 Preflight check → PF. 3.1 Visual inspection → Critical damage? —No→ PF. 3.2 Fuel check → PF. 3.3 Check control surfaces → PF. 3.4 Clear surroundings
Critical damage? —Yes→ High repairability? —Yes→ PF. 3.5 Maintenance
High repairability? —No→ PF. 3.6 End of life

TO. Take-off

TO. Take-off → TO. 1 Power up → TO. 2 Load Payload → TO. 3 Update ATC → TO. 4 Lift off

TO. 1 Power up → TO. 1.1 Turn on battery → TO. 1.2 Boot the computer → TO. 1.3 Start power generation → TO. 1.4 Perform diagnostics → Fail diagnostics? —No→ TO. 2 Load payload
Fail diagnostics? —Yes→ LN. 4 Power down

TO. 2 Load payload → TO. 2.1 Insert payload → TO. 3.2 Secure payload

TO. 4 Lift off → TO. 4.1 Ascend vertically → TO. 4.2A Measure altitude / TO. 4.2B Keep stable → (Join) → Reached climb altitude? —Yes→ TO. 4.3 Level off at climb altitude
Reached climb altitude? —No→ TO. 4.1 Ascend vertically

CR. Cruise

CR. Cruise → CR. 1 Transition to Cruise Configuration → CR. 2 Climb → CR. 3 Cruise → CR. 4 Descent

CR. 2 Climb → CR. 2.1 Climb to cruise altitude → CR. 2.2A Measure altitude / CR. 2.2B Control speed / CR. 2.2C Keep stable → (Join) → CR. 2.3 Communicate with ATC → Reached cruise altitude? —Yes→ CR. 2.4 Stop climb
Reached cruise altitude? —No→ CR. 2.1 Climb to cruise altitude

Legend

- Top level
- 2nd level
- 3rd level
- End of mission (circle)
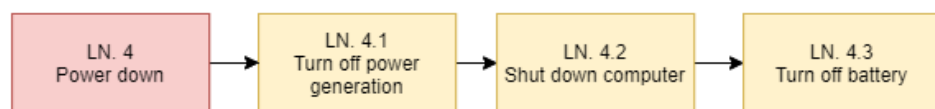- Functions (rectangle)
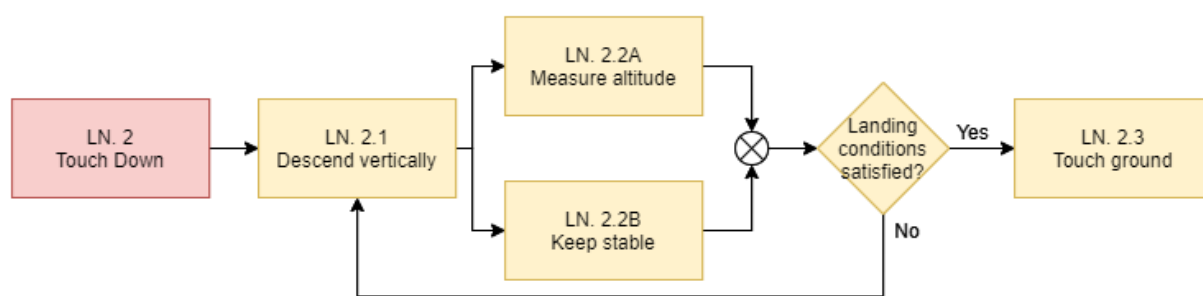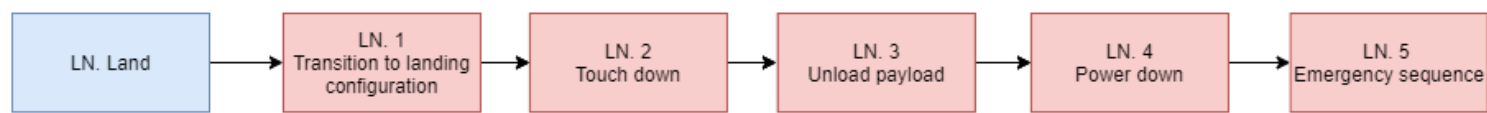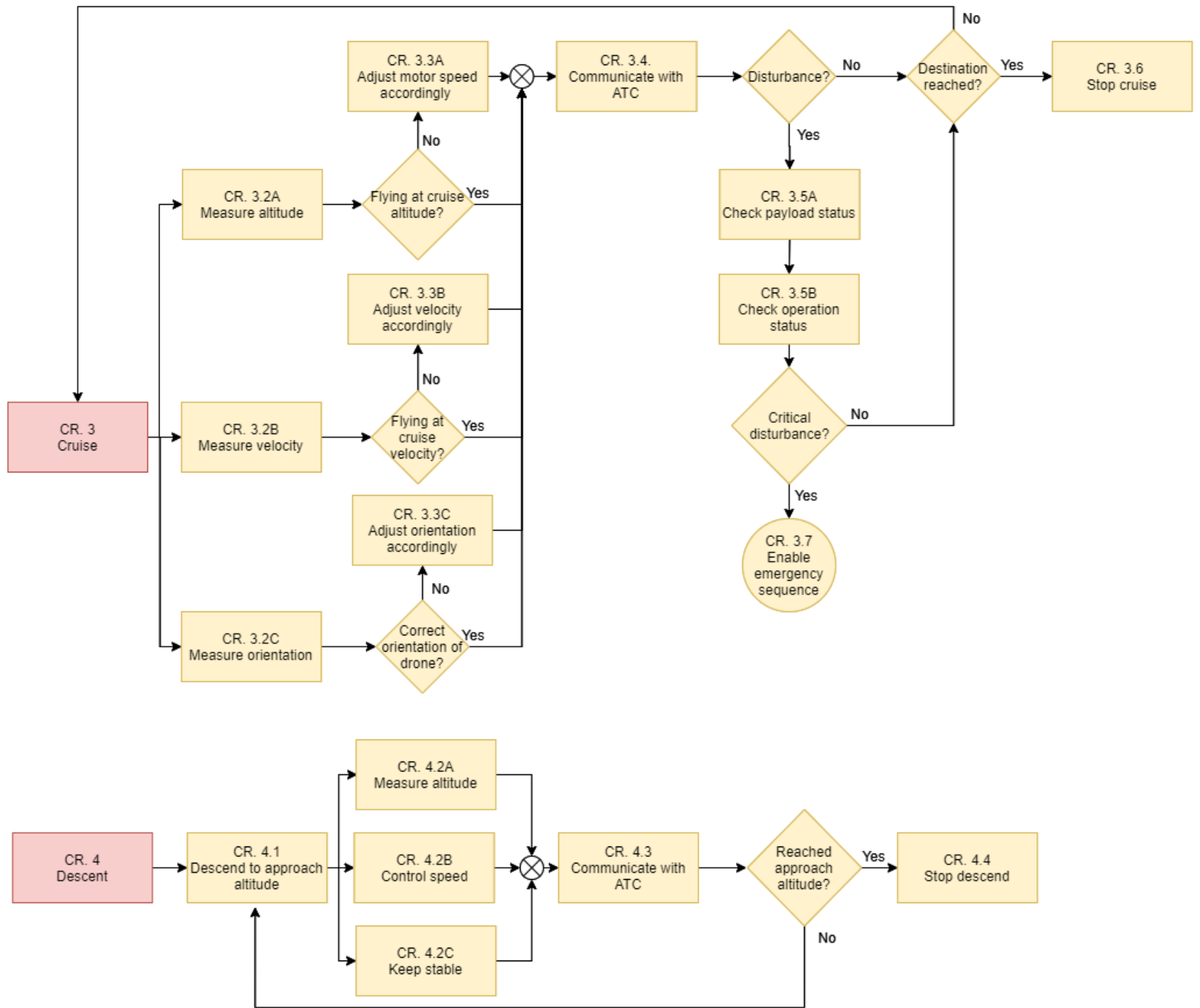- Join points (circle with X)
- OR gate (diamond)

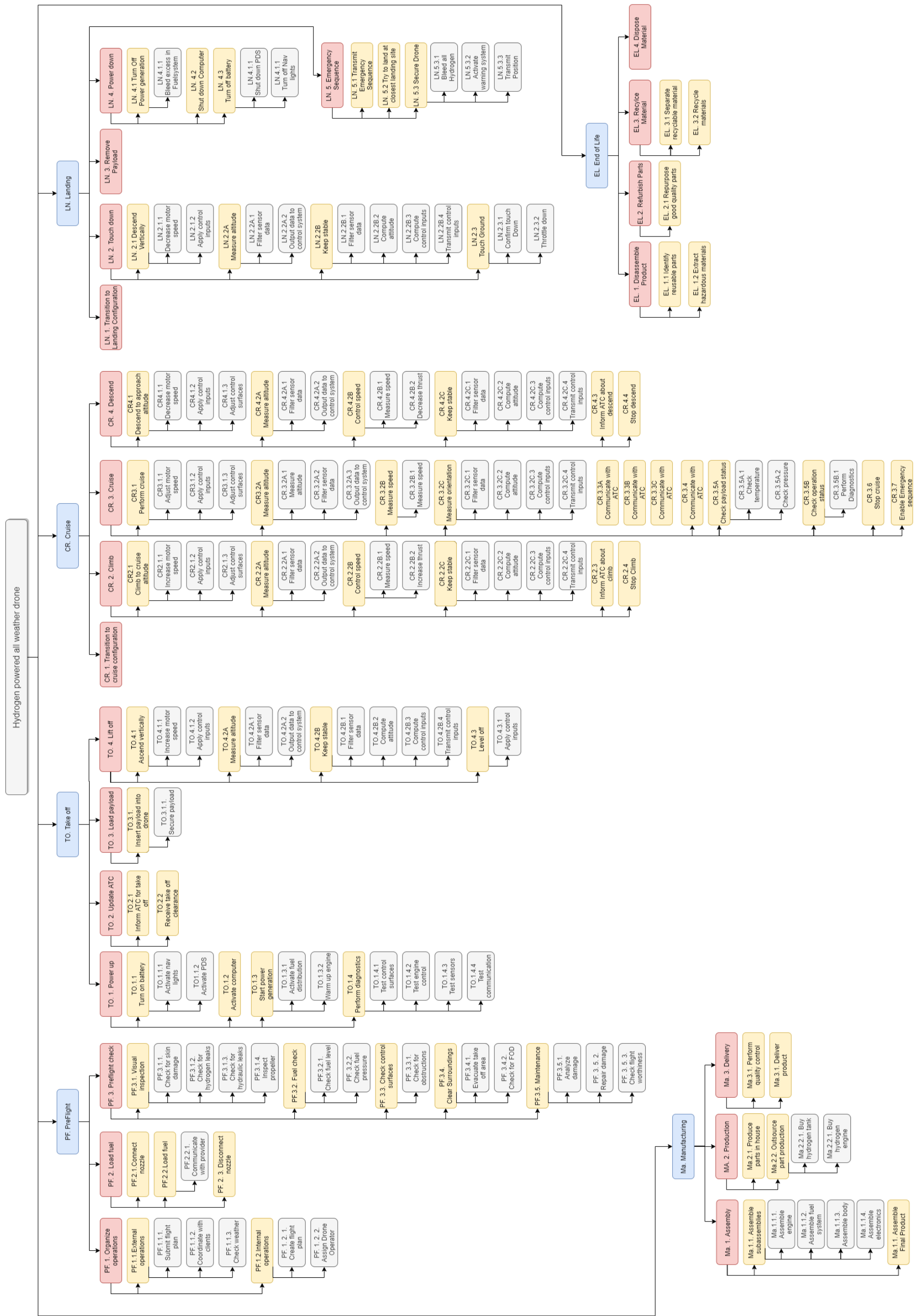Figure 4.1: Functional flow diagram

Figure 4.2: Functional Breakdown Structure

4.2. Requirements

In this section all top level requirements are listed. The requirements highlighted in bold are labeled as driving requirements, which means that these requirements drive the design more than average. The requirements in italic are key requirements which are of primary importance for the customer.

MD-SYS01: The drone shall not exceed dimensions of 2200 by 3000 by 800 [length x width x height] [mm].

MD-SYS02: The drone shall not exceed a dry mass of 35 [kg].

MD-SYS03: **The drone shall be able to carry a payload of at least 10 [kg]**

MD-SYS04: The drone shall be able to carry a payload of at least 200 by 200 by 200 [mm].

MD-SYS05: The payload shall be kept at a temperature between -10 and 45 [$°C$].

MD-SYS06: The payload shall be protected in case of a crash.

MD-SYS07: The system shall be deployable within TBD time.

MD-SYS08: The system shall not be damaged such that it is unable to continue its operation by forces imposed during mission operation.

MD-SYS09: ***The system shall be capable of handling all-weather conditions, reaching a dispatch reliability in 99% or more of the days.***

MD-SYS10: The system shall have a reliability acceptable for the transport of human transplant organs.

MD-SYS11: The system shall be able update its 3D position with a frequency of TBD [Hz].

MD-SYS12: The drone shall be able to determine its 3D position with an accuracy of TBD dimension during operation.

MD-SYS13: **The drone shall have a range of at least 100 nautical miles for a return trip.**

MD-SYS14: The drone shall be able to receive data over a distance of 100 [nm].

MD-SYS15: The drone shall be able to send data over a distance of 100 [nm].

MD-SYS16: The system shall adhere to all regulations set by ATC.

MD-SYS17: **The drone shall comply with the regulations of the specific risk category set by EASA.**

MD-SYS18: The system shall not produce more than TBD [dB] measured from the ground.

MD-SYS19: **The drone shall be able to take-off and land vertically.**

MD-SYS20: Vertical take-off and landing shall not require an area larger than a helipad.

MD-SYS21: **The drone shall have a self-loading and/or self-unloading system of the payload.**

MD-SYS22: The drone shall both be able to be controlled remotely and function autonomously throughout all flight phases.

MD-SYS23: *The unit cost of the drone shall not exceed a value of €100k.*

MD-SYS24: *The operational cost of the drone shall not exceed 0.05-0.10 [€/kg/km].*

MD-SYS25: *The drone shall be hydrogen powered.*

MD-SYS26: The hydrogen used to power the drone shall be available on-site.

MD-SYS27: The hydrogen used to power the drone shall be produced in a sustainable way.

MD-SYS28: The system shall be developed in a sustainable way.

MD-SYS29: The drone shall have zero [CO_2] emissions during flight.

MD-SYS30: **The drone shall have a circular design.**

MD-SYS31: The drone shall be reusable for 40% of its components at its end of life.

MD-SYS32: The components that are not reusable should have a lifetime of at least 10 years time.

MD-SYS33: The system shall use it resources with an efficiency of at least 40.

MD-SYS34: All employees of the system shall get at least the minimum wage according to their function as stated by Dutch regulations.

MD-SYS35: The system shall be designed such that it is possible to manufacture with current manufacturing techniques.

MD-SYS36: The system shall only use in-flight captured data for the purpose of fulfilling its mission.

MD-SYS37: The system shall not collect and store any personal information of citizens.

MD-SYS38: The system shall have a operational lifetime of 10 years time.

5

Aerodynamics

The aerodynamic subsystem design is important for the performance of the drone during hover as well as during cruise. Before starting with the design process, a functional analysis is performed and the work flow is described. Afterwards, the main wing of the drone and the fuselage are designed, followed by the main and back propellers and their integration into their ducts. In a last step, a final aerodynamic analysis of the drone will be performed and its sensitivity is be discussed.

5.1. Functional Analysis

The aerodynamic subsystem is responsible for providing lift during cruise phase, while also minimizing the effect of drag on the drone. Furthermore, it is responsible for the design of the propellers and their associated ducts. These designs shall be compatible with the size and power specifications set by the propulsion subsystem. Furthermore it has to provide cooling to the Fuel Cell and other subsystems.

5.1.1. Functional Breakdown Structure

The functions of the aerodynamics subsystem were determined before the design started off. This is shown in the form of a Functional Breakdown Structure in Figure 5.1.

5.1.2. Workflow Diagram

The Workflow of the aerodynamics subsystem is shown in Figure 5.2. Blue circles are the inputs, red rectangles are functions and the yellow diamonds are outputs.
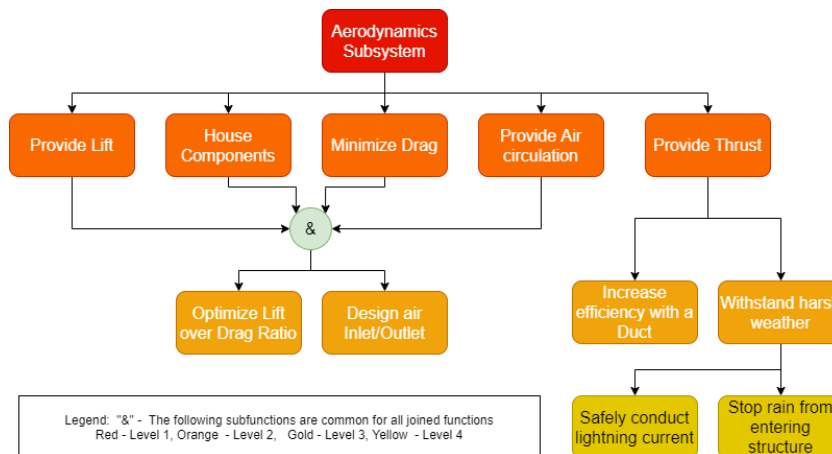

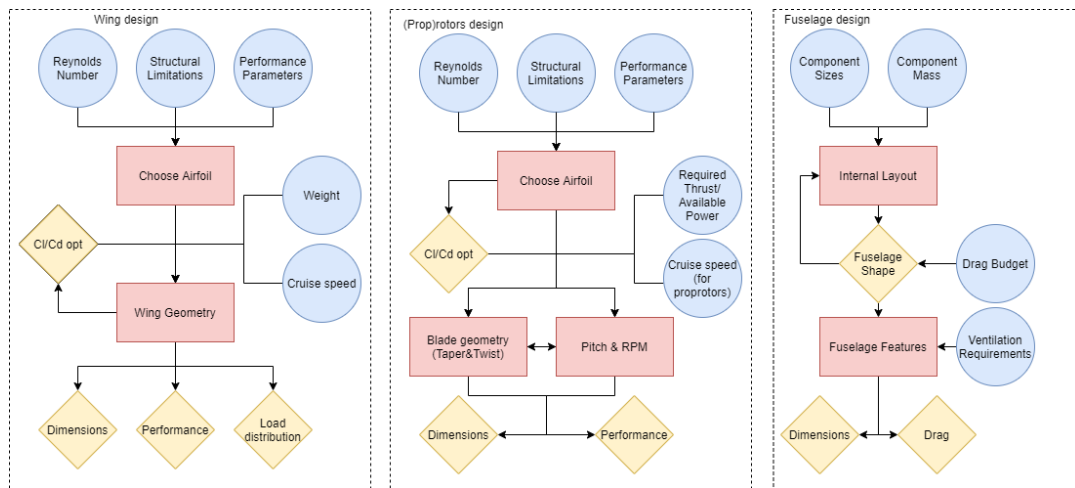Figure 5.1: Functional breakdown structure of Aerodynamics subsystem

Figure 5.2: Workflow diagram of Aerodynamics subsystem

5.2. Subsystem Requirements

MD-SYS09-AF01:   The drone shall be able to produce 345 [N] of lift during cruise.
MD-SYS09-AF02:   The drone shall have a propeller efficiency of at least 0.85 at the cruise speed.
MD-SYS09-AF03:   The drone shall provide a thrust of 64 [N] during cruise.
MD-SYS09-AF04:   The drone shall not use more than 4.2 [kW] of power during cruise.
MD-SYS09-AF05:   The drone shall have a C_{d0} of no more than 0.07.
MD-SYS09-AF06:   The drone shall be able to supply at least 90 [m^3/h] volume flow rate to the fuel Cells.
MD-SYS19-AF01:   The drone shall be able to produce a lift of 352 [N] during VTOL.
MD-SYS19-AF01-1:   The proprotors shall deliver a lift of 155[N] each during VTOL.
MD-SYS19-AF01-2:   The back rotors shall deliver a lift of 21 [N] each during VTOL.
MD-SYS19-AF02:   The drone shall not use more than 4.7 [kW] of power during VTOL.
MD-SYS19-AF02-1:   The proprotors shall not use more than 3.7 [kW] of power during VTOL.
MD-SYS19-AF02-2:   The back rotors shall not use more than 1[kW] of power during VTOL.

5.3. Aerodynamic Layout

In the following subsections, several aspects of the aerodynamic layout are discussed. First, the airfoil will be selected. Then, the layout of the wing will be investigated Finally, the design and integration of the fuselage will be discussed.

5.3.1. Airfoil selection

A first step in the aerodynamic design of the wing is the selection of an airfoil for the main wing. For this, first the Reynolds numbers during the operations of the drone are calculated. From the preliminary design phase, it is known that the drone will cruise at approximately 50 [m/s] and will have a chord between 0.5 [m] and 0.2 [m]. This equals a Reynolds range of $1.8\cdot10^6$ to $0.7\cdot10^6$. The airfoils shall have a high L/D ratio and shall be as thick as possible, in order to maximize efficiency and reduce structural weight. For the selection, the following airfoils were selected.

- NACA 0012

- NACA 2415

- NACA 5412

- CLARK Y (12% thickness)

- NACA 24112

These Airfoils were then analysed in XFLR5 for the afore mentioned Reynolds numbers. The results from this analysis can be found in Figure 5.3. It can be seen that the NACA 5412 has the highest C_l/C_d ratio of the analysed airfoils. However the Lift coefficient for this optimum ratio is very close to the maximum C_l of the airfoil. This means that during cruise, the aircraft is close to stalling, which is not favourable with respect to the all-weather requirements of the drone. Thus a CLARK Y airfoil is chosen, which has a more favourable optimum lift coefficient

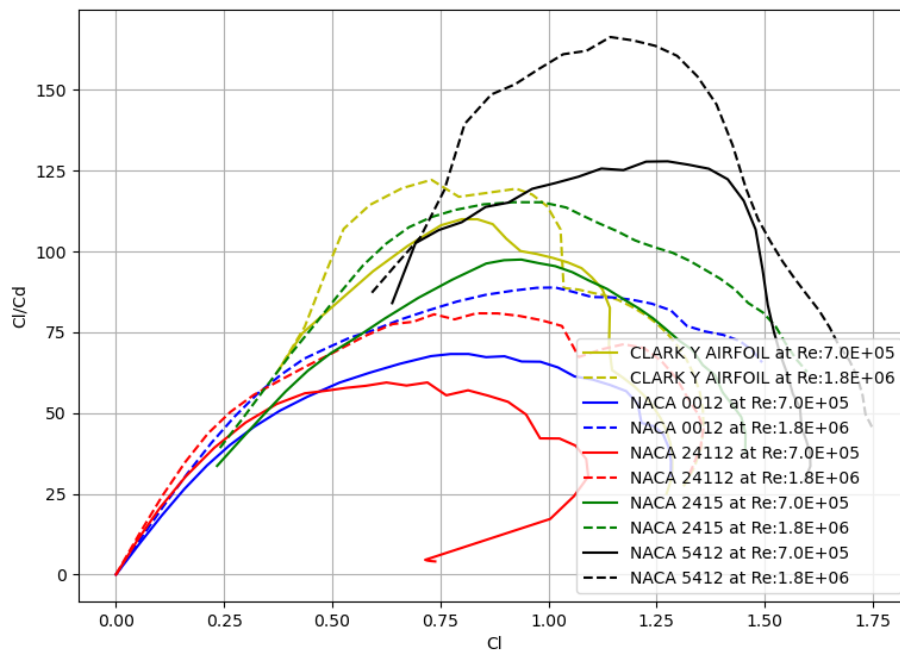of 0.74, which is further away from stalling than the previously discussed airfoil.

Figure 5.3: Comparison of Cl/Cd of different airfoils and Reynolds numbers

Furthermore, an airfoil for the horizontal tail and vertical stabilizer has to be chosen. As these surfaces have to be able to efficiently produce lift in both directions, a symmetric airfoil has to be used. For this purpose, a NACA 0012 airfoil is used, as this airfoil offers good low Reynolds numbers performance, as well as being a thick profile, which will reduce weight of the empennage assembly. Both airfoil profiles can be seen in Figure 5.4 and Figure 5.5 respectively.
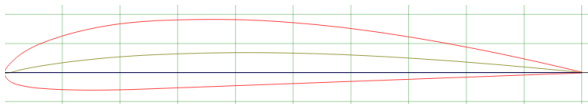

Figure 5.4: CLARK Y Airfoil

Figure 5.5: NACA 0012 Airfoil

5.3.2. Wing layout

For the layout of the main wing an aspect ratio of 5 was chosen. This is quite a low aspect ratio for an aircraft when compared to civil aircraft, this however is necessary, as the rotors will be integrated at the tip of the wing, thus the span of the wing has to be kept smaller than usual in order to comply with certification requirements for the specific category of drones set by EASA. As the flight regime is significantly below the compressibility limit, it is chosen that there is no sweep present a the quarter chord line. Furthermore the taper ratio of the wing is set to 0.6, as this is a good compromise between an optimal aerodynamic efficiency at a taper of 0.37 [38] and the increased structural weight of a higher taper ratio. This wing layout leads to a C_{d0} of 0.008. The wing will be mounted with 2.5° of incidence, to ensure optimum L/D characteristics during cruise, while keeping the fuselage at minimum incidence.

Similarly to the main wing, the taper ratio for the horizontal tail is chosen to be 0.6. However the Aspect Ratio is reduced to 4, as a higher aspect ratio increases the weight of the wing in return for higher lifting efficiency, this efficiency is however not needed, as in an optimal case, the horizontal tail shall not produce a significant amount of lift.
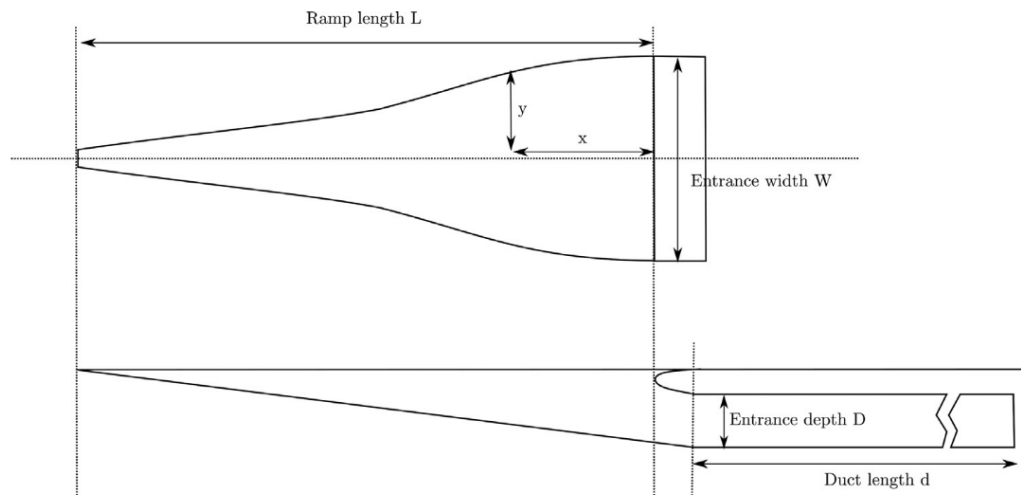
Figure 5.6: Geometry of a NACA Duct[42]

5.3.3. Fuselage Design and integration

In order to gain an understanding of the zero lift coefficient of the drone, the main body of the drone has to be designed. For this the internal layout of the drone has to be determined. For this the different components of the drone are positioned. These include the fuel cells as well as their connectors, a main computer, electronics and the payload. From this the body can be designed. The final shell of the drone has a frontal area of approximately 0.06 $[m^2]$. As the shape of the fuselage is similar to an elongated ellipsoid with an aspect ratio of 4.5, the drag coefficient can be approximated with 0.0921[12]. If this is scaled with respect to the wing area, this equals a drag coefficient of 0.035. The wing will be integrated in a high wing position, to ensure ground clearance for the propulsion system.

In chapter 6 it was determined that each fuel cell needs an airflow of 15 $[m^3/h]$. For the 6 used cells, this means a Volume flow rate of $6.9 \cdot 10^{-4}$ $[m^3/s]$. For this an intake has to be fitted to the fuselage of the drone, as well as an outlet. In order to prevent rain and snow from entering the interior of the drone, the intake will be fitted on the underbelly of the drone. The air will be forced into the intake by the movement of the drone. the outlet will be mounted on top of the fuselage and will also serve as a deflector for the intake of the back rotor, which will prevent air from entering the duct during cruise and will thus decrease the drag of the duct. The inlet will be a NACA duct, which will provide ventilation, while also reducing drag [17]. The general geometry of such an inlet can be seen in Figure 5.6, the angle of the ramp is chosen to be 7°. From the research done by Silveira et al. [11], it can be found that the ratio of mass flow through the duct vs the inlet Area ($A = D \times W$) is equal to 56%. As the required mass flow is very low, the intake area lies in the range of 30 $[cm^2]$ and thus its contribution to the total drag diminishes.

5.4. Proprotor Design

The proprotor design was done with the use of XFLR5 and JBLADE. JBLADE is based on XFLR5 and uses Blade Element Momentum theory for the calculations. The program allows for creating and analyzing of propellers out of made airfoils. The viscous flow setting was used for the airfoil analysis and the propeller simulation parameters included a root loss correction, 3D correction and foil interpolation. The tip loss correction was left out due to the use of a duct.

First of all the configuration is discussed, after which the airfoil selection is done. Thereafter the taper and twist of the blade are discussed. The airfoil selection and the taper & twist decisions is an iterative process as the taper and twist determine the requirements for good airfoil selection and vice versa. In addition, the proprotor has to be efficient in both VTOL and cruise. This means that the design has to take into account the efficiency requirements for both phases. A good balance had to be found in optimizing the design. In the section, lift properties are discussed. It should be noted that even though it is called lift, during cruise it is actually the thrust. As it is a proprotor, it has to provide lift during VTOL and thrust during cruise. For the blades, the thrust in cruise comes from the 'lift' that the blades generate due to rotating.

5.4.1. Configuration

In propulsion subsystem calculations, the radius, the required thrust and power available of the proprotor were determined. With these values, the optimum proprotor was designed. The radius of each of the proprotors is 0.37 [m] with a hub radius of 0.05 [m] and they should deliver each 110 [N] of thrust (neglecting the duct as explained in section 7.4) with an input power of 1.85 [kW] during VTOL. This thrust is without the duct efficiency. Furthermore, the cruise speed is 50 [m/s] which should be obtained by a thrust of 31.5 [N] and an available power of 2.1 [kW] for each proprotor. The number of blades was to be chosen during the aerodynamic design, as the input from propulsion is only the required thrust and available power. The proprotors consist out of 2 blades, which is reasonable for a UAV. Next to that, the same configurations were tried with using 3 or 4 blades. However, they were less efficient overall.

5.4.2. Airfoil selection

The aerodynamic design of the proprotor starts of with the selection of the airfoil or possibly airfoils. Same as for the wing, the airfoils are selected based on their performance at certain Reynolds numbers. The Reynolds numbers along the span of a blade vary drastically, as the airspeed is a lot higher at the tip of the blade than at the root (Reynolds number varies linearly with airspeed and chord). For this proprotor, the number can increase along the blade from zero to approximately 500,000, assuming an initial rpm and chord guess of 4,000 and 0.04 [m] respectively. Such a large difference in Reynolds number is however undesirable, as will be explained in subsection 5.4.3. Therefore, the airfoils are analysed on performance for Reynolds numbers up to 300,000.

Furthermore, for the low Reynolds numbers (<300,000) that the blade experiences, the best approach is to design an airfoil for optimal hover performance [60]. This has to do with the fact that optimizing for cruise efficiency effects the hover performance very negatively, whereas optimizing for hover performance only has a slight negative effect for cruise efficiency. The significant drawbacks for cruise efficiency only happen at larger Reynolds numbers. For larger Reynolds numbers, more of an optimization has to be found between hover performance and cruise efficient airfoils, because the the speed at some of the tip segments of the blade could go trans and supersonic which lowers the cruise efficiency drastically [60] [30]. Airfoils with good drag divergence numbers should be chosen and tip speed has to be reduced. In these cases optimizing for hover performance would thus lead to inefficient cruise flight. The airfoil for this design is thus mainly designed for the VTOL phase.

Good airfoil performance is characterized by high C_l/C_d values, high $C_{l\alpha}$, low $C_{m\alpha}$ and high stall angles. The first two are to ensure good lifting qualities. The low $C_{m\alpha}$ is required as the slender rotor blades are not able to withstand the aerodynamic moment. This causes distortion and thus makes the rotor inoperable [67]. This requirement eliminates highly cambered and thin airfoils, even though they have great lift over drag performances at low Reynolds numbers. High camber and little thickness are inherently related to high $C_{m\alpha}$. High stall angles are desired as the blade experiences large differences in angle of attack due to the twist (discussed in subsection 5.4.3). With these criteria in mind, the following three airfoils were found.

- NACA-11-H-09

- BELL/WORTMANN FX 69-H-083

- BOEING-VERTOL VR-5

These three airfoils were then analyzed in XFLR5 for Reynolds numbers of 50,000, 150,000 and 250,000. The results are shown in Figure 5.7 and Figure 5.8. It can be seen that the Bell/Wortmann airfoil has the most consistent performance for all three Reynolds numbers. It does have however a consistent lower lift over drag and lower stall angle. The NACA and Boeing airfoils are very similar with the Boeing getting the edge for the lower Reynolds numbers and slightly larger stall angles. The Boeing airfoil is thus the best option.
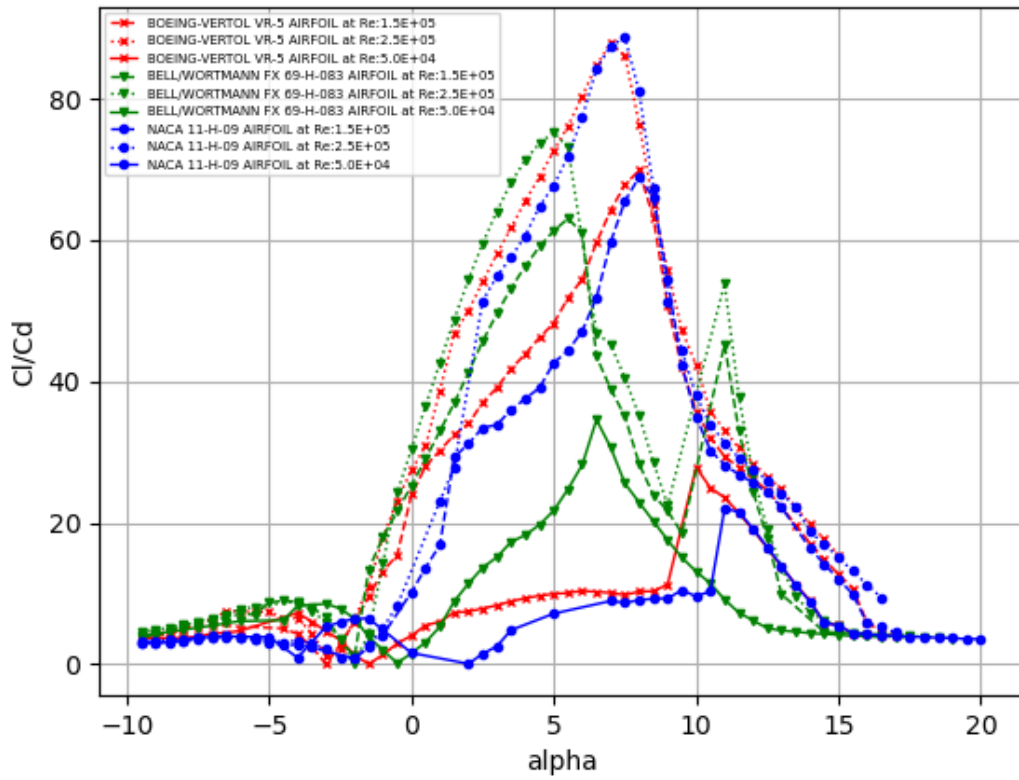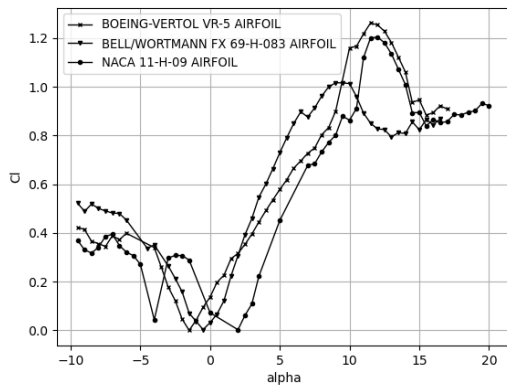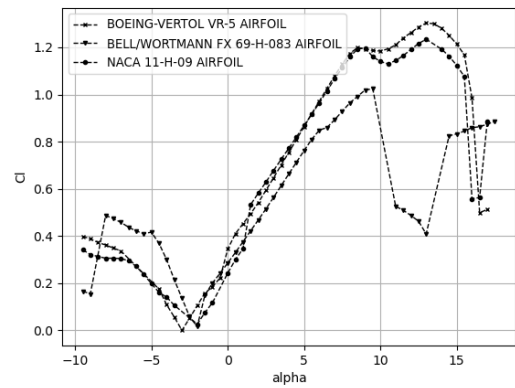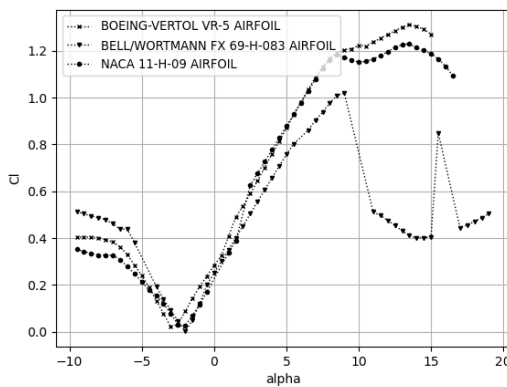
Figure 5.7: $C_L/C_D - \alpha$ curves

(a) $C_L - \alpha$ curve for Reynolds = 50000

(b) $C_L - \alpha$ curve for Reynolds = 150000

(c) $C_L - \alpha$ curve for Reynolds = 250000

Figure 5.8: $C_L - \alpha$ curves

As the Bell/Wortmann airfoil has much better characteristics at the low Reynolds number (Figure 5.8a), it was considered using this airfoil for the root sections as there the lowest Reynolds numbers occur. Due to the twist however (see subsection 5.4.3), the root section has the largest angle of attack and the airfoil here should thus have high stall angle of attack. This is important as local stall would decrease the thrust and increase drag. Even though this is the part with the lowest contribution to the thrust, it is best to avoid it in order to have better performance. The Bell/Wortmann airfoil lacks in this regard and thus cannot be used at the root. To conclude, the BOEING-VERTOL VR-5 is the selected airfoil for the proprotor blades and its layout is shown in Figure 5.9 [1], where the brown line represents the camber line. The characteristics are max thickness 12% at 35% chord and max camber 3.4% at 35% chord.
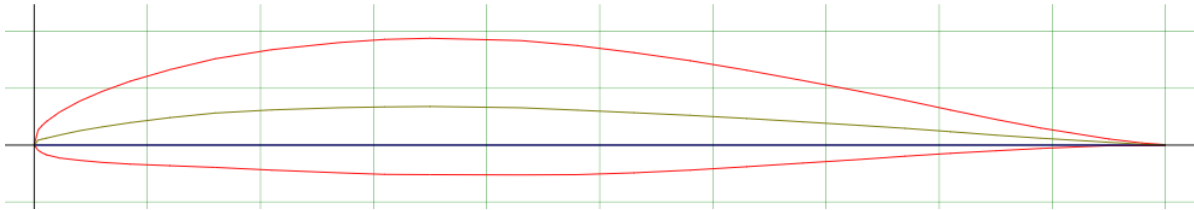

Figure 5.9: BOEING-VERTOL VR-5

5.4.3. Taper, Twist & RPM

The proprotors have multiple characteristics. The taper, twist and rotations per minute (RPM) will be calculated in the following consecutive paragraphs.

Taper

The problem with rotor blades without taper and/or twist is the exponential lift distribution. This means that the lift increases along the span of the blade. This causes undesired stresses in the structure and increases rotor-induced power [67]. This is mostly the case for the VTOL phase of the proprotor, as for the cruise the Reynolds number is about even along the span due to the high forward flight speed. The exponential distribution has several reasons. First of all, the airspeed increases along the span of the blade. A segment in the tip of the blade travels a larger distance than a segment in the root of the blade, but in the same time frame. Lift is calculated using Equation 5.1, where C_L is the lift coefficient, ρ is the air density, V is the airspeed and S is the surface area. Lift is thus proportional to the airspeed squared. Furthermore, Reynolds number is calculated with Equation 5.2, where Re is the Reynolds number, V is the airspeed c is the chord and ν is the kinematic viscosity.

$$L = C_L \cdot 0.5 \cdot \rho \cdot V^2 \cdot S \tag{5.1}$$

$$Re = \frac{V \cdot c}{\nu} \tag{5.2}$$

Airfoils usually generate higher values for C_l at higher Reynolds numbers. Evidently, the lift also increases with increasing airspeed. The surface S is proportional to the chord. With this it became apparent that $L \propto C_l \cdot Re \cdot V$, where C_l is the lift coefficient of the airfoil at a segment. Hence the lift distribution, for same α and chord along the span, heavily increases towards the tip of the blade due to increased airspeed and C_l.

Even though linearization of the lift distribution is necessary, it has obvious drawbacks. The blade generates less lift, as the contribution of the most valuable parts is reduced. It is therefore critical that the segments near the root of the blade generate more lift. This will not only compensate for the loss in force, but it will also add to a more evenly distributed lift. The way this was tackled was by taking the opposite measures for the root segments as for the tip segments.

In order to reduce the lift curve slope, two measures were taken. First of all the blade is tapered. This means that the chord of the blade decreases along the span, with the smallest value at the tip. This flattens the curve of the Reynolds number (and therefore also the lift curve). The optimization of the tapering was found by altering the taper ratio until the curve is flattened, but not to the extend that the Reynolds number drops. The difference between the non tapered and tapered blade is shown in Figure 5.10, for Reynolds numbers along the blade span during VTOL. The non tapered blade has a chord of 0.05 [m], whereas the tapered blade has a decreasing chord of 0.06

---

[1]http://www.airfoiltools.com/airfoil/details?airfoil=vr5-il

[*m*] to 0.027[*m*] (TR = 0.45). The chord at the root is higher than the initial chord to account for the decrease of lift in the tip segments. The chord is visualized in Figure 5.12 along with the twist for the positions on the blade span. The set RPM is 3,630, the RPM value for the hovering phase, which will be discussed later. RPM is important as it determines the airspeed at the blade segments.
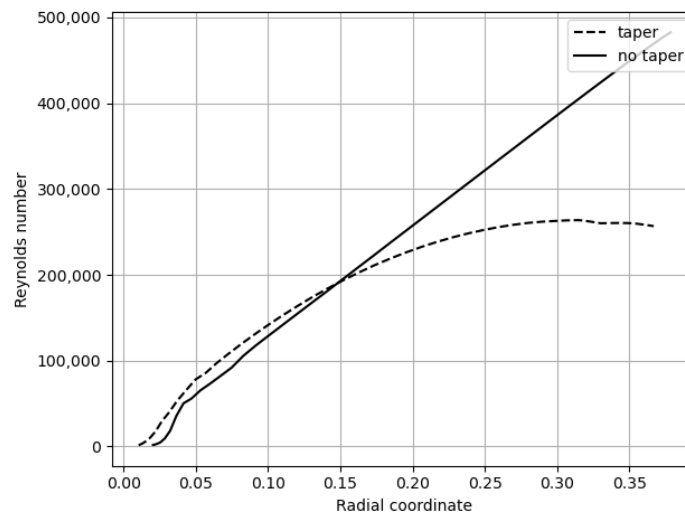

Figure 5.10: Reynolds numbers along the blade span for both tapered and non tapered blades

As can be seen from Figure 5.10 is that the maximum Reynolds number experienced for the tapered blade is a little under 300,000, which is why this maximum value is used in the airfoil selection analysis. The non tapered blade has the number running up all the way to over 450,000, which means the lift at the tip is reduced by over a third at this segment.

Twist

The second measure is negative twist. The negative twist decreases the angle of incidence and therefore the effective angle of attack along the blade, ensuring consistence or even decrease in lift coefficient. As previously stated, the C_l increases towards the tip due to increased Reynolds number, which is why this measure is necessary and efficient. Twist is important because of another reason as well. This reason is the inflow angle. The inflow angle is the angle the airflow makes with the airfoil. The pitch at a blade segment is the sum of the inflow angle and the angle of attack. If the pitch is lower than the inflow angle it thus means that there is a negative angle of attack. This is visualized in Figure 5.11, where θ is the pitch, α is the angle of attack and ϕ is the inflow angle.

In order to make the segments operate at a more efficient c_l/c_d angle of attack, the pitch and twist need to be adjusted for this inflow angle. Next to that, the inflow angle is highest at the root and decreases towards the tip due to the increase in airspeed [9][60]. For equal pitch along the blade this would mean that the angle of attack actually increases towards the tip. Hence, the negative twist has to be adjusted for the decreasing inflow angle as well in order to ensure a slight decrease in angle of attack. For hovering in the VTOL phase, this inflow angle is significantly lower than for the cruise phase. In cruise, inflow angle can go up to 90° at the root section [73]. Hence, the twist for the cruise phase, where the proprotor acts as a propeller, has to be greater than in hover phase for the most efficient design. The problem with optimizing the twist for the cruise phase is that in the hover phase the angles of attack are higher than the optimal value. Most of the sections at the root will stall due to this high angle of attack. The problem with optimizing twist for the hover phase is that in cruise the angles of attack are too small to create good lift (thrust) and will drastically increase toward the tip. Part of the problem is taken care of by using a change in blade pitch for which a simple blade pitch mechanism is included. Pitching the blades after the VTOL phase counters the effect of increased inflow angle. However, the change in inflow angle is still greater for cruise, which means that the angles of attack are different for both phases.

The optimized twist was found by fitting the requirements of Thrust and Power, as described in subsection 5.4.1, for both cruise and VTOL. This optimization was an iterative process where also the RPM was altered to find the best twist. That is because the RPM determines the provided Thrust and the Power needed, which need to fit the
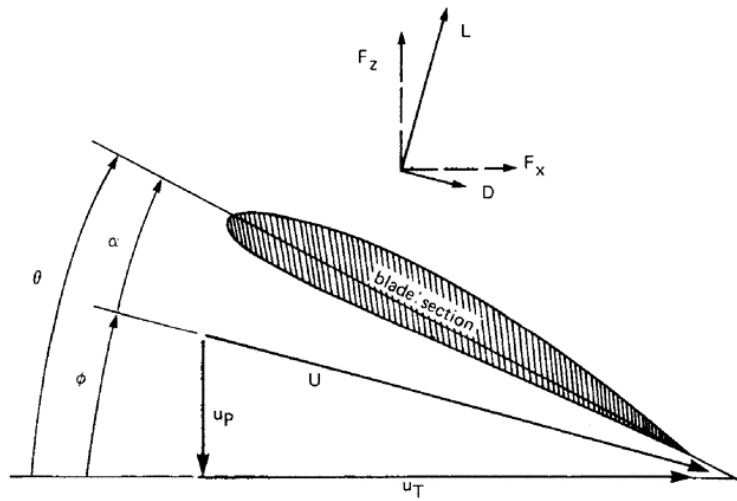
Figure 5.11: Pitch of a blade section [25]

requirements. However, the RPM dictates the airspeed along the blade as well, which means that the inflow angle depends on it and thus the twist. The final twist is a decrease of 18° from root to tip, where the root is set at +18° so that the tip is at a 0° angle. The twist is a linear decrease that starts at 7.2 [cm] from the root. The inflow angle only starts to decrease at this point, which is why that is where the twist starts. The negative twist is a linear decrease as the inflow angle decreases linearly as well. Furthermore, it usually gives better manufacturability and less costs than a non-linear decrease, but that depends on the production methods [67]. The twist is visualized in Figure 5.12 together with the chord distribution for positions along the blade span. Both graphs start close to zero as this is where the hub is.
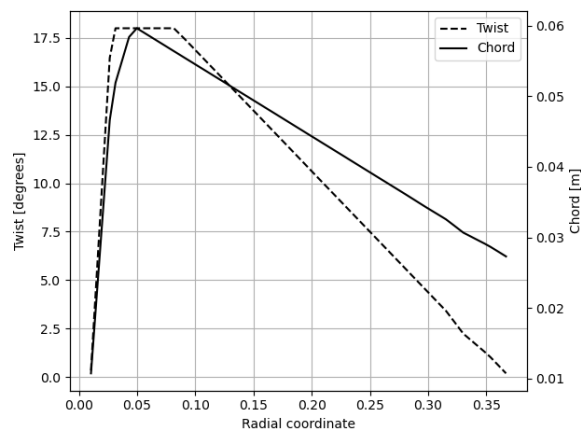

Figure 5.12: Twist & Chord distribution along the blade span

Pitch & RPM

With the twist and taper, the pitch and RPM were changed in order to fit the power and thrust requirements stated in subsection 5.4.1. If the pitch is increased, it means higher angles of attack and thus higher lift (thrust). However, this also requires more power at the same RPM. Increasing RPM also means that more lift is generated, but that the required power increases as well. The pitch was set for both cruise and hover at their best fit. This would ideally be so that the angles of attack at the blade segments are for optimal C_L/C_D. For the Boeing airfoil, this is at 8.5°. The RPM is an important parameter. As stated earlier, most of the factors such as airspeed, inflow angle and resulting lift coefficient (due to Reynolds number) depend on it.

For the VTOL phase, the blades operate at almost static conditions (no windspeed). As discussed earlier, the inflow angles are thus not as high as in cruise. Hence, a pitch of 10° is enough to have the optimal angle of attack at

the root sections. The RPM needed to provide the required lift was then found to be 3,630. The resultant power required and generated thrust are then 3.7 [kW] and 220 [N]. With the increased duct efficiency it leads to a thrust of $220 * \sqrt{2} = 311.1$ (see section 7.4). The angles of attack along the blade span and the resultant lift coefficient are shown in Figure 5.13a and Figure 5.13b respectively. From the figures it is clear that the negative twist efficiently decreased the angle of attack. The resultant lift coefficient curve is flattened and even lowered as a result. It can be seen that the lift coefficient is relatively low at the highest angles of attack, because these sections are close to the root. This means that the Reynolds number is relatively low and thus generates the blade lower lift coefficients.
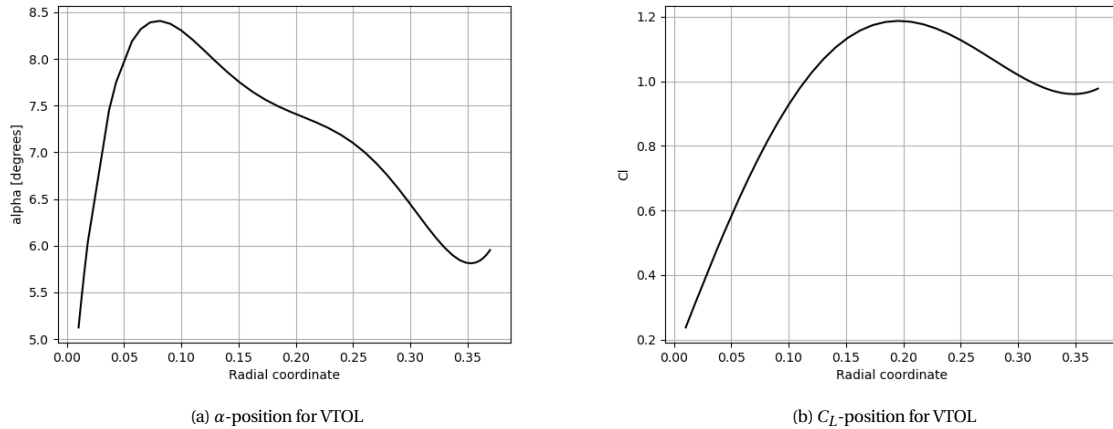

(a) α-position for VTOL

(b) C_L-position for VTOL

Figure 5.13: VTOL α&C_L

For the cruise phase, simply setting the pitch so that the angles of attack are in the right range is not enough since the RPM then has to change to fit the required Power and Thrust. Changing the RPM changes the inflow angle and thus the angles of attack, meaning that the pitch has to change again. One parameter that helps finding the optimum combination is the propeller efficiency. This has to be as high as possible for the cruise speed of 50 [m/s]. The efficiency-windspeed curve shifts by altering the RPM and pitch. This is shown in Figure 5.14 for a few different RPM and pitch. First of all, in Figure 5.14a, the RPM set for the hover phase and then increased pitch from 10° (hover) to 20° to 30°. The 30° pitch has a good efficiency for the cruise speed of 50 [m/s]. However, the RPM of 3,630 is relatively high and the propeller would deliver more thrust than needed and use more power than is available. In Figure 5.14b, the 30° pitch is now set with a RPM of 3,000. It can be seen that the propeller is now less efficient, but it is actually closer to the power and thrust requirements. The RPM was then lowered even further and pitch was increased to obtain the final settings: 2,050 RPM and 42° pitch. For these values, the propeller has an efficiency of 0.88, a required power of 2 [kW] and thrust of 32 [N].

(a) Propeller efficiency for different pitch

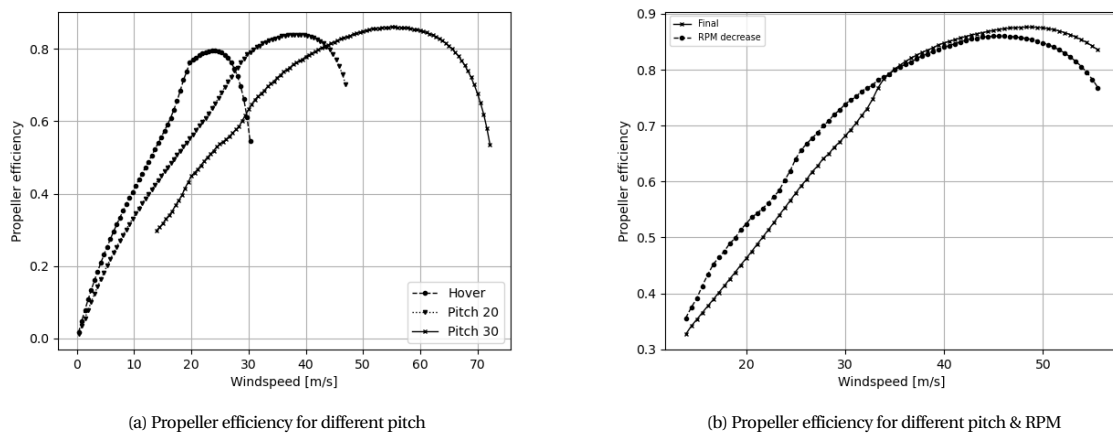(b) Propeller efficiency for different pitch & RPM

Figure 5.14: Propeller efficiency as a function of windspeed for different pitch angles and RPM

The optimal RPM and pitch were found by looking at the angles of attack along the blade as well. As discussed

earlier, different RPM values need different pitch to obtain the same angles of attack. Since the inflow angles at the root of the blade are significantly larger than for the VTOL phase, the angles of attack are less uniform. The goal was to have as much part of the blade as close to the optimal angle of attack as possible (8.5°). In Figure 5.15 the curves for C_L and α are shown for the chosen RPM and pitch.

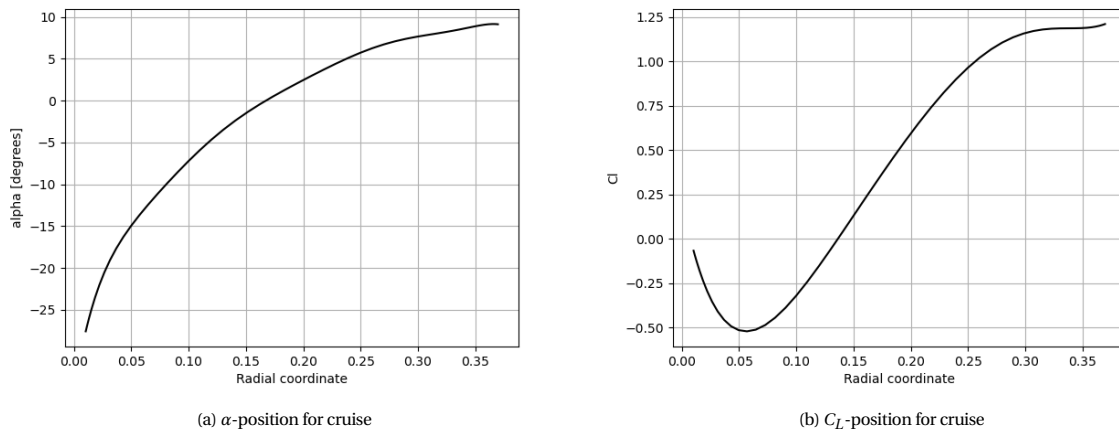(a) α-position for cruise

(b) C_L-position for cruise

Figure 5.15: Cruise α&C_L

It is clear that the angle of attack varies more than in cruise, which leaves the problem of the uneven lift distribution. However, in cruise the airspeed along the blade is more uniform due to the high cruise speed. In addition, Reynolds number is constantly 200,000 along the blade. Due to these factors, the lift distribution is not a critical problem for the structure. A picture of the propeller blade is shown in Figure 5.16 for visualization purposes.

(a) Front view of the blade

(b) Back view of the blade

Figure 5.16: 3D images of the proprotor blade

5.5. Back Rotor

The back rotors were designed in the same way as the proprotors with the same programs and methods. The requirements for the back rotors is a generated thrust of 21 [N] for each rotor with an available power of 960 [W] in total. The back rotors have a radius of 0.135 [m]. The difference with the proprotors is that the back rotors do not tilt and thus only need to be optimized for the VTOL performance. The back rotors each have three blades, because it requires less RPM than two blades and is efficient enough to produce the required thrust with the available power. The hub radius is 0.013 [m].

The back rotors have a significantly smaller radius than the proprotors. This would mean that the Reynolds numbers are smaller. However, the back rotors have to operate at a higher RPM which increases the airspeed. The Reynolds numbers vary from 0 to 180,000 for the final rpm, which means that from the airfoil selection analysis in the proprotor design it was concluded that the BOEING-VERTOL-VR-5 is the best option.

The problem that arose for the proprotor regarding the lift distribution is less of a problem for the back rotors. The back rotor blades have a smaller difference in local airspeed and they are not as slender as the proprotor blades. Therefore, taper is unnecessary in the blade. This is also convenient as it gives the rotor a better manufacturability.

The chosen constant chord is 0.03 [m]. Twist on the other hand is still necessary in order to overcome the inflow angle. Using the same methods as for the proprotor blades, it was found that the optimal linear twist is from +18° at 0.013[m] till 0° at the blade tip. The pitch and RPM values, in order to meet the power and thrust requirements while being as close to the optimal angle of attack as possible, are 23° and 6250 respectively. The resultant power required and generated thrust are then 960 [W] and 43 [N] respectively. The same as for the proprotor, the graphs for α and C_L along the span are shown in Figure 5.17. The blade is shown in Figure 5.18 for visualization purposes.
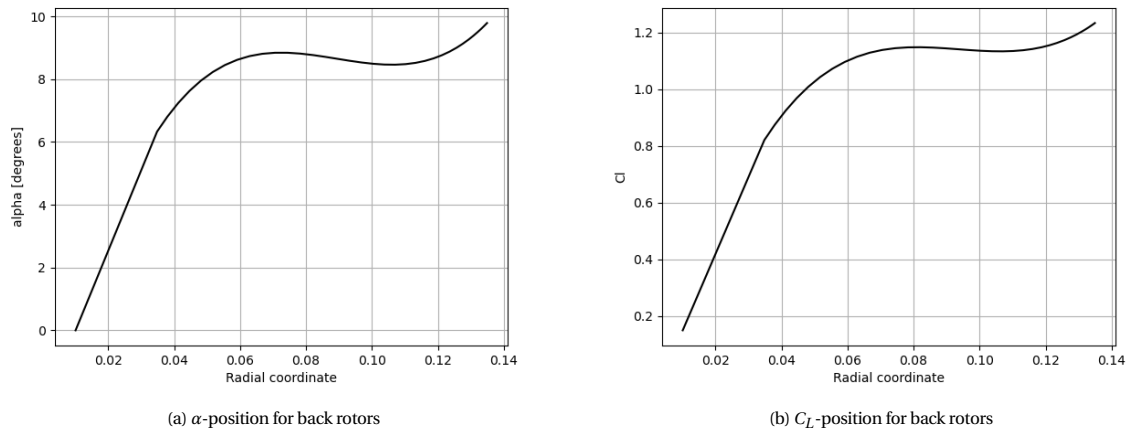

(a) α-position for back rotors

(b) C_L-position for back rotors

Figure 5.17: Back rotors α&C_L

(a) Front view of the blade

(b) Back view of the blade

Figure 5.18: 3D images of the back blade

5.6. Duct Design

In order to utilize the performance increase of the ducted fans in contrast to an open propeller, the inlet and the duct of the fan has to be properly designed in order to minimize intake losses. Improper design of the intake can make the ducted fan less efficient than an equivalent open propeller as discussed by Wahl et al. [70].

The restrictions on the inlet vary between the front and back fans, as their integration into the aircraft is different. The back fan can duct can be integrated into the fuselage structure and can thus use an elliptical bellmouth shaped inlet. Furthermore as discussed in chapter 7, the duct will expand with a ratio of 1.2 from the propeller are to the exit of the duct.

For the duct of the front fans, this inlet can not be used as the space required for such an inlet is not acceptable on the tip of the wings. Thus a different duct has to be designed. A study of different inlet geometries was performed by Graf et al. [20]. This study found that 2 profiles performed the best during VTOL and cruise. these profiles had a thickness of 12% of the chord, and a leading edge radius of 3.65% or 3.75% respectively. Both profiles placed "the leading edge near the exterior of the profile to allow more room for the pressure gradient to change gradually."[20]. It was found that the second profile performed best during both situations, due to the better attachment of flow.

These experiments were performed at an aspect ratio of 2 with $AR = d/c$, thus it is chosen to have the duct have the length equal to the radius of the fan.

From Figure 5.24, C_{d0} of an 12% thickness airfoil can be found to be 0.006. Using the duct circumference times its chord as the reference area and rescaling it to the reference area of the wing, this equates to a C_d of 0.02 for both ducts together. The geometry of the ducts can be seen in Figure 5.19 and Figure 5.20.
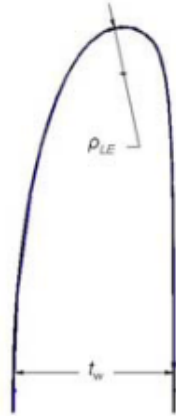

Figure 5.20: Geometry of back rotor inlet

Figure 5.19: Geometry of the Duct lip for the main rotors. The left side of the profile corresponds to the inside of the duct [20]

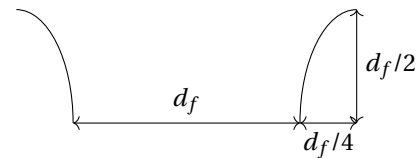As the ducts of the main rotor are not integrated into the fuselage, their mass has to be estimated. From the geometry described previously, the volume of a single duct can be estimated to be 0.019 $[m^3]$, and the wetted area to be 1.2 $[m^2]$. The duct itself only carries minimal loads, including only its own weight and drag, thus the structure can be very light. For this a sandwich structure can be used, in which the core consists of Rigid Polyurethane Foam structure with a density of 48 $[kg/m^3]$ [2], which is covered by a composite material of circa 1400 $[kg/m^3]$, as this covering only serves to protect the internal foam structure, it can be as thin as 0.2 $[mm]$. The internal Foam does not need to fully fill the core, but a 30% filling can be enough if the internal layout is chosen wisely. This design will yield a mass of 0.6 $[kg]$ per Duct.

5.7. Final Analysis

Now that the aerodynamic design is finalized, the final analysis can be done. First, a drag budget is made and shown in subsection 5.7.1. Then, the final aerodynamic analysis is presented in subsection 5.7.2. Also, a sensitivity analysis is performed on the final aerodynamic design. This is presented in subsection 5.7.3.

5.7.1. Drag Budget

In order to validate the drone against the required drag budget, the drag contributions of each part of the drone has to be summed up. For the empennage, a C_{d0} of 0.018 has been determined using XFLR5, this is with respect to the surface area of the empennage. Scaling this to the reference area of the Wing, a C_{d0} of 0.007 is determined. Together with the previously calculated values these are presented in Table 5.1

Table 5.1: Drag Budget

Component	C_D
Wing	0.018
Fuselage	0.012
Ducts	0.02
Empennage	0.007
Margin	0.01
Σ	0.067

---

[2]https://www.generalplastics.com/rigid-foams

5.7.2. Aerodynamic Analysis

A final Aerodynamic analysis of all lifting surfaces is performed using XFLR5. The simulation is run at cruise speed with a root chord Reynolds number of $2.1 \cdot 10^6$. The lifting surfaces as well as the center of gravity is placed according to the positions determined in chapter 8. The Drag Polar is shown in Figure 5.21 and the Optimum L/D ratio in Figure 5.22. It can be seen that an optimum lift over drag ratio is achieved. From the analysis it was found that the drag coefficient during cruise is 0.02, which agrees very well with the estimated result in the previous section.
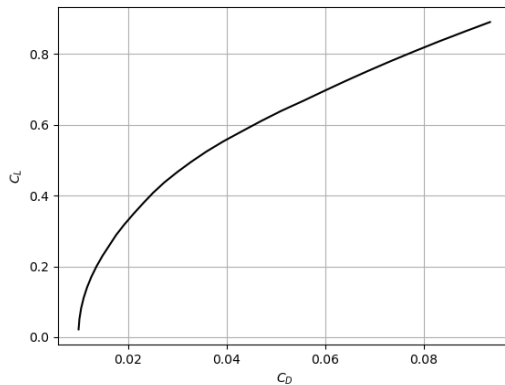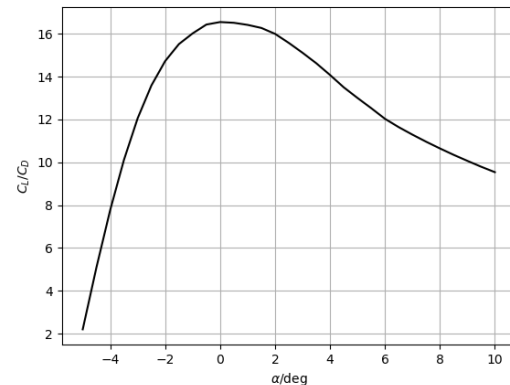

Figure 5.21: Lift Drag polar

Figure 5.22: L/D ratio versus angle of attack

From XFLR, the Lift distribution during cruise as well as before stall has been determined. This distribution will be used during the structural design of the main wing.

5.7.3. Sensitivity Analysis

As can be seen in subsection 5.7.2, the current angle of attack during cruise is right at the maximum of lift over drag curve. If the weight of the drone would increase, the angle of attack would also increase if the wing area stays constant, however the lift over drag ratio would not significantly decrease for approximately 1°. This change in angle of attack would result in an increase of lift of circa 43 [N], which is more than 10% of total Lift. This means that the aerodynamic design of the Wing is very robust against changes in weight, as well as changes in drag budget inversely.

As explained in section 5.4, the blades of the proprotor are designed for specific thrust and power requirements and a certain radius. Changes in weight could change the required radius and thrust of the proprotors and thus change the optimal blade design. However, although it might not be optimum, the reduction in efficiency is small. The current blade design can give higher and lower thrust characteristics if the power is increased or decreased respectively. The RPM and pitch can be adjusted for the optimal setting. When the required thrust is increased by 10% during VTOL due to weight increase fore example, the new power required for one proprotor becomes 2100 [W]. This is a power increase of ((2100-1850)/1850*100) 13.5%. The efficiency thus decreases, but not very significantly for small changes. It was therefore important that the blade design did not start when there were still big changes in the propulsion subsystem. Once the values were about finalized with only small changes possible, the optimal blade configuration was found.

5.8. Verification and Validation

All tools used in the design of the aerodynamic layout need to be validated. Therefore, XFLR5 and JBLADE are validated. Also, the duct design is validated.

5.8.1. Validation of XFLR5

In order to validate XFLR for airfoil selection and wing layout, the tool has been tested against experimental results from wind tunnel experiments on an NACA 0012 airfoil performed by Abbot et al. [3]. This experiment has been performed at a Reynolds number of 6 million, which is the same order of magnitude as the Reynolds numbers experienced during cruise. This comparison can be seen in Figure 5.23 and Figure 5.24. It can be seen that the lift

---

[3]https://turbmodels.larc.nasa.gov/naca0012_val.html

coefficient matches very well for all behaviour not involving stall. For the drag polar it can be seen that the drag of the airfoil is slightly underestimated.
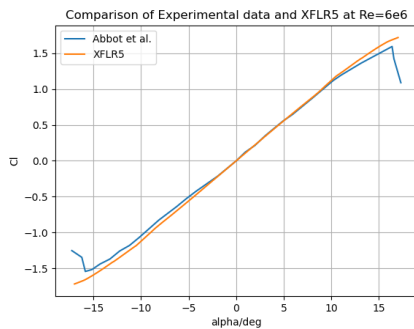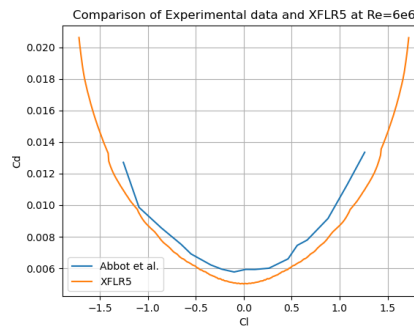

Figure 5.23: Validation of XFLR5

Figure 5.24: Validation of XFLR5

For the 3 dimensional simulation, a viscous 3D panel method is used. This method is validated by the creators of XFLR5 [1] for low Reynolds numbers (10^5) and the results are reproduced for validation. This Reynolds number is 1 magnitude lower than the Reynolds numbers of the wing. The viscous effects however are interpolated from the 2d analysis of the airfoil, which was validated beforehand, thus it can be assumed that this method will also produce valid results for the flow over the wing.

5.8.2. Validation of JBLADE

JBLADE is a tool that is based on XFLR5. The validation was done by comparing with experimental results and results from QBLADE and JAVAPROP. The experimental results come from the wind tunnel tests in the NACA Technical Report 594 [4]. The results are shown in Figure 5.25 [5]. To obtain the most accurate numbers of the design characteristics, experimental data has to be obtained by use of wind tunnels. This is beyond the scope of this design project.

5.8.3. Validation of Duct Design

As discussed by Zhang et al. [72], designing and evaluating the performance of ducted fans is still an open research problem. There exist some low order methods for performance evaluation and flow simulation. These however have not been validated against experiments. Higher order methods based on CFD simulations have been performed and partially validated against experiments, the use of such methods for a preliminary design is limited. Thus for choosing the geometry of the duct and the inlet, experimental results have been used, which have been performed in approximately the same Reynolds number range as the expected Reynolds numbers during operation.

5.9. Compliance Matrix

The compliance with the previously mentioned subsystem requirements is presented in Table 5.2. It can be seen that during this preliminary design, the system complies with all requirements. However their compliance has to be reevaluated with more advanced and higher accuracy analysis tool.

---

[4] `https://ntrs.nasa.gov/archive/nasa/casi.ntrs.nasa.gov/19930091669.pdf`

[5] `https://sites.google.com/site/joaomorgado23/printscreens`
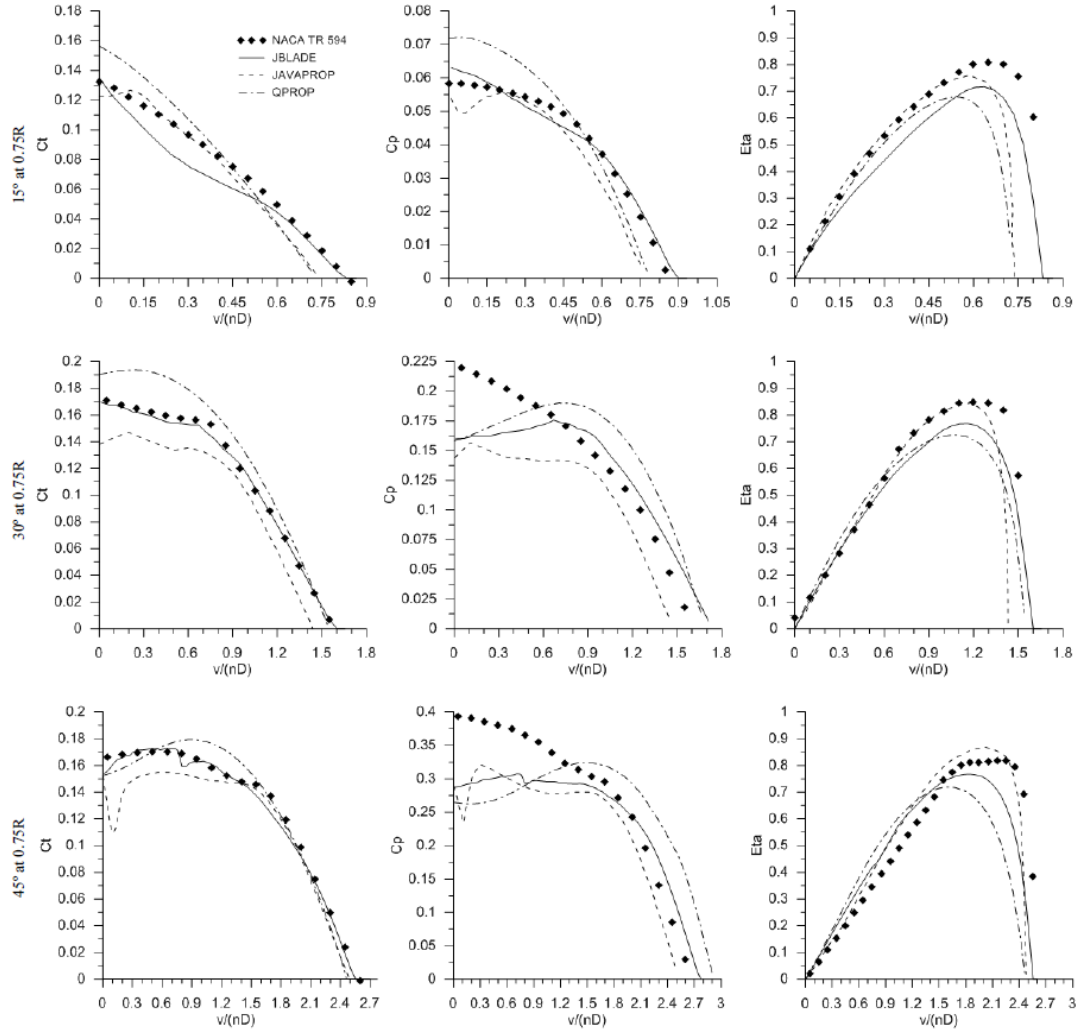
Figure 5.25: Validation results of JBLADE

Table 5.2: Compliance Matrix

Requirement	Required	Actual	Fully met	Partially met	Not met	To be investigated
MD-SYS09-AF01:	345 [N]	350 [N]	✓			
MD-SYS09-AF02:	0.85	0.88	✓			
MD-SYS09-AF03:	64 [N]	66 [N]	✓			
MD-SYS09-AF04:	4.2 [kW]	4 [kW]	✓			
MD-SYS09-AF05:	0.07	0.035	✓			
MD-SYS09-AF06:	90 [m^3/h]	90 [m^3/h]	✓			
MD-SYS19-AF01:	352 [N]	354.1 [N]	✓			
MD-SYS19-AF01-1:	155 [N]	155.6 [N]	✓			
MD-SYS19-AF01-2:	21 [N]	21.5 [N]	✓			
MD-SYS19-AF02:	4.7 [kW]	4.66 [kW]	✓			
MD-SYS19-AF02-1:	3.7 [kW]	3.7 [kW]	✓			
MD-SYS19-AF02-2:	1 [kW]	0.96 [kW]	✓			

6

Hydrogen

As for sustainability reasons, HEALR will be hydrogen-powered. Hydrogen powered systems are used to not emit any CO_2. In section 6.1, the functions which the hydrogen subsystem has to perform are explained. Then, the design process of the subsystem is explained in section 6.2. The final design is presented in section 6.3. This final design has to be verified and validated. This can be found in section 6.4. Finally, it has to be checked if the system complies to all requirements. This is done with a compliance matrix, found in section 6.5

6.1. Functional Analysis

To start with designing hydrogen subsystem, first the functions of this system are determined. Figure 6.1 shows the functional breakdown structure in which all the functions the hydrogen subsystem needs to fulfill are shown.
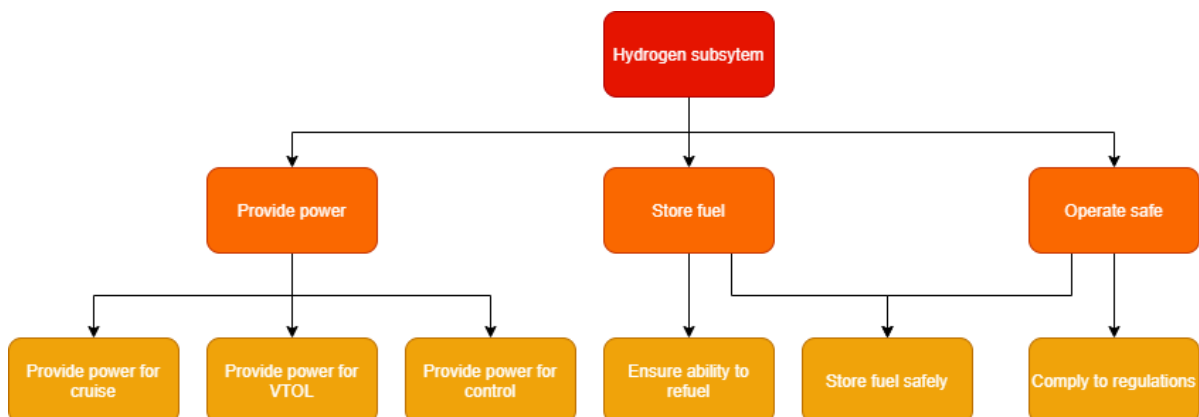
Figure 6.1: Functional breakdown structure of the hydrogen subsystem

Looking at this three functions were identified and are described in the list below. To provide the power a fuel cell is used, which is explained in subsection 6.2.1. To store the fuel a liquid hydrogen tank is used. The storage is discussed in subsection 6.2.2. Also, the refueling will be discussed in subsection 6.2.3.

- **Power:** Provide sufficient electrical power to the whole system to fulfill the mission.
- **H_2 storage:** Safely store the energy needed in the form of hydrogen.
- **Refueling:** Make safe on-site refueling possible, while ensuring all accompanied operations comply with regulations and do not compromise safety, while minimizing risks.

6.1.1. Subsystem requirements

In the Baseline Report [62] requirements were set. However, no subsystem requirements on the fuel cell nor fuel tank were determined. Therefore, all (sub)system requirements influencing the fuel cell and fuel tank will be mentioned below. Also, some subsystem requirements are added. These are labelled as MD-SYSx-HYx. All of these new subsystem requirements are based on the needs of the propulsion subsystem.

Power

MD-SYS25:   The drone shall be hydrogen powered.
MD-SYS19-HY1:   The fuel cell system should provide a peak power of at least 6 [kW].
MD-SYS19-HY2:   The fuel cell system should provide a peak power for at least VTOL time.
MD-SYS19-HY3:   The fuel cell system should provide a nominal power of at least 4.8 [kW].

H$_2$ storage

MD-SYS17:   The drone shall comply with the regulations of the specific risk category set by EASA.
MD-SYS24-RISKH2: Track shall be kept of the hydrogen levels inside the fuel tank.
MD-SYS25-RISKH2: The drone's tank shall have an anti-leak lining.
MD-SYS09-ST13:   The tank structure shall be able to withstand a pressure difference of $3.00 \cdot 10^6$ [Pa].

Refueling

MD-SYS17:   The drone shall comply with the regulations of the specific risk category set by EASA.
MD-SYS26:   The hydrogen used to power the drone shall be available on-site.
MD-SYS27:   The hydrogen used to power the drone shall be produced in a sustainable way.
MD-SYS26-RISKH4: Hydrogen for the drone shall be produced in more than one facility.
MD-SYS27-RISKH4: There shall be an on-site hydrogen storage facility at the project's headquarter.

6.1.2. Workflow Diagram

The workflow of this subsystem is shown in Figure 6.2. The blue circles are inputs, the red rectangles are functions and the yellow diamonds are outputs. As one can see, the workflow is split up into the three functions. These functions can be run in parallel.
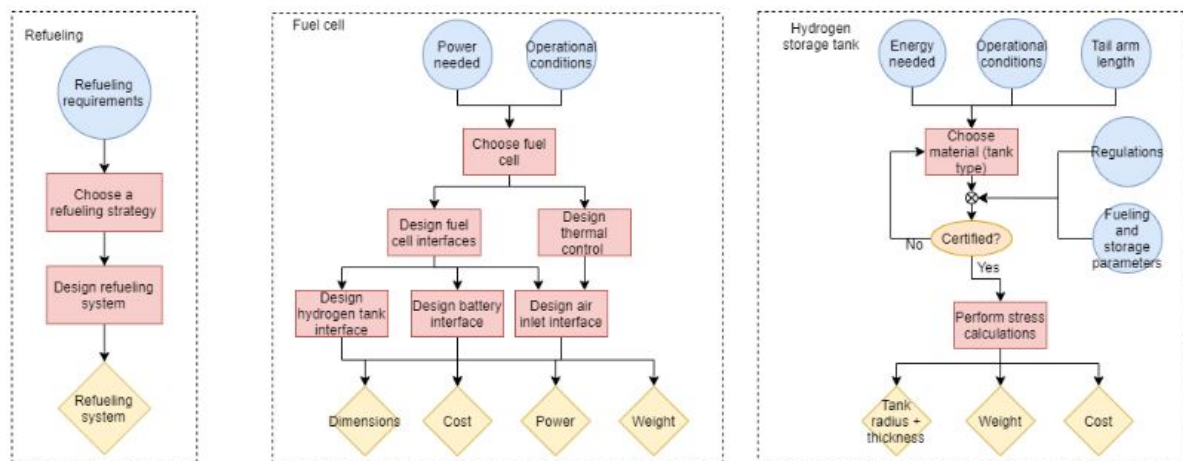
Figure 6.2: Work flow diagrams of the three functions of the hydrogen subsystem

6.2. Design

The design of the hydrogen system contains three parts, based on the functions that are established in section 6.1. To provide the power, the fuel cell is designed in subsection 6.2.1. The hydrogen needs to be stored in a tank, which is designed in subsection 6.2.2. Last bot not least, the refuelling system is designed in subsection 6.2.3.

6.2.1. Fuel cell

In the Baseline Report [62] it was established that a proton exchange membrane fuel cell (PEMFC) will be used. These cells consist of a cathode and anode, with an electrolyte in between them. This electrolyte is a membrane that conducts protons. Between the electrodes and the membrane, a catalyst is present. A schematic of this is presented in Figure 6.3 [3]. This also shows the respective thicknesses of each layer. One fuel cell delivers a theoretical voltage of 1.23 [V], hence multiple fuel cells are stacked into a fuel cell stack. This creates a fuel cell that delivers a higher voltage.

Figure 6.3: Schematic of a PEM fuel cell [3]

It was decided that an off-the-shelf fuel cell would be used to provide all the functions described in section 6.1. Two companies selling UAV-specific fuel cells, HES Energy Systems and Intelligent Energy, were looked into. These are two companies in Europe in the front line of the development of UAV-specific fuel cells. From these companies, multiple cells were selected. These cells and their characteristics can be seen in Table 6.1. While doing research on the different fuel cells, two interviews were conducted to gain more info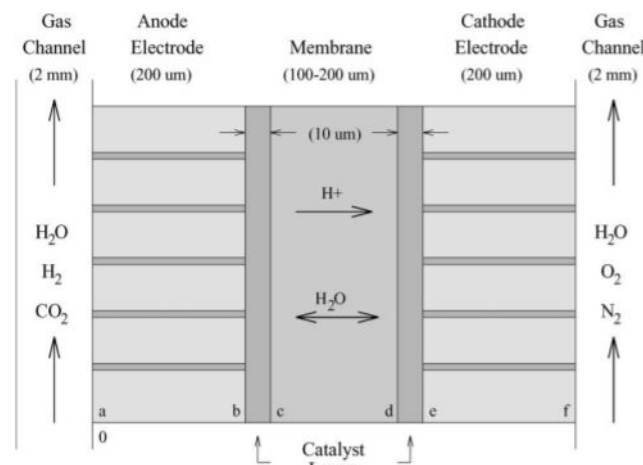rmation. The first interview was done with Pieter Lantermans, sales representative of Intelligent Energy in the Benelux and Germany, and founder of the HyFly drone [1]. The second interview was done with Olga Lubbers, Chief Engineer of 'Project Phoenix'[2], done by a student team of the TU Delft.

Both of them gave a lot more understanding in the fuel cell system. The costs in Table 6.1 are estimated based on the interviews with Pieter Lantermans and Olga Lubbers. The power and volume are retrieved from datasheets found on the respective company's website [3] [4].

Company	Power [W]	Weight [kg]	Dimensions [dm]	Volume [L]	Voltage [V]	Cost [k€]
Intelligent Energy	2,400	4.4	1.28x4.42x2.33	13.18	50-70	± 30
Intelligent Energy	800	0.93	1.96x1x1.4	2.74	19.6-25.2	± 10
Intelligent Energy	650	0.81	1.96x0.88x1.4	2.41	19.6 - 25.2	± 8
HES	1,000	1.8	1.94x1.27x1.93	4.76	39.0 - 61.8	± 12
HES	1,500	2.8	3.02x1.2x1.45	5.25	32.4 - 51.3	± 20
HES	2,000	3.8	3.3x1.6x2	10.56	38.0 - 59.8	± 25

Table 6.1: Fuel cell characteristics with respect to power, weight, volume and cost

As described in chapter 7 and defined in subsection 6.1.1, the drone needs a power of 4.8 $[kW]$. None of the fuel cells in Table 6.1 provides enough power. Therefore, a combination of multiple fuel cells needs to be considered. Intelligent Energy provides a power path module to connect two 800 $[W]$ or two 2.4 $[kW]$ Power Modules to each other. This means that there are two options for the fuel cell configurations. The first one being two cells of 2.4 $[kW]$, using a connector between them to add the power. The second configuration is using six cells of 800 $[W]$, also having to connect them to produce 4.8 $[kW]$. Considering the weight and volume of both the 2.4 $[kW]$ module and the 800 $[W]$ module, it was found that using six 800 $[W]$ modules would be both lighter and smaller. However, having to connect six cells increases the complexity of the system. The difference in weight and volume however, is significant and deemed more important than the increase in complexity. Therefore, it was chosen to use six fuel cells of 800 $[W]$. As mentioned before, Intelligent Energy provides power paths modules to connect two fuel cells to each other. According to Pieter Lantermans it is hard to design a connection between the two connected cells and a third (or fourth, fifth, etc.) cell. However, adding the three powers to each other in parallel, such that the output voltage stays the same, will not be too complicated to design. Therefore, it is decided that a 3x2 configuration is used. This means that there are three pairs of 800 $[W]$ fuel cells, all three connected by a power path module. These three power path modules will then be connected to each other in parallel. A diagram can be seen in Figure 6.9.

---

[1] https://www.hyfly.tech/

[2] https://aerodelft.nl/project-phoenix/

[3] HESEnergySystems:https://www.hes.sg/aerostak

[4] IntelligentEnergy:https://www.intelligent-energy.com/our-products/uavs/

Humidifier

A fuel cell produces heat due to the high current flow. This can cause the polymer membrane to dry out, which will slow down the transport of ions. Therefore, it is important to humidify the fuel cell. The fuel cell considered for this project, the Intelligent Energy 800 [W] Power Module, is self-humidifying. That means that the incoming air and hydrogen are humidified by the fuel cell itself and no separate equipment is needed.

Hydrogen regulator

The fuel cells work at a pressure of 1 [bar]. HEALR will not fly at high altitudes, implying no significant decrease in pressure at the flight altitude of the drone. The hydrogen therefore needs to be delivered to the fuel cell at that same pressure. When liquid hydrogen is used, the pressure in the tank is 3 [bar] (see subsection 6.2.2, hence the pressure needs to be regulated before the hydrogen enters the fuel cell. A hydrogen regulator is also needed to smooth out the potential pressure differences between the tank and the fuel cell.

A hydrogen regulator has a second function, namely controlling the fuel flow to the cell. The regulator provides communication between both systems. If the pressure in the hydrogen storage tank falls away when there is no more fuel, the regulator will communicate this to the fuel cell. If this is the case the fuel cell will shut down.

Cooling and oxygen intake

The chosen fuel cell has an efficiency of 0.53, which means that there is waste heat production. This implies that the fuel cell needs to be cooled. The fuel cell from Intelligent Energy is air-cooling, meaning that a fan at the back of the cell pulls air through the module. This air is also used for the oxygen intake. Some of the air is filtered in the system, such that its oxygen can be used to produce power. The rest of the air is used for cooling. It is of importance that there is fresh air around the fuel cell, such that the fan can do its work. It is therefore decided that a hole in the skin is made to let a stream of fresh air enter the compartment where the fuel cells are in. The design of and details about this duct are discussed in subsection 5.3.3.

All-weather requirement

The operating temperatures of the fuel cell are -5 [°C] and 40 [°C] [5]. As can be found in the Baseline report [62], the drone needs to withstand temperatures between -10 [°C] and 45 [°C]. This means that when the outside temperature exceeds 40 [°C] the fuel cell needs special cooling, as the outside air will not provide this anymore. Also, when the outside temperature is lower than 5 [°C], the cell will need heating as the air will cool the fuel cell to a too low temperature.

Another weather aspect that needs to be considered is rain and hail. As the air inlet will use free stream air, this might contain hail and/or rain. To provide this hail and rain from coming into the fuel cell, a filter (sieve) is placed at the inlet.

Battery

During VTOL the drone needs more power than during cruise. The 4.8 [kW] the fuel cells provide is enough to take-off and land, however, when there are large wind gusts more power is required. This power will be provided by batteries. Intelligent Energy provides a battery with the fuel cell. The battery it provides with an 800 [W] fuel cell can deliver a power of 600 [W] for 3 minutes. Since a peak power to counteract the wind gusts of 1200 [W] is needed, a total of two batteries and six fuel cells provide enough. This is under the assumption that the batteries will not have to deliver their peak power for more than 3 minutes straight. The batteries get recharged again when the fuel cells use less than nominal power.

6.2.2. Tank

As described earlier in the Baseline Report [62], the decision was made to store the hydrogen fuel on-board in the form compressed gas instead of using cryogenic technologies or storing them chemically such as in metal hydrides. After multiple iterations on the power budget and flight time, it was found out that a hydrogen tank (350 [bar]) of 28.5 [L] would be needed to store all the hydrogen. This would result in a tank weight of 16 ± 0.5 [kg]. This exceeds the preliminary estimate with 10 [kg], meaning that the drone would not be able to fly with this tank weight. Therefore, another solution had to be found. The first and most straightforward solution would be to put the tank under a pressure of 700 [bar], which would be able to increase the gravimetric storage density significantly. However, use of these kinds of (such small) tanks on a UAV have not been developed (yet), which might mainly be

---

[5]https://www.intelligent-energy.com/uploads/product_docs/800W_datasheet_GfJCLTu.pdf

due to concerns regarding safety and regulations, according to interviews with Lantermans. Hence, it was decided to use liquid hydrogen, which is able to achieve even higher gravimetric efficiencies.

Calculation on required H$_2$ fuel

Using the energy content of liquid hydrogen 120 $[MJ/kg]$ and the requirement that there should be enough hydrogen to provide $2.29 \cdot 4.8 = 10.97$ $[kWh]$, an amount of 330 $[g]$ of hydrogen is needed. The fuel cell, however, has an efficiency of 0.53 [6]. Accounting for this, $\frac{330}{0.53} = 622$ $[g]$ is needed. Now, as one liter of pure liquid hydrogen weighs 71 $[g]$, a tank volume of at least 8.77 $[L]$ of hydrogen is needed.

However, the above has only considered the required fuel for a nominal flight. Therefore, it is safe to say that it should be considered the absolute minimum fuel weight value. To allow for safe operation and increased reliability, several contingency factors are added onto the previously calculated minimum value. Firstly, for reserve fuel, a factor of 5% is added to accommodate for unexpected routing changes or potential restrictions posed by air traffic management, as is also recommended in ICAO Annex 6 [7]. In addition, a factor of 3% is added to take into account trapped and unusable fuel, described by Verstraete [68]. Here, a smaller factor is taken, but it was chosen to take more to compensate for the fact that a larger aircraft was considered. Next, extra fuel is taken on-board as boil-off tends to occur. Evaporation losses on today's tanks are somewhere between 0.3 and 3% per day [21]. It should be noted however that tanks which have a lower surface-to-volume ratio inherently have less losses due to a relatively small surface area and thus inward heat leakage. Thus, to allow for sufficient fuel capacity in case the drone has to be on stand-by for a longer period, 5% was taken as contingency for boil-off.

Considering the rough estimations made in a conservative manner, these aforementioned factors may be reduced to be able to make diverging to another nearby hospital (with helipad) possible, upon further analysis. This is due to the fact that a reserve fuel of 5% on a 100 $[nmi]$ return mission is a rather limited increase in range, in order to reach an alternative location. The amount of trapped fuel and the losses due to boil-off can be reduced with a more efficient tank design with improved vapor extraction of GH$_2$ and reduced stand-by time after refueling and/or on-demand fueling at comparable operational costs.

Lastly, in case of strong headwinds and more adverse weather conditions, longer flight times are needed to achieve similar ranges. To maintain equal mission range, extra fuel is also added for this. The amount is based on an average headwind at an altitude of 200 $[m]$ for both ways during a return, which would be the worst-case scenario. Headwinds are up to 10 ± 0.5 $[m/s]$ in the Netherlands and neighboring countries, as reported by an interactive tool of DTU and the World Bank[8]. The contingency factor for headwind was found by combining the nominal cruise speed and its reduced value to this same headwind, effectively taking into account this factor as an efficiency loss. All of the discussed factors indicated in Table 6.2.

Table 6.2: Fuel weight, with breakdown of several additional contingency factors.

Contingency	Factor [%]
Trapped fuel	3.0
Reserve fuel	5.0
Boil-off	5.0
Headwind	28.6
Total factor	**46.0**
Initial fuel weight	623 $[g]$
Total contingency	*287 $[g]$*
Total fuel weight	**910 $[g]$**

Tank design

Storage of liquid hydrogen has its particular challenges. Since this is done cryogenically, heat transfer by means of convection, conduction and radiation shall be minimized in order to prevent premature evaporation of the liquid hydrogen. In the design considered, a double-walled vessels is used for this. This consists of an inner tank and an outer container, separated by vacuum layer functioning as insulation. To minimize radiation of heat, this space is

---

[6]https://www.intelligent-energy.com/uploads/product_docs/Cylinder_Guide_August_2019_web_7wtWLeD.pdf
[7]https://www.skybrary.aero/index.php/Fuel_-_Flight_Planning_Definitions#Contingency_Fuel_.2F_Route_Reserve
[8]https://globalwindatlas.info/

generally also filled with multi layer insulation (MLI), which can be made with alternating layers of glass fibers (or Mylar) and aluminum foil. Radiation is one of the main contributors of the total heat leak of a fuel storage system [48][49].

The main challenges of designing a LH$_2$ tank arise from trying to match the evaporation rate of the liquid hydrogen with the consumption rate of gaseous hydrogen of the fuel cell. If the evaporation rate is too low, the flow rate of the fuel to the power unit is insufficient, which leads to failure to produce power. On the other hand, if evaporation rates are too high, maximum tank pressures will be reached, after which hydrogen has to be vented to maintain pressure within operational bounds, which translate into direct fuel losses. Furthermore, while on stand-by, heat leak should be minimized, to ensure minimal losses due to boil-off of the liquid hydrogen.

Tank pressure and volume

First step in the tank design, is to determine the tank volume. Prior to doing so, the relevance of tank pressure will be discussed. Pressure increases are directly related to the boil-off rate; once the liquid hydrogen evaporates, tank pressure rises. If this same gaseous H$_2$ is not consumed at the same rate, maximum allowable pressure can be reached in the tank. This has to be relieved by venting, in order to keep the tank pressure within operational values. Therefore, venting pressure can be set equal to the maximum allowable pressure. To make this possible, a certain gaseous volume fraction has to be set within the tank, such that pressure relief, but also (gaseous) fuel flow, is possible at all times. This value is set to be 0.03, which means that the liquid volume fraction has a maximum value of $y_{max} = 0.97$. Choosing the venting pressure leads to a certain fuel density, for which the tank volume then can be determined given the required amount of fuel.

Besides that the pressure chosen could be used to reduce the tank volume (and thus the tank weight too), for safety reasons, the operation pressure of tank should be kept above the highest expected ambient pressure. If this is not the case, ambient air would tend to flow into the tank, which creates an highly explosive gas mixture with catastrophic consequences if structural failure occurs or if ignited. For this reason, the nominal tank pressure was set to be 2 [bar]. In combination with setting a venting pressure of 3 [bar], this provides an adequate liquid volume fraction for fuel storage while still allowing some room for pressure (and thus liquid volume fraction) fluctuations within the tank during the mission, see Figure 6.5.

Using the mixture rule to calculate the mean density of the liquid-vapor hydrogen mixture in the tank, its value is found to be equal to 63.4 [kg/m^3]. This value, with the required fuel mass, were used to determine the tank volume, and was obtained as follows. Reading from the Figure 6.5, the liquid volume fraction is equal to 0.93, given a venting pressure of 3 [bar] and a filling pressure of 2 [bar]. Density of LH$_2$ at this pressure is about 68 [kg/m^3] (assuming a linear graph), while that of GH$_2$ found using the ideal gas law shown in Equation 6.1.

$$\rho_{H_2} = \frac{p_{GH_2}}{\frac{R}{M(H_2)} \cdot T} = \frac{2.0 \cdot 10^5}{\frac{8.314}{2.02 \cdot 10^{-3}} \cdot 23} = 2.1 \ [g/L] \tag{6.1}$$

Plugged in are the tank pressure p_{GH_2}, universal gas constant[9] R, molecular mass of hydrogen[10] $M(H_2)$ and tank temperature of 23 [K] (based on $p = 2$ [bar] from Figure 6.4a).

Tank Materials and Insulation

As discussed in [68], the tank wall materials considered are required to have the following properties: resistant to cryogenic temperatures, minimal permeation of hydrogen and resistance against hydrogen embrittlement, amongst others. Also, low density and high strength, stiffness and fracture toughness are favourable characteristics [7]. With this, only several types of steel and aluminum remain as realistic options. Al-2219 is deemed a suitable candidate as it has a relatively low density, is one of the few known metals known to only show minimal susceptibility to hydrogen embrittlement [68]. Hydrogen embrittlement is defined as 'the phenomenon where certain metal alloys experience a significant reduction in ductility when atomic hydrogen penetrates into the material' [65]. According to [68], in a study of NASA (led by Brewer et al.), this was found to be suitable material as it has been extensively research in that study, after considering different metals. Furthermore, this alloy has also been used for the construction of LOX and LH$_2$ tanks for the Ariane 4 and 5 launcher.
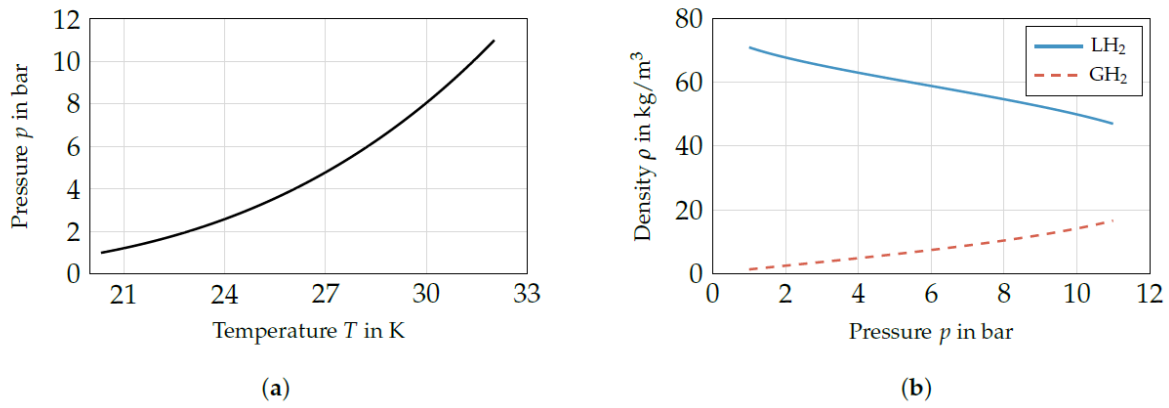
---

[9]https://www.britannica.com/science/molar-gas-constant
[10]https://ciaaw.org/hydrogen.htm

Figure 6.4: **(a)** (p,T)-curve for saturated hydrogen, **(b)** Density of LH$_2$ and GH$_2$ for saturation conditions.
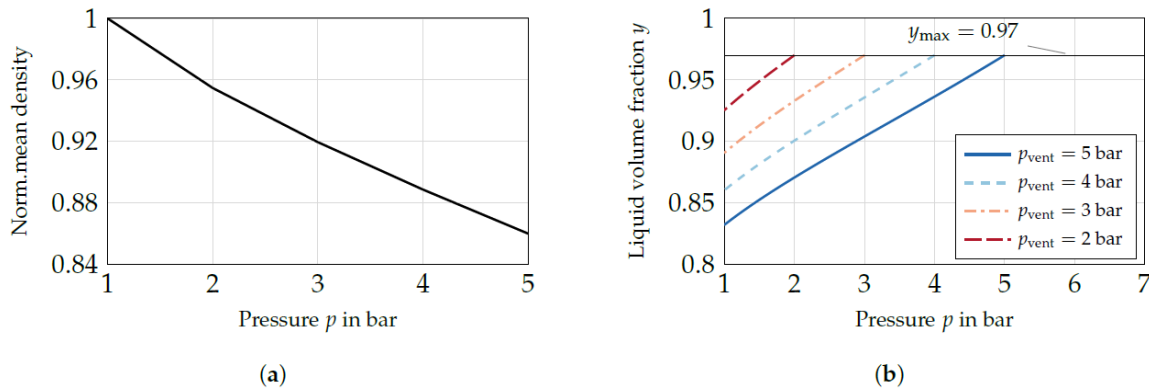

Figure 6.5: **(a)** Mean storage density related to pressure, given liquid volume fraction $y=0.97$, for saturation conditions. **(b)** Liquid volume fraction y against tank pressure, for different venting pressures [7].

$$s_w = \frac{p_p \cdot d_i}{v\left(2K/SF - p_p\right)} \tag{6.2}$$

In Equation 6.2, p_P is the proof pressure, or burst pressure, which follows from the maximum overpressure p of 3 [bar], while adding a safety margin of 2.5 on top. Plugging this in for weld efficiency $v=0.7$ [11], p_P with a safety factor of 2.5, K representing the limit stress in operational conditions of the Al-2219 alloy, being 172.4 [MPa], and ultimately another safety factor SF of 2, gives a cylinder wall thickness of 1.52 [mm].

From [7], it is described how a minimum wall thickness for elliptical shaped tanks can computed (in an iterative manner) using Equation 6.3.

$$\frac{K}{S} \geq p_P \left[\frac{a+c}{2s_w}\left(1+2\left(1+3.6\frac{p_P}{E_Y}\left(\frac{a+c}{2s_w}\right)^3\right)\left(\frac{a-c}{a+c}\right)\right)+\frac{1}{2}\right] \tag{6.3}$$

However, one may figure intuitively, that an an elliptical tank is generally not an effective geometry for the fuel storage type considered. In [7], a qualitative comparison was made for tanks for varying ϕ (see Figure 6.6). It was concluded rather simply that non-circular tanks lead to a substantial increase in tank-wall thicknesses (more than double for $\phi=1.2$, given $V_t = 20$ [m^3] for the overpressure considered) and even higher of tank-wall masses. Not only is this highly unfavorable, it would also increases the surface-to-volume ratio. Therefore, elliptical tanks should generally be avoided and circular tank will be developed for the design under consideration.

Thus, for circular tanks, Equation 6.3 can be simplified into Equation 6.4.

$$s_w = \frac{d}{\frac{2\cdot K}{SF\cdot p_P}-1} \tag{6.4}$$

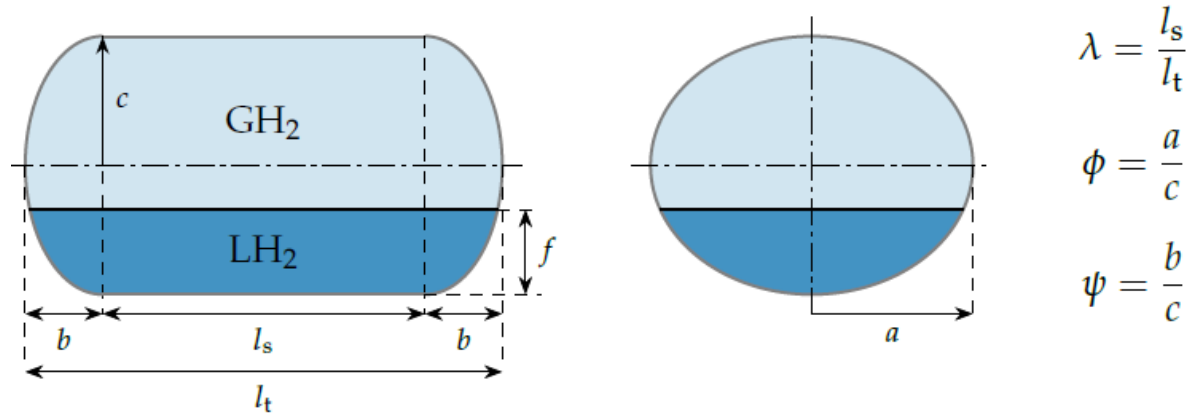[11]`https://www.pveng.com/joint-efficiency/`

Figure 6.6: Side view (left) and sectional view of the hydrogen tank (right) with equations indicating several dimensionless tank geometry parameters [7].

For a circular tank, $d = 2r$ and $r = a = c$, while K, SF and p_P use the same values as for the calculations for the tank wall thickness for the cylindrical part in the center section. Filling in the unknowns return a wall thickness s_{wall_s} = 1.05 [mm] for the (hemi)spherical end caps. To reduce stresses between these caps and the cylindrical center section of the vessels, the s_{wall_s} is increased to match the wall thickness of the center part.

For the choice of insulation between the two nested tanks, different options exist. Common viable material and methods are to be discussed hereafter. From the table in 6.7, it can be concluded that polymer foams and multi layer insulations (MLI) are the most suitable options, considering their mass density and thermal conductivity, alongside with aerogels. The combination of MLI with a vacuum jacket is has comparable densities, while having an apparent thermal conductivity that is approximately two orders of magnitude lower than the best low-conductivity foams [61].

Although aerogels have low densities and seem to have promising thermal performance properties, more research still has to be done to improve its mechanical properties - for example using reinforcement with polymers - without compromising its thermal properties. Furthermore, cost plays a role here [36]. Therefore, they will not be considered for the current design. Additionally, foams, aerogels and vacuums do not provide sufficient resistance to radiation heat transfer [61][68]. To conclude, for this design, the chosen insulation method will be the use strong vacuum in combination with MLI. This method of insulation was also used by the three reference LH$_2$ UAV fuel storage systems [29][40][49], which were considered for the fuel storage system weight estimations. It should be noted however that the (sudden) loss of vacuum might have catastrophic consequences on the fuel storage system. It is therefore important that this is design with minimal margins and shall be thoroughly tested prior to operation. Testing for insulation quality can be done with other cryogenic liquids such as N$_2$.

The nested cylindrical tanks were made such, to accommodate for the MLI insulation. Maximum heat transfer due to conduction $\dot{Q}_{\text{MLI,cond}}$, given is characterized by Equation 6.5.

$$\dot{Q}_{\text{MLI,cond}} = \frac{k_{MLI} \cdot A \cdot \Delta T}{t} \tag{6.5}$$

where k_{MLI} is the thermal conductivity of the MLI wrap, for which the *CRS Wrap 1303B* from Lydall [12]. It must be noted that this value is extrapolated slightly from its given mean temperature value of 285 [K], after which a reasonable margin was added on top, while considering a strong vacuum in the order of 10^{-3} torr. Furthermore, A, ΔT and t_{MLI} are simply the (mean conductive) area, difference in temperature and material thickness, respectively. By taking the average between the 'surface' area of the inner and outer vessel, $\dot{Q}_{\text{MLI,cond}}$ is be calculated to be 0.37 [W]. As mentioned earlier, a strong vacuum is a prerequisite to maintain high levels of insulation, minimizing heat leak. For a less strong vacuum, k_{MLI} increases the order of 10^{-3}-10^{-4} [$W/(m \cdot K)$], which means that in the order of 1 [Pa], leaks due to conduction might increase to 4-5 [W]. For other modes of heat leaks, rough estimations were made based on values of comparable fuel storage systems [29][40][49] and can be seen in Table 6.3.

---

[12] http://communications.lydallpm.com/acton/attachment/15386/f-0172/1/-/-/l-0022/l-0022:242a/CRS_Wrap_1303B.pdf

Foams	
Advantages	Currently in use, well established
	Low cost, easy to implement
	Light weight and low density
Disadvantages	Relatively high thermal conductivity
	Low resistance to thermal radiation
	Potential damage from environmental hazards

Aerogels	
Advantages	Extremely low thermal conductivity[a]
Disadvantages	New material, not well characterized
	Limited mechanical properties

Vacuum	
Advantages	Near zero thermal conductivity
	Well established
Disadvantages	Heavier tank walls required
	Costly to implement and maintain
	No resistance to radiation heat transfer
	Near catastrophic failure upon loss of vacuum

Multi Layer Insulation	
Advantages	Very low thermal conductivity and radiation heat transfer[b]
	Extremely low density
	Well established
Disadvantages	High vacuum required
	Heavier tank walls required
	Costly to implement and maintain
	Near catastrophic failure upon loss of vacuum

[a] The balance between structural an thermal properties can be altered to optimize for the application.
[b] MLI is available in graded form to improve the thermal properties and to reduce the density, but at a higher cost.

Figure 6.7: Advantages and disadvantages for several insulation methods[61] [68].

Table 6.3: Heat leak breakdown, estimations based values of comparable LH$_2$ fuel storage systems.

Heat leak type	Rate [W]
Supports	0.2
Radiation	2.0
Tubes & Vents	0.2
Conduction (MLI)	0.4
Estimated total	**2.8 $\pm$ 0.3**

Tank mass calculation

Using the calculated wall thicknesses from the previous sections, the overall weight of the fuel storage system can be found by adding the vessel masses to the necessary components for the fuel storage systems. For this, the component weights of comparable UAV LH$_2$ storage systems are used, which will be added to the component weights in the next subsection.

The weight of the vessels can be found by multiplying the density of the chosen material by the volume of the material needed ($m = \rho \cdot V$). The vessels chosen are cylindrically shaped, with end caps in the shape of a hemisphere. The volume of the vessels can simply be computed with Equation 6.6, given its length l and radius r, assuming a thin-walled structure.

$$V_{wall} = \left(2\pi r \cdot (l - 2r) + 4\pi r^2\right) \cdot t = 2\pi r l t \tag{6.6}$$

The length of the tank l was set to be 0.60[m]. Reason for this is that the fuel storage system was designed to serve as a tail arm; a slightly elongated cylindrical tank increased the surface-to-volume ratio and tank weight minimally, but ensured a reasonable tail arm length. From this, the tank radius was calculated by equating inner tank volume to the required fuel volume accordingly.

The formula to find the volume of the cylindrical vessel, with hemispherical end caps on both ends is described in Equation 6.7.

$$V_t = \pi r^2 \cdot (l - 2r) + \frac{4}{3} \pi r^3 = \pi r^2 \cdot (l - \frac{2}{3} r) \tag{6.7}$$

Besides the weight of the metal cylinders, weight of the insulation shall also be taken into account. As described earlier in this chapter, it was decided to choose the high vacuum multi layer insulation between the two vessels as insulation method. The main reasons for this choice is motivated by the fact that it has superior thermal conductivity characteristics, is very lightweight and is relatively easy to manufacture. The density of a high-vacuum MLI is stated to be 1.5 [lb/ft^3] [55]. Converting these to metric units [13], the weight of the MLI can be calculated multiplying this density of 24 [g/L] with the volume of the material - inner tank volume subtracted by outer - returning a weight of 0.238 [kg]. This means that the vessel and insulation together have a weight of 3.63 [kg].

Tank components

Besides the weight of the metal cylinders and the insulation material, additional components are needed in the fuel storage system. In the following, the components will be briefly discussed, while in Table 6.4, the combined weight of these components will be estimated based on the fuel storage system intended for the Genii UAV, which was designed by Adam and Leachman[29]. The total estimated mass of these components were summed and scaled by the ratio of their volumes, which resulted in 4.24 [kg], see Table 6.4.

Components to construct a functional LH$_2$ onboard a UAV include: inner vessel supports, vapor extraction tube, liquid hydrogen (fueling or fill) tube, a baffle system, heat controller, tank pressure regulators and sensors, control electronics and pressure relief valves. Supports for the inner vessels have to be able to withstand cryogenic temperatures while having minimal thermal conductivity. These are typically made from G10 or G10-CR and are relatively lightweight. As their names suggest, the tubes for vapor extraction and liquid hydrogen filling provide connections to the fuel cell and from the outside into the tank. A baffle system is installed inside of the tank in the form of several vertical metal plates, to reduce sloshing during maneuvers (in more severe weather, for example). A controlled heater is installed in case the evaporation rate has to be increased, to provide a sufficient fuel flow of GH$_2$ for power. Tank pressure sensors and other control electronics are installed on the tank to measure the fuel tank pressure and the vacuum level between the tank, with the necessary control electronics to provide regulation and monitoring of these from the drone's main control system. Ultimately, the pressure relief valve forms an indispensable part of the tank as pressure values above the venting pressure - its maximum allowable value - may lead to structural disintegration of the fuel tank. For this reason, typically an extra valve installed for redundancy, provided it is lightweight and (more) reliable: a solenoid valve which is controlled electronically under nominal operation and an additional (back up) mechanical pressure relief valve for intervention of the control electronics in case of power loss or vacuum failure of the storage tank.

Table 6.4: Component weights of a comparable LH$_2$ fuel storage system, designed by WSU for the Genii UAV [29].

Component	Mass [kg]
LH$_2$ tube system	1.01
Vapor extraction tube system	0.28
Baffle system	0.18
Supports (G10)	0.02
Other components	1.02
Total - NRL	**2.51**
Scaling factor ($V_{tank_{MD}}/V_{tank_{WSU}}$)	*1.69*
Estimated total	**4.24**

---

[13]https://converter.eu/

Table 6.5: Similar UAV LH$_2$ fuel storage system weights

Fuel storage system	Weight [kg]	H$_2$ [kg]	wt% H$_2$ [%]	H$_2$ Volume [L]	Tank size l, d [m]
NRL (IonTiger) [49]	4.53	1.34	29.6	20.46	(unknown)
Hylium (6L Test) [40]	3.0	0.42	14.0	6.0	0.50, 0.195
WSU (Genii) [29]	6.54	0.604	9.23	9.35	0.61, 0.20
Designed system	**7.86**	**0.910**	**11.52**	**14.35**	**0.60, 0.244**

Finally, the total weight of the fuel storage system is found to be 7.86 [kg].

Tank Integration

Naturally, the designed tank should be integrated with the rest of the (sub)system(s). The fuel storage system is designed to be an integral part of the structure. As the tank is located at the rear end of the drone, it shall have attachment points to the aft fuselage while doubling up as tail arm to accommodate the empennage. The horizontal and vertical tailplanes will be attached to the tank, by means of induction welding. This is made possible by constructing the tank such that its outer sleeve is composed of the same flax fiber composite as the rest of the lifting surfaces and fuselage, while keeping an aluminum liner on the inside of the outer vessel. To keep these two elements together, it is decided to make this liner slightly bigger. During assembly, this shall be cooled down and fitted into outer composite sleeve, such that it expands and adheres to this sleeve due to thermal expansion. Using this method, the use of adhesives (and the need for pre-treatment) or fasteners is eliminated, which is better when seen from an environmental and financial point of view. This choice may come with its risks, as will also discussed later in subsection 13.2.2. Lastly, tank-empennage assembly will be made detachable from the aft fuselage for ease of operations during (routine) maintenance and inspections. This shall be attached in using a bolt-like principle, where the threads on the aft fuselage make the tank fit onto it. Further research and development can be done to potentially improve this last attachment, as well as the design of this liner and sleeve combination, while taking into account effective fuel storage, sustainability, manufacturing and its costs.

6.2.3. Refueling

The drone needs to be refueled a large amount of times during its life. Several design options were considered to fulfill this requirement, which are listed below.

- **Refueling at headquarters**: The headquarters have a fueling station to which the drone can be connected.

- **Refueling at hospital**: Every hospital has a fueling station to which the drone can be connected.

- **Detachable tank**: Every hospital buys the tanks themselves and mounts it on the drone before it has to take-off.

The detachable tank idea is discarded, as in the beginning of the final design phase, it was determined that the fuel tank would be used as tail arm, to provide multifunctionality to the system. A detachable tank would make it hard to implement this function. Also, as liquid hydrogen is used, the filled fuel tank should be used as soon as possible. Therefore, if a hospital wants to use the drone, they should have a fuel tank that has been filled for less than 3 days. After 3 days, the small leakage of the tank has made sure that too much hydrogen is boiled off. A third reason for discarding the detachable tank is requirement MD-SYS21. This requirement states that the payload should be self (un-)loading. Having to replace the fuel tank manually, violates that idea of a fully self operating drone. Because of these three reasons, it was decided that an integrated tank is used.

There are two other options. These are refueling at a headquarters and refueling at the hospital. Refueling at the hospital seems the most feasible option, as the drone does not have to fly an extra distance. However, building a fueling station at every hospital is very expensive. Also, it is not evident that every hospital has an installation that makes liquid hydrogen, nor a big hydrogen tank that can be used to store the liquid hydrogen. Therefore, it is decided that there will be a headquarters where the drone can refuel, undergo its maintenance and from where it can be operated.

The tank will have a connection to which the fueling tube can be connected. The fueling station itself will have a regulator connected to this tube, such that it can measure the pressure during fueling. Also, this connection checks if the temperature is low enough.

6.3. Final Analysis

All the details of the fuel cell and fuel tank can be found in Table 6.6. The total weight of the fuel cell is 6.63 [kg] and the total weight of the fuel tank is 7.86 [kg]. Therefore, the total weight of the whole subsystem is 14.49 [kg]. This weight, however, is not including the structural weight that is needed to connect the tank to the fuselage and empennage. The placement of the components inside the fuselage will be presented in the final design overview chapter 12.

Table 6.6: Final component list fuel cell system

Component	Weight [kg]	Dimensions [dm]	Amount
Fuel cell	0.93	1.96x1.0x1.4	6
Battery	0.3	1.4x0.3x0.2	2
Power Path Module	0.15	1.1x0.95x0.25	3
Fuel tank	7.86	$r,l = 1.22, 6.00$	1
Total	**14.49**		

A diagram with all the system components and their interfaces can be seen in Figure 6.8. It should be noted that the fuel cell module from Intelligent Energy has the oxygen/cooling filter and interfaces in the module, so no extra components are needed. The batteries are connected in parallel. This means that some power of the fuel cells will go to the batteries to charge them. If they are fully charged, all the power will go to the power control unit. It is assumed that the batteries are charged at take-off, due to them being charged in the previous flight. Therefore, all the power of the fuel cells and the batteries can be used during take-off.

The box outlined with a dashed line called 'fuel cell system' in Figure 6.8 represents the working of one fuel cell module, however, this drone will use six. This is represented in Figure 6.9. The waste product, water comes out of the fuel cells, while the power comes out of the power path modules that connect two fuel cells. The power of these power path modules will be added up, such that the drone can deliver a nominal power of 4.8 [kW].
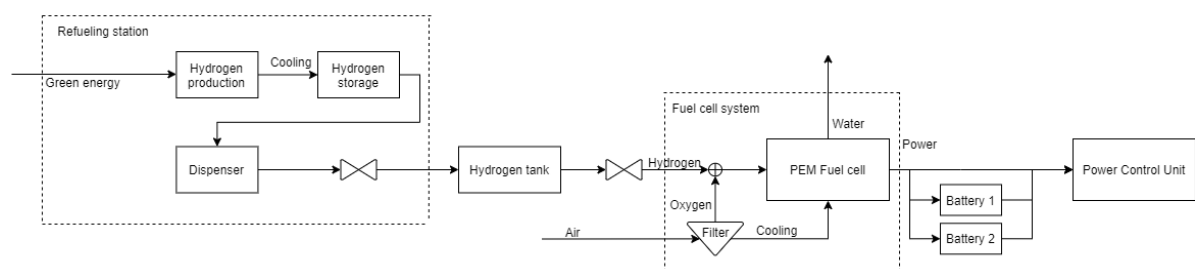

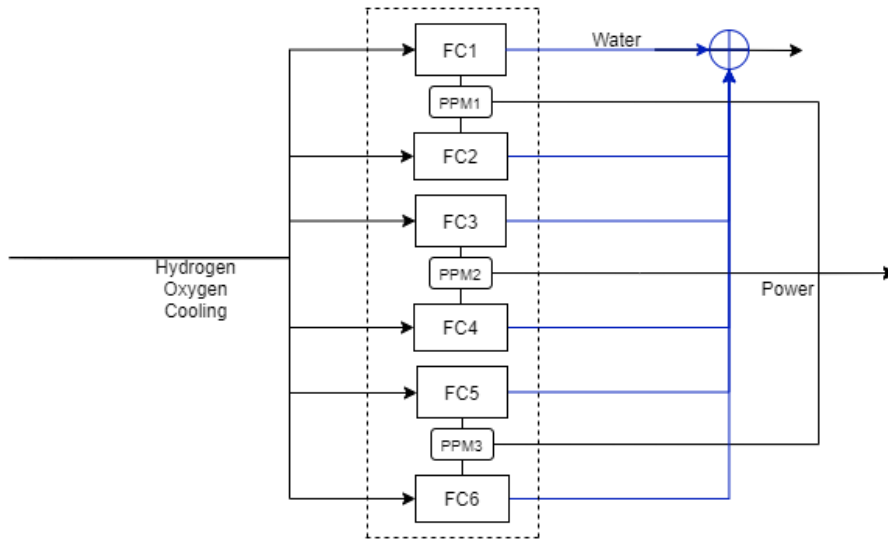
Figure 6.8: Schematic overview of the hydrogen subsystem

Figure 6.9: Configuration of the six fuel cells and three power path modules

Sensitivity Analysis

To assess how sensitive changes in the hydrogen subsystem to the overall system performance, a brief sensitivity analysis is presented in Table 6.7. Several hypothetical changes have been proposed and its influence on performance are indicated, by means of comparing the change in mass (Δm), the MTOW (after convergence due to iterations, ΔMTOW) and the range R. The changes considered include adding extra fuel cells - capable of delivering an additional 800 [W] each, as described earlier - and adding a battery, which would be able to increase the VTOL time by a factor 1.5 (approx. 3 minutes). Furthermore, the effect of varying the tank volume and its insulation thickness are indicated as well.

Main conclusions from Table 6.7, would be that increasing the number of fuel cells has great impact on the MTOW, which is consistent with the fact that fuel cells still have a relatively low power density. Changes in tank volume also impacts the performance; having a smaller volume has a relatively bigger influence on the MTOW. The low energy density of batteries would also increase the MTOW significantly when one or two batteries are added, to for example increase VTOL time. Decreasing amount of insulation material used has minimal effect on (weight) performance, and thus could further be investigated to come to a more efficient tank design. If the evaporation rate needs to be increased with factor of several times compared it its current value, to match the consumption rate of the fuel cell, this opportunity could be explored during a more detailed analysis of the fuel storage system.

Table 6.7: Comparing sensitivity in MTOW changes due to different alterations of the fuel cells, batteries and fuel storage system.

Component change	Δm [kg]	ΔMTOW [kg]	Tank change	Δm [kg]	Δ MTOW [kg]	ΔR [nmi]
Fuel cell (+1, 7 total)	+0.93	+3.1	Volume (-10%)	-0.60	-4.14	-10
Fuel cell (+2, +1 PPM, 8 total)	+2.01	+7.3	Volume (+10%)	+0.60	+0.90	10
Battery (+1, 3 total)	+0.3	+1.0	MLI thickness (-20%)	-0.04	-0.11	(n/a)
Battery (+2, 4 total)	+0.6	+2.0	MLI thickness (-40%)	-0.09	-0.24	(n/a)

6.4. Verification and Validation

During the (detailed) design process, no iterative tools or spreadsheets in Python, Microsoft Excel or other programs were used. Therefore, no programs or code need to be verified nor validated. However, the data that are used as inputs on the design, should be verified. This includes mostly fuel cell data and data on insulation properties. The data used comes straight from the manufacturer of the fuel cell and insulation materials, namely *Intelligent Energy* and *Lydall*. This data has the potential to be biased, as a company wants to show the best data in order to be competitive on the market. Therefore, this data needs to be verified and validated by comparing it to other (experimental) data, by means of demonstration or testing.

Considering the fuel cell data, the data shown in Table 6.1 shows data from two companies. This data is put into two graphs, Figure 6.10a and Figure 6.10b, showing the relations between the power and the weight/volume. As one can see, the R^2 values (0.972 and 0.938, respectively), are almost 1, meaning that the trendline fits almost perfectly. This means that the data of both companies is comparable, implying that Intelligent Energy does not give false data. However, it can still be the case that both of the companies present their data better than it actually is. This is hard to verify and validate, as, for example, the prices of the fuel cells is confidential and are not stated anywhere.

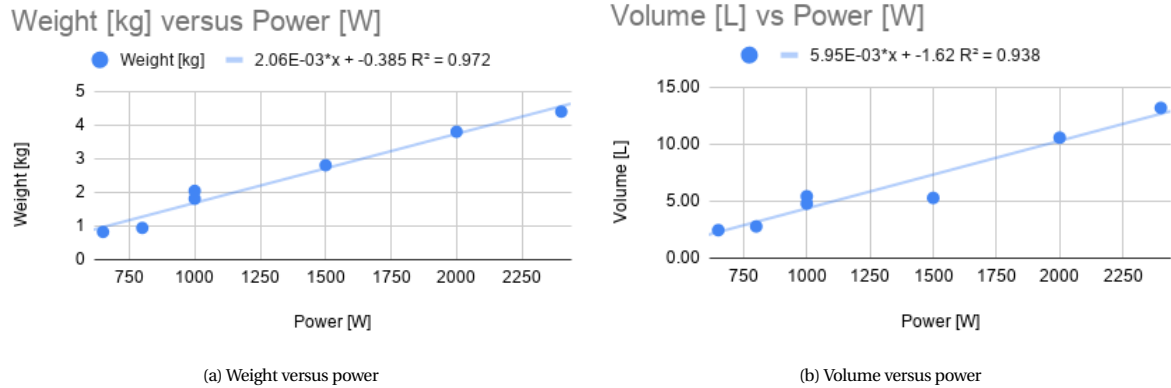(a) Weight versus power

(b) Volume versus power

Figure 6.10: Graphs comparing data on fuel cells from both Intelligent Energy as HES Energy Systems

6.5. Compliance Matrix

In the beginning of this chapter, subsection 6.1.1, all the requirements for this subsystem were listed. Now that the subsystem is designed, it should be checked if it fulfills all requirements. This can be seen in Table 6.8. As one can see, both MD-SYS17 and MD-SYS27 are still to be tested/investigated. This has to do with the fact that there not yet exists an extensive certification or regulation document to which the design can comply at this moment in time. Subsystem requirement MD-SYS23-RISKH2 is said to be partially met. There is a hydrogen regulator connecting the fuel tank and the fuel cell. This regulator does check if the pressure of the hydrogen is sufficient to keep having hydrogen go to the fuel cell. This regulator, however, does not show at all times what the hydrogen level is. Therefore, it can only be known if there is fuel in the tank at all or not. This is not what the requirement requires. Also, subsystem requirement MD-SYS26-RISKH4 is considered to be partially met. Although, hydrogen is produced in more than one facility, it is not yet known if this drone will make use of those. This would be a recommendation for further research.

Table 6.8: Requirements compliance matrix of the hydrogen subsystem

Requirement	Required	Actual	Fully met	Partially met	Not met	To be investigated
MD-SYS25	Hydrogen powered	Hydrogen powered	✓			
MD-SYS19-HY1	6 [kW]	6 [kW]	✓			
MD-SYS19-HY2			✓			
MD-SYS19-HY3	4.8 [kW]	4.8 [kW]	✓			
MD-SYS17	n/a	n/a				✓
MD-SYS24-RISKH2				✓		
MD-SYS25-RISKH2	n/a	n/a	✓			
MD-SYS09-ST13	$3.00 \cdot 10^6$ [Pa]	$3.00 \cdot 10^6$ [Pa]	✓			
MD-SYS26	n/a	n/a	✓			
MD-SYS27	n/a	n/a				✓
MD-SYS26-RISKH4	n/a	n/a		✓		
MD-SYS27-RISKH4			✓			

7

Propulsion

As a start of the chapter, a functional analysis of the propulsion subsystem will be presented in section 7.1. From this functional analysis the subsystem requirements are defined and shown in section 7.2. Then, section 7.3 shows the electrical block diagram and the data flow diagram. The following subsections show the propulsion design for VTOL, transition and cruise. Then, the motors are presented in section 7.8. Then, after the designing, the final design needs to be analyzed. First, section 7.9 shows the all weather capability of the subsystem. Then, a sensitivity analysis is performed as well as verification and validation, shown in, respectively, section 7.10 and section 7.11. Finally, the compliance of the subsystem to its requirements is shown section 7.12.

7.1. Functional Analysis

The propulsion subsystem is responsible for creating horizontal thrust during cruise, but also vertical thrust during VTOL, which is done using rotors. In this process it is of key importance that the design of the propeller characteristics is consistent with what was found during the design of the propellers in the aerodynamics subsystem. Furthermore, attention has to be paid to the total power which can be provided by the fuel cells.

7.1.1. Design Method

To visualize the design process two diagrams have been made, these are the work flow diagram and the functional breakdown structure.

The functional breakdown structure can be seen in Figure 7.1. Within this diagram the different tasks are broken down to see what must be achieved by the propulsion systems during operations.
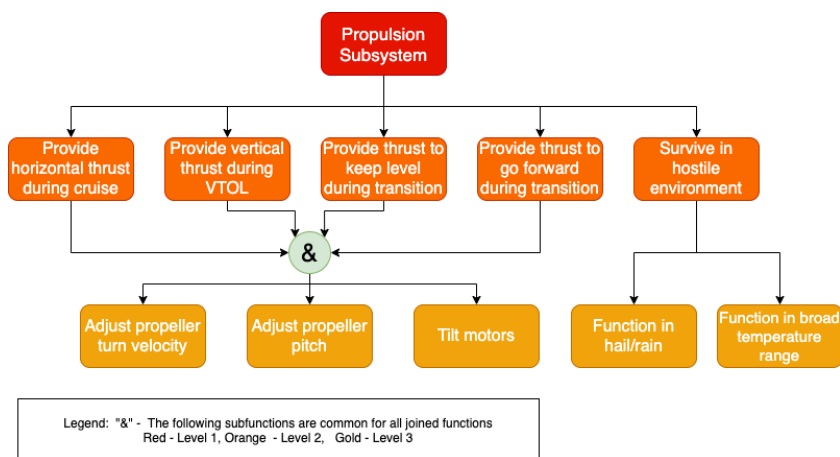
Figure 7.1: Functional breakdown structure for propulsion

Thus the functional breakdown structure shows everything that the propulsion system must be capable of. To design this system the work flow diagram has been made, which gives an overview of the order in which the design process is executed. This diagram can be seen in Figure 7.2, in which the inputs are shown by blue circles, the functions as red rectangles and the outputs as yellow diamonds.
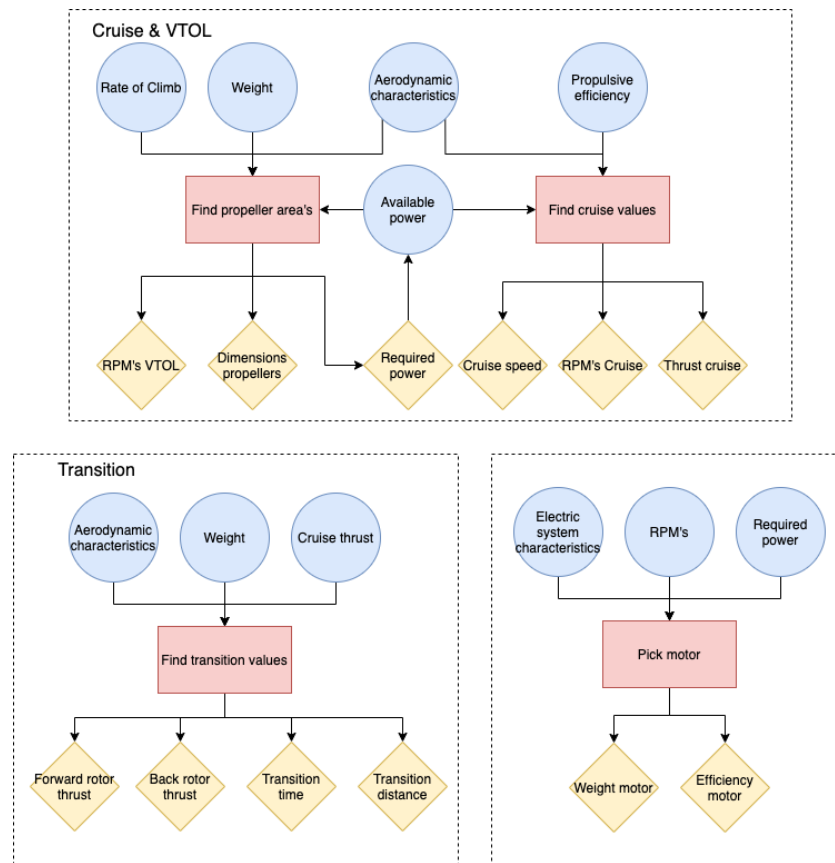
Figure 7.2: Work flow diagram for propulsion subsystem

With this diagrams the design process has been planned and during the design they will be guiding the process.

7.2. Subsystem Requirements

For the design process it is important to look back and see what the requirements for the design are. These requirements are shown below and are several points that the propulsion design has to conform to.

MD-SYS09-PP01:   During cruise the drone shall fly at a minimum of 40 $[m/s]$.
MD-SYS19-PP03.1:   During transition between VTOL and cruise the drone shall not change the altitude at which it is flying with more than 10 $[m]$
MD-SYS19-PP04.1:   The minimum rate of climb of the drone during VTOL shall be 3 $[m/s]$
MD-SYS19-PP05:   The total efficiency from the output of the fuel cell to the rotors shall be above 70%
MD-SYS19-PP06:   The motors shall be able to operate in 99% of the weather conditions
MD-SYS19-PP07:   The motors shall not use more than 4.8 $[kW]$ outside of peak consumption

These requirements formed the base of the design process and will guide the subsystem to a more detailed form.

7.3. Electrical Block & Data Flow Diagram

The electrical block diagram will provide a clear overview of the complete electrical circuit and its components. The base of this design part was to create a circuit that would be as efficient as possible to ensure the highest amount of useful power. Firstly, all the components that would be a part of this circuit had to be listed. Then a basic circuit was created which visualized the connections between all the electrical systems. The next step was to find the locations which needed converters to make sure every part received the required voltage. Most converters have an efficiency of not much higher than 90% [27]. By minimizing the number of converters which are placed in series, the overall efficiency is kept as high as possible. To achieve this paths were made as short as possible and parts that required the same voltage were bundled if possible. Using these optimizations the electrical block diagram shown in Figure 7.3 was developed. The output voltage of the fuel cells is 25$[V]$. The front motors were chosen such that they turn with the correct rpm in cruise with this voltage. This way there was no need for a converter here.
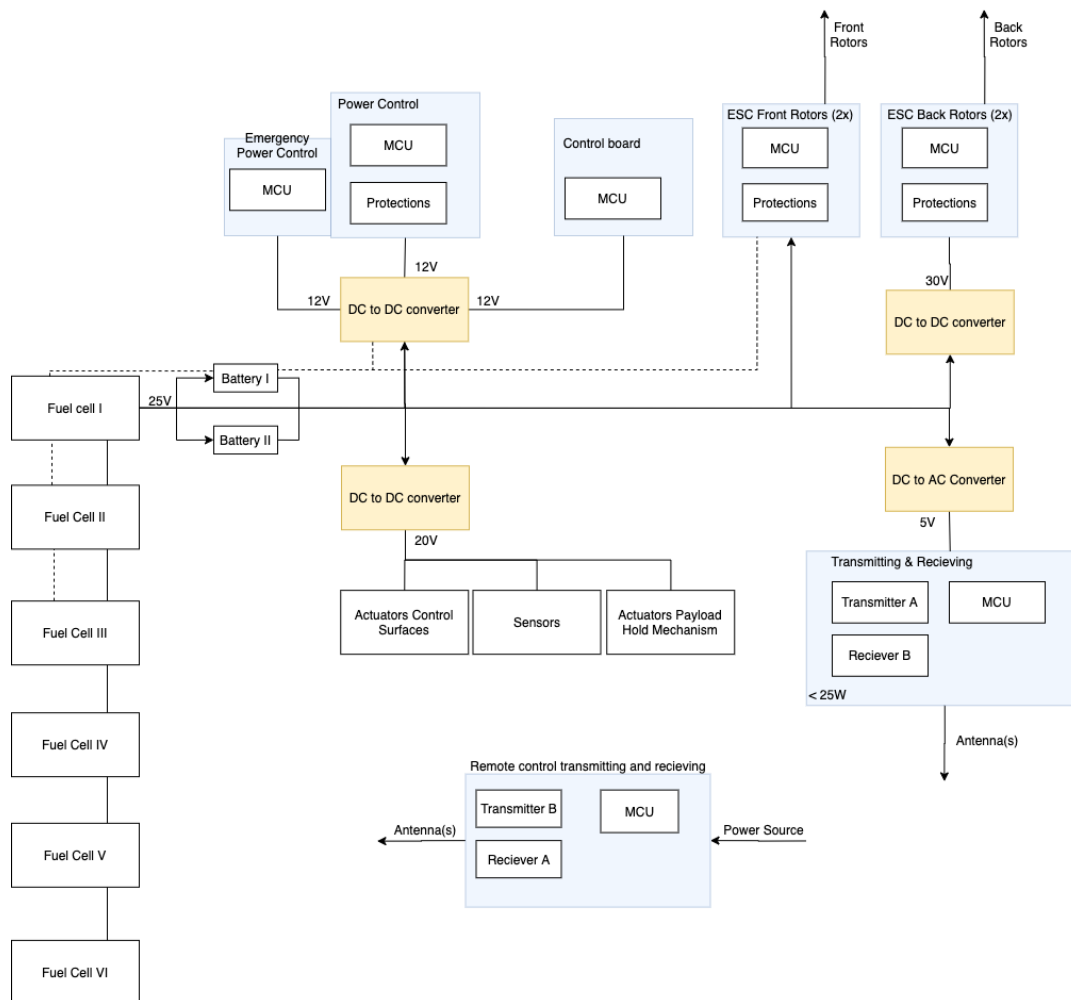
Figure 7.3: Electrical block diagram

7.4. Propulsion Lay-out

The final design that was decided on is one with four propellers, of which two tiltable propellers in the front and two non-tiltable co-axial rotors in the back. These two back rotors help during lift-off and for stability. All of these propellers are so called ducted fans, which improves their propulsive efficiency [39]. This improvement is with a factor of $\sqrt{2 \cdot ER}$ where ER is the expansion ratio and is equal to one. The ER is defined as the outlet diameter divided by the fan diameter and those are the same. The increase is thus $\sqrt{2} = 1.41$. This is taken into account for the aerodynamic design of the proprotors, as the program software does not work with duct efficiency.

The front propellers start tilting during the transition phase to create forward momentum, which will in turn transfer more of the lift generation to the wings. When the stall speed is achieved, all of the lift is generated by the wings and no vertical thrust is needed anymore. These two tilting propellers are attached to the sides of the wing. Here, the wake of the propellers have less effect on any other systems of the drone than when they would be placed near the fuselage.

The two back rotors create an interesting design in terms of aerodynamics and propulsion. Since they are placed on top of each other they will not provide the same amount of lift for a certain power as two separate rotors. This reduced lift generation has to be accounted for during the design phase. This design will form the basis when looking at the different phases of flight.

7.5. VTOL

The take-off will be one of the most driving conditions for the design of the propulsion systems. During VTOL all of the required lift force, to move the drone upwards, has to be produced by the rotors. In this phase, the wing and tail surfaces are actually only a burden, because they create extra drag and weight. To fly at stall speed around 20% of the power required during VTOL is needed. This is the VTOL power it takes the engines to stay at the minimum

rate of climb. The first step in the design process is finding the required power to achieve the minimum speed. Requirement MD-SYS19-PP04 states that the minimum rate of climb shall be higher than 3 $[m/s]$. The height at which the transition between VTOL and cruise will happen is around 150 $[m]$. This means the VTOL phase takes 30 $[s]$.

If the rate of climb is known, the thrust required for take-off can be estimated by combining the weight and the drag at this speed. Because the velocity is low, propeller momentum theory is used to arrive at the maximum static thrust[57]. With this an estimate of the power required is found. This required power to perform the take-off depends on the radius of both the front and back rotors. There are two constraints to keep in mind while designing these radii. First, the total power used is not allowed to be higher than 5 kW. This constraint is imposed because this is the part of the peak power from the fuel cells which can be used during VTOL for propulsion. This leaves enough power for thrust variation to keep the drone stable. The constraint of back rotor radius was set on 0.2 $[m]$. Any larger would mean the rotors would not fit nicely in the fuselage anymore. With these two constraints in place Figure 7.4 was created. In this graph the required power is given for values of area ratio and front rotor radius. It can be noted that the power cut-off here is at 4.2 kW. This is because the motor efficiency is now also taken into account. The area ratio is defined with Equation 7.1

$$Area\ ratio = \frac{2 \cdot A_{front}}{2 \cdot A_{front} + A_{back}} \tag{7.1}$$

Where these are the area's of the front and back rotor disks. It is desired to keep this ratio as high as possible, while also keeping the front rotor radius as low as possible. A high ratio means a smaller back rotor, which makes it easier to implement in the fuselage. The front rotors will be next to the wing. If this rotor radius is large, the overall dimensions of the drone are too massive.

Taking all these things into account a front rotor radius of 0.37 $[m]$ and a back rotor radius of 0.19 $[m]$ were chosen. However, all calculations were done with the assumption that there would only be one back rotor. The thrust that this rotor has to deliver is actually provided by two rotors above each other. This means the radius of the back rotor disk can decrease. Two rotors above each other provide around 1.6 times the thrust of only one rotor with the same disk area [46]. However, the power required also increases. This means the radius of the back rotor can decrease to 0.135 $[m]$. The area ratio then becomes 0.85. The power required for VTOL increases to 4660 $[W]$. But this is fine if an efficient motor is used. In Table 7.1 all propulsion values for VTOL can be found.
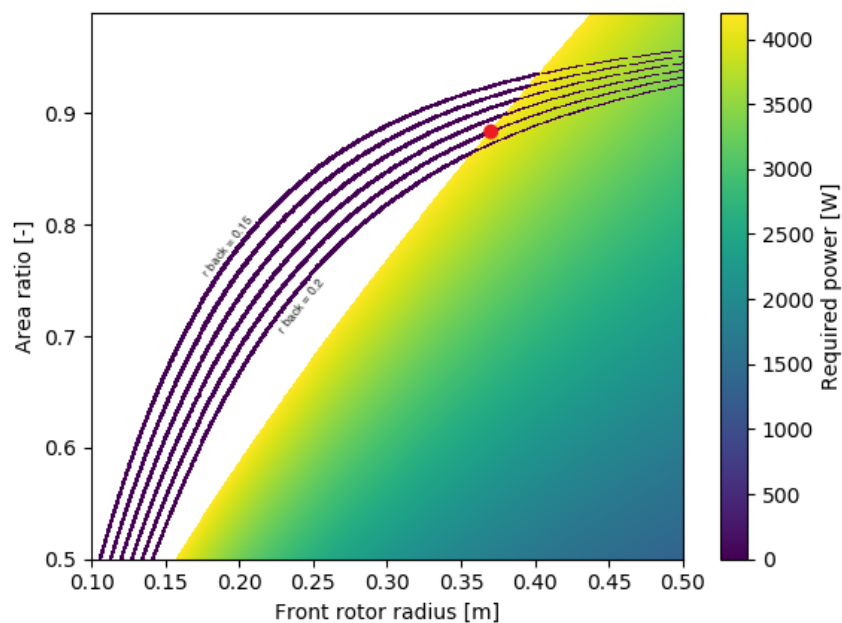

Figure 7.4: Required power for certain area ratio's and front rotor radii

Table 7.1: Propulsion values for VTOL phase[67][5]

Variable	Magnitude	Unit
Area ratio	0.85	$[-]$
Front rotor radius	0.37	$[m]$
Back rotor radius	0.135	$[m]$
Front thrust (1 rotor)	155	$[N]$
Back thrust (both rotors)	41.3	$[N]$
Front turn velocity	3600	$[rpm]$
Back turn velocity	6300	$[rpm]$
Front power	3700	$[W]$
Back power	1000	$[W]$
Total power VTOL	4700	$[W]$

7.6. Transition

The transition phase is interesting for the propulsion subsystem, because of the variation in thrust that is needed to keep the drone at the same altitude. During VTOL there is no horizontal velocity, which means the wing and tail do not create lift. In the transition the front rotors will tilt forward, creating a force forward as well. Depending on the pitch angle the lift and back rotor thrust will also have a horizontal component. To find the thrust levels necessary it is important to take two constraints into account:

- The drone stays at the same altitude during transition -> the sum of forces in vertical direction is zero: $\sum F_y = 0$

- The drone stays at the same pitch angle, possibly after an initial change in pitch -> the moment around the c.g. is zero: $\sum M_{c.g.} = 0$

The values of thrust were found by using a statistical approach in y-direction. Newton's second law was used with the sum of forces in x-direction to find the horizontal acceleration. In Figure 7.5 the used definitions for forces and distances can be found. Force and moment equilibrium gives Equation 7.2a and Equation 7.2b:

$$\sum F_y : (T_f \cdot sin(\alpha) + L_{wing} + T_b + L_{tail}) \cdot cos(\beta) - W = 0 \tag{7.2a}$$

$$\sum M_{c.g.} : T_f \cdot arm_f + L_{wing} \cdot arm_w - T_b \cdot arm_b - L_{tail} \cdot arm_t - D_w \cdot arm_{Dw} + D_t \cdot arm_{Dt} = 0 \tag{7.2b}$$

In these two equations the only forces that can be varied are T_f and T_b, which are the total thrust of the front rotors and the back rotors respectively. When solving for the thrust levels needed to satisfy the constraints, unreasonably large values were found. This is because the moment created by the tail and wing at high speeds. If the stall speed is approached, control surfaces become effective in changing the lift created to counteract the moments. This was accounted for and thrust levels were found and are given in Figure 7.5. The pitch angle β is set to 10°. To create this pitch angle, the back rotors shall create a short peak in thrust after the VTOL phase. If the drone is pitched down, the thrust of the back rotors will also have a horizontal component. This way the drone will get up to speed quicker. As can be seen, the thrust of the back rotors first has to increase before it can go down to zero. This is because the vertical thrust of the forward rotors decreases and the wings do not create much lift yet. When the back rotors are turned off, the velocity increases at a lower rate than before. The time and distance for the total transition are shown in Table 7.2.

Table 7.2: Propulsion values for Transition phase[5]

Variable	Magnitude	Unit
Total time	18	$[s]$
Distance travelled	400	$[m]$
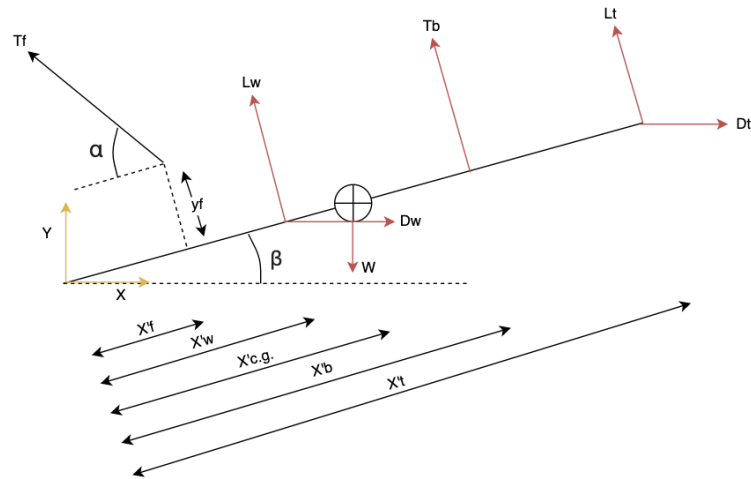
Figure 7.5: Forces during transition from Take-Off to Cruise
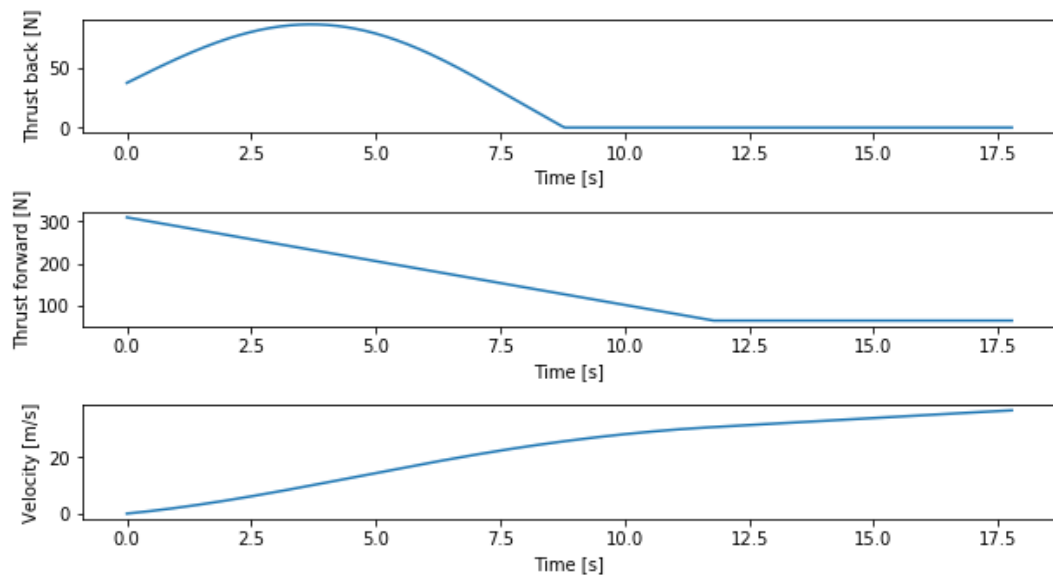
Figure 7.6: Thrust levels and velocities during transition from hover- to cruise configuration

7.7. Cruise

The power of the drone is designed for the VTOL phase. The cruise power will just equal the power which the fuel cells can consistently deliver, after sizing them for VTOL. The cruise speed is found at the point where the thrust is equal to the drag. The thrust of the propellers varies with airspeed according to the relation in Equation 7.3, where η_j indicates the propulsive efficiency[52]. This efficiency also varies with airspeed.

$$T = \eta_j \frac{P_{br}}{V_0} \tag{7.3}$$

After combining this equation with the drag equation, the cruise speed is calculated and given in Table 7.3.

7.8. Motors

Brushless DC motors (BLDC) will be used to turn the rotors. Brushless motors have a longer life time than motors with brush. They have higher power/size ratios and are very resistant to rust. This is important, since the drone needs to fly in all-weather conditions and it should function in a humid environment. These motors require less maintenance, which saves on operational cost. Additionally, the efficiencies of BLDC motors are higher than efficiencies of motors with brush. The average difference is around 15-20%. The main downside of BLDC motors is that they are more complex to control. The BLDC motor is very well developed and there are many efficient

Table 7.3: Propulsion values for CRUISE phase

Variable	Magnitude	Unit
Cruise speed	49.8	$[m/s]$
Propulsive efficiency	0.88	$[-]$
Front thrust	2x32	$[N]$
Back thrust	0	$[N]$
Turn velocity	2050	$[rpm]$
Front power	4200	$[W]$

motors available on the market. It is desired to use a motor which can operate on the voltage that is given by the fuel cells (25 Volts). This means no converter is necessary to change the voltage. These converters are never one hundred percent efficient and they create heat. Quite some heat would be generated by the converter, since so much power is going through. Another requirement for the motors is that they should be able to provide rotational speeds of 4,300 and 6,000 rpm for the front and back respectively. Lastly, it should be able to take at least 1.8 kW of power. In Table 7.4 multiple options can be found. These are all from a site for hobbyists[1], while for the actual design industrial grade motors will be used. However, it does show that BLDC motors in these ranges of power and voltage are widely available and that they are relatively small in size. It can be deducted that both the front and back motor used will be around 400-700 grams. These motors have an efficiency around 90%[34].

Table 7.4: Examples of available BLDC motors

Name	[RPM/V]	Weight [g]	Max Current [A]	Max Voltage [V]	Power [W]	Dimensions (LxD)[mm]
Turnigy Aerodrive SK3	213	706	65	37	2550	72x59
KD 53-20	240	500	80	37	1700	56x63
Turnigy RotoMax 1.40	228	715	75	37	2700	83x80

The motors will need to be cooled. This can be done with the help of the airflow that is created by the rotors. The motors will be immediately behind those. If casing will be used around the motors, it is important that the air can still reach them.

The rotors will be tilted using rotary actuators. These actuators are placed in the sides of the ducts, since the thickness of the wing is not large enough to integrate them in it. All the loads on the propellers and the ducts transfer through this actuator and its attachment. This is further discussed during the design of the structure in chapter 9.

7.9. All-Weather Analysis

The motors need to be resistant to cold temperatures. To achieve this heat needs to be transferred to the motors to make sure the mechanism does not freeze. During flight the weather might create problems for the propellers. Hail and rain can create problems for the propeller. During hail and rain propellers are quickly damaged which can quickly increase the risk of failure. This is a difficult risk to mitigate and will mostly be minimized by using a strong and durable material for the propellers. Another way to minimize the risk of failure is by inspecting the drone often, which is could be done each time it returns to the distribution centre.

During heavy headwind the forward flight velocity drops. From the market study it was found that the maximum wind speed that the drone will encounter is 14 $[m/s]$. This will reduce the travel speed of the drone by 14 $[m/s]$, resulting in a cruise speed of 35.8 $[m/s]$. This is a steep reduction in speed, however there is little that can be done about it. If speed is really of the essence it is possible to use the extra batteries to provide peak power for a limited duration.

---

[1] www.hobbyking.com

7.10. Sensitivity Analysis

It is important to have a good understanding of the critical input values, which can change the design significantly. This is why a sensitivity analysis was conducted. Changes in multiple inputs are investigated.

A reasonable change in rate of climb does not make a large difference for the design. Since the upward velocity stays relatively low, the drag is almost insignificant in comparison with the weight. Options to climb faster are definitely still open if desired.

Next the available power was changed to see the effect this has on the required rotor area. The power constraint was changed from 4200 $[W]$ to 4000 $[W]$, while keeping the back rotors radii constant. As a result of this change the front propeller radii changed from 0.37 $[m]$ to 0.415 $[m]$. Thus a change of less than 5% in the power resulted in a 10% increase in the front propeller radii. Thus

7.11. Verification and Validation

Now that the design is in its final state it needs to be verified and validated. During the propulsion subsystem design several programs have been created, which have been attached in the appendix. To verify this code several methods have used. Calculations with single equations have been checked by hand to make sure the results are the same. Firstly, the code that calculated design parameters was verified. The first test that was performed was checking the singularities, to see if the program could handle boundary values. For every program the inputs were one by one changed to zero to see what the effect would be. When errors occurred with a certain input at zero, it was first checked if this value could ever go to zero in realistic conditions. If this was not the case, a check was added to make sure the input is always larger than zero. If the value could go to zero the code was changed to give the proper result. For example once the propellers tilt to a really small angle, they would have to provide a negligible amount of thrust, but since the angle of the propellers was so small this still required large amounts of power. In this case the vertical thrust for small angles was set to zero. As a result the drone might start descending for the final seconds of the transition, however this will not create problems.

Next the code was tested with JavaProp, which is a validated program to simulate propeller performance[2]. The main differences between both programs is the different inputs used and that JavaProp is designed to simulate a single propeller, however the inputs in the propulsion code allowed for such a change. Since the inputs and outputs of both programs differed it was impossible to start off with the exact same values. Instead the program was tested by using the outputs of one as the inputs for the other in a cycle. During this the wing geometry and shared inputs stayed constant . As a result for each type of propeller that was tested both programs converged to the same results for the same inputs.

For the transition phase the code was validated using flight test data from a hybrid VTOL drone, from which one of the graphs is shown in Figure 7.7[3]. This was compared with the the graphs received from the transition phase code.
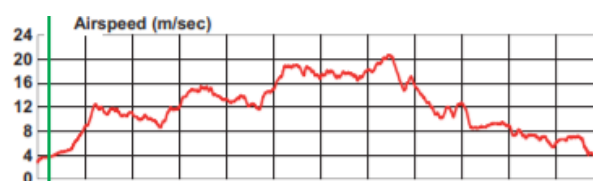
Figure 7.7: Flight test airspeed data during take-off and landing[3]

During the take-off in the flight test there was downtime between tilting the propellers. This can be seen as the decrease in airspeed in the graph. The hybrid drone used in this flight test is lighter at 4.2 kg and with only half the lift generating surface area. Thus instead of a numerical comparison, the airspeed and tilt graphs were compared. When the downtime in the flight test is left out the graphs look very similar with a steep increase at the start which slowly falls off after during the second half of the rotation. The airspeed for both is significantly different, however this is explained by the different lift requirements due to weight.

To validate the propulsion results the disk loading of the designed drone was compared with other drones that transported similar amounts of payload. Comparing the disc loading to drones that carry the same amount of

---

[2]https://www.mh-aerotools.de/airfoils/java/JavaProp%20Users%20Guide.pdf
[3]http://icas.org/ICAS_ARCHIVE/ICAS2012/PAPERS/936.PDF

payload reveals that the disc loading of the drone is almost twice as high as other drones. This is however compared to drones that only use rotors as a means of lift generation, since there are insufficient hybrid drones with the same payload capacity available. Taking this into account the disc loading for Osprey like planes was investigated. This showed that planes with this setup had a much larger disk loading than the previously mentioned drones.

To explain this difference in disc loading the power loading was looked at. Osprey generally have a higher power loading than helicopters, this is caused by the smaller rotor area that needs to create the same amount of lift. The designed drone has a much lower power loading then comparable aircraft during VTOL, however this is when looking at the minimum values calculated to perform the take-off. When the peak power consumption is considered the power loading increases. Resulting in a design that falls between a helicopter and Osprey like planes.

7.12. Compliance Matrix

After the design for this subsystem has been finished it was time to see whether the requirements that formed the basis of this design were properly fulfilled. Therefore a compliance matrix is constructed, which can be seen in Table 7.5. In this matrix an overview is given of which requirements have been met by the design. Three requirements are fully met, two partially met and one is to be investigated further. It is still unclear how well the motors perform in critical weather conditions. This can be examined by testing. The two requirements that are partially met were designed for without considering wind gusts. This means the speed and altitude might differ so that the requirements is not met anymore.

Table 7.5: Compliance Matrix

Requirement	Required	Actual	Fully met	Partially met	Not met	To be investigated
MD-SYS09-PP01	40 [m/s]	50 [m/s]	✓			
MD-SYS19-PP03.1	10	unkown		✓		
MD-SYS19-PP04.1	3	3		✓		
MD-SYS19-PP05	70%	89%	✓			
MD-SYS19-PP06	N.A.	N.A.				✓
MD-SYS19-PP07	< 4.8 [kW]	4.6 [kW]	✓			

8

Stability and Control

This chapter covers the design process and its results for the stability and control subsystem of the drone. In section 8.1 the goals and functions of the stability and control subsystem are described. In section 8.2 the design method used for the design process is explained. In section 8.3 the design process is executed and in section 8.4 a sensitivity analysis of the design is performed. Verification and validation of the design tools is done in section 8.5 and the chapter is concluded in section 8.6 with a compliance matrix showing which, and to what extend, subsystem requirements are met.

8.1. Functional analysis

The goal of the stability and control subsystem design is provide active and passive stability whilst also providing control to the drone in both the cruise phase, the vertical take-off and landing phase, and transition phase. The surfaces to be designed to provide passive stability and control during cruise include the horizontal tail for longitudinal passive stability and the vertical tail for lateral passive stability. For control during cruise the following control surfaces are designed: ailerons for roll control, rudder for yaw control and elevator for pitch control. The drone is capable of vertically taking-off and land, and since the drone is not passively stable in this configuration the stability and control subsystem must provide active stability and control during this flight phase. The functional breakdown of the drone can be found in Figure 8.1 which shows all tasks that the subsystem must provide and is designed for.
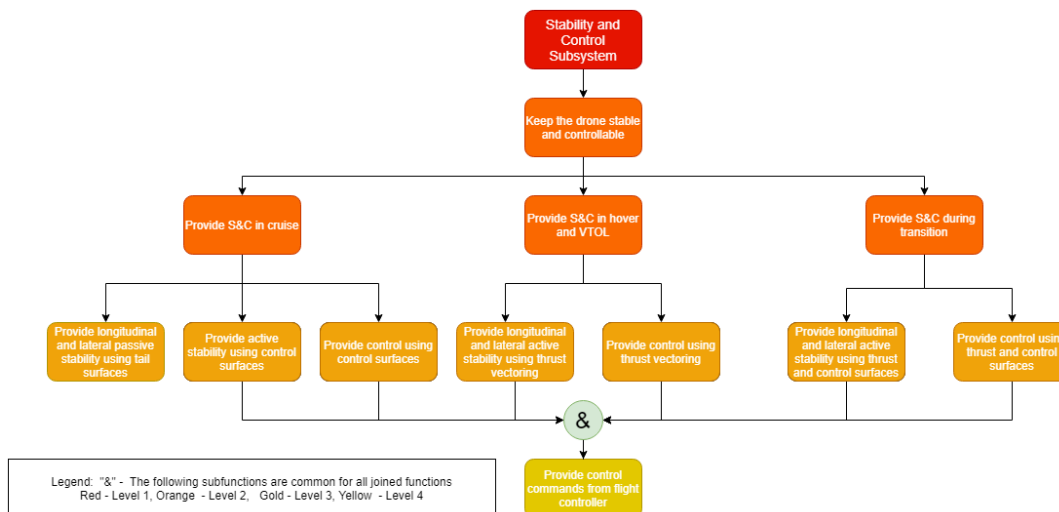

Figure 8.1: Functional breakdown structure for stability and control

The following subsystem requirements apply to the stability and control subsystem:

MD-SYS09-CS01 :   The drone shall be longitudinally, directionally, and laterally statically stable.
MD-SYS09-CS02:   The drone shall be dynamically stable.
MD-SYS09-CS02.1:   The drone shall positively damp any combined lateral-directional oscillations.
MD-SYS09-CS03:   The drone shall be able to reach a trim condition throughout all flight phases.
MD-SYS09-CS04:   The drone shall be in equilibrium when on the ground.
MD-SYS09-CS05:   The drone shall be controllable when introduced to 14 [m/s] wind speed and 24 [m/s] gust
                    speed in all directions throughout all flight phases.
MD-SYS09-CS07:   The drone shall be controllable in case of an engine failure.
MD-SYS09-CS08:   The drone shall have a maximum pitch acceleration of 0.07 [rad/s^2] during cruise.
MD-SYS09-CS09:   The drone shall have a minimum yaw acceleration of 0.07 [rad/s^2] during cruise.
MD-SYS09-CS10:   The drone shall be able to roll 60° in 1.3 seconds.
MD-SYS09-CS11:   The drone shall have a minimum roll acceleration of 45 [°/s^2] during VTOL.
MD-SYS09-CS12:   The drone shall have a minimum pitch acceleration of 45 [°/s^2] during VTOL.
MD-SYS09-CS13:   The drone shall have a minimum yaw acceleration of 45 [°/s^2] during VTOL.

Requirements 01, 03, 05 and 07 are covered in subsection 8.3.2, subsection 8.3.3 and subsection 8.3.4, requirement 02 and 05 in subsection 8.3.5, and requirements 03 and 08 until 13 in subsection 8.3.4. Also, it must be noted that requirements MD-SYS-CS08 and MD-SYS09-CS09 are obtained from Brian Roth (2009) [54].

8.2. Design Method

To give an overview of how the subsystem is designed, a workflow diagram was made which is shown in Figure 8.2. For the longitudinal sizing, the horizontal tail surface area is calculated based upon aerodynamic parameters and the location and masses of all components in the drone. From this a so-called 'scissorplot' is constructed, in which a horizontal tail surface area can be selected based on the wing position and stability- and control requirements. It was checked if this surface area would provide enough control due to the thrust moment generated by the engines. If this calculated surface area was sufficient to counter balance the additional pitch moment from the engines, the horizontal tail would be acceptable. With the surface area determined, it was possible to determine the incidence angle required to have zero elevator deflection during cruise to reduce drag. Lateral tail sizing has been done for the following critical conditions: lateral crosswind and one engine inoperative. The crosswind requirement results in a required lift coefficient of the vertical tail and a corresponding sideslip angle. This can be used to size the surface area of the vertical tail in case of an engine failure during cruise. For the flight phases VTOL and cruise are considered. The transition phase is analyzed in more detail in chapter 7. For VTOL the amount of power required and the corresponding rotation angle of the engines are calculated such that they comply with the roll, pitch, yaw and wind gusts requirements during hover. For cruise conditions, the control surfaces are designed according to the yaw, pitch and roll requirements in cruise conditions. With the dimensions, the hinge moments can be calculated and consequently suitable servos can be selected. The reference frame considered throughout the analysis is the body reference frame, with the x-axis going through the nose of the drone, the y-axis pointing to the right (seen from the perspective of the drone) and the z-axis pointing down to complete a right-handed system (see Figure 8.5). Rotation around the x-axis is referred as rolling, rotation around the y-axis as pitching and around the z-axis as yawing.

8.3. Analysis

In this section the tail configuration is determined, the longitudinal and lateral tail are sized, the stability and control during the VTOL and cruise phase stability is designed and the flight controller design is presented.

8.3.1. Tail configuration

A T-tail configuration has been chosen in order to reduce the amount of down-wash experienced by the horizontal vertical tail from the main wing. Consequently, the down-wash gradient can be assumed to be $\frac{d\epsilon}{d\alpha} \approx 0$ and the air velocity ratio of the horizontal tail and main wing $\frac{V_h}{V} \approx 1$.

8.3.2. Horizontal tail sizing

The horizontal tail has been sized such that the drone is both statically stable and controllable. The drone is said to be longitudinally statically stable when in case of an angle of attack increase, the resulting moments decreases the increase in angle of attack. In other words, $\frac{dC_M}{d\alpha} < 0$. The design has been done under the following assumptions:
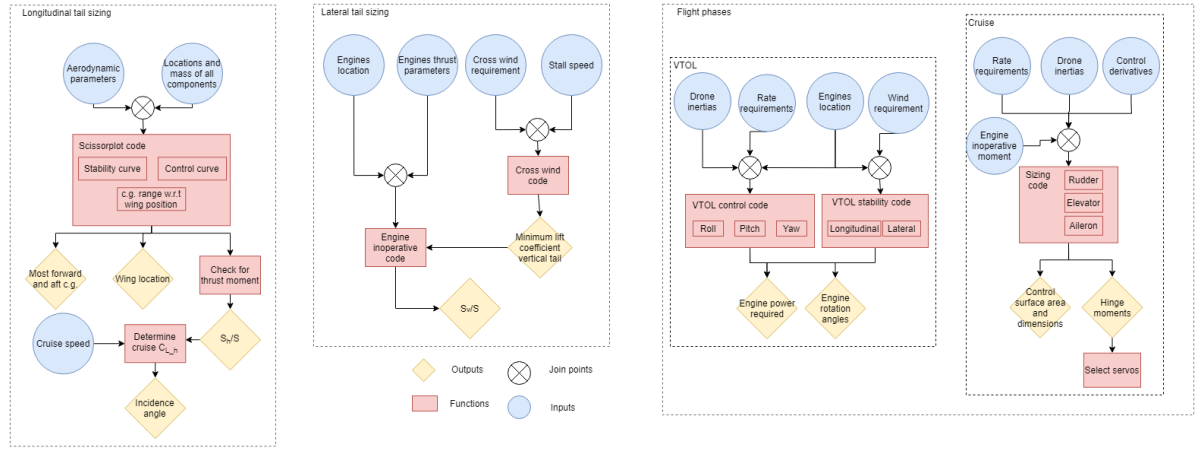
Figure 8.2: Work breakdown of the stability and control subsystem design process

- Cruise configuration is considered (the two front propellers are pointing forward and the back propeller does not provide any lift or thrust)

- Neglect drag

- Neglect the effect of vertical displacements

- Neglect the effects of speed (assume subsonic)

- Stick-fixed analysis (no elevator deflection)

- The horizontal tailplane has a symmetric airfoil hence the aerodynamic moment of the tailplane around its aerodynamic center is zero [23]

- The OEW c.g. includes all components of the drone except the fuel and the payload

- The c.g. location of the fuel is assumed to be in the geometrical middle of the fuel tank

- The c.g. location of the payload is assumed to be in the geometrical middle of the payload box

- The (horizontal) resultant thrust vector is assumed to go through the c.g. introducing no pitch moments

In order to have $\frac{dC_M}{d\alpha} < 0$, the c.g. must be in front of the neutral point. Taking the change in moments around the neutral point, subtracting a stability margin (SM), and after rewriting, Equation 8.1 presents the horizontal tail area and main wing area ratio with respect to the c.g. location [44].

$$\frac{S_h}{S} = \left(\frac{1}{\frac{C_{L\alpha_h}}{C_{L\alpha_{A-h}}}(1-\frac{d\epsilon}{d\alpha})\frac{l_h}{c}(\frac{V_h}{V}^2)} \right) \bar{x}_{cg} - \frac{\bar{x}_{ac}-SM}{\frac{C_{L\alpha_h}}{C_{L\alpha_{A-h}}}(1-\frac{d\epsilon}{d\alpha})\frac{l_h}{c}(\frac{V_h}{V})^2} \tag{8.1}$$

The drone is said to be controllable if it is possible to maintain a trim condition: equilibrium condition in which all moments are zero. Taking the moments around the c.g., setting this to zero and rewriting, results in Equation 8.2. This shows the relation of the horizontal tail area and main wing area ratio with respect to the c.g. location [44].

$$\frac{S_h}{S} = \left(\frac{1}{\frac{C_{L_h}}{C_{L_{A-h}}}\frac{l_h}{c}(\frac{V_h}{V})^2} \right) \bar{x}_{cg} + \frac{\frac{C_{mac}}{C_{L_{A-h}}}-\bar{x}_{ac}}{\frac{C_{L_h}}{C_{L_{A-h}}}\frac{l_h}{c}(\frac{V_h}{V})^2} \tag{8.2}$$

The c.g. location and aerodynamic center location are measured with respect to the leading edge of the MAC (LEMAC) position (measured from the front of the drone), in percentage of the MAC. Note: the aerodynamic center for the stability curve and the aerodynamic center for the control curve are not the same. The location of the aerodynamic center depends on the speed; it moves forward with increasing speed [44]. For the stability curve the sizing condition is the most forward aerodynamic center position, hence stability is assessed at high cruise speed. The control curve is assessed at minimum speed, this is the sizing condition for the controllability of the drone. This

means that the control curve is analyzed at stall speed.

In order to determine the minimum $\frac{S_H}{S}$ ratio, the most forward c.g. position and most aft c.g. position that the drone will encounter during operations must be determined. This has been done by calculating the c.g. location of the operational empty weight (OEW) and the c.g. location after fueling and adding the maximum payload of 10 [kg] (and the combination of having no payload and being fully loaded with fuel). This resulted in a c.g. excursion. Since the wing position has a great influence on the c.g. excursion, shifting the wing gives different c.g. excursions. This has been done for different wing positions along the fuselage. The c.g. locations are calculated as a percentage of the MAC with the LEMAC being the origin, which enables to plot the c.g. excursions for different wing positions in the same graph as the control curve and the stability curve. See Figure 8.3 in which the stability curve, control curve and the c.g. excursions with respect to wing locations are plotted: the so called 'scissorplot'.
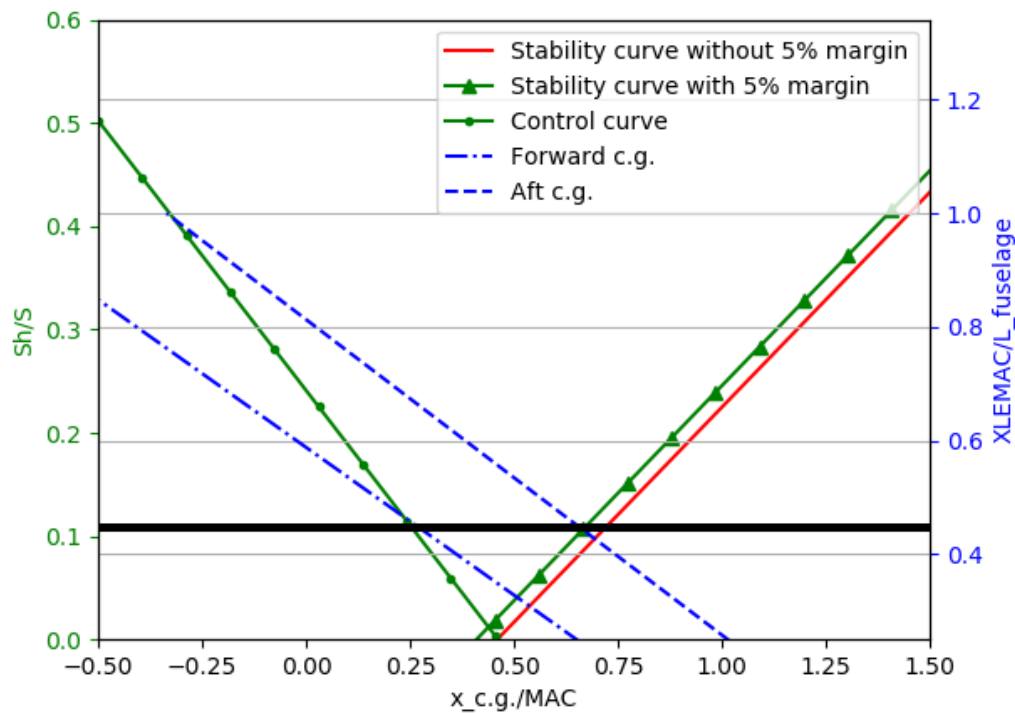

Figure 8.3: The control curve and stability curve together with the c.g. range for different wing positions: the horizontal line intersects the minimum surface area ratio with the corresponding wing position.

The wing positions are in terms of percentage of the fuselage length, measured from the nose. Based on the c.g. range and the wing position, it is possible to select the smallest value of $\frac{S_H}{S}$ such that the c.g. range fits completely within the stability and controllability margins. Taking a stability margin for the stability of 5% and a safety margin of the c.g. range of 5% for both aft and forward c.g. to take into account shifts in weight components during operation (for example payload and fuel shifts during flight), the minimum $\frac{S_H}{S}$ results in 0.11 (the vertical tail area is thus 11% of the total main wing area) with a LEMAC position of 45% of the fuselage length from the nose. A summary of the obtained values from the scissorplot can be found in Table 8.1. It should be noted that the c.g. range lies within the front and aft rotor location, which is necessary for hover. It can be observed that the distance between the most forward c.g. and the location of the front rotor is rather small, but this will most likely not be exceeded since a 5% margin is taken for the c.g. position and on top of this the most forward c.g. position is in case of having no fuel in the tank. Hence the calculated forward c.g. will not be encountered during VTOL phase, since it is not possible to fly with zero fuel in the tank and thus safe VTOL is guaranteed. The c.g. for full payload and fuel loading is located slightly in front of the wing a.c., hence during cruise the horizontal tail has to provide negative lift to ensure trim condition.

Longitudinal thrust moment

In the scissorplot, it was assumed that the horizontal thrust from the engines do not introduce any moments. However, the horizontal thrust from the engines might have a slight vertical off-set with respect to the center of

Table 8.1: Data resulted from the scissor plot. Locations are measured from the nose of the drone.

Parameter	Value
Most forward c.g.	0.68 [m]
Most aft c.g.	0.89 [m]
Total c.g. (fully loaded)	0.72 [m]
Stability margin (SM)	5%
Safety margin c.g.	5%
MAC	0.541 [m]
Tail arm	1.3 [m]
Front rotor force application position (VTOL)	0.65 [m]
Wing a.c. position	0.81 [m]
Length to tail	2.11 [m]
Length tail from end fuselage	0.913 [m]
$(\frac{S_H}{S})_{scissorplot}$	0.11 [-]
$(S_H)_{scissorplot}$	0.06 [m^2]

gravity. This introduces an additional pitch moment which must be taken into account in order to be able to trim the aircraft. Hence it is necessary to check if the required S_H obtained from the scissor plot is sufficient to trim the aircraft with the moment introduced by the vertical thrust off-set. The following assumptions hold:

- Size using cruise level density and at minimum control speed using most aft c.g. position

- Minimum control speed is assumed to be 25% higher than the stall speed [44]

- The two propellers are symmetrically placed with respect to the x-axis and z-axis

- The back propeller does not produce any vertical thrust (in the case of cruise configuration)

Equating the moments and rewriting for the tail surface area results in Equation 8.3.

$$S_H = \frac{F_{maxthrust} \cdot z_{engine-cg}}{\frac{1}{2} \cdot \rho_{cruise} \cdot V_{mcs}^2 \cdot C_{Lh} \cdot (x_{htail} - x_{aft_{c.g.}})} \tag{8.3}$$

With $z_{engine-cg}$ the vertical distance between c.g. and propellers and x_{htail} the distance from the nose to the a.c. of the horizontal tail plane. This results in a value for S_H of 0.02 [m^2]. Compared to the value found from the scissor plot, the value from the scissorplot is sizing.

Incidence angle determination

With the found horizontal tail surface area and considering cruise condition, the required lift coefficient of the horizontal tail in order to have a trim condition can be calculated. With the horizontal tail wing characteristics, the corresponding angle of attack can be determined, which in terms defines the incidence angle of the horizontal tail. This turned out to be 2.0° down (indeed producing negative lift during cruise). See Figure 8.4 for a visualization of this configuration. The incidence angle enables to fly with zero elevator deflection during cruise, which reduces drag and saves power as the cruise flight takes most of the mission time.
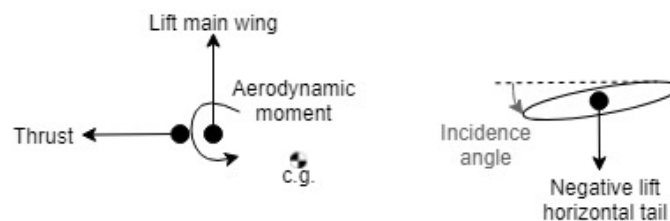

Figure 8.4: Simplified visualization of incidence angle set up (not on scale)

8.3.3. Vertical tail sizing

The size of the vertical tail must be sufficiently large in order to counter act the maximum yawing moment encountered during operation. The assumptions used in the longitudinal thrust moment calculations also hold in the vertical tail sizing. In this case no rudder is considered and the vertical tailplane has a symmetric airfoil. The sizing conditions include one engine inoperative and a maximum wind speed encountered at an angle of 90° with respect to the x-axis during cruise. Since a symmetrical airfoil is used for the vertical tail, as a consequence the so-called weather-vane stability applies. This means that in case of disturbance in sideslip angle, the vertical tail produces a moment resulting in reducing this disturbance (the drone has a tendency to turn into the direction of the disturbance). Therefore the vertical tail design ensures lateral passive stability directly.

Maximum crosswind condition

The following assumptions hold:

- Crosswind pressure acting primarily on the vertical tail, moment effect due to wind pressure on the fuselage is neglected

- Zero bank (roll) angle

From requirement MD-SYS-09-CS05 the vertical tail must be able to counter-act wind speeds of 24 $[m/s]$. The sizing condition is when this wind speed hits the drone at a 90° angle with respect to the x-axis, introducing a maximum yaw moment. It is assumed that the wind provides pressure on the vertical tail surface only, which has the largest moment arm and thus introduces the largest yaw moment encountered and can be considered the sizing condition. The effect of the pressure of the wind to the fuselage is omitted since the c.g. lies close to the center of the fuselage, hence the total resultant moment due to a 90° wind pressure on the fuselage will be close to zero. In order to counter-act the resulting moment, the vertical tail must be able to produce a counter moment. The dynamic pressure of the wind is calculated with Equation 8.4

$$q_{crosswind} = \frac{1}{2} \cdot \rho \cdot V_{wind}^2 \cdot S_v \tag{8.4}$$

The total moment from the lift force produced by the vertical tail must be equal and greater than the force resulting from the dynamic pressure of the crosswind in order to restore the resulting moment. This results in Equation 8.5.

$$\frac{1}{2} \cdot \rho \cdot V_{mcs}^2 \cdot S_v \cdot C_{L_v} > q_{crosswind} \cdot S_v \tag{8.5}$$

Rewriting results into Equation 8.6 in order to provide sufficient counter-force to restore from the wind.

$$C_{L_v} > \frac{V_{wind}^2}{V_{mcs}^2} \tag{8.6}$$

With C_{L_v} the lift coefficient of the vertical tail and V_{mcs} the minimum control speed (25% higher than V_{stall} [44]).

Table 8.2: Vertical tail design requirements

Parameter	Value
V_{wind}	24 $[m/s]$
V_{mcs}	34 $[m/s]$
C_{L_v}	> 0.5 [-]
Sideslip angle	7 [°]

Results can be found in Table 8.2. In order to fly in a trimmed condition in case of a 24 $[m/s]$ 90 degrees cross wind, the drone will fly at a sideslip angle of 7°.

One engine inoperative

The following assumptions hold:

- The drag of the inoperative engine is assumed to introduce a drag moment of 10% of the total moment introduced from the operative engine

- The c.g. is assumed to lie along the x-axis which is assumed to lie on the symmetry axis of the drone

- Sizing is done using 100% of the total thrust of the operative engine

In case of an engine failure, the other engine is still producing thrust. This introduces a yawing moment equal to $M = T_{max} \cdot y_{engine}$ with T_{max} 100% of the total thrust engine force and y_{engine} the location of the engine along the y-axis. The vertical tail must be able to counter-act this moment. The total force required can be found by dividing this yaw moment by the longitudinal distance of the vertical tail to the most aft c.g. location $F = \frac{M}{(x_{vtail} - x_{aftcg})}$). The required vertical tail surface area can then be found using Equation 8.7.

$$S_v = \frac{F}{\frac{1}{2} \cdot \rho_{cruise} \cdot V_{mcs}^2 \cdot C_{L_v}} \tag{8.7}$$

With F the force required to balance the yaw moment and V_{mcs} the minimum control speed. It is assumed that the drone can have a maximum sideslip angle of 7°. With the corresponding C_{L_v} the surface area can be found to be $S_v = 0.39\ [m^2]$. Note that due to the resulting force from the vertical tail and due to a vertical offset with respect to the c.g. location, the drone will have a roll moment as a result. Normally, the drone will have a bank angle in the direction of the working engine in order to balance the tail rolling moment with a weight component. For now it is assumed that the ailerons are capable of counteracting the resulting roll moment to keep a bank angle of zero°. The total area is 70% of the total main wing area, which is rather large. This is obviously due to the large thrust and the large arm of the engine. A possible way to reduce the area is to increase the tail arm, however since the fuel tank is used as load bearing structure, increasing the tail arm length would require extra structural components for the tail which would increase the total weight. A more straightforward solution, in order to size the vertical tail for the engine inoperative condition, is to take the rudder sizing also into account to reduce the vertical tail surface area needed to safe weight. After the sizing it is checked whether the yaw requirement during cruise MD-SYS09-CS13 can still be met and that the area and rudder is sized according to the critical condition. This is done in subsection 8.3.4.

So far the sizing of the vertical and horizontal tail has been done for passive stability and control with the assumption of zero elevator and zero rudder deflection. In order to be able to accomplish a certain yaw and pitch the rudder and elevator is sized accordingly in subsection 8.3.4 (for the rolling requirement the ailerons are sized accordingly).

8.3.4. Flight phases
The flight phases considered for control include the VTOL phase and the cruise phase. The following assumptions hold:

- The horizontal thrust force of the engines go through the c.g. and hence do not introduce any pitch moments

- Delta thrust from the engines are instantaneous

- The two forward placed engines can rotate both forwards and backwards

- The back engine cannot rotate and can only provide vertical thrust

- The two rotors of the back engine cannot change its rotational speed individually but change simultaneously with the same amount

- For the rolling motion it is assumed that the drone can increase in altitude without problems

Vertical take off and landing phase
During the VTOL phase the drone needs to be able to move in all degrees of freedom, besides this it also needs to adhere to requirements: MD-SYS09-CS11, MD-SYS09-CS12 and MD-SYS09-CS13. In this subsection each motion is explained in more detail together with the respective required thrusts and rotation angles of the engines to perform these maneuvers. For these motions a basic representation of the rotor layout is shown in Figure 8.5. This layout is not on scale but is used to visualize the reference frame and engine locations.
For each rotation acceleration requirement, the required torque can be calculated with Equation 8.8: the moment of inertia around the corresponding rotation axis.

$$T = I \cdot \alpha \tag{8.8}$$

With α the rotational acceleration in $[\frac{rad}{s^2}]$ and I the moment of inertia in $[kg \cdot m^2]$. For each motion, different engines have to provide a certain delta force, and need a different tilt angle to perform the motion. This is discussed per rotational motion. Note that the tilt angle of the engine here is indicated with θ; a positive θ indicates a forward engine rotation around the y-axis in the direction of the x-axis (towards the nose), a negative θ indicates a backward rotation (around the y-axis negative direction of the x-axis, towards the back engine). The engines can rotate 90 ° forward and 90° backward from their vertical upward position. Furthermore, since the c.g. has a range, in order to
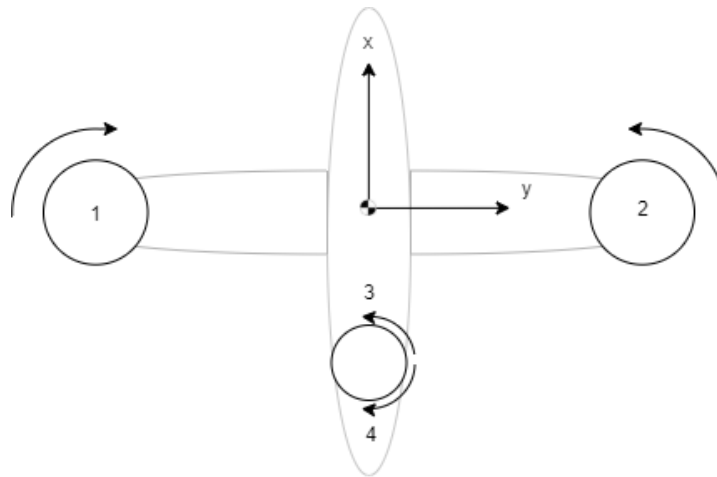
Figure 8.5: Graphical representation of the top-view layout and rotation directions, x-axis pointing through the nose of the drone

calculate the critical theta and thrust force, the c.g. location that results in the shortest moment arm is considered for each case. Furthermore it is assumed that the back rotor cannot tilt, and its force application is on the x-axis, passing through the c.g.. Because of this, no roll moment is introduced by the back rotor. The motions performed are indicated in figures 8.6, 8.7 and 8.8. In order to accomplish an opposite motion, the same approach applies but mirrored. Due to having three engines (instead of 4 symmetrically placed), there is a strong coupling between the yaw and rolling motions. In the following calculations it is assumed that these motions are decoupled to perform a preliminary analysis. With the required force required to perform the motions known, next the power required from the engines is calculated via Equation 8.9 [57].

$$P = \sqrt{\frac{\Delta T^3}{2\rho A}} \tag{8.9}$$

With A being the disk area of the propeller.

Yaw When the drone needs to yaw in a certain direction, a change in moment needs to be created around the z-axis. There are two ways of doing this. The first way would be by means of differential torque, in the case of the proposed layout that would mean that either one of the front rotors would have to increase rotational speed. This increase in rotational speed will induce a torque around the Z-axis, however it will also create a rolling moment due to the increase in thrust. Since there are three engines, the only way to counter the rolling moment is to increase the thrust of the other front engine but this will also counteract the desired yawing. Therefore, a different approach to yaw the drone was chosen.

To introduce a yawing motion the tilting mechanism is used. For example, to introduce a counter clockwise yawing motion the right front rotor is tilted forward. This means that the thrust is at an angle and therefore a component of the thrust is now pointing in the positive x-axis direction which in turn introduces a counter clockwise yaw moment. This component can be calculated with the acceleration requirement and since the drone still needs to be in vertical equilibrium (and to prevent any pitch moments), consequently the angle and the resultant force can be calculated. Note that it is assumed that the horizontal thrust force of the engines go through the c.g. and hence do not introduce any pitch moments. See Figure 8.6 for a visual representation of the yaw motion. As mentioned earlier, the increase in thrust would impose an extra torque on the system which would have to be counteracted, this counteraction would in turn affect other forces etc. However the increase in force for yaw is so small that this coupling can be neglected.

In Table 8.3 the thrust angles and values can be found to enable a yaw acceleration to meet MD-SYS09-CS13.

Table 8.3: Motor outputs for VTOL yaw acceleration

Negative yaw acceleration	Motor 1	Motor 2	Motor 3&4
θ [°]	0	3.0	0
Δ Thrust [N]	0	0.2	0
Power required [W]	0	0.09	0
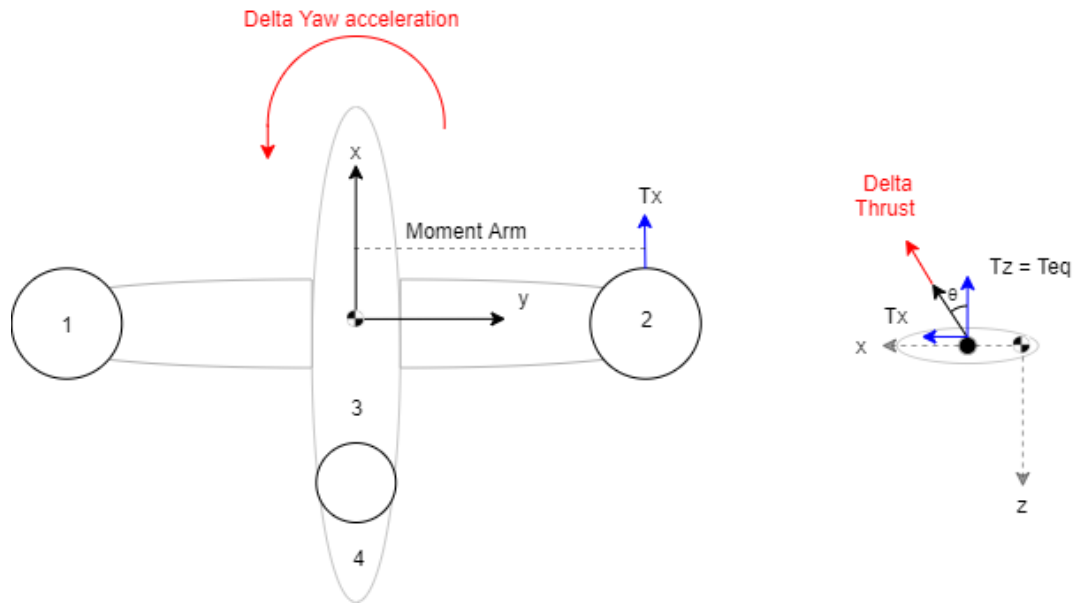
Figure 8.6: Graphical representation of yawing motion and forces needed

Roll   To introduce a rolling motion a moment is needed around the x-axis. This can only be created with the two larger rotors as they have a moment arm to create this motion. To introduce a rolling moment, one of the main rotors must increase its thrust. As a side-effect of this increase, a torque around the z-axis is also introduced. With the selected drone lay-out, the only way to counteract this yaw torque is by tilting the other front rotor forward or backward accordingly. This should counteract the yaw torque introduced and keep the drone from yawing when rolling. Furthermore, in order to counteract the resulting pitch moment, the back rotor has to increase its thrust as well. In Figure 8.7 the thrusts are shown, as can be seen a counteracting force of engine 1 is also required to counteract the yaw created by increasing the thrust.

Figure 8.7: Graphical representation of Rolling motion and forces needed

In Table 8.4 the thrust angles and delta forces can be found to meet MD-SYS09-CS11.

Table 8.4: Motor outputs for VTOL roll acceleration

Negative roll acceleration	Motor 1	Motor 2	Motor 3&4
θ [°]	≈ 0	0	0
Δ Thrust [N]	≈ 0	3.9	1.2
Power required [W]	≈ 0	7.5	3.4

Pitch　For a pitching motion, a moment around the y-axis needs to be introduced. This is a bit less complicated than the previous motions since the change in thrust can be done in such a way that there is no coupled motion. This means that a pitching motion does not induce a yaw or roll moment. To create a moment around the y-axis the thrust of the front two rotors can be changed, or the thrust of the back two rotors. Since the moment arm for pitch is relatively small for the front rotors, it will require less power to operate the back rotors for pitching since they have a far greater moment arm. In Figure 8.8 An example can be seen of what thrust would result in the required pitching motion. Note that when introducing a pitch up moment, the drone will lose altitude and when pitching down, the drone will gain altitude. Hence to remain on the same altitude, the delta force added from the back engine should be subtracted from the front engines (or vice versa), which results in a greater moment acceleration than designed for.
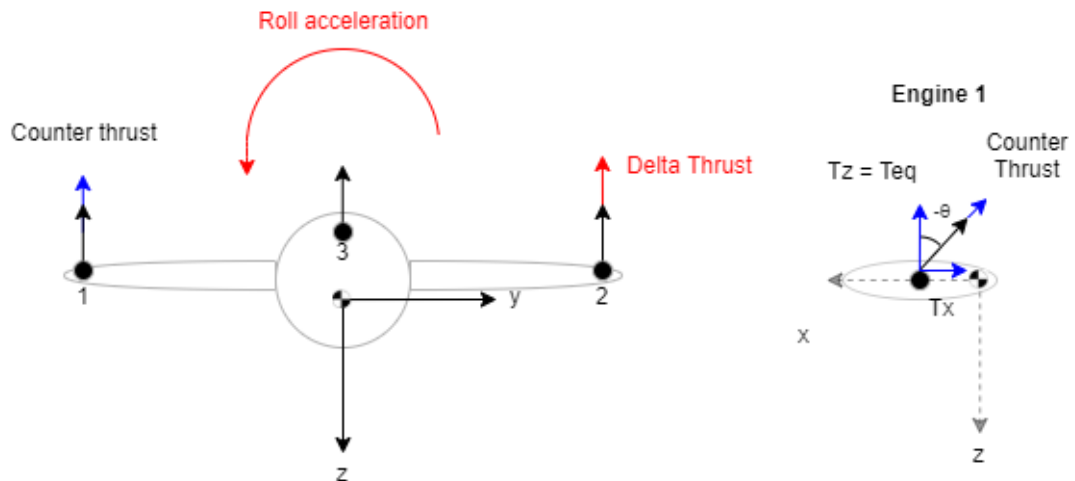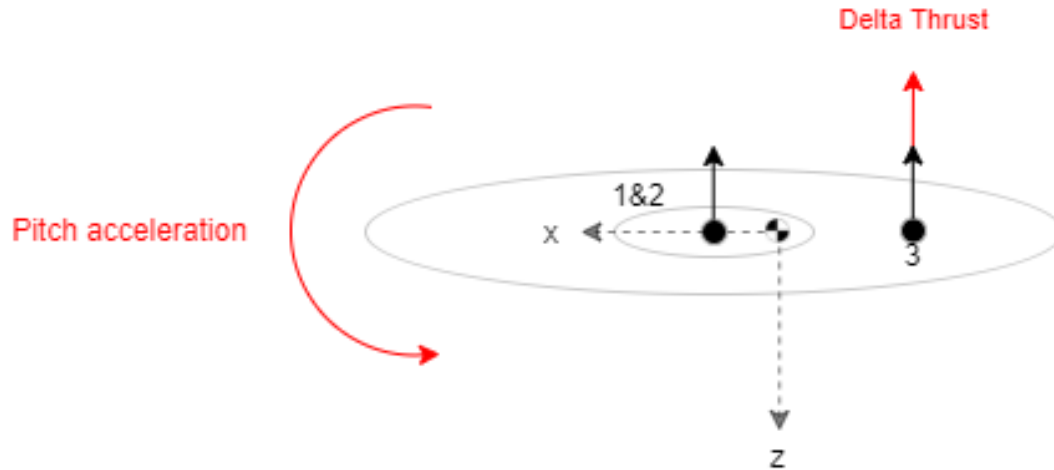

Figure 8.8: Graphical representation of pitching down motion and forces needed

In Table 8.5 the thrust angles and values can be found to enable a pitch acceleration imposed by MD-SYS09-CS12.

Table 8.5: Motor outputs for VTOL pitch acceleration

Negative pitch acceleration	Motor 1	Motor 2	Motor 3
θ [°]	0	0	0
Δ Thrust [N]	-2.9	-2.9	5.8
Power required [W]	-4.8	-4.8	38

Cruise phase

So far the vertical and horizontal tail have been sized for stability, trim condition, cross winds and in case of an engine inoperative. In order to accomplish certain roll, yaw, or pitch accelerations stated in MD-SYS09-08, MDSYS09-09 and MD-SYS09-10, the elevator, rudder and ailerons need to be sized. The requirements impose design constraints on the control surfaces, which results in control surface areas, dimensions and hinge moments. With the hinge moments suitable servos can be selected. An overview of the control surfaces characteristics can be found in Table 8.7

Aileron　The drone has to fulfill the following requirement; MD-SYS09-CS10 The drone shall be able to perform a 60 deg roll within 1.3s. This requirement was the main sizing parameter for the aileron, meeting this requirements also ensures to remain at zero bank angle during one engine inoperative (as mentioned in subsection 8.3.3). To obtain the roll rate of the drone, the control derived of the aileron and the roll damping coefficient are used. The control derivative of the aileron is found with Equation 8.10:

$$C_{l_{\delta a}} = \frac{2c_{la}\tau}{S_{ref}b}\int_{b_1}^{b_2} c(y)y\,dy \tag{8.10}$$

The roll damping coefficient can be found using Equation 8.11.

$$C_{l_P} = -\frac{4(c_{l_\alpha}+c_{d_0})}{S_{ref}b^2}\int_0^{b/2} y^2 c(y)\,dy \tag{8.11}$$

Here b represents the span of the full wing and using b_1 and b_2 the span of the aileron can be determined. Finally τ represents the control surface effectiveness and this can be obtained using Figure 8.9
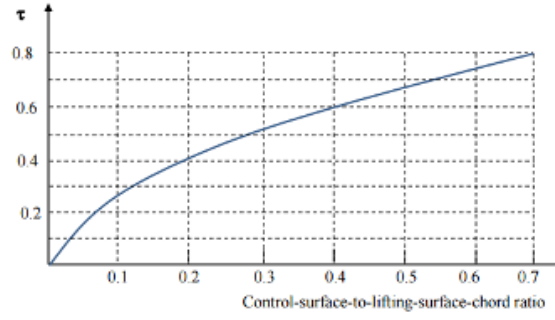

Figure 8.9: Figure to obtain the control surface effectiveness

Analysing the performance of the roll can be done as by using the following formula Equation 8.12 [45]

$$p = -\frac{C_{l_{\delta a}}}{C_{l_P}} \delta a \left(\frac{2V}{b}\right) \tag{8.12}$$

To size the aileron for the appropriate roll rate, p, different geometries are used that in turn change the derivatives. Furthermore, different roll rates are achieved at different aileron deflections. The maximum deflection is assumed to be 25deg [51]. To achieve requirement MD-SYS09-CS10 and to stay within the maximum deflection range, the aileron shall have a span of 0.242 [m] and a chord of 0.164 [m]. The aileron shall be located at 60% of the span until 90%.

Elevator   The horizontal tail has an incidence angle that corresponds to the lift coefficient needed to stay trimmed during cruise. When flying near the stall speed, the drone still needs to be trimmed. Here the elevator comes into play. Besides trimming, the drone also needs to meet the pitch acceleration requirement. The difference in lift produced and the lift required to trim and reach a pitch acceleration results in a ΔC_{L_v} that is needed which can be delivered by deflecting the elevator. Given a maximum elevator deflection angle of 30° and the $C_{L_{\alpha_h}}$ of the horizontal tail, the required elevator effectiveness coefficient can be determined, and from Figure 8.9, the control-surface-to-lifting-surface-chord ratio can be linked. Due to the elevator effectiveness for trim condition and pitch acceleration required by MD-SYS09-CS08, the value for this ratio is 0.14. This in turn results in a chord ratio for the elevator with respect to the horizontal tail chord of 0.4. After assuming the length for the elevator to be 80% of the horizontal tail span, the total area of the elevator can be determined.

Rudder   Due to the otherwise large size of the vertical tail and because the drone has to be controllable in all phases of flight, a rudder is incorporated into the design. The same load case, engine inoperative, is used to size the rudder and new vertical tail dimensions. For the rudder design the method described in Airplane Design by Jan Roskam is used [51]. First the maximum angle with which the rudder can be deflected is taken to be 25deg. This deflection angle is calculated using Equation 8.13.

$$\delta_r = \frac{N_D + N_{t_{crit}}}{\bar{q}_{mc} S b C_{N_{\delta_r}}} \tag{8.13}$$

In Equation 8.13, $N_{t_{crit}}$ refers to the yawing moment generated by a wing engine when the other engine is inoperative. N_D is the drag induced yawing moment and it is approximated using $N_D = 0.25 N_{t_{crit}}$. Furthermore $\bar{q}_{mc}$ is the dynamic pressure at minimum control speed (which is about $1.2 V_{stall}$). $C_{N_{\delta_r}}$ can be calculated using Equation 8.14

$$C_{N_{\delta_r}} = \frac{-C_{y_{\delta_r}} (l_v cos(\alpha) + z_v sin(\alpha)}{b} \tag{8.14}$$

Here, $C_{y_{\delta_r}}$ is calculated using Equation 8.15

$$C_{y_{\delta_r}} = \left(C_{L_{\alpha_v}} / c_{l_{\alpha_v}}\right) \left(k' K_b\right) \left\{(\alpha_\delta)_{C_L} / (\alpha_\delta)_{c_l}\right\} *$$
$$* \left(C_{l_\delta} / c_{l_{\delta \text{theory}}}\right) c_{l_{\delta_{\text{theory}}}} (S_v / S) \tag{8.15}$$

Table 8.6: Sizing parameters for the rudder

Parameter	Value
l_v	1.28 [m]
z_v	0.4 [m]
b	> 1.62 [m]
S_v	0.15 [m^2]
S	0.53 [m]
$C_{L_{\alpha_v}}$	0.075 [deg^{-1}]
$C_{l_{\alpha_v}}$	0.09 [deg^{-1}]
k	0.65 [-]
K_b	0.95 [-]
$\alpha_{\delta_{C_L}} / \alpha_{\delta_{C_l}}$	1.1 [-]
$C_{L_\delta} / c_{l_{\delta_{theory}}}$	0.8 [-]
$c_{l_{\delta_{theory}}}$	5 [-]

Changing the dimension of the rudder affects the variables stated in Equation 8.15, in turn changing the maximum deflection angle. By iteration the following values are found to yield a maximum deflection angle of 25 ° at zero angle of attack:

Using the parameters listed in Table 8.6 and making sure the deflection angle stays below 25° we obtain a rudder that has the following dimensions; a span of 0.55 [m] and a chord of 0.08 [m].

With the rudder and vertical tail sized to account for an engine failure, it should be checked whether the sizing results are also suitable to meet MD-SYS09-CS09 (yaw acceleration). The total torque required can be calculated from the yaw acceleration requirement and the moment of inertia around the z-axis. With the distance from the vertical tail a.c. to the most aft c.g. and the amount of force the vertical tail can produce with maximum deflection angle at minimum control speed, the total yaw moment can be calculated.

Hinge moment In order to calculate the maximum hinge moment that can apply on the hinges of the control surfaces, the resultant force at maximum deflection is placed on quarter chord length of the control surface. The resulting moments must be counteracted by the hinges and hence suitable servos must be selected. In Table 8.7 the maximum hinge moment is at least 100 N·cm, a servo that is capable of handling this torque is for example [1].

Table 8.7: Control surfaces design

Parameter	Aileron (1 out of 2)	Elevator (1 out of 2)	Rudder
Span length [cm]	24.2	28	54.6
Chord length [cm]	16.4	4	8
Surface area [cm^2]	396.9	112.0	436.8
Hinge moment [N·cm]	92	8	51

8.3.5. Controller design

Flight Controller In this section the flight controller for the drone is elaborated on. The controller itself is meant to be able to control the drone in wind gusts up to 24 [m/s] as stated in MD-SYS09-CS05. On top of this it is designed to perform the more conventional functions. This means it is capable of a VTOL to a certain altitude where it transfers into a transition phase and finally arrives at a cruise configuration. During these phases the flight controller is meant to keep the drone stable and operating according to the pre-determined flight path.

Designing the actual full flight controller is something that is too extensive to do in this phase of the design. Therefore, a general flight controller architecture is shown in Figure 8.10[2].

---

[1] https://www.conrad.nl/p/hitec-speciale-servo-d845wp-digitale-servo-materiaal-aandrijving-metaal-1534808
[2] https://www.youtube.com/watch?v=GK1t8YIvGM8&t=10s
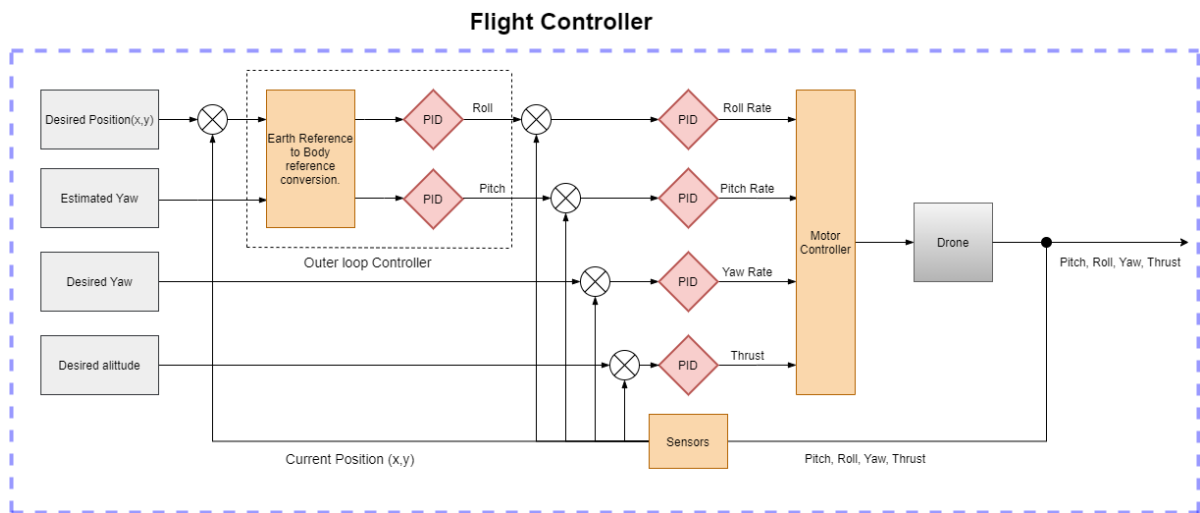
Flight Controller

Figure 8.10: Flight Controller Architecture for Hover

This controller is specified for hover, to create one that also works for other flight phases extra loops can be added describing for instance the speed of the drone. The controller works by taking desired states which are defined by the flight phase, using the desired state and the measured state an error is created which determines the controlling commands. In the case of hover, this would mean that the desired altitude is fixed to a certain hover altitude, the (x,y) position is set to a position the drone needs to hover (with respect to the earth reference frame), if the drone is not at this position the error will define what control commands are needed to do so. When looking at Figure 8.10 it can be seen that there are two yaw inputs, this is due to the fact that the drone needs information about what the estimated yaw is to convert from the earth reference frame to the roll and pitch commands desired to arrive at the desired state. Furthermore, something that is used throughout many flight control systems is a proportional-integral-derivative (PID) controller, this PID controller makes sure that the change in certain commands is tuned in a good manner. This means that if there is an altitude error, the change in thrust is done in a way that, for instance, the overshoot is minimal. The PID controller makes use of the current error in combination with information from the 'past' as well as information about the rate of change of the error.

Finally the orange blocks describe systems that have many more layers of depth but are not elaborated on in this report. The conversion of reference frame is mainly a mathematical conversion which is relatively straightforward to apply. Further more the motor controller is something that is quite complex, it needs to convert the inputted rates into actual motor commands, the relation between these inputs and what the drone has to do are mainly governed by the corresponding equations of motion. Lastly, the sensor block represents the fact that the states that are experienced by the drone need to measured using sensors, these sensors also introduce an extra layer of uncertainty and therefore filters also need to be applied within this block. The type of sensors that could be used to measure certain states can be found in Table 8.8 some of these sensors are further explained in chapter 10.

Table 8.8: Sensors and sensor types

State	Sensor Type
Speed and position	GPS
Altitude	Pressure Sensor
Attitude	Inertial Measurement Unit

Pitch Control   To show how one of these loops would work in practice, a simplified version of the pitch controller was designed. This simplified version is based on the assumption that the drone is fixed in all directions and can only rotate. The all weather requirement states that the drone can withstand a wind gust of 24$[m/s]$. In the case that this gust comes from the front of the drone, the dynamic pressure of the wind can be seen as a resultant force with a certain point of application. To be as conservative as possible the arm of this force creating the moment is assumed to be at the top of the fuselage (when looking at the front view). This results in a applied moment disturbance of 32.7 $[Nm]$ and it is applied for a duration of 5 seconds. To create the corresponding transfer function the EOM was derived by taking the moments around the c.g., furthermore the controlling thrusts can be seen as a couple-moment, this couple moment is due to the fact that one set of propellers is ahead of the c.g. and one

is behind the c.g. therefore the moment that needs to be created can be seen as a couple-moment. This lead to Equation 8.16.

$$\Delta\ddot{\theta} = \Delta T \cdot \frac{D}{I_y}$$
(8.16)

Here $\Delta\ddot{\theta}$ is the change in rotational acceleration, ΔT is the total change in thrust that is needed (which can be divided over the front and back rotors) and D is the distance between the main rotors and the rear rotor. Using Equation 8.16 a block diagram was made where the pitch and pitch rate are used as measured states. This block diagram is shown in Figure 8.11.
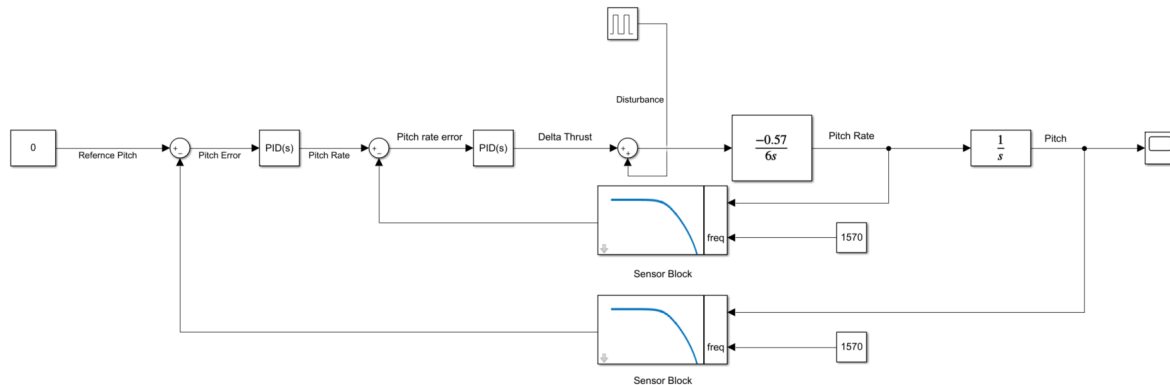

Figure 8.11: Simplified pitch controller

When looking at Figure 8.11 it can be seen that the structure is very similar to that of Figure 8.10. To use this controller the PID's have been tuned using the auto-tune function that Simulink offers. The disturbance is modeled as a pulse input with the values corresponding to the wind gust discussed earlier. The inner loop is the Feedback corresponding to pitch rate, this loop is "faster" than the outer loop for pitch. This is because controlling based on pitch rate is more efficient than pitch angle since the rate can be felt earlier than the pitch angle. Finally, the two sensor blocks are there to represent a preliminary simulation of the IMU sensor, which measures the rotational motion. This is a low-pass filter with a cut of frequency which is equal to the Nyquist rate of the sample frequency that the IMU uses. The sampling frequency of the IMU was set to 500 [Hz][8]. Now having set up the Simulink model the following results can be seen, Figure 8.12 shows the necessary change in thrust whereas Figure 8.13 shows the pitch angle. It can be seen that the change in thrust is around 40 [N] at maximum which is within the performance range of the engines. Further, it can be seen from Figure 8.13 that the drone arrives at equilibrium conditions at around 30 seconds.

8.4. Sensitivity Analysis

A sensitivity analysis is done for the subsystem in order to investigate how the design changes by changing major input system parameters. In this way critical parameters can be identified to which the stability and control subsystem design is sensitive to. For the scissor plot, a major input parameter that has a high potential to change is the total payload weight. In Table 8.9 the changes of values are indicated in percentages. The calculations have been done for a 10% and 25% increase in payload mass. It can be observed that adding more payload has a great influence on the c.g. shift. Since the payload is located far on the front, adding weight shifts the c.g. more forward. As a result, when keeping the tail arm constant, the area of the horizontal tail increases as well. The design seems not too sensitive to an increase in weight, since the corresponding order of magnitude of increase in tail surface area can be accounted for with only minor changes (only the surface area is changed the most).

Another important input parameters are the moment of inertias for the control design during VTOL. So far the values are roughly estimated via a CATIA model, but these values will most likely change as the design gets worked out in more detail. Hence it is interesting to see how sensitive the design is by changing their input values. The result for a 10% increase in moment of inertias can be found in Table 8.10. The increase in powers required are rather large. This is because the torque required is directly related to the moment of inertia and the required rotational acceleration. Hence the power required is very sensitive to the inertias of the drone to which a lot of attention should be paid. So far very conservative moment of inertias have been considered, and an increase in magnitude is not
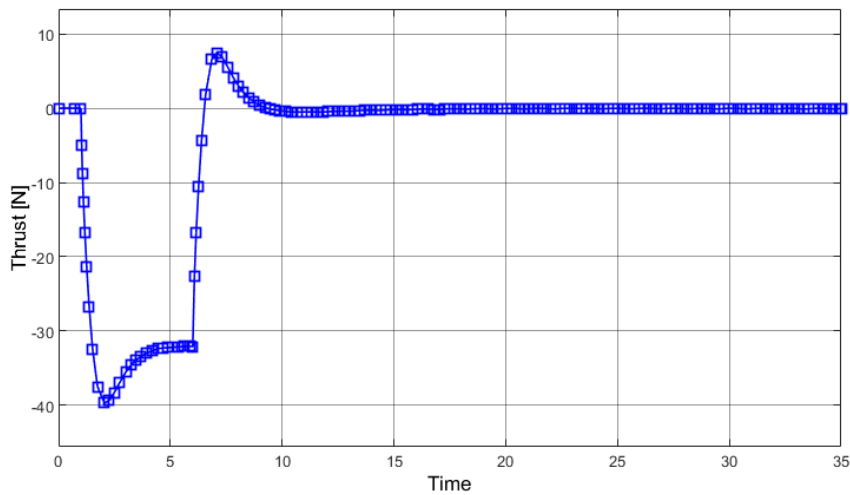
Figure 8.12: Thrust responses needed due to a wind gust
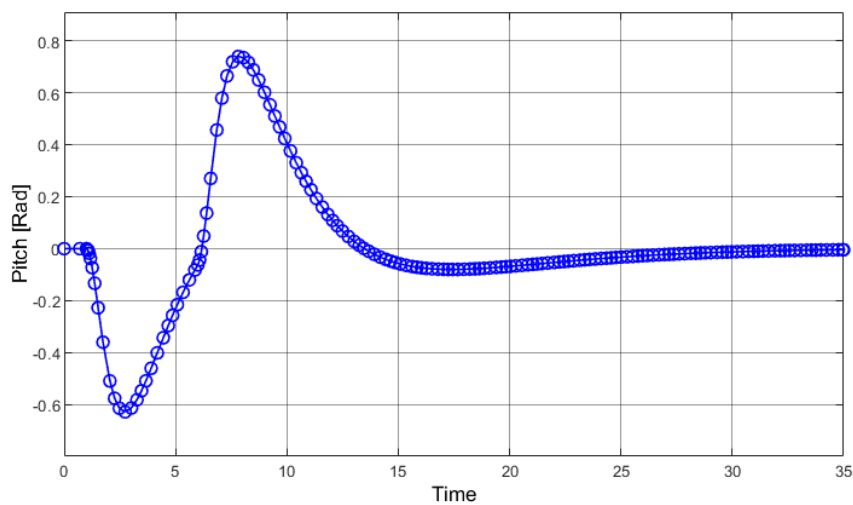
Figure 8.13: Pitch response due to a wind gust

Table 8.9: Effect of the increase in payload mass on the horizontal tail design, main wing- and tail position.

Parameter	+10% Payload Mass	+25% Payload Mass
Most forward c.g.	-2.24%	-5.45%
Most aft c.g.	-0.18%	-0.55%
Total c.g. (fully loaded)	-2.06%	-5.00%
Wing a.c. position	-1.70%	-2.63%
Length to tail	-0.42%	-1.01%
$(\frac{S_H}{S})_{scissor plot}$	+5.27%	+12.48%

to be expected. Furthermore it should be noted that also the requirements impose a very conservative roll, pitch and yaw acceleration with respect to the mass and size of the drone. Therefore it is not likely that the drone will encounter any problems with regards to power shortage for control during VTOL once the design enters to a next more detailed design phase. However it is important with this information that in later stages of the design phase, attention should be paid to the acceleration requirements, the moment of inertias and the power available. If it turns out that too much power is required, either the requirements, the power available or the design lay-out of the drone should be reconsidered on time.

Table 8.10: Effect of the increase in moment of inertias on the power required to meet pitch, yaw and roll requirement during hover.

Parameter	+10% Moment of Inertia
Power required for yaw	+33.1%
Power required for roll	+15.6%
Power required for pitch	+15.6%

8.5. Verification and Validation

In order to check if the results from the methods used for calculations of the design represent the expected outputs that is designed for, each method is verified. Verification of the code has been done by doing unit tests to see if the results behave as expected by inputting variables for which the output or behavior is known. To make sure that the results more or less approximate reality, the results are compared and checked with existing designs.

For the tail it was assumed that $\frac{d\epsilon}{d\alpha} \approx 0$ and $\frac{V_h}{V} \approx 1$ due to the T-tail configuration. A simulation in XFLR5 for the drone configuration shows that this approximation can be considered valid (for verification and validation of XFLR5 see chapter 5). For the horizontal tail sizing a scissorplot has been constructed. To see if this has been implemented correctly, the control curve, stability curve and c.g. range has been exposed to unit tests. For example, for the control curve the tail arm has been increased, and as a result the control curve slope became flatter and the slope of the stability curve decreased as expected. Furthermore inputs are checked to have the correct sign, which results in a positive slope for the stability curve, and a negative slope for the control curve. For the loading diagram, the number of components inputs are reduced and for a given wing position the results were compared to a simple hand calculation checking the correctness of the code. The resulting $\frac{S_H}{S}$ value of 0.11 which results in $S_H = 0.06$ [m^2] can be validated by comparing to drones with a similar lay-out. Typically this comparison is done with a given tail volume coefficient. Since it is difficult to find these data for similar drones, a typical tail volume coefficient for a sailplane is considered since the horizontal tail has been designed for gliding flight. From [47] comes Equation 8.17.

$$\frac{S_h}{S} = \frac{c_h \bar{c}_w}{l_{mh}}$$

(8.17)

With c_h the horizontal tail volume coefficient, $\bar{c}_h$ average chord of the main wing and l_{mh} the moment arm. This results in $\frac{S_h}{S} \approx 0.19$ which is slightly higher than the found value for the drone. However this makes sense as a sailplanes have slightly larger dimensions and fly slower than the drone. The found value for the horizontal tail can be considered validated.

For the vertical tail sizing, given the calculated lift coefficient and yaw angle, the amount of force calculated by hand can be compared to the force introduced from the wind acting at the vertical tail. If they were equal, the calculations are verified. The same has been done for the one engine inoperative condition. For validation the same method as for the horizontal tail can be used with Equation 8.18[47].

$$\frac{S_v}{S} = \frac{c_v b}{l_{mv}}$$

(8.18)

With c_v the vertical tail volume coefficient, b span of the main wing and l_{mv} the moment arm. Since the vertical tail has been designed for a one engine inoperative condition, the tail volume coefficient is taken from a twin turbo prop which results in $\frac{S_v}{S} = 0.11$. The calculated value for the drone has a value of 0.28. This more than 50% larger than the value for a twin turbo prop. Since the drone has its engines on the tip of the wing, the moment arm for one engine inoperative is twice as large in comparison with a twin turboprop (which usually has its engines not even at half the wing). Hence it makes sense that the vertical tail for the drone is designed twice as large than for a twin turboprop, and thus the found value can be considered as validated.

For the VTOL phase, the power calculations are checked by putting in zero acceleration requirements, in this way the delta thrust and hence the corresponding required power would go to zero. Furthermore, one case has been calculated by hand with simplified input values.

For validation of the calculated control surface areas and chord lengths, they can be compared to the ranges shown in Figure 8.14.

For the elevator $\frac{S_E}{S_h} = 0.037$, the the aileron $\frac{S_A}{S} = 0.07$, and rudder $\frac{S_R}{S_v} = 0.3$. The span values for the elevator $\frac{b_E}{b_h} = 0.72$, aileron $\frac{b_A}{b} = 0.3$ and rudder $\frac{b_R}{b_v} = 0.8$. The chord values for the elevator $\frac{C_E}{C_h} = 0.4$, aileron $\frac{C_E}{C_h} = 0.3$ and the rudder $\frac{C_R}{C_V} = 0.4$. All values fall within the typical values of control surface design.

Control surface	Elevator	Aileron	Rudder
Control surface area/lifting surface area	$S_E/S_h = 0.15{-}0.4$	$S_A/S = 0.03{-}0.12$	$S_R/S_V = 0.15{-}0.35$
Control surface span/lifting surface span	$b_E/b_h = 0.8{-}1$	$b_A/b = 0.2{-}0.40$	$b_R/b_V = 0.7{-}1$
Control surface chord/lifting surface chord	$C_E/C_h = 0.2{-}0.4$	$C_A/C = 0.15{-}0.3$	$C_R/C_V = 0.15{-}0.4$
Control surface maximum deflection (negative)	−25 deg (up)	25 deg (up)	−30 deg (right)
Control surface maximum deflection (positive)	+20 deg (down)	20 deg (down)	+30 deg (left)

Figure 8.14: Typical values for control surface sizes [56]

For verification of the controller, the disturbance input is removed. This should lead to nothing happening as the reference is equal to zero and there is nothing that is going to change this. When doing this the controller indeed behaves as expected giving no control inputs or pitch changes. Next a test can be done with a different reference input, again if the controller works as expected a different reference input would mean that the controller settles at this same input. After performing this test it again responds as expected, from this it can be concluded that the tool is verified.

8.6. Compliance Matrix

In Table 8.11 the compliance matrix for the stability and control design can be found. All requirements are met except for MD-SYS09-CS02, MD-SYS09-CS02.1 and MD-SYS09-CS05. Requirement MD-SYS09-CS02 still needs to be investigated which can be done in case of adding a self-developed or purchased flight controller in which damping can be tuned, for example to implement a yaw-damper mechanism. This also applies for requirement MD-SYS09-CS02.1. MD-SYS09-05CS is partially met since it is not yet fully investigated for the VTOL phase, but it is met for the vertical tail, horizontal tail and control surfaces design.

Table 8.11: Compliance Matrix

Requirement	Required	Actual	Fully met	Partially met	Not met	To be investigated
MD-SYS09-CS01:	n.a.	n.a.	✓			
MD-SYS09-CS02:	n.a.	n.a.				✓
MD-SYS09-CS02.1:	n.a.	n.a.		✓		✓
MD-SYS09-CS03:	n.a.	n.a.	✓			
MD-SYS09-CS04:	n.a.	n.a.	✓			
MD-SYS09-CS05:	All flight phases	Cruise		✓		✓
MD-SYS19-CS07:	n.a.	n.a.	✓			
MD-SYS19-CS08:	$0.07\ [rad/s^2]$	$0.07\ [rad/s^2]$	✓			
MD-SYS19-CS09:	$0.07\ [rad/s^2]$	$0.07\ [rad/s^2]$	✓			
MD-SYS19-CS10:	60 deg in 1.3 s	60 deg in 1.3 s	✓			
MD-SYS19-CS11:	$45\ [deg/s^2]$	$45\ [deg/s^2]$	✓			
MD-SYS19-CS12:	$45\ [deg/s^2]$	$45\ [deg/s^2]$	✓			
MD-SYS19-CS13:	$45\ [deg/s^2]$	$45\ [deg/s^2]$	✓			

9

Structures

This chapter is about the structural design of the drone. section 9.1 and section 9.2 show the requirements and the functional breakdown structure of the structures subsystem. Then, section 9.3 presents the design methodology of the subsystem. After the designing, a functional flow diagram is established in section 9.4. After this, an initial design is made, as shown in section 9.5. This includes a sensitivity analysis and verification an validation. After the initial design, an updated design is performed. This updated design is showed in section 9.6. As the design is now finalized, the all-weather capability is shown in section 9.7 and the compliance of the subsystem to the requirements is shown in section 9.8.

9.1. Introduction and Requirements

The structure subsystem ensures that the different components of the drone assembly are able to sustain any loads applied on them during the operation of the drone. Moreover, the structures department selects the material that the bulk of the drone's structure will be built of, taking into consideration not only strength and stiffness, but sustainability and cost as well. Lastly, this department must inspect how reliable the structure is in extreme weather conditions such as thunderstorms and hail storms. These constraints on the design of the structural subsystem are also showcased by the requirements imposed.

MD-SYS01-ST01 :	The structure shall not exceed a total dimension of 2.2 x 3.0 x 0.8 [length x width x height] $[m]$.
MD-SYS01-ST02:	The dimensions of the payload container structure shall not exceed 0.2 x 0.2 x 0.2 $[m]$.
MD-SYS02-ST03:	The structure mass shall not exceed 20 $[kg]$.
MD-SYS06-ST04:	The structure of the payload container shall be able to withstand a heat of 45 [°C] for 1 hour.
MD-SYS06-ST05:	The payload-carrying structure shall be able to withstand a load of at least 100 $[N]$ or 100 $[Nm]$ in all directions.
MD-SYS08-ST06 :	The structure shall be able to withstand vibrations between 300 and 1500 $[Hz]$ along all axes.
MD-SYS09-ST07:	The structure shall be able to withstand 14 $[m/s]$ wind speed and 24 $[m/s]$ gust speed in all directions.
MD-SYS09-ST08:	The drone shall be able to withstand a lightning strike.
MD-SYS09-ST08.1:	The structure shall be able to discharge 300 $[kV]$s.
MD-SYS09-ST08.2:	The structure shall be able to discharge a current between 3-200 $[kA]$.
MD-SYS09-ST09:	The structure shall be corrosion resistant.
MD-SYS09-ST10:	The structure shall be water proof at IPX6 level.
MD-SYS09-ST11:	The structure shall withstand hail stones impact energy of 1.26 J.
MD-SYS09-ST12:	The structure shall be able to withstand temperatures between -10 and 40 [°C].
MD-SYS31-ST14:	The structure shall be 60 percent reusable.
MD-SY08-ST15:	The primary structure shall be designed with a safety factor of 1.5.
MD-SYS23-ST16:	The production cost of the structure shall not exceed 15000 €.

In order to verify all of these requirements at the same time, a parallel design approach should be applied. The first step is to identify the parts of the drone that the structure department should work on as detailed in section 9.2. Next, the design methodologies for each part are covered in section 9.3. The initial configuration of the structural elements and the resulting stresses and deflection, along with verification and validation are then shown in section 9.5. During this analysis a material is also selected as detailed in subsection 9.5.4. Finally, an updated structure and recommendations for the future are shown in section 9.6 along with a conclusion in Table 9.8.

9.2. Functional Breakdown Structure

The goal of the functional breakdown is to identify the different elements of the drone's structure and what functions they must fulfil. As evident from Figure 9.1, there are four main elements: the wing, the horizontal and vertical stabilizers and the fuselage. In addition, environmental resistance was added on the same level, since it must be guaranteed for the drone as a whole. The functions that these elements must cover are then shown in lower levels.
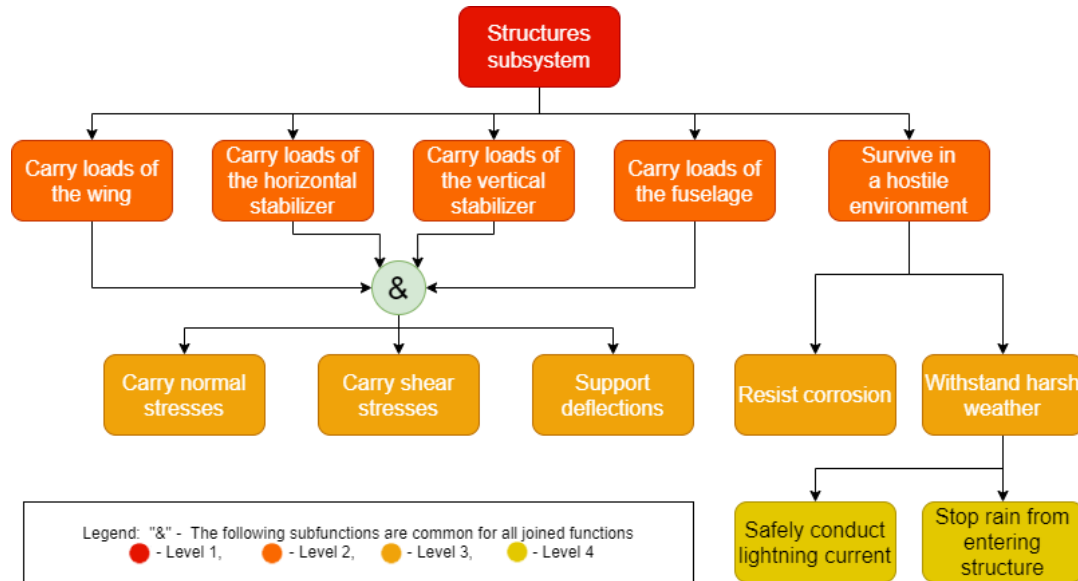

Figure 9.1: Functional breakdown for the structural subsystem

9.3. Design Methodology

This section covers the theoretical approach behind the numerical tools for the wing, fuselage and the tail structural configuration. It starts by analyzing the loads received from the aerodynamic department while applying a load factor for the most extreme scenario. Then, the reaction forces coming from the free body diagrams are all taken into account in order to calculate the stresses and the deflections.

9.3.1. Flight Envelope

Since there are no available regulations on aircrafts of this size, the flight envelope was constructed based on requirements of the Very Light Aircraft size using the same method as described in [18]. First, the maneuver V-n diagram was constructed, then second the gust V-n diagram was plotted and at the end they were overlapped in order to find the maximum load factor. In the Table 9.1 the class II estimation of parameters serves as reference in order to see if they indeed comply with the requirements.

Table 9.1: General Class II Estimation Parameters

Parameter	Symbol	Value	Units
Air vehicle mass	MTOW	36	$[kg]$
Wing area	S_{wing}	0.53	$[m^2]$
Maximum lift coefficient, positive	C_{lmax}	1.2	[-]
Maximum lift coefficient, negative	$-C_{lmax}$	-0.6	[-]
Cruise speed	V_{cruise}	50	$[m/s]$
Wing aspect ratio	AR	5	-
Stall speed	V_{stall}	27	$[m/s]$
Angle of attack during gust	α_{gust}	20	$[deg]$

This load factor is the ratio between the lift force and weight, as shown in Equation 9.1. The angle of attack during gust, α_{gust}[50] is defined with Equation 9.2.

$$n = \frac{L}{W} \tag{9.1}$$

$$tan(\alpha) = \frac{V_{gust}}{V_{dive}} \tag{9.2}$$

From CS-VLA 335 it follows that the maximum cruise speed is defined as shown in Equation 9.3.

$$V = 2.4 \cdot \sqrt{(m \cdot g)/S} = 61 [m/s] \tag{9.3}$$

This complies with the maximum cruise speed of $V_{max} = 1.3 \cdot V_{cruise} = 61.1 [m/s]$. According to CS-VLA, the positive load limit factor is $n_{pos} = 3.8$ and the negative load limit factor is $n_{neg} = -1.9$. Together with the dive speed, which is equal to $V_{dive} = 1.4 \cdot V_{cruise} = 65.8$, points F and G of the manoeuvre V-n diagram can be plotted, which respectively are (V_{dive}, 3.8) and (V_{dive}, -1.9). To find the coordinates of points A, B, J, K it is necessary to use equations that involve C_{lmax} and the maneuvering and stall speeds. The stall speed is calculated with Equation 9.4 and the maneuvering speed is based on the Equation 9.5 which is the upper load limit equation with the maximum positive load limit. The value of the maneuvering speed is 57 [m/s]. Therefore, point A has coordinates (29.6, 1) and point B has coordinates (57 , 3.8).

$$V_{stall} = \sqrt{\frac{2 \cdot m \cdot g}{\rho \cdot S_{wing} \cdot C_{lmax}}} = 29.6 [m/s] \tag{9.4}$$

$$n = \frac{L}{W} = \frac{0.5 \cdot rho \cdot V^2 \cdot S_{wing} \cdot C_{lmax}}{W} \tag{9.5}$$

In the same way, point K is the equivalent of point A on the lower part of the graph and it is calculated using Equation 9.6, this gives the coordinates of point K to be (41.9, -1). The lower curve of the graph is calculated using equation Equation 9.7 which also gives point J with coordinates (57.9, -1.9).

$$V_{stall,i} = \sqrt{\frac{-2 \cdot m \cdot g}{\rho \cdot S_{wing} \cdot -C_{lmax}}} = 41.9 [m/s] \tag{9.6}$$

$$-n = \frac{-L}{W} = \frac{0.5 \cdot rho \cdot V^2 \cdot S_{wing} \cdot -C_{lmax}}{W} \tag{9.7}$$

Now that the manoeuvre V-n diagram is constructed, the gust V-n diagram can be looked at. The equation for the load coefficient variation with speed is calculated using Equation 9.8

$$n = 1 (+/-) \frac{K_g \cdot V_{gust} \cdot V \cdot \alpha^{-1} \cdot \rho \cdot S_{wing}}{2 \cdot W} \tag{9.8}$$

where K_g is the gust alleviation factor and the gust speeds were determined from the weather literature study [62] to be 24 [m/s] during cruise and 12 [m/s] during dive. The gust alleviation factor is calculated through Equation 9.9 by making use of Equation 9.10 which calculates the air vehicle mass aspect ratio.

$$K_g = \frac{0.88 \cdot \mu_g}{5.3 + \mu_g} \tag{9.9}$$

$$\mu_g = \frac{2 \cdot m}{\rho \cdot c_{MAC} \cdot \alpha^{-1} \cdot S_{wing}} \tag{9.10}$$

Where c_{MAC} is the mean aerodynamic chord. From Figure 9.2 it can be seen that the load factor has a value of $n = 3.8$. The gusts do not actually influence the load factor at the operating speeds and it is only relevant for lower speeds. It is also interesting to see that due to such a small C_{lmax} and a small S_{wing}, the maneuvering speed is very high, making the drone agile in turns. The value of the load factor is later on used in the aerodynamic loads by multiplying the lift and the moment generated by the wing directly by this load factor and by multiplying the induced drag by the square of the load factor as per the drag polar.
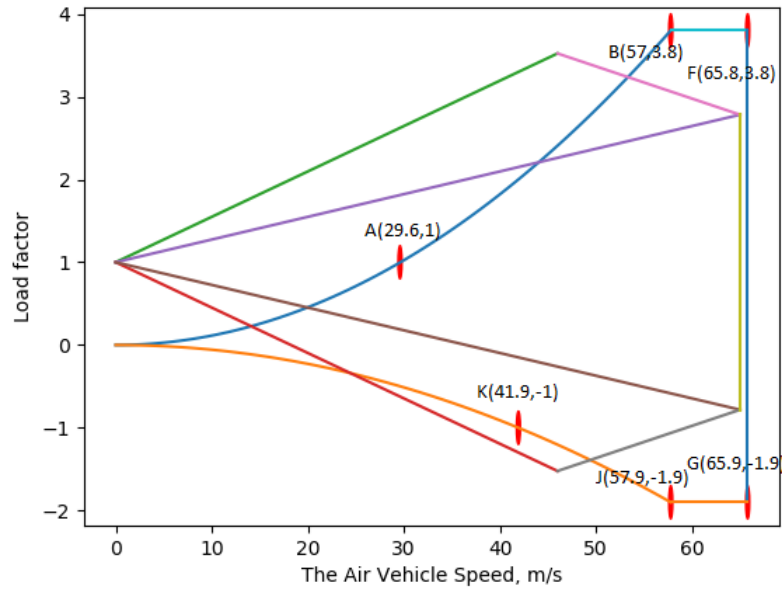
Figure 9.2: V-n diagram of the aircraft

9.3.2. Aerodynamic loads

The aerodynamic loads are treated for the wing, the horizontal tail and the vertical tail for the two principal operation modes: cruise and VTOL. The aerodynamic loads consist of the drag and the lift on the lifting surface and also an aerodynamic moment because the loads are assumed to be at the quarter chord instead of the centre of pressure.
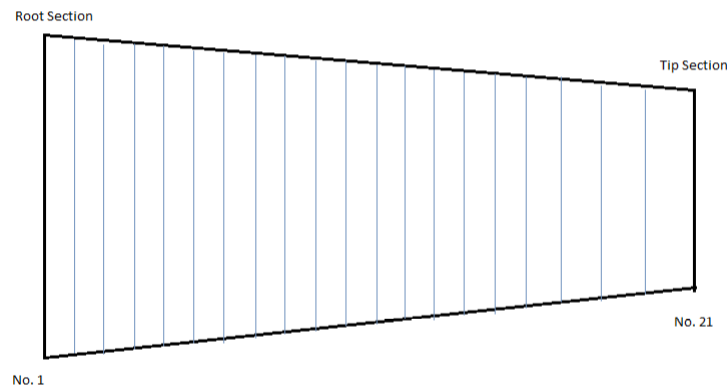
Figure 9.3: Distribution of aerodynamic loads along the span of the wing

Figure 9.3 represents the stations at which the XFLR simulation gave the amplitude of the distributed lift, drag and moment coefficients for the wing. They are not equally spaced but rather based on the mesh from XFLR. For the cruise phase, the lift, the drag and the aerodynamic moment were then calculated using Equations 9.11 - 9.13 at each individual point. In between points, so in the sections, the distribution is assumed to be constant and it takes the value of the edge closer to the tip, meaning that section number 1 does not actually contribute to the distribution.

$$L = 0.5 \cdot \rho \cdot V_{cruise}^2 \cdot c \cdot C_l \cdot n \tag{9.11}$$

$$D = 0.5 \cdot \rho \cdot V_{cruise}^2 \cdot c \cdot (C_{d,p} + C_{d,i} \cdot n^2) \tag{9.12}$$

$$M = 0.5 \cdot \rho \cdot V_{cruise}^2 \cdot c^2 \cdot C_{m,q/4} \cdot n \tag{9.13}$$

From these equations, the influence of the load factor can also be seen. For example, the drag coefficient is split between the parasitic drag and the induced drag and only the induced drag is scaled with the load factor. Furthermore, so that these loads become distributed loads in their respective sections with $[N/m]$ units, the formula only includes the chord and not the whole surface of the wing. The analysis is exactly the same for the tail section, with the exception of the number of sections, which is 18. For the VTOL flight phase of the aircraft, the horizontal lifting surfaces do not actually produce any lift and therefore there is also no aerodynamic moment. The drag is approximated to be the drag of a flat plate with the surface area of the respective lifting surface. The drag coefficient for this was taken to be $C_d = 1.28$ and the drag was calculated using Equation 9.14.

$$D = 0.5 \cdot \rho \cdot V_{VTOL}^2 \cdot S_{wing} \cdot C_d / b \tag{9.14}$$

9.3.3. Reaction forces, Loads and Free Body Diagrams

With the aerodynamic loads imposed on the structure and their positions now being known, free body diagrams (FBDs) can be constructed for the wing, horizontal and vertical tail and the fuselage. These help with determining the reaction forces applied on these parts, as well as the construction of V and M diagrams. Each part of the structure experiences different loads, so they will all be covered separately.

FBDs of the wing

The diagram during vertical take off and landing is presented in Figure 9.4, while the one for the cruise condition is shown in Figure 9.5.
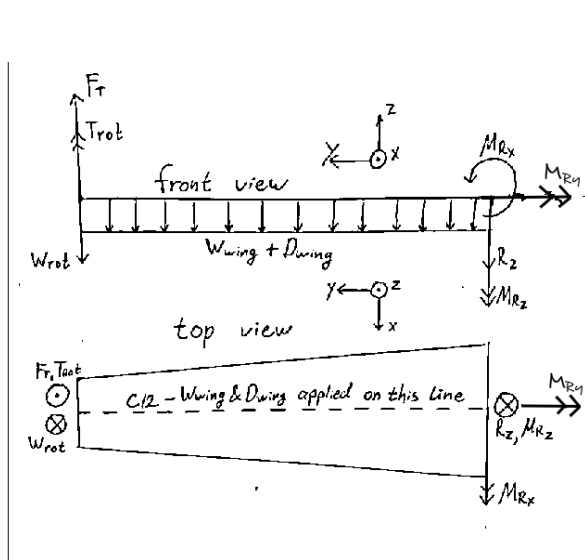
Figure 9.4: Free body diagram: wing during VTOL   Figure 9.5: Free body diagram: wing during cruise
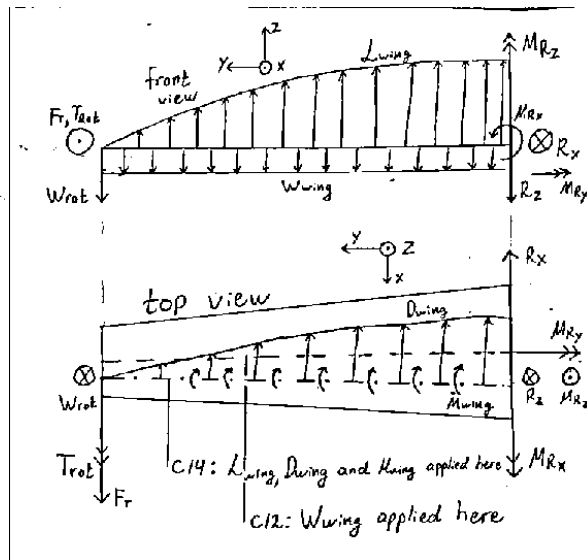
From these diagrams, the reaction forces for the wing can be calculated for the VTOL and the cruise stage. The VTOL reactions are calculated in equations 9.15-9.18, while for the cruise the equations are 9.19-9.23.

$$R_z = (W_{wing} + D_{wing}) \cdot l_{wing} - (F_T - W_{rot}) \tag{9.15}$$

$$M_{Rx} = (F_T - W_{rot}) \cdot l_{wing} - (W_{wing} + D_{wing}) \cdot \frac{l_{wing}^2}{2} \tag{9.16}$$

$$M_{Ry} = F_T \cdot l_{ax} \tag{9.17}$$

$$M_{Rz} = T_{rot} \tag{9.18}$$

Here F_T is the thrust of one of the wing mounted rotors during VTOL, W_{rot} is its weight, W_{wing} and D_{wing} are the wing's distributed weight and drag respectively. Note that here the drag is approximated as a constant distributed load unlike during cruise. This is due to the flat plate assumption. The used dimensions are l_{wing}, the distance from wing root to wingtip, as well as l_{ax}, which is the offset of the rotor's axis of thrust from the central axis about which moment equilibrium is performed (which is the halfchord).

$$R_x = F_T - D_{wing} \cdot l_{wing} \tag{9.19}$$

$$R_z = (L_{wing} - W_{wing}) \cdot l_{wing} - W_{rot} \tag{9.20}$$

$$M_{Rx} = M_{fromLift} - W_{wing} \cdot \frac{l_{wing}^2}{2} - W_{rot} \cdot l_{wing} - T_{rot} \tag{9.21}$$

$$M_{Ry} = F_T \cdot l_{ax} + L_{wing}] \cdot l_{wing} \cdot \frac{c}{4} + M_{wing} \cdot l_{wing} \tag{9.22}$$

$$M_{Rz} = M_{fromDrag} - F_T \cdot l_{wing} \tag{9.23}$$

While the notation used is mostly the same as for VTOL, there are several important things to note. First, the magnitude of F_T will be different, as now the rotors do not have to lift most of the drone, but just provide thrust. Second, all aerodynamic forces are now considered to be applied in the center of pressure. However, as it changes locations with angle of attack, it is more convenient to "move" all forces to the aerodynamic center at quarterchord, which introduces an aerodynamic moment M_{wing}. Finally, for all aerodynamic loads (including the moment), a distribution obtained from the XFLR5 analysis is used. It assumes that loads are 0 at the tips. [1]. Due to this more complex representation, their moment contributions can no longer be obtained simply by multiplying with $l^2/2$, hence the terms $M_{fromLift}$ and $M_{fromDrag}$. The function developed to calculate these moments is explained in subsection 9.3.6.

FBD of the horizontal tail

The free body diagram of the horizontal tail during cruise is shown in Figure 9.6. It immediately becomes apparent that this loading case is very similar to the one of the wing during cruise. The only difference is the lack of an engine at the wingtip. Due to this minor difference, the FBD for the VTOL case is not shown here, as it is a copy of Figure 9.4 without the engine-related loads F_T, T_{rot} and W_{rot}. It follows that one can use equations 9.15-9.23 to also calculate the reaction forces for the horizontal tail, as long as they omit all engine-related terms and modify the magnitudes of all dimensions and loads to hold for the horizontal stabilizer rather than the wing (so for example L_{wing} is replaced with L_{htail}, W_{wing} with W_{htail}, etc.).
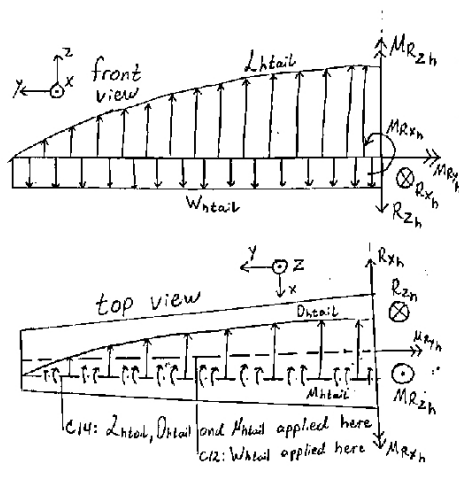
Figure 9.6: Free body diagram: horizontal tail during cruise
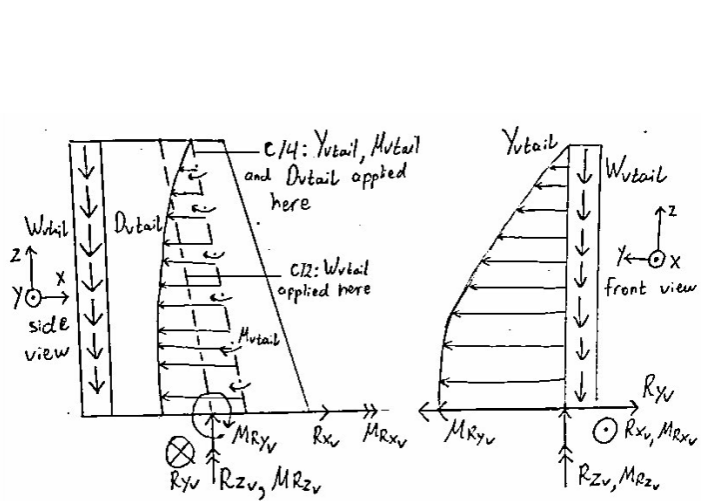
Figure 9.7: Free body diagram: vertical tail during cruise

FBD of the vertical tail

The vertical stabilizer is tilted 90° with respect to the wing. Due to this, while experiencing the same loads as the horizontal stabilizer, it experiences them along other coordinate axes. Furthermore, as showcased by Figure 9.7, the weight is now an axial load and causes no bending.

Equations 9.24 - 9.29 show how the reaction forces of the vtail are calculated during cruise.

$$R_{xV} = D_{vtail} \cdot l_{vtail} \tag{9.24}$$

$$R_{yV} = Y_{vtail} \cdot l_{vtail} \tag{9.25}$$

---

[1] In reality, this assumption only holds for the horizontal tail. For the wing, the rotor ducts act as winglets, so the lift at the wingtips is not exactly 0. The same holds for the vertical tail, for which the horizontal tail creates the same effect due to the T-tail configuration. These effects are complex to model and so are omitted from the analysis. However, they must be quantified in the future stages of this project.

$$R_{zV} = W_{vtail} \cdot l_{vtail} \tag{9.26}$$

$$M_{RxV} = -M_{fromSideforce} \tag{9.27}$$

$$M_{RyV} = M_{fromDragV} \tag{9.28}$$

$$M_{RzV} = -Y_{vtail} \cdot l_{vtail} \cdot \frac{c_V}{4} - M_{vtail} \tag{9.29}$$

Where Y_{vtail}, D_{vtail}, M_{vtail} and W_{vtail} are the sideforce, drag, aerodynamic moment and weight of the vertical stabilizer, l_{vtail} is the distance from its root to the tip and c_V is the chord. $M_{fromSideforce}$ and $M_{fromDragV}$ are moments that cannot be simply expressed due to the eliptical distribution of the forces causing them, but will be calculated with the function in subsection 9.3.6.

FBD of the fuselage

The free body diagram of the fuselage is shown in Figure 9.8. Of the forces shown in this picture, the reaction forces from the wing are expected to be largest in magnitude.

Figure 9.8: Free body diagram: fuselage

Note that there are no separate reaction forces applied on the fuselage, as it is free in the air and not attached to anything. Instead, the reactions from the other elements (wing, horizontal tail and vertical tail) get applied on the fuselage as additional loads. An exception is the yet unanalyzed loading case of a rough landing, but due to its complexity this is left for subsequent stages of the design.
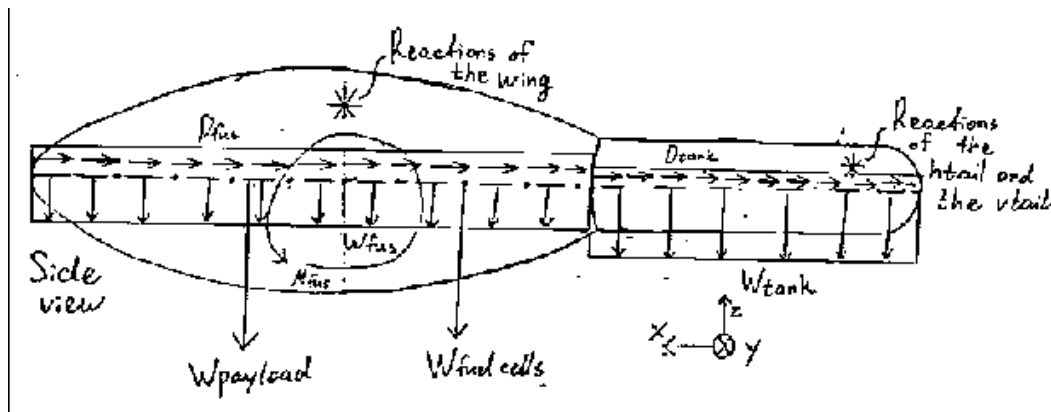
9.3.4. Fuselage analysis

Because there are no reaction forces applied on the fuselage, it is not in static equilibrium. Due to this, it is not immediately clear which forces contribute to the deformation of the fuselage and which only account for its rotation and translation in the air. Furthermore, the wing is expected to be more heavily loaded than the fuselage, since it provides the majority of its lift. Hence, priority was given to the wing. The horizontal and vertical stabilizers were analyzed too both because of their similarity to the wing as well as their importance for the drone's stability in cruise.

As a result, structural design predominantly focused on the wing and the empennage. Detailed design of the fuselage is left as a recommendation for further research. For the time being, the fuselage will use the shape determined by the aerodynamics department and shall be built from the same material as the wing.

9.3.5. Tail arm analysis

A part of the fuselage is the tail arm, which is also the fuel tank. Nevertheless, due to its double-shell structure, the tasks that the tank must fulfil are split between the shells; the inner shells contains the fuel, while the outer shell is responsible for carrying the loads. It has a relatively large radius of 0.1 m, making it quite stiff. Due to this, it is expected that it will be able to carry the loads applied on it by the horizontal and vertical tail without significant deflections. Nevertheless, this is only qualitative analysis. A more detailed calculation is recommended for future research along with the fuselage analysis.

9.3.6. Stresses and deflections methodology

Now that all loads applied on the different parts of the aircraft are known, analysis can begin on the stresses and deflections. First, the critical buckling stress is addressed because it is often a limiting case for the thickness of the

structure. Then, the wing and the horizontal and vertical tails are treated together, as they were analyzed with the same tool.

Critical buckling stress

The critical buckling stress is based on the geometry of the wing-box and the selected material. When the wing is deflected, the plate which is contracted can potentially fail because of skin buckling. Equation 9.30 shows the way this critical stress is calculated. Generally, the length considered is the spacing between the ribs, which are included in the initial wing-box design. The buckling constant was chosen for the case where the root and the tip are clamped and the leading edge and trailing edge are simply supported (CSSC) and it has a value of $C = 5.41$ for an aspect ratio of 5.

$$\sigma_{cr,buckling} = C \cdot \pi \cdot \frac{E \cdot I}{(1 - v^2) \cdot A \cdot L^2} \tag{9.30}$$

Lifting Surfaces Stresses and Deflection

The coordinate system used for the analysis of the wing is shown in the FBD's and it has its origin at the root. The x-axis is pointing towards the leading edge, z is pointing upwards and y is pointed to the tip of the wing.

The first function used by the analysis tool is a function for the loads and their respective application points. This function takes as inputs the distance from the root, the current flight stage (cruise or VTOL) and the current part that is being analyzed. The distance from the root is used to create arrays for the lift, the drag and the moment of the lifting surface for each section between the root and the point of the span that is currently analyzed. These arrays are then later used in conjunction with a Macaulay step function to generate expressions for moments and shear forces. The other loads, as seen in subsection 9.3.3 are the weight of the wing, with a constant distribution along the span and the loads coming from the rotors which are all placed at the tip of the wing: the reaction torque, the thrust and the weight. For the VTOL case, the only loads that change are the aerodynamic loads as explained in subsection 9.3.2.

The next function used in the analysis tool is one that is used to define the geometry for the current part at a certain distance from the root. The rectangle wing-box is tapered linearly according to the taper ratio of the wing. It has a constant thickness on all four walls. The thickness to chord ratio t/c is also kept constant throughout the span. The width of the wing-box is multiplied by 0.6 such that the root width is $0.6 \cdot c_{root} = 0.396 [m]$ and the height is multiplied by 0.7 such that the root height is $0.7 \cdot h_{root} = 0.055 [m]$. These multiplications are done in order for the wing-box to fit inside the airfoil cross-section. The skin of the airfoil is considered to not carry any loads for this initial wing-box design. Finally this tool also calculates the moments of inertia that are later on used to determine stresses. For example, the calculation of I_{xx} is shown in Equation 9.31.

$$I_{xx} = w \cdot h^3 / 12 - (w - 2 \cdot t) \cdot (h - 2 \cdot t)^3 / 12 \tag{9.31}$$

The main analysis tool that created the shear forces and the moments is the Macaulay step function, shown in Equation 9.32.

$$f_n(y) = <y - a>^n \tag{9.32}$$

This function only activates for a load once the distance a of that particular load is reached on the span. This function has the power n changed according to the type of load and it accounts for the distance automatically. With a different integration rule than usual functions, it is also easy to use when for example the moments have to be turned into deflections. While this is function works well for constant distributed loads along the span and point loads such as the ones from the rotor, some adaptations had to be made in order to use the same function for the aerodynamic loads. First, the function identifies the section that is currently being analyze and then it computes the contribution of the aerodynamic loads from that section all the way to the tip. Then, to only take the section treated into account, the contribution from the beginning of the section all the way to the tip is added and the contribution from the end of the section all the way to the tip is subtracted.

The next part of the analysis tool starts calculating the moments and the shear forces at a certain distance from the root. The flexibility of the Macaulay step function also allows for the these to be computed starting from the tip. This allows the analysis to not include the reaction forces. For example, when looking at the wing during the cruise phase the moments and the shear forces are under the form shown in Equations 9.33 - 9.37.

$$M_x = aeroMcly('wing', y, 2, 'L') - W_{wing} \cdot <y - 0>^2 - T_{rot} \cdot <y - 0>^0 - W_{rot} \cdot <y - 0>^1 \tag{9.33}$$

$$M_z = aeroMcly('wing',y,2,'D') - F_T \cdot <y-0>^1 \tag{9.34}$$

$$T_y = l_{cp} \cdot aeroMcly('wing',y,0,'L') + aeroMcly('wing',y,0,'M') + (F_T - W_{rot}) \cdot l_{ax} \cdot <y-0>^0 \tag{9.35}$$

$$V_x = -aeroMcly('wing',y,2,'D') + F_T \cdot <y-0>^0 \tag{9.36}$$

$$V_z = -aeroMcly('wing',y,1,'L') + W_{wing} \cdot <y-0>^1 + W_{rot} \cdot <y-0>^1 \tag{9.37}$$

where aeroMcly represent the Macaulay function for the aerodynamic loads with the current part, $y = b/2 - rootdistance$ the distance from the tip, the power of the Macaulay step function and L, the load case, as the inputs. This function also directly takes into account the division by the power that arises when a Macaulay step function is integrated. W_{rot} is the weight of the rotor, T_{rot} is the torque of the rotor and F_T is the thrust. l_{cp} is the distance from the centre of pressure to the middle of the wing-box. The torque equation also makes use of l_{ax} which is the distance from the center-line of the wing-box to the point of application of the rotor loads. The horizontal and vertical tail moments and forces are calculated in the say way with the exception of the rotor loads. For the VTOL case is calculated using the same functions for the loads presented in the FBD.

Moving on to the stresses of the structure, the case for the wing in the cruise phase has its procedure detailed again. With biaxial bending around the x and z axes, the vertical and the horizontal plates of the wing-box are subjected to compression and tension, therefore it is often the case that two perpendicular plates have stresses that add up in the corner. This is why each corner was checked and the maximum was chosen. Bending stress uses Equation 9.38.

$$\sigma_y = \frac{M_x}{I_{zz}} \cdot \frac{h}{2} + \frac{M_z}{I_{xx}} \cdot \frac{w}{2} \tag{9.38}$$

The next type of stress that was considered was pure tensile loading for the vertical tail. As this is not a critical case and it has no implications on the other parts, it is not going to be detailed here. Then, the only stress that remains to be analyzed is the shear stress. Same as before, this is detailed for the wing in the cruise flight phase. The shear centre is in the middle of the wing-box. This stress has two components, one coming from the torsion which represents the redundant shear, flow and one coming from the shear forces which represents the base shear flow. The first component is computed with Equation 9.39 and the second component is computed with Equation 9.40. Afterwards, Equation 9.41 adds them together to find the shear stress by multiplying with the constant thickness.

$$q_{s,0} = \frac{T}{2 \cdot A_m} \tag{9.39}$$

$$q_b = -\frac{V_z}{I_{xx}} \cdot \int_0^s t \cdot z \, ds - \frac{V_x}{I_{zz}} \cdot \int_0^s t \cdot x \, ds \tag{9.40}$$

$$\tau_s = t \cdot (q_{s,0} + q_b) \tag{9.41}$$

Now that the stresses have their procedure detailed, the same can be done for the deflections. The deflections of the wing during the cruise phase are caused by M_x along the z axis and by M_z along the x axis. The first step in calculating the deflection was comprising a list with the moments at the 21 stations across the span along with a list of the actual span positions of the stations. Then, the moments were transformed from a discrete function to a continuous function by using a least squares third order polynomial fit. Then, the rate of deflection and the actual deflections were computed by integrating the polynomials twice with another function. Since the boundary conditions state that the rate of deflection and the deflection at the root have to be equal to 0 and due to the nature of the polynomial, the constants of integration were also 0.

Finally, for the torsional deflection, the twist angle, an approach more similar to how the stresses were calculated was chosen. The torque was calculated at the stations along the span by making use of the Macaulay step function and the integration was done by creating a system of 2 equations with the boundary condition that the twist is 0 at the root of the wing. The rate of twist was calculated using Equation 9.42.

$$\frac{d\theta}{dy} = \frac{T}{4 \cdot A_m^2 \cdot G} \cdot \oint \frac{1}{t} ds \tag{9.42}$$

9.4. Functional Flow Diagram

With the determined methods for the calculations, a functional flow diagram can be constructed as shown in Figure 9.9.
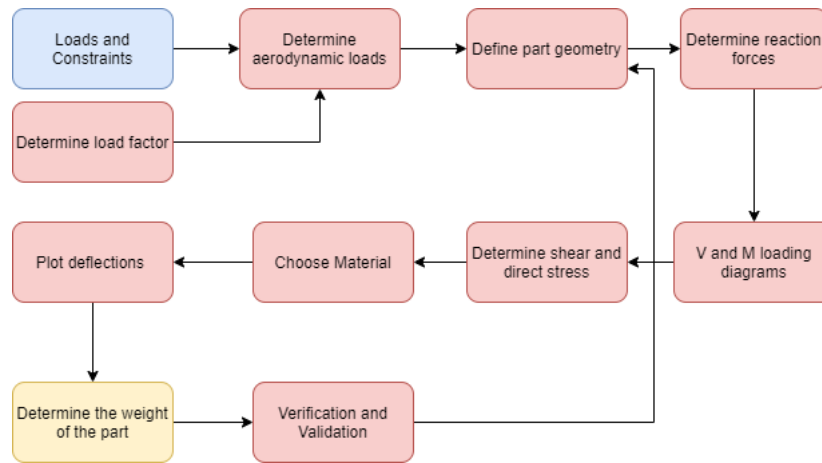
Figure 9.9: Functional flow diagram of the structures department

9.5. Configuration and Results of the Initial Layout

The initial layout of the structure of the drone is shown in this section. It includes the assumptions used, loading diagrams, stress calculations and a material trade-off. Also, this design is verified, validated and a sensitivity analysis is performed.

9.5.1. Geometry and Assumptions

The initial layout of the wing-box design aims for simplicity and fast results. As mentioned in subsection 9.3.6 the cross-section is tapered linearly with the taper ratio of the wing. Moreover, the thickness is constant throughout the wing-box. An important constraint for the design of the wing-box was the attachment to the actuator of the propeller at the end of the wing. The actuator needs to be attached to the wing-box in a single point with a strong support structure, because it has to be able to rotate around that point. For this initial design, the front spar is the attachment point. Table 9.2 shows the most important geometric parameters.

Table 9.2: Initial wing-box parameters for the wing

Parameter	Symbol	Value	Units
thickness	t	2	$[mm]$
width at the root	w_{root}	0.396	$[m]$
height at the root	h_{root}	0.033	$[m]$
width at the tip	w_{tip}	0.24	$[m]$
height at the tip	h_{tip}	0.02	$[m]$
ribs spacing	L	0.09	$[m]$
root moment of inertia	$I_{xx_{root}}$	8.27e-8	$[m^4]$
tip moment of inertia	$I_{xx_{tip}}$	1.51e-8	$[m^4]$

9.5.2. Loading diagrams

With the use of the free body diagrams shown in subsection 9.3.3, shear force and moment diagrams (shown in figures 9.10-9.11) are created for each part and loading condition. As the moments directly correlate with bending stresses and the forces directly correlate with shear stresses, they can also be used to make initial predictions about stresses.

Similar graphs to Figure 9.10 and Figure 9.11 were also constructed for the horizontal tail and the vertical tail. They showed that the loads experienced on these components are smaller than those on the wing. This makes sense, as in VTOL the wing is the part most affected by the rotors, while in cruise it is responsible for providing the majority of the aircraft's lift. Furthermore, as made clear by section 9.2, the wing is also designed to carry the increased loads
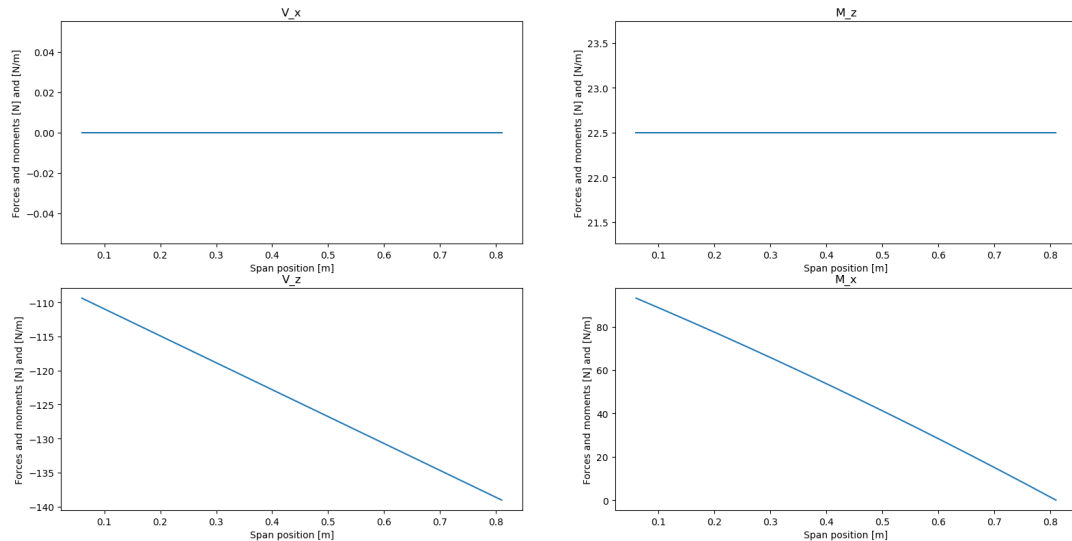
Figure 9.10: V and M diagrams: wing during VTOL. N and N/m on the y axis and span position on the x axis.
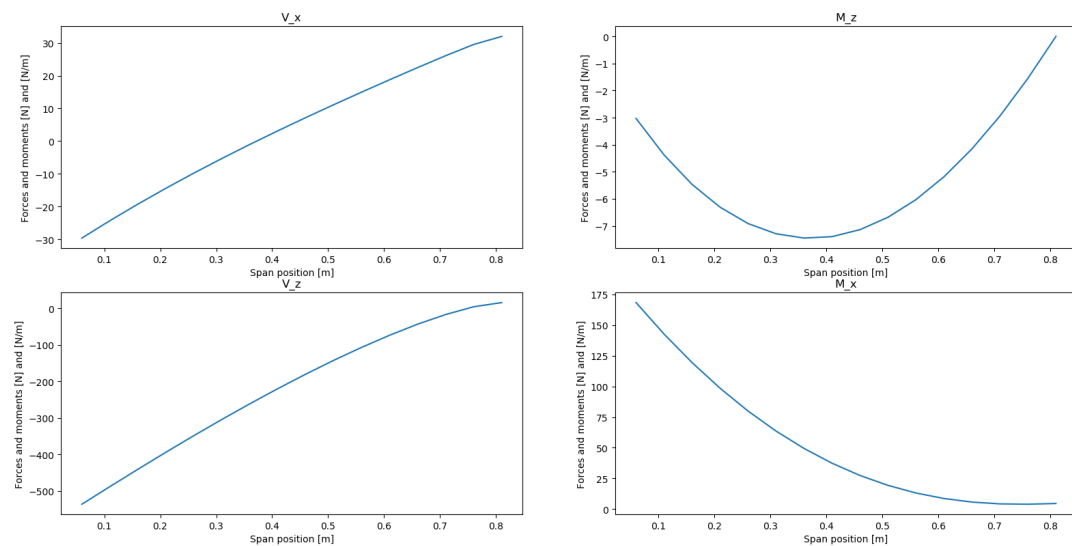
Figure 9.11: V and M diagrams: wing during cruise. N and N/m on the y axis and span position on the x axis.

during maneuvering. Due to this, it can be expected that the wing will also showcase the highest stress values.

Of these extra graphs constructed, one had zero shear forces and moments applied on it. This was the vertical tail during VTOL. During VTOL, the incoming flow velocity is assumed to be 0, hence the drone experiences no aerodynamic forces. Furthermore, for the vertical stabilizer the weight acts as an axial force, so it does not contribute to the shear forces. As bending moments are integrals of the applied forces, it follows that they should also be equal to zero. This means that the results of the code are correct. Therefore, this result can be considered as a sort of a verification for the loading diagrams code.

Of course, the assumption about the aerodynamic forces is violated in the case of a strong gust. Nevertheless, the effect of such gusts was deemed much stronger during cruise, so it was only accounted for during that case. Since if the structure can sustain gusts in cruise, it can also sustain them during VTOL, the analysis was simplified for the VTOL case. Crosswind can also violate this assumption and so must be researched in the future.

9.5.3. Stresses

The stresses caused by shear forces, bending moments and (for the vertical tail) also the axial force of the weight are shown in Table 9.3. For each part and condition, the maximal value of the stress has been recorded, as it varies along the span. It is clear that the highest stresses experienced by the structure occur in the wing during cruise.

Table 9.3: Maximal stresses experienced by the structure

Part	Condition	Maximal normal stress [Mpa]	Maximal shear stress [Mpa]	Maximal von Mises stress [Mpa]
Wing	VTOL	12.6	17.7	30.7
	cruise	23.3	34.8	64.6
Horizontal tail	VTOL	≈ 0.0	0.1	0.1
	cruise	0.4	4.3	7.4
Vertical tail	VTOL	$\approx - 0.0$	0	≈ 0.0
	cruise	0.1	3.2	5.5

Due to this, it is this condition that will be the main deciding factor when a material is selected. It is also the most restricting condition when it comes to the design of the cross-section. Seeing as this condition is so important, the plots for all of these stresses are displayed in Figures 9.12-9.14 for reference.
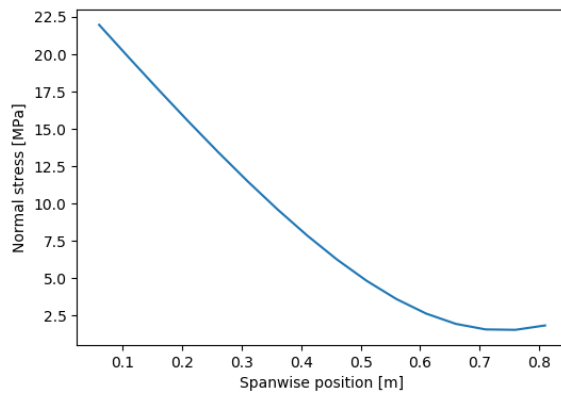
Figure 9.12: Normal stress of the wing in cruise

Figure 9.13: Shear stress of the wing in cruise
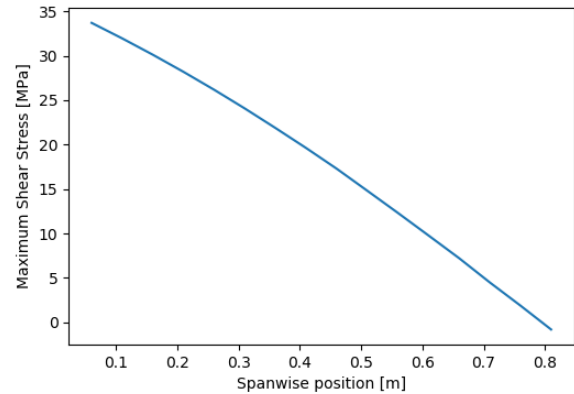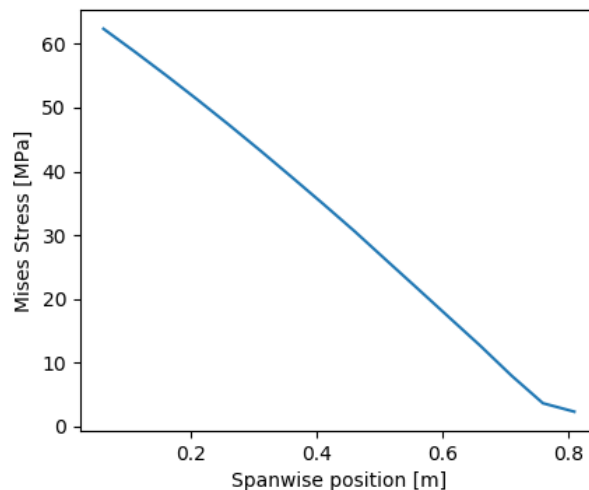

Figure 9.14: Von Mises stress of the wing in cruise

9.5.4. Material Trade-off

With these stresses in mind, a material could now be selected. The options initially considered are shown in Table 9.4. Data on the metals was obtained from ASM [2]. The carbon fiber composite used is an off-the-shelf product offered

[2] https://www.aerospacemetals.com/

by Toray Inc. [10]. The glass fiber composite is also commercially available [22]. Finally, for the biocomposite, the properties of the cellulose propionate (CP) resin [19] and flax fibers [32] were separately researched and the properties of the composite were then calculated with the rule of mixtures.

Table 9.4: Considered materials and their properties

	Density [kg/m3]	Flexural modulus [GPa]	Flexural yield stress [MPa]	Ultimate (tensile) strength [MPa]	Shear modulus [GPa]	Shear strength [MPa]	Poisson ratio [-]
Al 7075-T6	2810	71.7	503	572	26.9	331	0.33
Ti-5Al-2.5Sn	4480	110	827	861	48	520	0.31
17-7 PH Stainless Steel	8000	195	240	620	77	77	0.27
Carbon fiber reinforced plastic (CFRP)	1750	169 (parallel) 31.4(transverse)	1650 (parallel), 316.7 (transverse)	2690 (parallel) 430.2 (transverse)	78.3 (parallel) 14 (transverse)	131 (parallel) 20.9 (transverse)	0.29
Glass fiber reinforced plastic (GFRP)	1450	9.7 (parallel) 1.8 (transverse)	328 (parallel) 63 (transverse)	230 (parallel) 36.8 (transverse)	3.76 (parallel) 0.7 (transverse)	186 (parallel) 29.7(transverse)	0.29
Flax fiber reinforced CP resin	1362.5	17.2 (parallel) 3.2 (transverse)	199 (parallel) 38.2 (transverse)	222 (parallel) 35.5 (transverse)	6.7 (parallel) 1.2 (transverse)	133.2 (parallel) 21.3 (transverse)	0.29

Furthermore, since the drone is expected to contribute to the 2030 environmental goals, the environmental impact of each material is shown in Table 9.5. The tablen data was obtained from an australian survey on metallurgy [6], as well as numerous articles on the lifecycle of composites [71][26][59]. Note that the value for flax fiber does not account for the CO_2 absorbed during growth of the flax plant. Due to this, a flax fiber composite is actually carbon negative [32].

Table 9.5: Environmental friendliness of considered materials

Material	Recyclability	Embodied CO_2 emissions (kg of CO_2/kg)	Embodied energy -[MJ/kg]
Al 7075-T6	Easy	22.4	211
Ti-5Al-2.5Sn	Easy	35.7	22
17-7 PH Stainless Steel	Easy	2.3	361
Carbon fiber composite	Hard	22.4	289
Glass fiber composite	Hard	2.0	48
Flax fiber composite	Easy	0.7	6.5

To choose a material for the design, two procedures were used. First, stresses experienced by the wing in cruise were compared to the relevant stress values of each material to check if they can carry the load without failing. It became apparent that all of the materials are strong enough to sustain the normal stresses. However, due to their inferior properties in the direction perpendicular to the fibers, the composites would fail in shear. Therefore, the options were only limited to the metals for the time being. Steel and titanium were also eliminated due to the high mass of any components built from them. This left aluminium as the only choice. However, this was far from optimal. Being a metal, aluminium also had a higher density than the composites. Furthermore, even though it could carry bending and shear, such a structure proved very vulnerable to buckling, which required the addition of more ribs, further raising the mass of the components.

In an effort to solve this issue, the composite materials were revisited. Special attention was paid to the flax fiber composite because it has the lowest density. While inferior in its material properties to carbon fiber and glass fiber composites, this material is nonetheless strong enough to carry all loads except the shear as mentioned before. To prevent shear failure, the decision to modify this composite was made. Its fiber volume ratio was increased from 50% to 60%, with 50% of fibers aligned in a spanwise direction and 50% in the perpendicular direction. The material properties of this new material are shown in Table 9.6.

Table 9.6: Modified flax fiber composite properties

	Density [kg/m3]	Flexural modulus [GPa]	Flexural yield stress [MPa]	Ultimate (tensile) strength [MPa]	Shear modulus [GPa]	Shear strength [MPa]	Poisson ratio [-]	Recyclable?
Modified flax fiber reinforced CP composite	1393	11.7 (parallel) 11.7 (transverse)	136.02 (parallel) 136.02 (transverse)	136.47 (parallel) 136.47 (transverse)	4.5 (parallel) 4.5 (transverse)	81.9 (parallel) 81.9 (transverse)	0.29	Yes

It can be seen that while the properties in the parallel direction have worsened, the ones in the transverse direction have drastically improved. In fact, they are now the same as for the parallel direction, since there are now fibers

also running in that direction. This new version of the flax fiber composite proved capable to sustain normal and shear stresses 1.5 times higher than what is expected for the structure. At the same time, its density is less than half that of aluminium. Due to these reasons, it is this material that was selected as the main constituent of the drone's structure.

The thermal resistance of this material needs to be addressed, since it must be able to withstand temperatures inside the -10 to 40 [°C] range according to requirements. This range is not an issue for the materials selected. Both the resin [19] and the fibers [32] have processing temperatures much higher than 40 [°C], therefore they are able to sustain this temperature without reduction in their properties, e.g. softening of the resin (which only happens at 93 [°C]. The lower limit of the temperature range is also not low enough to cause damage.

9.5.5. Deflections

With the material selected, the deflections can now be calculated and compared. These are shown in Table 9.7. Note that due to its different orientation, these deflections fall along different axes for the vertical tail. The effect of the load factor of 3.8 is accounted for in cruise for all parts.

Table 9.7: Deflections of the structural components

Part	Condition	Maximal deflection along z (x for vtail) [mm]	Maximal deflection along x (y for vtail) [mm]	Maximal twist angle [°]
Wing	VTOL	21.6	- 0.02	4.0
	cruise	69.3	- 0.04	2.2
Horizontal tail	VTOL	-0.06	0.0	0
	cruise	- 56.9	- 0.02	0.04
Vertical tail	VTOL	0.0	0.0	0
	cruise	-2.2	0.5	0.04

The maximal deflection experienced along z (or x for the vertical tail) is maximal for the wing in the cruise condition. This is also true for the twist angle. These deflections are shown in Figure 9.15 and Figure 9.16.
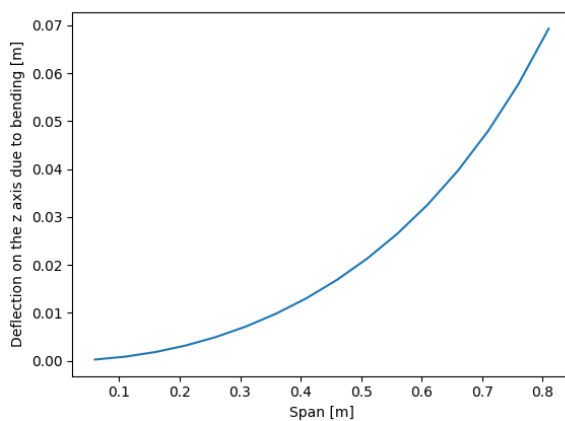

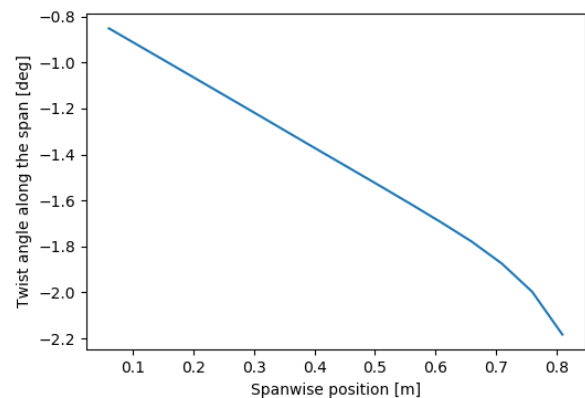Figure 9.15: Deflection of the wing along the z axis in cruise

Figure 9.16: Twist angle of the wing in cruise

For the maximal deflection along x (or y for the vertical tail), the vertical stabilizer showcases the largest deflection, as also seen in Figure 9.17.
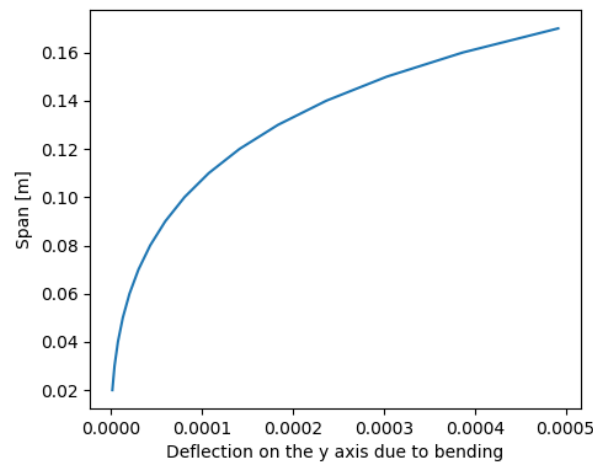
Figure 9.17: Deflection of the vertical tail along the y axis in cruise

9.5.6. Sensitivity analysis

To establish which parameters are of most importance for the drone's structure, a sensitivity analysis was performed on the wing, shown in Table 9.8. The analysis was not performed for the horizontal and vertical stabilizers. However, the same code used to design the wing was also used for them, so the reactions to parameter changes would be identical.

Table 9.8: Sensitivity of the wing design

	Mass [kg]	Maximal normal stress in wing [MPa]	Maximal shear stress in wing[MPa]	Maximal z deflection [mm]	Buckling stress of wing [MPa]
Base values	2.0	22.0	33.75	69.25	28.07
Thickness -10 %	1.8 (-10 %)	24.0 (+9.09 %)	36.75 (+8.89 %)	74.13 (+7.0 %)	22.74 (-19 %)
Height - 10 %	1.97 (-1.5 %)	25.1 (+14.1 %)	38.75 (+14.8 %)	89.25 (+28.9 %)	No change
Width - 10 %	1.81 (-10.5 %)	24.5 (+11.4 %)	No change	77.0 (+11.2 %)	No change
Number of ribs - 10 %	1.99 (-0.5 %)	No change	No change	No change	22.18 (-26.6 %)

Height of the wingbox proves to be the most important parameter, as it leads to a non-linear increase in the stresses experienced in the wing, as well as its deflection along z (which is always larger than the deflection in x, as was seen in Table 9.7). This is because the largest force on the wing, the lift, bends the wing about the x axis, while a decrease in wingbox height cubically reduces the moment of inertia about this axis, as seen in Equation 9.31. The number of ribs is also quite important. Using fewer of them has barely any effect on the mass, but causes a significant reduction of the buckling stress. Therefore, the design should pursue other ways of reducing weight if this proves necessary in the future.

9.5.7. Verification

A first form of verification of the code comes from the moment and shear force diagrams. If there is no force or no stand-alone moment at the tip of the wing, the shear forces and the moments and the tip of the lifting surfaces should be 0. As shown in subsection 9.5.2 the loading diagrams do indeed go to 0 except when the weight, torque and the thrust of the rotor are present.

A second form of verification was done by comparing the wing deflection at the tip in the VTOL phase with the cantilever beam standard solution under a distributed load. Because the moment of inertia also changes along the span, a value of $7.0 \cdot 10^{-8}$ was chosen for it, which is in between the value at the root and the value at the tip. Another assumption made in here is that there is no plate drag, no wing weight and no weight for the rotor, such that only the thrust force is considered. Equation 9.43 shows the result of this analysis which shows a difference of +36% compared to the initial result of 0.021. Although the percentage is high, the increase is in line with the assumption of removing every load except the thrust force, as all of those loads decrease the deflection in this case. In order to fully

verify the code, it is indicated for future reference to perform more unit tests such as this one in order to cover all the necessary ares.

$$v_z = \frac{P \cdot L^3}{3 \cdot E \cdot I} = \frac{155 \cdot 0.81^3}{3 \cdot 11.7 \cdot 10^9 \cdot 7 \cdot 10^{-8}} = 0.0335 [m] \tag{9.43}$$

9.5.8. Validation

The validation of the analysis tool is done by using a 3D modelling software [3] in the case of the wing for the cruise phase, more particularly, this validation looks at the deflection on the vertical axis. All of the loads are included in this simulation; a difference with respect to the model is that the aerodynamic loads are no longer applied at the beginning of the interval but rather at the middle. The constraint at the root is an elastic one, with a stiffness constant value as shown in Equation 9.44.

$$k = \frac{E \cdot A}{L} = \frac{11.7 \cdot 10^9 \cdot 0.837 \cdot 10^{-3}}{0.81} = 12.09 \cdot 10^6 [N/m] \tag{9.44}$$

As can be seen from Figure 9.18, the deflection of 6.2 cm (shown in meters) is around 11% lower than the expected 6.9 cm that comes from the analysis tool. From this, it can be concluded that there is some uncertainty regarding the analysis tool, but the estimation is more conservative.
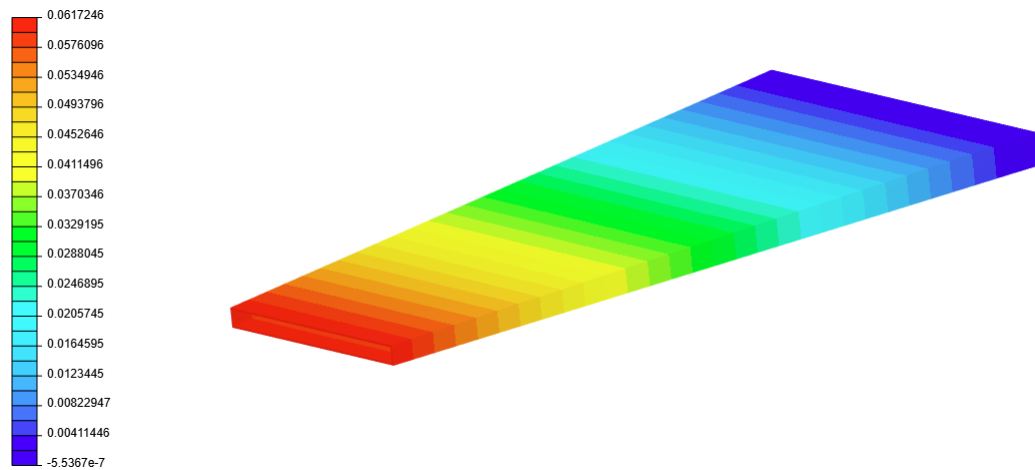
Figure 9.18: Deflection of the vertical axis for the wing in the cruise phase (Simscale software)

9.6. Configuration of the Updated Layout
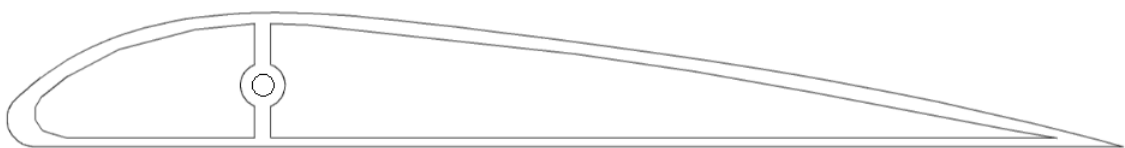
Figure 9.19: Configuration of the updated wing-box

Now that the tools used for the analysis of the wing and the other parts of the drone are complete, for future work, an updated layout such as the one in Figure 9.19 is suggested. As one can see, the cross-section no longer consists of a rectangular box, but rather the supporting structure now has the same shape as the airfoil. The skin thickness is distributed along the chord, with more reinforcement at the leading edge and the trailing edge. Furthermore, it was preferred to go for a single spar configuration. This single spar is also then used on its own to support the weight, thrust and torque of the rotor by inserting the actuator and the necessary cabling through the hole in the middle of the spar.

---

[3]https://www.simscale.com/

9.7. All-weather Resistance

Lightning strike can be the reason for significant damage to the drone if the structure does not conduct electricity well enough. This is not an issue for aluminium aircraft. However, the main material selected for the drone is a flax fiber composite. This spoils its conduction properties and puts it in serious risk of lightning damage [16]. In order to avoid this, aluminium fibers will be integrated into the composite material so that the lightning current can safely pass through without causing damage. This allows the structure to fulfill requirements MD-SYS09-ST08.1 and MD-SYS09-ST08.2, since aluminium is able to conduct such currents without issues, as showcased by its length use in civil aviation [16]. This measure is only necessary near possible lightning attachment areas, such as the nose and the tips of the wings, the horizontal and the vertical stabilizer, as well as in especially under-risk components like the outer shell of the fuel tank.

At the current time, the structure has not been inspected for its performance under vibration. Its resistance to corrosion and water have also not been the subject of analysis yet. Therefore, these tasks are postponed for the following stage of the design, when time again becomes available.

9.8. Compliance Matrix

With the structural subsystem fleshed out, the requirements can be revisited. Table 9.9 shows that most of the requirements have been met. For all requirements, the required value is shown in the 'Required' column, while the values for the design are shown in 'Actual'. Note that some of the values shown in 'Actual' are calculated in other chapters, like for example the recyclability (in chapter 15) and the assembly cost (in chapter 12).

Table 9.9: Compliance Matrix

Requirement	Required	Actual	Fully met	Partially met	Not met	To be investigated
MD-SYS01-ST01:	2.2 x 3.0 x 0.8 [m]	2.1 x 3.0 x 0.8 [m]	✓			
MD-SYS01-ST02:	0.2 x 0.2 x 0.2 [m]					✓
MD-SYS02-ST03:	20 kg	5.07 kg	✓			
MD-SYS06-ST04:	45[°C] for 1 h					✓
MD-SYS06-ST05:	100 [N] 100 [Nm]					✓
MD-SYS08-ST06:	300-1500 [Hz]					✓
MD-SYS09-ST07:	14 [m/s] 24 in gust	14 [m/s] 24 in gust	✓			
MD-SYS09-ST08:			✓			
MD-SYS09-ST08.1:	300 [kV]	300 [kV]	✓			
MD-SYS09-ST08.2:	3-200 [kA]	3-200 [kA]	✓			
MD-SYS09-ST09:						✓
MD-SYS09-ST10:	IPX6					✓
MD-SYS09-ST11:	1.26 [J]					✓
MD-SYS09-ST12:	-10 to 40[°C]	-10 to 93[°C]	✓			
MD-SYS31-ST14:	60 %	100 %	✓			
MD-SY08-ST15:	1.5	1.5	✓			
MD-SYS23-ST16:	15 000 Euro	7350 Euro	✓			

9.9. Recommendations about Future Research

The effect that the ducts have on the aerodynamic forces at the tip of the wing must be modelled. The same holds for the effect of the horizontal tail on the vertical one due to the T-tail configuration. The fuselage is still pending detailed analysis. The structure as a whole also has only been the subject of static analysis. Dynamic analysis (of the vibrations) must also be performed before the final product is released. Non-mechanical properties of the flax fiber composite such as its resistance to moisture and corrosion require additional research. Last but not least, more unconventional loading cases need to be considered, such as a rough landing, crosswind during VTOl or an impact with an obstacle, because they might have a significant effect on structural design.

10

Communication, Navigation and Guidance

This subsystem design starts of with a functional analysis in section 10.1. From this analysis, requirements are defined in section 10.2. Then, the design of the communication subsystem, navigation subsystem and guidance subsystem are shown in section 10.5, section 10.3 and section 10.4 respectively.

10.1. Functional Analysis

The Communication, navigation and Guidance system is responsible for providing a down-link from the drone to the ground station, as well as providing an up-link for controlling and communicating with the drone. It should also make sure that the HEALR drone is flying at the right location and stays on route. A graphical representation of these functions can be found in Figure 10.1.
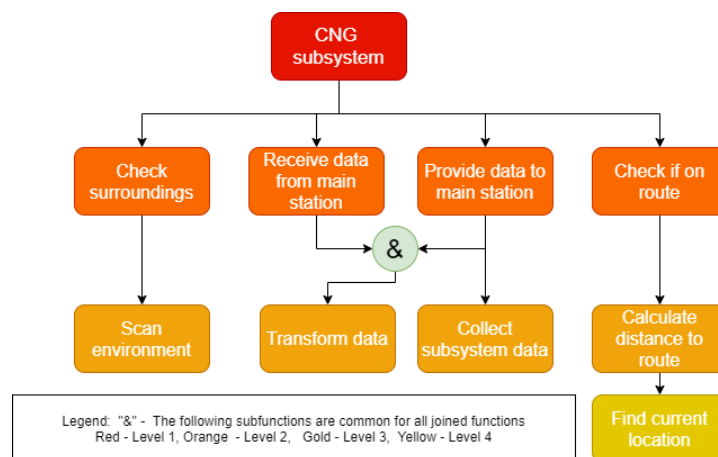

Figure 10.1: Functional breakdown for the CNG subsystem

These functions need to be fulfilled by the communication subsystem and will enable a good information flow both to and from the drone.

10.2. Subsystem Requirements

For this subsystem there is once again a list of requirements which the subsystem should adhere to.

MD-SYS11-CNG01:   The drone shall be able to store 128 [GB] of data.
MD-SYS12-CNG02:   The drone shall be able to determine its 3D location with 1 [m] accuracy.
MD-SYS12-CNG03:   The drone shall be able to determine its speed with 0.5 [m/s] accuracy.
MD-SYS14-CNG04:   The CNG system shall be able to receive data of 5 [Mb/s].
MD-SYS11-CNG04.1:   The CNG system shall be able to receive data with a frequency of 380 [MHz].
MD-SYS15-CNG05:   The CNG system shall be able to send data of 40 [Mb/s].
MD-SYS11-CNG05.1:   The CNG system shall be able to send data with a frequency of 380 [MHz].
MD-SYS22-CNG06:   The drone system shall be able to detect objects within a radius of 100 [m].
MD-SYS22-CNG06.1:   The drone system shall be able to detect objects with a certainty of 99%.
MD-SYS22-CNG07:   The drone shall be able to fly according to a preset flight path with an accuracy of 15 [m].
MD-SYS17-CNG07.1:   The flight path shall not make use of the restricted airspace, such as military and airport
                        airspace.

10.3. Navigation

Once the drone is in airborne it needs to know the way. Therefore navigation is needed. For navigation the GNSS (Global Navigation Satellite System) network will be combined with IMU's (Inertial Measurement Unit). With this the position of the drone can be determined using high precision GNSS technology. Combining this with the IMU providing the heading and velocity, the drone can be tracked with high precision. This in turn allows the drone to fly along predetermined paths. During flight the GNSS will provide a location, from which each iteration the new position can be found using the data from the IMU. Since the data from the IMU can be used to calculate the current position it is possible to continue flying even if the GNSS signal drops. However, the time that the drone can fly on only the IMU is limited, since errors within its calculations could become increasingly larger [24].

During flight the drone needs to be aware of its surroundings this will be done with the use of a camera and recognition software. This provides an overview of the obstacles that are on its path. The recognition software can then also be used during landing to make sure that the proper landing site is targeted. For this terrain recognition software there are already several options on the market. This video footage is saved in case it needs to be used later. For this there is a local storage on the drone, consisting of a 256 [GB] SD card. This should be sufficient storage for a high quality recording of the operation and all the other flight data.

10.4. Guidance

During operations the drone will fly along predetermined paths. These operation paths have to be planned in advance and need approval from instances to allow their execution. Depending on the final classification of the drone, either specific or certified, these paths have to be either approved once or before each operation respectively. Since the aim is to get a specific classification, this will be assumed. In that case all of the operational paths have already been approved and are programmed into the drones navigational system. Since the paths are planned in advance the drone can simply follow this path using the position found by the navigation system.

10.5. Communication

In order to transmit data to the drone and from the drone, a radio communication system has to be used. According to the Electronic communication Committee (ECC), the alloted frequency range for Medical Air-Ground-Air systems lays between 380 and 385 [MHz][15]. This frequency is on the low end of Ultra high frequency transmission and as such only works in line of sight, thus distributed ground-stations have to be used in order to keep contact with the drone. The modulation of the signal will be Digital Spectrum Modulation. As can be seen in the requirements, the data rate required for the downlink is 5 Mbits/s. Using $B = DR/\eta$, where DR is the data rate and η is the spectrum utilization, which is assumed to be 0.9, the bandwidth B for the drone is 5.5 [MHz].

This should suffice for the data communication between the drone and the ground station.

Another option for the transmission is to make use of the 4G network or in the future the 5G network. This offers a simple to implement solution which does not require extra ground stations. The largest drawback of this is the coverage of this network is limited and will not reach for across open water. This method is still being researched and improved, however it is showing a lot of potential.

Both of these options will suffer from interference when flying near populated area's. Since there will be a lot of other signals there, for example Wi-Fi signals. This is however mostly a problem if the 4G network is used [28]. If the Medical Air-Ground-Air system is used, there will be less interference on that frequency and due to the shorter distance the signal travels between ground-stations.

To transfer across these networks a antenna is needed. The placement of this antenna is important to reduce the noise and influence from other systems in the drone. Furthermore placing them perpendicular to the drone will

also increase their performance. Therefore it was decided to place the antenna's on the bottom near the front of the drone, parallel to each other and perpendicular to the drone. This placement increases their distance towards the motors, reducing their interference.

In Figure 10.2, the data-flow/communication diagram can be found. This diagram shows the communication between different electrical elements. All of the data flow goes to the control board. This is where most of the information is stored and where the instructions for other components are sent from. The power control instructs the fuel cell on how much power they should be producing. There is an emergency power control present, in case of failure for other components. In case of an emergency this component makes sure the fuel cells produce enough power to keep the drone from falling out of the sky.
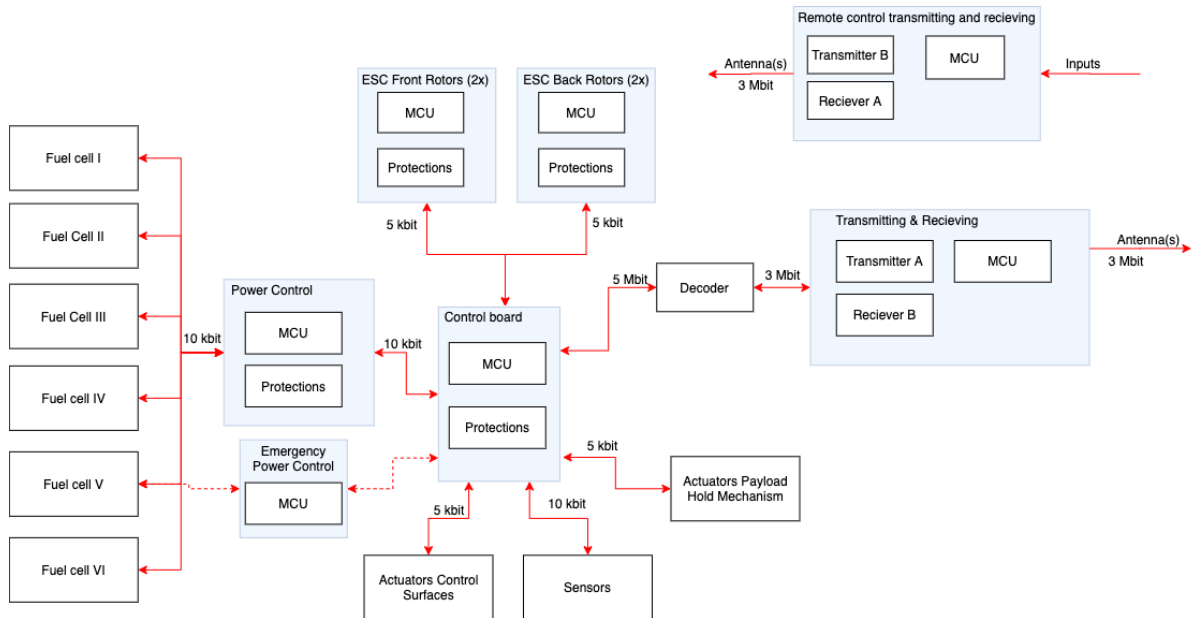
Figure 10.2: Data-flow/Communication diagram

10.6. Compliance Matrix

To see how the design ends up compared to the initial requirements the compliance matrix has been created. Within this matrix the status of each of the requirements is indicated to see if they need further improvement down the line. This compliance matrix can be seen in Table 10.1.

Table 10.1: Compliance Matrix

Requirement	Fully met	Partially met	Not met	To be investigated
MD-SYS11-CNG01	✓			
MD-SYS12-CNG02	✓			
MD-SYS12-CNG03				✓
MD-SYS14-CNG04				✓
MD-SYS11-CNG04.1				✓
MD-SYS15-CNG05				✓
' MD-SYS11-CNG05.1	✓			
MD-SYS22-CNG06				✓
MD-SYS22-CNG06.1				✓
MD-SYS22-CNG07	✓			
MD-SYS17-CNG07.1				✓

11

Product Verification and Validation

In this chapter, the system requirements are shown along with their respective validation procedure. The four methods that are employed for this validation are described here and assigned to each requirement in Table 11.1.

- Inspection (I): the compliance of the product to the requirement can be inspected (visually)

- Analysis (A): the compliance of the product to the requirement can be analysed by a mathematical tool or another analysis tool

- Demonstration (D): the compliance of the product to the requirement can be established by a demonstration

- Test (T): the compliance of the product to the requirement can be tested by using a (representative) model in representative circumstances

Requirement	Method	Requirement	Method	Requirement	Method	Requirement	Method
MD-SYS01	I	MD-SYS11	T	MD-SYS21	T	MD-SYS31	D
MD-SYS02	D	MD-SYS12	T	MD-SYS22	T	MD-SYS32	A
MD-SYS03	T	MD-SYS13	T	MD-SYS23	D	MD-SYS33	A
MD-SYS04	I	MD-SYS14	T	MD-SYS24	A	MD-SYS34	I
MD-SYS05	T	MD-SYS15	T	MD-SYS25	T	MD-SYS35	D
MD-SYS06	T	MD-SYS16	D	MD-SYS26	D	MD-SYS36	A
MD-SYS07	D	MD-SYS17	T	MD-SYS27	D	MD-SYS37	A
MD-SYS08	T	MD-SYS18	T	MD-SYS28	D	MD-SYS38	A
MD-SYS09	A	MD-SYS19	T	MD-SYS29	T		
MD-SYS10	A	MD-SYS20	D	MD-SYS30	D		

Table 11.1: Verification method for each system requirement

For example, MD-SYS06 (*'The payload shall be protected in case of a crash.'*) can be tested by setting up a safe environment in which the payload container, containing an organ test dummy, is going to be involved in a crash that simulates real life. With adequate sensors on the test organ, the amount of damage received can be seen and recorded.

MD-SYS08 (*'The system shall not be damaged such that it is unable to continue its operation by forces imposed during mission operation'*) can also be tested by setting up a similar environment. The most critical load case can be artificially imposed on the structure and strain gauges can measure displacements.

Other requirements, such as MD-SYS23 (*'The unit cost of drone shall not exceed a value of € 100k.'*) or MD-SYS02(*'The drone shall not exceed a dry mass of 35 kg'*) are going to become evident once the product is finished and no external test is needed for it.

Other validation methods which can be employed in the future are custom experiments such as wind tunnel testing, a simulated obstacle course to test and train the AI software of the drone and pressure testing of the tank. With

these kind of tests, it is possible to inspect individual subsystems of the drone before assembling the whole drone, potentially saving investments in money and time.

Another form of verification is done by looking back at the market analysis presented in the Baseline Report [62]. Using the formulas in Figure 11.1a and Figure 11.1b, it can be calculated that the expected MTOW is between 22.66 and 51.85 [kg], as one can see in Table 11.2. The actual weight is 36.03 [kg], which fits perfectly in the expected range. This range, of course, is very big. However, the weight of the drone is still considered validated.

Relationship	Expected output [kg]	Actual value [kg]
MTOW vs Range	22.66	36.03
MTOW vs Payload	51.85	36.03

Table 11.2: Validation of the maximum take-off weight of the drone

(a) MTOW versus payload
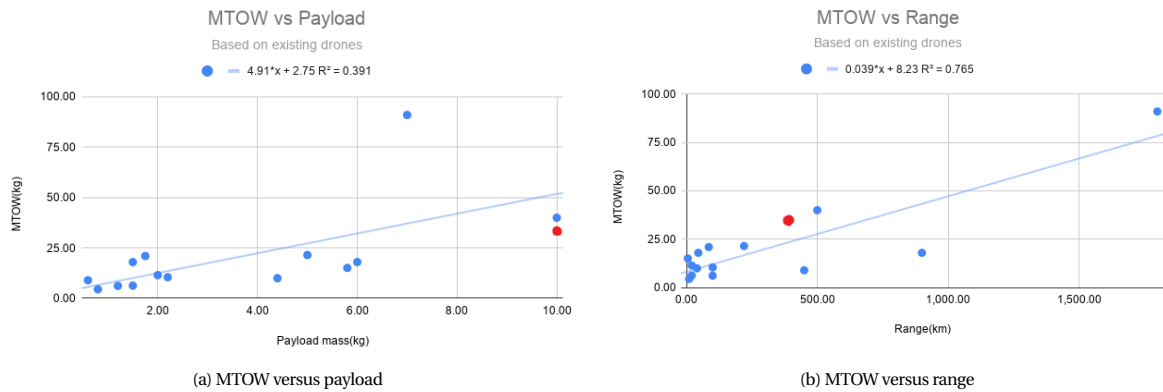
(b) MTOW versus range

Figure 11.1: Graphs comparing the MTOW of multiple existing drones to their range and payload, with the red dot being HEALR

<div align="right">

12

</div>

Final Design Overview

Now that all subsystems are designed, they can be integrated into one structure. This starts with a system overview, discussed in section 12.1. This is continued in section 12.2. Mass, power and cost breakdowns are shown in section 12.3. Then, a sensitivity analysis is performed in section 12.4. Also, a flight envelope is shown in section 12.5. The loading and unloading mechanism is shown in section 12.6. As the whole drone is designed now, its compliance to the requirements can be tested in section 12.7.

12.1. System Overview

With the integration of different subsystem into each other, a total system overview can be constructed. This system overview consists of all active components of the drone. A diagram of the system can be seen in Figure 12.1. As the drone uses electric servo motors for actuating all control surfaces as well as for securing the payload, no hydraulics system is used. Furthermore, all engines used for propulsion run on electric power. Next to the electric cabling, the gaseous connections are an integral part of the design. This includes a hydrogen connection from the hydrogen storage to the fuel cell stack as well as a fueling adapter for the hydrogen. In order to provide oxygen and cooling to the fuel cells, air is routed from an inlet to the fuel cells. This air will then also carry the produced water vapor away and will release it into the atmosphere. All data connections are defined by the USB standard.

Besides the hardware diagram, a software diagram can also be constructed which illustrates the architecture of the drone's controller. Several inputs are given to the controller, some from the environment others from the ground station or internal components. These inputs are then send through several logic gates where different inputs mean different resulting output. The full diagram can be seen in Figure 12.2.

12.2. Characteristics Overview

When combining the design of the different subsystems, the final layout of the drone is obtained. The most significant features of the drone, are the large ducts of the main rotors, which are mounted at the tip of the wing. These rotors provide 90% of the total thrust of the drone. The smaller back rotors are mounted inside a duct in the fuselage and is used during take off and landing, to increase maneuverability of the drone and ensure stability with shifting center of gravity locations. The ducts are used to increase hover efficiency of the drone. In order to mount the empennage at a sufficient distance from the center of gravity, the fuel tank is used as an integral structure of the tail arm. The single fuel tank contains all the needed liquid hydrogen for the total duration of the mission. In order to generate the needed power during the mission, 6 fuel cells are used, which each produce a power of 800 [W] during steady state operation, but can produce 1400 [W] peak power for a limited amount of time. This peak performance is mainly needed during the transition phase and hover. The medical payload is stored in a passively cooled box in the nose of the drone. This placement makes the payload easily accessible for ground operations. The drone is able to fly at 50 [m/s] during cruise which means, that it will reach its maximum destination of 100 [nmi] in a circa an hour. Finally, a 3 view of the drone can be seen in Figure 12.3.

12.3. Budget Breakdown

12.3.1. Class II budget estimation

Before starting the more detailed subsystem, a Class 2 weight and power estimation was performed. During this analysis the weight of different components like the wing was determined by statistical estimates[53]. For the fuel
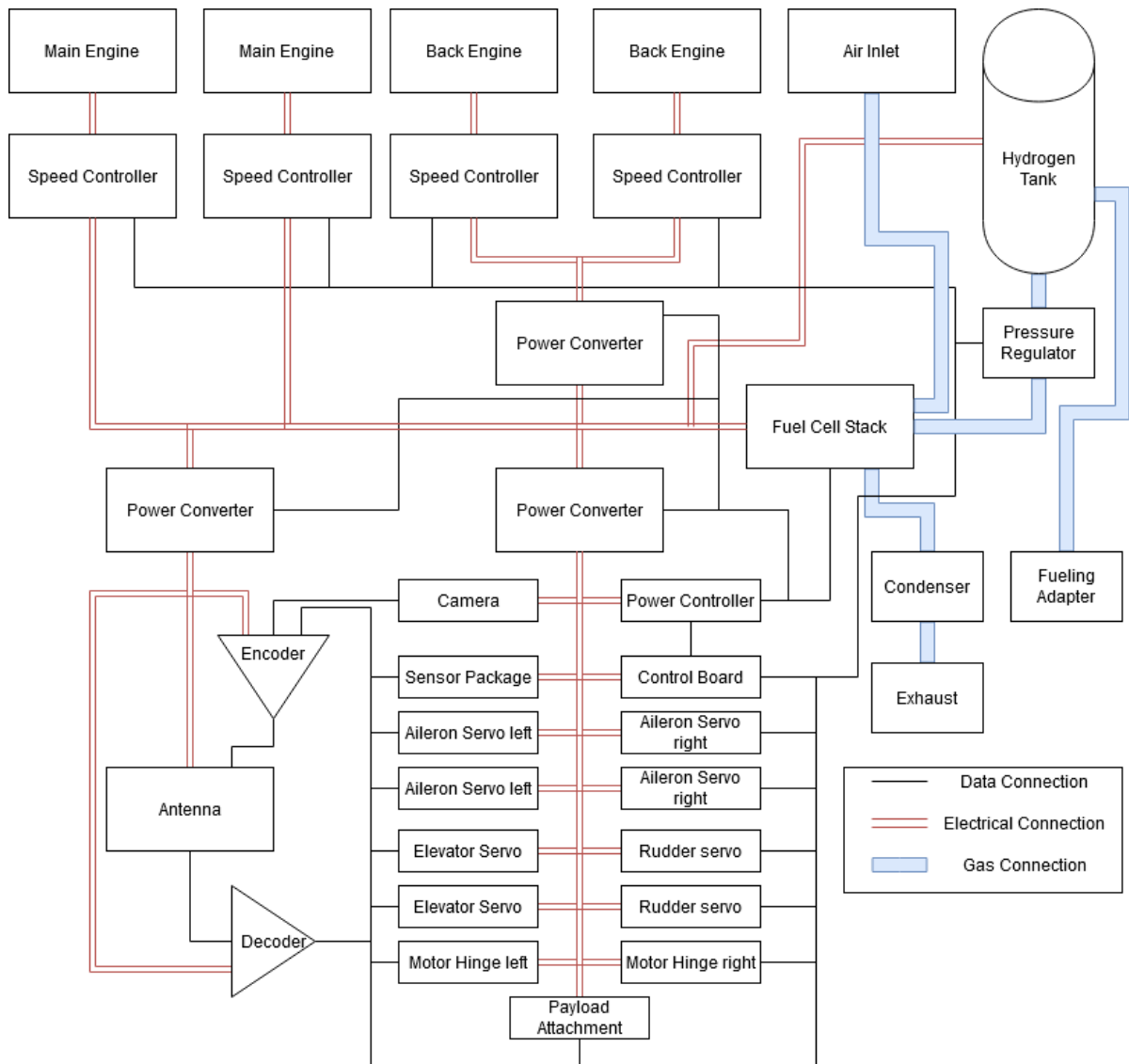
Figure 12.1: Hardware Diagram of the drone

cells and electric engines, a database of commercially available products was performed, from which the weight of the drone could be estimated. Furthermore the needed hydrogen fuel was estimated by its calorific value and the approximate efficiency of fuel cells. The fuel tank was treated as a simple cylindrical pressure vessel.

12.3.2. Mass Budget

The final zero-fuel weight of the drone is determined as the sum of the masses of the different subsystems. As a contingency, for components that are hard to estimate during this design phase, such as plumbing, electrical components and actuators, a constant mass of 2.2 [kg] is assumed. This breakdown can be seen in Table 12.1. From this table it can be seen that the drone has a very high payload mass fraction. Furthermore, it can be seen that the hydrogen system makes up a large fraction of the overall weight. This is expected, as fuel cell systems and hydrogen storage systems have a lower gravimetric power density than conventional propulsion systems. In contrast to the Baseline Report, the total mass budget has been decreased significantly. The biggest changes are present in the weight of the structure, and the weight for the hydrogen storage. On the other hand, the fuel cell weight has been estimated quite accurately.

As can be seen from Table 12.1 the Class II mass budget estimation has a value of 34.1 [kg] while the mass of the final design has a value of 35.1 [kg]. This suggests that the mass was underestimated by 1 [kg]. For the structures subsystem, on one hand, the wing managed to have a lower weight than what was expected due to the light material that was chosen, on the other hand, the empennage weight was more than doubled as the area needed increased in accordance to the small length of the tank, which is also the tail arm. For the hydrogen department, the mass
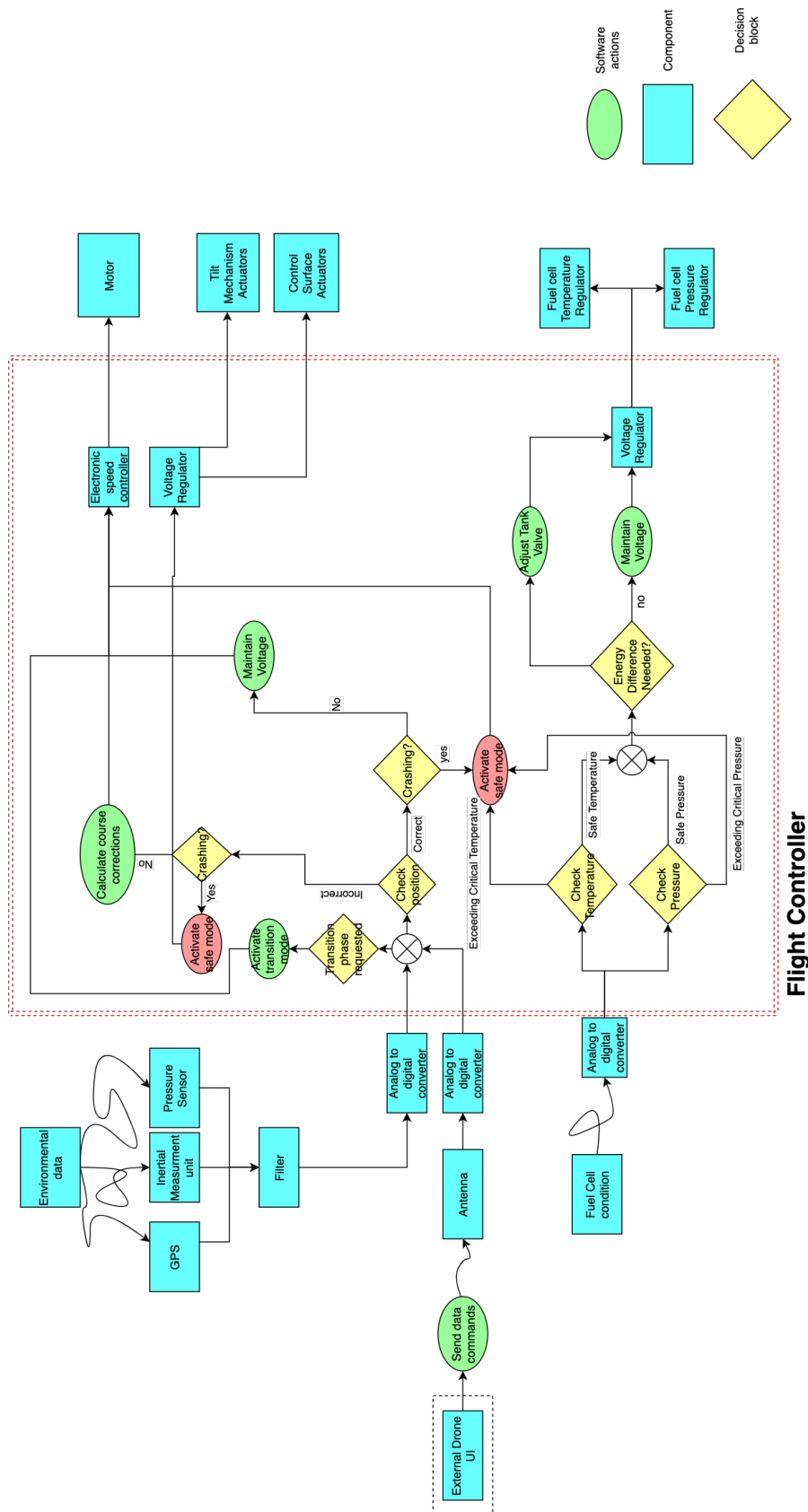
Figure 12.2: Software Diagram of the drone

of the fuel cells was decreased due to the smart coupling of lower power fuel cells which removed the need for a single bulky power delivery unit. Unfortunately, this reduction in weight was overshadowed by the fuel tank weight,
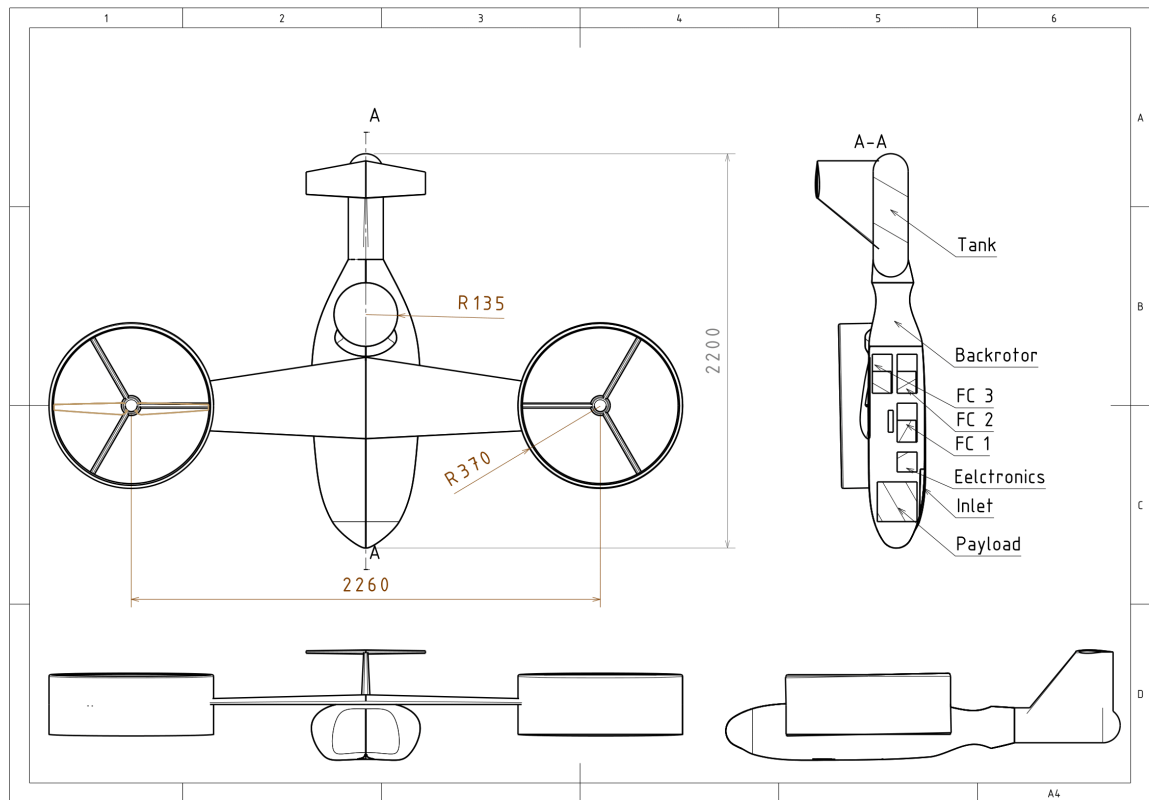
Figure 12.3: 3 view of the drone

which was underestimated with a factor of 2 because insulation was not taken into account. For the propulsion system, the electrical components and the motors were both slightly overestimated. Finally, the ducts, which were not considered in the Class II estimation, also added to the final weight of the drone.

Table 12.1: Mass Breakdown of the Drone

System	Mass [kg]	Mass Class 2 Estimation [kg]
Wing	2.0	3
Empennage	0.37	0.14
Fuel Cells	6.03	8.82
Fuel Tank	8	3.45
Motors + Propellers	2.6	3.2
Fuselage	1.5	1.5
Ducts	1.2	n/a
Payload	10	10
Electrical + Plumbing	3.4	4
ZFW	35.1	34.1

12.3.3. Power Budget

The drone is equipped with 6 fuel cells, which each produce 800 [W] of power during steady state operation. Two of the fuel cells are equipped with batteries, so they can provide a peak power of 1400 [W] for 3 minutes. This extra power is needed during the VTOL phase as well as during transition. The highest percentage of power is distributed to the propulsion system. Because of this, the main motors are run directly on the 25[V] from the fuel cell, to minimize losses. The auxiliary motors in the back however have a higher required rpm and thus a converter has to be used to increase the voltage for these motors. The total power budget of the drone is presented in Table 12.2 and Table 12.3. The power that is reported, is the power that the consumer is taking directly from the fuel cells, with all efficiencies already taken into account. In contrast to the Baseline Report [62], the power budget has been severely underestimated during cruise and has been slightly overestimated during hover phase.

Table 12.2 and Table 12.3 also indicated the values of the power that comes from the class II estimation. It can be seen that both the cruise budget and the VTOL budget were underestimated. This was because some efficiencies were overestimated and the number of rotors the powers had to be distributed to increased from 2 to 3.

Table 12.2: Power Budget during cruise

Consumer	Power [W]	Class 2 [W]
Propulsion	4670	4600
Communication	25	25
Miscellaneous	100	100

Table 12.3: Power Budget during VTOL

Consumer	Power [W]	Class 2 [W]
Propulsion	5220	4600
Communication	25	25
Miscellaneous	100	100

12.3.4. Cost breakdown

It is important to have a good estimation of the development cost for the drone, what one drone would cost and how much money are spent during a mission. In this section these three are given and explained. If the costs are too high the design is unacceptable and changes need to be made to the design. Requirements MD-SYS23 and MD-SYS24 in section 4.2 give demands for the maximum costs.

Unit cost

The cost of one drone is found by looking at the cost of all the separate elements. These can be found in Table 12.4. Most of the prices were found by looking at similar parts used in other flying vehicles. It must be noted that there is a very high uncertainty in the cost of some of these parts. The specific price needs to be further investigated in later stages of the design. For the tooling and manufacturing cost it is assumed that 4-5 drones are worked on at the same time.

Table 12.4: Cost breakdown for a single unit

Subsystem	Part/action	Price
Hydrogen	Fuel cell	€60,000
	Tank	€5,000
	Isolation material	€1,000
Propulsion	Motors	€1,000
	Rotors	€1,600
	ESC's	€1,000
	Actuators	€950
Structures	Adhesive	€400
	Material	€350
	Tooling	€7,000
	Manufacturing	€350
Electrical	Antenna	€300
	Servos	€1800
	Hinges	€300
	Control board	€400
	Wiring	€100
Total		€82,950

Development cost

Developing a high-tech product, especially one that was not attempted before, consists of a sustained team effort. During the course of this development, it is often the case that unexpected situations like a subsystem redesign, fund retraction or mishandle of a prototype arise which may all lead to substantial setbacks. These are all factors that have to be taken into account and as such, a development cost factor is defined with a value of $n = 1.5$. The development cost itself consists of multiple parts [69]:

- Salaries for the 20 engineers and scientists that develop the drone. These are set to an average of 90,000 € per year.

- Manufacturing and assembling a full scale first prototype. This has the same price as the unit cost presented in Table 12.4.

- Testing custom set-up builds and airworthiness authorities certification. An approximated 200,000 € is allocated for this.

- Manufacturing and assembling a full scale second prototype with the same unit cost.

- Another 10% of this cost added for marketing, finance and management sectors.

Then, Figure 12.4 provides a timeline for the development of the drone based on which the total development cost can be calculated.
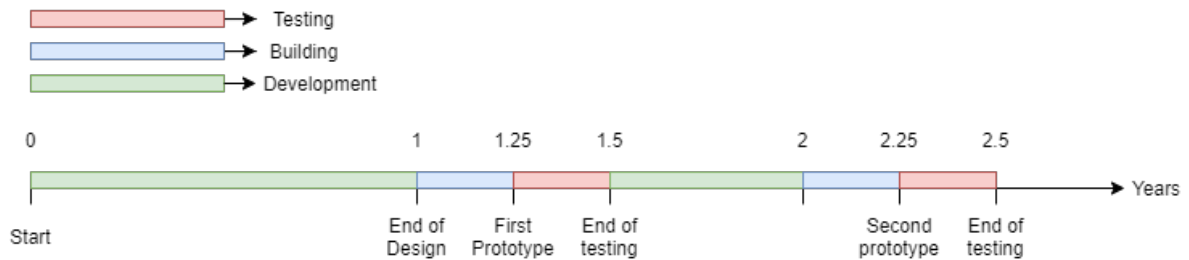

Figure 12.4: Development cost timeline

With this set timeline and by taking into account the contingency factors the development rounds out to 5.05 million €. For a more visual breakdown of the origins of the costs, one can refer to chapter 16, see section 16.3 and the diagram in Figure 16.1. Now that this value and the unit cost are calculated, one can find out after how many units sold (for 100,000 €) the business producing these drones would become profitable. With a 17000 € profit per product, 300 drones would need to be sold to reach the break even point.

Operational cost

The operational cost of the drone is critical for the customers. If this system is to replace the current means of medical transport, the price is a very important factor. It can be much faster than present options, but if the drone costs significantly more, it will not replace them. The operational cost is divided in five categories, found in Table 12.5.

Table 12.5: Operational cost breakdown

Part	Cost [€/km/kg]
Facilities	0.029
Employees	0.0654
Fuel	0.0019
Maintenance	0.00074
Total	0.097

A few assumptions were made for this calculation. Firstly, the rent of a facility is taken to be around €4,000 per month. Next, the operators are paid 38 € and the mechanics 30 € per hour. These are the gross salaries, so a higher number is taken into account in the operational cost.

Comparison With Current Situation

Most transport of medical payload, such as blood, is done either by car or by helicopter. Between these two the medical transport by car is the cheapest option, hence this will be the benchmark with which the drone will be compared.

Drones are able to go faster than ambulances, an ambulance is able to travel a maximum of 120 [[$\frac{km}{h}$]] whilst the drone has a cruise speed 170 [[$\frac{km}{h}$]]. From a sustainability point of view the drone will be hydrogen powered compared to the gasoline powered ambulance car, making the drone more sustainable. Furthermore the unit cost of the drone is below 100k whilst an ambulance can cost around €200k [1]. The big advantage that an ambulance

---

[1] https://www.rijnmond.nl/nieuws/108906/Nieuwe-ambulances-voor-Zuid-Holland-Zuid

has, is that it can carry much more payload than the drone, however for small payloads such as blood or medicine a drone would be the better option from a sustainable point of view, but also a financial one.

Customer break even point

The customer break even point happens when the product sold starts bringing in profit. Referring back to **??** and limiting this analysis to the Netherlands, it is supposed that only 3 of these drones are in operation at the same time. So, if hospitals in a region were to buy one of these drones, their break even point can be calculated by dividing the unit cost with the yearly profit. With an approximated 1500 organ transplants and blood transfusions per year, assuming that the need for emergency blood transports is equal to the number of organ transplants per year [2] and with a factor for the market share and the operations where there is no need for transportation, the break even point rounds out at 6.6 years as shown in Table 12.6. As expected, this break even point takes a long time to reach due to the high cost of the power unit inside the drone.

Table 12.6: Customer break even point

Parameter	Value
€/ride [3]	435
Op. cost/ride [€]	370
Profit/ride [€]	65
Rides/year	700
Yearly profit [€]	15166
Profit time [years]	6.6

12.4. Sensitivity Analysis

In order to assess the stability and feasibility of the design, a sensitivity analysis is performed. This is done by varying the maximum return range of the drone as well as the payload capacity. The design process is then performed for those varied parameters and the MTOW and fuel cell power are recorded. This analysis is performed around the user required parameters with a range of ±15%. These results are presented in Table 12.7 and Table 12.8. It can be seen that the current design is very sensitive to changes in payload mass. This sensitivity also applies to general changes of non-functional mass. Furthermore, the design is sensitive to changes in maximum range, however to a lesser extent. This high sensitivity most likely originates from the relatively low power density of the used fuel cells. With further improvements in this area, the sensitivity of the drone can be reduced to a great extent. Even though all designs in the considered design space are possible, the heavier designs need a lot more fuel cells and thus increase the cost of the drone drastically. This makes these designs less attractive to customers and as such still might make the design unfeasible.

Table 12.7: Change in MTOW [kg] vs varying range and non-functional mass

		-1.5	-1	-0.5	Δm [kg] 0	0.5	1	1.5
	-15	-8.3	-6.2	-5.1	-3.9	-2.6	-1.2	0.4
	-10	-6.2	-5.1	-3.9	-2.6	-1.2	0.3	-1.5
	-5	-5.0	-3.9	-2.7	-1.3	0.1	1.8	3.6
ΔR [nmi]	0	-3.9	-2.7	-1.4	0.0	1.6	3.3	5.2
	5	-2.7	-1.5	-0.1	1.4	3.0	4.8	6.7
	10	-1.5	-0.2	1.2	2.8	-0.5	6.5	8.7
	15	-0.3	1.0	2.5	4.2	6.0	8.1	10.5

It should be noted, that the estimations for mass and power used during this analysis are only validated for the values which are present in the final design.

---

[2] https://www.transplantatiestichting.nl/publicaties-en-naslag/cijfers-over-donatie-en-transplantatie/organen-jaarcijfers/aantal-orgaantransplantaties

Table 12.8: Change in fuel cell power [kW] vs varying range and non-functional mass

		-1.5	-1	-0.5	Δm [kg] 0	0.5	1	1.5
	-15	-1.4	-1.1	-0.9	-0.7	-0.5	-0.2	0.1
	-10	-1.1	-0.9	-0.7	-0.5	-0.2	0.1	-0.3
	-5	-0.9	-0.7	-0.5	-0.2	0.0	0.3	0.7
ΔR [nmi]	0	-0.7	-0.5	-0.2	0.0	0.3	0.6	1.0
	5	-0.5	-0.3	-0.0	0.2	0.5	0.9	1.3
	10	-0.3	-0.0	0.2	0.5	-0.1	1.2	1.6
	15	-0.1	0.2	0.5	0.8	1.1	1.5	2.0

12.5. Flight Envelope

The flight envelope consists of three main phases. The first phase during airborne operations, is the vertical takeoff and climbing phase. This phase will last up to 3 minutes, while the drone climbs with a maximum of 3 [m/s], up to a maximum altitude of 250 [m]. During the next phase, cruise, the drone will follow a pre-planned flight plan. This phase will take place inside U-space airspaces as defined by EASA [13]. In the last flight phase, the drone will perform a vertical landing at its destination. This phase will last up to 3 minutes as well. The maximum range of the drone with a payload of 10 kg, is 100 [nmi] return trip. The ferry range of the drone is 138 [nmi] return trip. The maximum range for different payload weights can be seen in Figure 12.5. It is noted, that for ranges higher than the design range, no additional fuel can be loaded into the tank. Thus the slope of the diagram is very steep and features no second kink, which would correspond to maximum fuel tank capacity.
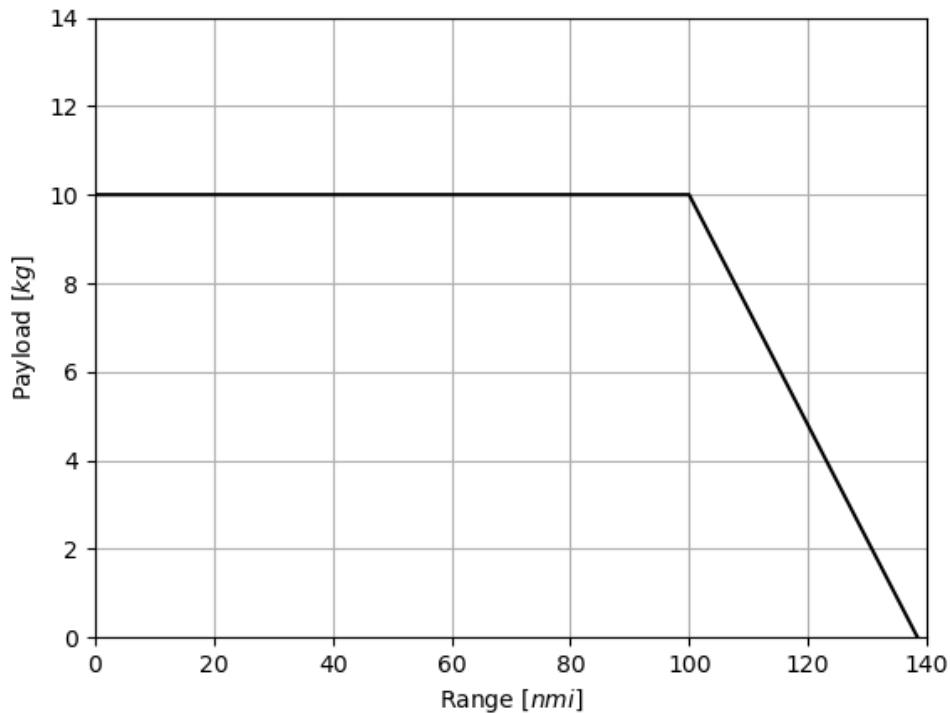

Figure 12.5: Payload Range Diagram of the drone

12.6. Loading and Unloading Mechanism

The purpose of the drone is to transport either organs or blood from one hospital to another. In this chapter the integration of this payload in the design is discussed. First, the requirements that have to do with the payload are given. Then the loading mechanism is explained.

Requirements

MD-SYS05.1:   In case of transferring red blood cells, the payload shall be kept at a temperature between 2 and 10 [$°C$].

MD-SYS05.2:   In case of transferring blood plasma, the payload shall be kept at a temperature below -25 [$°C$].

MD-SYS05.3:   In case of transferring blood platelets, the payload shall be kept at a temperature between 20 and 24 [$°C$].

MD-SYS05.4:   In case of transferring organs, the payload shall be kept at a temperature below 2 [$°C$].

MD-SYS06:   The payload shall be protected in case of a crash.

MD-SYS21:   The drone shall have a self-loading and/or self-unloading system of the payload.

Loading mechanism

Requirement MD-SYS21 states that the drone needs to be self (un)loading. This makes the drone easier to use and takes away the risk of an operator getting injured while being near the drone. There is a variety of options to let the drone unload itself. The choice was made to have the payload inside the fuselage, instead of keeping it on the outside. This has major advantages when it comes to the aerodynamics of the drone, but it does complicate the loading. A cut-out will be present in the body of the drone in which the payload fits. The drone can fly above the payload and slowly lower itself. The cut-out needs to be larger than the payload, so it has no problems with covering it.

After the drone has landed, encasing the payload with its body, they need to be attached. The drone will have two sliding pin mechanisms. These mechanisms can close around the ring, which is attached to the top of the payload. Both are strong enough to carry the payload by itself. This way the payload shall not be lost in case of failure. These pins carry the weight of the payload during flight. The sliding pin mechanism and a 3D view of the payload can be seen in Figure 12.6
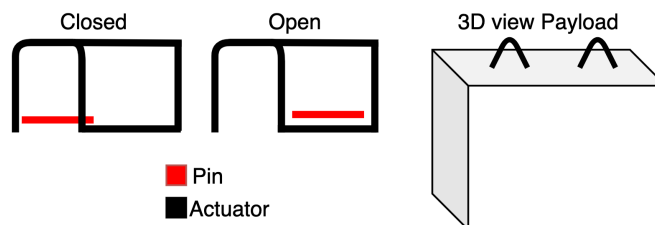
Figure 12.6: Sliding pin mechanism with 3D view of the payload (not to scale)

During flight, the extra space around the payload would let it swing around. This problem is solved by having extenders which apply a bit of pressure on all four sides of the payload, keeping it still. However, in case of high accelerations it needs to be ensured that the payload does not take too high loads. This is why springs with dampers will be used for the arms. Further analysis is needed to find the spring constant and damper ratio for these. Moreover, the lengths of the arms need to be defined carefully, as they might not have enough space in the drone to extend. This lay-out is shown in Figure 12.7.

Payload Compliance Matrix

In Table 12.9, the compliance of the design with the requirements is shown. All the requirements that have to do with temperature are not met by the current design. However, in the current transport situation the payload box also has its own cooling inside. This is why it was assumed that the cooling will be included in the 10 [kg] of the payload. If, after further investigation, it appears that external cooling is needed, such a system needs to be added. The bottom of the payload is open to the airflow, so in colder weather conditions this could be useful for cooling.
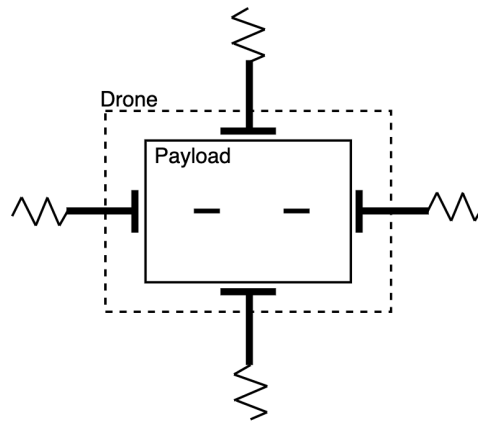
Figure 12.7: Top view of payload inside drone

Table 12.9: Compliance Matrix

Requirement	Fully met	Partially met	Not met	To be investigated
MD-SYS05.1:				✓
MD-SYS05.2:				✓
MD-SYS05.3:				✓
MD-SYS05.4:				✓
MD-SYS06:	✓			
MD-SYS21:	✓			

12.7. System Compliance Matrix

At the end of the design process, the compliance with the system requirements is checked. This compliance matrix can be found in Table 12.10. The majority of requirements are fully met. Requirement *MD-SYS36: "The system shall only use in-flight captured data for the purpose of fulfilling its mission"* is not fully met, as routing information is send to the drone via a ground station. This however does not impact the performance of the drone. A large amount of requirements is marked, that in order to evaluate compliance, more detailed analysis or physical tests have to performed. These requirements relate to complex aspects of the drone like MD-SYS18, which relates to the noise produced by the drone. The compliance with those requirements will be reassessed in a future stage of the design process.

Table 12.10: Requirements compliance matrix of the hydrogen subsystem

Requirement	Fully met	Partially met	Not met	To be investigated
MD-SYS01:	✓			
MD-SYS02:	✓			
MD-SYS03:	✓			
MD-SYS04:	✓			
MD-SYS05:				✓
MD-SYS06:				✓
MD-SYS07:				✓
MD-SYS08:	✓			
MD-SYS09:				✓
MD-SYS10:				✓
MD-SYS11:	✓			
MD-SYS12:	✓			
MD-SYS13:	✓			
MD-SYS14:	✓			
MD-SYS15:	✓			
MD-SYS16:	✓			
MD-SYS17:	✓			
MD-SYS18:				✓
MD-SYS19:	✓			
MD-SYS20:	✓			
MD-SYS21:	✓			
MD-SYS22:	✓			
MD-SYS23:	✓			
MD-SYS24:	✓			
MD-SYS25:	✓			
MD-SYS26:				✓
MD-SYS27:	✓			
MD-SYS28:	✓			
MD-SYS29:	✓			
MD-SYS30:		✓		
MD-SYS31:	✓			
MD-SYS32:		✓		
MD-SYS33:	✓			
MD-SYS34:				✓
MD-SYS35:	✓			
MD-SYS36:		✓		
MD-SYS37:	✓			
MD-SYS38:	✓			

13

Technical Risk Assessment

This chapter addresses the risks that threaten the success of the medical drone project. These risks are sorted into two categories: risks associated with the manufacturing and assembly of the drone and risks encountered during operation.

13.1. Production Risks

Before risk assessment can begin, accurate scales for impact and probability need to be defined so that each risk can be ranked objectively. These scales are shown in Table 13.1.

Table 13.1: Scales of production risks

Impact	Explanation	Probability	Explanation
Severe	Specimen unusable, its production must restart	Imminent	Guaranteed to happen immediately and will keep happening
High	Unacceptable flaw, repairs needed	High	Will happen repeatedly during production
Moderate	Flaw noticeably worsens performance	Moderate	Will happen at least once during production
Low	Flaw slightly worsens performance	Low	Unlikely to happen
Very low	Negligible flaw	Very low	Will practically never happen

The production risks can be further split into two subcategories: risks associated with part manufacturing and risks related to assembly.

13.1.1. Part manufacturing risks

PM1- Rough surface: The outer surface of the drone must be reasonably smooth or it will generate unwanted drag, which corresponds to a moderate impact. Considering that the entire outer surface of the drone will be produced from the flax fiber reinforced CP composite, this risk directly relates to the mold used for injection molding. This mold can be inspected before production begins and any unwanted surface feature can be eliminated. Therefore, the probability of this risk is low.

Mitigation of PM1: In the unlikely event that imperfections in the mold are not detected on time, the rough surface will immediately be seen on the first part produced. It can then be filed smooth, which reduces the impact to very low.

PM2- Injection screw damage: Injection molding is the process used to manufacture all composite parts in the drone. The CP resin used is a thermoplastic, meaning that micro-granules [58] must be added to it so that it liquefies when the screw is moving. These micro-granules may be abrasive and cause damage to the screw. This reduces the speed of injection molding, which may cause slight flaws in the created part. This corresponds to a low impact. Since micro-granules must be added, this risk has an imminent probability.

Mitigation of PM2: Attention must be paid when selecting the material for the micro-granules so that they cause no damage to the screw. Alternatively, inserts or a more resistant screw could be used. In both cases, the granules no longer cause damage, reducing the impact to very low.

PM3- Fiber misalignment: Before the resin is injected, the fibers have to be carefully arranged inside the mold. Nevertheless, there are multiple reasons for small misalignments: human error, the push from the resin flow, etc. Due to this, this risk has a moderate probability. With the fibers misaligned, the loads that the structure can carry slightly reduce, giving it a low impact.

Mitigation of PM3: With careful inspection, at least human error can be eliminated as a reason for misalignment, reducing the probability to low.

13.1.2. Assembly risks

AS1-Clamping failure during FSW Friction stir welding (FSW) is the main method used to join components due to the being applicable on composites. However, it requires the parts to be strongly clamped. In case clamping fails, the plates are free to move. This may cause them to become damaged from the spinning head of the FSW tool. It would require repair of the parts, corresponding to a high impact. Nevertheless, clamps are relatively simple and reliable components, so their likelihood of failure is low.

Mitigation of AS1: Software protocols must be developed for scenarios like these, ensuring that the tool ceases to rotate when the clamping is not secure. This precludes damage to the components, reducing the impact to very low.

AS2-Bond unsuitable for FSW While it is a very convenient technology, friction stir welding has its limits. Namely, it cannot be applied to areas with thickness variations or non-flat surfaces [37]. This means that assembly is impossible in highly curved regions like the tank surface. This has a severe impact on production and is imminent, because the drone will certainly have non-flat areas.

Mitigation of AS2: Induction welding is another alternative for composite joining, provided that the composite is implanted with so-called ferromagnetic susceptors which heat up from the induction and locally melt the material. Applying this technique in addition to FSW enables assembly everywhere. This reduces the impact to very low.

13.2. Operational Risks

A different scale is used for the operational risks. It is shown in Table 13.2.

Table 13.2: Impact and probability scales

Impact	Explanation	Probability	Explanation
Catastrophic	Damage or destruction of the drone and damage to its surroundings	Imminent	Likely to happen within 10 missions
Very high	Destruction of the drone	Very high	Likely to happen within 100 missions
High	Termination of current mission	High	Likely to happen within 1000 missions
Moderate	Delay of multiple hours	Moderate	Likely to happen within 10000 missions
Low	Delay of less than an hour	Low	Likely to happen once in a lifetime
Very low	Mission practically unaffected	Very low	Will practically never happen

Most of these risks were already identified per subsystem during the baseline stage of the project. Here the relevant ones are shown again, along with some new risks that were identified as the design went into more depth. Furthermore, the mitigation strategies for some of these risks have also been refined.

13.2.1. Aerodynamics

A1- Non-aerodynamic Shape *"Damage to the drone from e.g. hail may alter its shape and spoil its aerodynamic qualities. As the drone is designed to fly in such conditions, this risk has a high probability. Worse aerodynamic qualities mean more drag and more hydrogen that needs to be expended, but the mission can still succeed. Hence, the impact is moderate."*

Mitigation of A1:   Big hailstones are a relatively rare occurrence. Most of the time their size does not exceed the one of a hazelnut. These smaller hailstones will dent the surface of the drone, but the dent will not significantly spoil aerodynamic performance. In case a strong hailstorm is expected, weather data can be used to devise an alternative route to the hospital so that the drone is not damaged too much. This causes a delay in the delivery, so there is a still low impact.

13.2.2. Hydrogen

H1- Engine Failure   *"In the worst case scenario, this will happen while the drone is mid-air. As a result, it will fall down and crash, corresponding to a very high impact. The likelihood of this is moderate, because engines are complex systems and small imperfections may lead to loss of function."* However, this risk was identified at a time when it was not yet clear if the design would feature wings. Now this is certain, so unless the drone's wing is damaged or it is uncontrollable for some reason, it cannot crash down during cruise. Instead, it glides down to the ground. The mission still fails in that case, but the drone survives, so the impact is high rather than very high.

Mitigation of H1:   The fuel cells come with batteries added that are responsible for peak power demands. Nevertheless, in the event that one or more fuel cells malfunctions, the batteries can also supply the missing power to the system. Of course, this is not a long term solution, as they have not been sized for this. Still, it should allow the system enough time to command the remaining fuel cells to produce more power to compensate for the missing ones. The impact is reduced to low, as the mission is only slightly affected.

H2- Fuel Leakage   *"There are multiple possible causes for leakage: oversights during tank design, fatigue cracking, etc. Due to this variety of reasons, leakage has a high probability. If this remains undetected, in the worst case scenario the drone will suddenly run out of fuel, fall out of the sky and crash. Hence fuel leakage has a very high impact."* However, this risk was identified at a time when it was not yet clear if the design would feature wings. Now this is certain, so unless the drone's wing is damaged or it is uncontrollable for some reason, it cannot crash down during cruise. Instead, it glides down to the ground. The mission still fails in that case, but the drone survives, so the impact is high rather than very high.

Mitigation of H2:   The inner shell of the tank (the one holding the liquid hydrogen) is made from aluminium, which leaks rarely when compared to composites [66]. Nevertheless, this does not guarantee leaks will not happen. To prevent that, a layer of self-healing material can be added to the outside of the inner shell. This stops hydrogen from leaving the tank, and if this second layer cracks as well, it will heal over time. This reduces the probability of this risk to low.

H3-Tank liner failure   The outer shell of the tank, while being produced mainly from the flax fiber composite, also has an aluminium liner on the inside. This maintains the vacuum between the two shells of the tank, which in turn keeps the liquid hydrogen inside at the required temperature. Nevertheless, both friction stir and induction welding cannot be used to join the metal and composite due to their different melting temperature.

For this reason, thermal expansion is used to keep the two elements in contact. The liner is sized to be larger in radius than the shell in which it fits. In assembly, it is cooled down and put inside. Afterwards, it expands and adheres to the inner wall of the outer shell. This means that the liner is under constant compressive stress. The value of this stress changes with the ambient temperature, loading the liner in fatigue. Due to this, it will eventually fail. Since the composite is not airtight, the crack in the aluminium allows air to slowly leak through. Over time, this will eliminate the vacuum layer between the tank shells and enable heat transfer with the environment. This will cause the liquid hydrogen to evaporate faster, building up pressure in the tank until it explodes. This risk therefore has a catastrophic impact and a moderate probability.

Mitigation of H3:   The first measure to be taken is equipping the tank with a safety valve that releases gaseous hydrogen to the environment when the pressure increases too much. This eliminates the possibility of explosion. Now the worst case scenario is that the drone unexpectedly runs out of fuel and has to glide down to the ground. This corresponds to a high impact. Furthermore, fatigue cracking takes a long time to develop, especially when considering that the liner is pre-loaded in compression which seals the cracks. Due to this, with regular inspection any cracks can be discovered way in advance and the liner can be swapped out before it causes an issue. This reduces the probability of this risk to low.

H4- Delays in H_2 **Delivery/Production** *"Like any industrial process, the production of hydrogen is vulnerable to both technical risks (like a broken component) and organisational ones (like worker's strike). These setbacks are common enough that it can be expected that the hydrogen will not reach the drone when necessary more than once in a lifetime, corresponding to a high probability. Without fuel, the drone cannot respond to emergencies, so this has a high impact."*

Mitigation of H4: *"Delivery of hydrogen from one facility can be unreliable. Therefore, it is better that the team gets their hydrogen from two or three facilities, so that there is always another choice. This reduces the probability that hydrogen can't be supplied to low. Another strategy to be employed is having hydrogen stored on site. In that case, even if all production facilities are unavailable, the team can rely on stored supply until the situation returns to normal. This would reduce the impact of this risk to low."*

13.2.3. Propulsion

P1- Damage to Propeller/Rotor *"Drone rotors are not very strong and can easily be damaged by small projectiles like hailstones. As the drone must fly in 99% of weather conditions, it will have to fly in hailstorms. Over time, damage to rotors may cause one or more of them to break off. In case only one fails (scenario P11), the drone can still fly, though control becomes a harder task, so the impact is moderate. If more fail, however (scenario P1X), it will probably crash, giving it a very high impact. The probability that one rotor fails is high, but the probability for more to fail during the same mission is low."* However, this risk was identified at a time when it was not yet clear if the design would feature wings. Now this is certain, so unless the drone's wing is damaged or it is uncontrollable for some reason, it cannot crash down during cruise. Instead, it glides down to the ground. The mission still fails in that case, but the drone survives, so the impact is high rather than very high.

P2- Damage Caused by Propeller/Rotor *"Rotors spin at very high angular velocities and are often sharp. They can have a catastrophic impact on any object that is within their range and can injure someone severely. The possibility that a child or animal comes near the drone during take-off or landing cannot be excluded, so this risk has a moderate probability."*

Mitigation of P1 and P2: The addition of ducts to all rotors not only increases their efficiency, but also limits their contact to other objects. By adding safety nets in front of the rotors, spanning each duct, the probability is further reduced, making the likelihood of risks P11, P1X and P2 very low.

P3- Rotor stops during cruise A rotor might cease to operate due to either a malfunction in the electric motor or the power line connecting it to rotor. Because of multiple possible reasons for failure, this risk has a high probability. The torque of the remaining engine can be compensated by the rudder, meaning that the drone can land safely. However, that loads it to its limits and it cannot be used for maneuvers, so the drone must land and the mission cannot continue. This corresponds to a high impact.

P4- Rotor stops during VTOL or transition The same malfunction mentioned in P3 leads to much more serious consequences if the drone is taking off, landing or transitioning. During these stages, the rotors are responsible for the control of the drone. It is not a big issue if one of the back rotors stops spinning, since the other one is powered separately and provides redundancy. Nevertheless, if one of the front ones stops working, a large roll moment is suddenly generated. This will destabilize the drone and cause it to tumble, leading to a crash. This corresponds to a very high impact. Since the causes for this risk are the same as before, the probability is again high.

Mitigation of P3 and P4: By adding an additional electric motor and power line for each front rotor, redundancy is also introduced in the front of the drone. Since they are only for emergencies, these motors will only be sized for hover. They add about 0.5 [kg] of extra weight to the drone. Now in the case of a primary motor failure, power can be rerouted to the secondary motor. In cruise, the secondary motor will be enough to provide thrust, so the motor failure has no impact. During landing, there will be no change either, since the motor is sized for hover. Therefore, the impact of risk P3 is reduced to very low.

The only problem arises during take-off, as the secondary motor is not powerful enough for the drone to ascend. In that case, power will be throttled back on the other engines to achieve equilibrium and the drone will land back onto the helipad. After repairs are made to the primary electric motor that malfunctioned, the mission can continue. Due to the delay, the impact of risk P4 is reduced to low rather than very low.

13.2.4. Stability and control

SC1- Collision with Small Flying Object   *"The drone is meant to fly at low altitudes occupied by a variety of objects like birds and other drones. The latter is bound to become a bigger problem in the future as drones are gaining popularity for all sorts of logistical tasks. The drone will probably collide with another flying object at least once in its lifetime, so this risk has a moderate probability. If the control system is designed well, the drone should be able to stabilise and resume the mission. Because of that, this scenario has a low impact."*

SC2- Collision with Large Object   *"At its typical altitude the drone can also encounter agricultural planes and hot air balloons. It is also possible for the drone to hit a building or a tree when ascending/ descending. Hitting any of these objects will cause the drone to crash, so the impact is very high. However, these objects are easy to spot and it is almost certain that the drone (and its operator) will be able to avoid them, so this risk has a very low probability."*

Mitigation of SC1 and SC2:   The drone will be autonomous and will be equipped with sensors to study its environment. This will enable it to avoid obstacles and thus prevent collisions entirely. This reduces the likelihood of these risks to very low.

SC3- Unexpected Wind Conditions   *"As the drone must operate in 99% of European weather conditions, it will need to operate in extreme weather. However, weather can change rapidly and there is a very high probability that it becomes even worse while the drone is in the air. This may lead to gusts with speeds exceeding the ones the drone was designed for. In such cases a crash is very likely, corresponding to a very high impact."*

Mitigation of SC3:   In the case that weather conditions turn out worse than what the drone is designed to fly in, a command will be sent from the main headquarters of the project, asking it to land as soon as possible. This results in the drone surviving, but the mission is put on hold. This means that the impact is high.

SC4- Control Surface Malfunction   *"There is a moderate probability that control surfaces malfunction before end-of-life. Nevertheless, thrust differential of the propellers/rotor would still allow the drone to be controlled, though to a lesser extent. Therefore, the impact is moderate, as the mission can still be completed."*

Mitigation of SC4:   If thrust differential proves insufficient to control the drone, use can also be made of the tilting mechanism of the rotors. This allows a limited amount of thrust vectoring and can be used for pitch (if both wing rotors tilt) and roll (if only one tilts) control. Furthermore, the back rotors can also be used for pitching if necessary. Overall, there are a multitude of ways to control the drone if the control surfaces fail, therefore the impact is reduced to low.

13.2.5. Control, navigation and guidance

NC1- CPU Crash   *"The central processing unit (CPU) is responsible for communicating with the operator and translating their inputs to system commands. Alternatively, if the drone is autonomous, the CPU controls the drone on its own. In both scenarios, it is the brain of the system. Therefore, malfunction in this element leads in the worst case to a crash of the drone, so a very high impact. Since the code for the CPU will probably be in the order of hundreds of lines, it is certain that a few programming errors will slip through even after code verification. However, errors big enough to cause a crash are much less likely to go unnoticed, and so the overall probability for this risk is only moderate."*

Mitigation of NC1:   A watchdog timer can be implemented with the CPU. This timer will get constantly reset by the CPU during normal operation. However, when the CPU crashes, the watchdog timer will time out and force a hard refresh of the processor. This will restore functionality. Hence a watchdog timer reduces the impact to low, as the drone becomes uncontrollable only for a brief time.

NC2- Communication Failure   *"There are many ways for the drone to lose contact with its operator- interference with other signals, hardware and software malfunctions on the operator side. These are common issues so the probability is very high. [...] If the drone is autonomous (scenario NC2-AUTO), it resumes its mission and only stops transmitting data for a while. Hence, the impact is low."*

Mitigation of NC2:   This risk already has a low impact. However, its probability can be reduced to high if an algorithm is implemented on the drone that makes it fly below the clouds when communication gets interrupted. This will solve a significant portion of the communication issues.

13.2.6. Structure

S1- Structural failure   Flying in all-weather conditions may face the drone with loads its structure cannot sustain. This will likely result in the wing breaking off, as it is the most highly loaded component. The impact of this is very high, as the drone will certainly crash without its wing, on which 2 of its rotors are also placed. This is an event that is expected to happen once in a lifetime, so it has a moderate probability.

Mitigation of S1:   This issue was anticipated during the design process. The structure was designed in such a way that it is able to carry loads 1.5 times higher than what it is expected to encounter during its lifetime. Because of this, the probability of this risk is reduced to very low.

S2- Payload Holding Mechanism Failure   *"This risk is highly dependent on the design chosen for the payload bay, which in turn is connected to the self-loading/unloading requirement. This requirement encourages a design in which the payload is easy to detach from the drone, as otherwise self-unloading becomes too complicated. However, easy detachment means that there is a moderate probability for the payload to come loose on its own. The loss of the payload is a risk with a high impact, because the drone itself is unaffected."*

Mitigation of S2:   The sliding pin mechanism used in the loading/unloading mechanism can have 2 pins that hold the payload. In that case, if one fails, the payload will still hold on to the other and not drop out from the drone. This reduces the probability of the payload detaching to low.

S3- Lightning Strike   *"The drone is meant to fly in all-weather conditions and thunderstorms are a relatively frequent occurrence. As most other flying objects are down on the ground in such weather, the drone will probably be the highest object in its vicinity. This means that the probability of lightning strike is very high. It has a catastrophic impact because it can easily detonate the tank."*

Mitigation of S3:   By adding aluminium fibers inside the composite at areas threatened by lightning strike (such as the tank), the drone's local conductivity can be drastically improved. Since the source of lightning damage is poor conductivity [16], this protects the vulnerable elements of the drone from direct damage. Therefore, the impact of lightning strike is reduced to very low.

13.3. General Mitigation Strategy for Unexpected Landings

It can be seen that a lot of the risks, even in the mitigated case, end with the drone landing somewhere else than its destination. This means that the hospital has not received resources, corresponding to a mission failure and a high impact. Since this scenario is so common, a protocol has been developed to further mitigate the impact of such risks. In the case of a landing away from the destination, a team will be dispatched to the location of the drone to pick it up and deliver it to the final destination. This further reduces the impact to low, as the mission concludes successfully, though with a delay. This mitigation strategy can be applied to risks H2, P11, P1X, P2 and SC3 in addition to their existing mitigation strategies. For risk H1, it acts as an alternative to its mitigation strategy.

13.4. Risk Maps

With all risks identified and their mitigation strategies developed, risk maps can be created to visualise them. Each risk is shown pre- and post-mitigation, with Figure 13.1 showing the production risks and Figure 13.2 showing the operational risks.
Three different categories are defined for the risks. The red sector represents unacceptable risks. They pose a great danger to the drone and mitigating them is a priority for the design. Yellow marks the watchlist risks. They are less dangerous, so they are only to be mitigated if the rest of the design allows it. Finally, the green portion of the graph is the section of the negligible risks, which are not harmful and do not require mitigation.

The risk maps show each risk twice. The regular one shows the risk's probability and impact before mitigation, while the italic and underscored one shows them after mitigation. Note that the general mitigation strategy for unexpected landings is not accounted for in Figure 13.2. This is in order to identify how necessary it is. By inspecting the risk map, it can be seen that it is mandatory, as otherwise risk SC3 remains unacceptable also post-mitigation. Therefore, this strategy will be adopted by the drone project.

Impact ↑	Very low	Low	Moderate	High	Imminent
Severe					AS2
High		AS1			
Moderate		PM1			
Low		*PM3*	PM3		PM2
Very low		*PM1*, *AS1*			*PM2*, *AS2*

Figure 13.1: Production risk map

Impact ↑ Probability→	Very low	Low	Moderate	High	Very nigh	Imminent
Catastrophic	*P2*		H3,P2		S3	
Very high	*SC2*,*S1*		NC1,S1	P4	SC3	
High	*P1X*	*H2*,*H3*, *S2*,P1X	H1,S2 SC1	H2,H4, P3	*SC3*	
Moderate	*P11*			A1,P11		
Low	*SC1*	*H4*	*H1*,*SC4*, *NC1*,SC4	*A1*,*NC2*, *P4*	NC2	
Very low				*P3*	*S3*	

Figure 13.2: Operation risk map

14

Operations and Logistic Concept

HEALR should be able to transport medical goods from hospital to hospital. There is a lot of logistics involved in this process. First, both an operations plan and a logistics plan are developed. These are shown and explained in section 14.1 and section 14.2. Then, a RAMS (reliability, availability, maintainability and safety) analysis is performed in section 14.3. Finally, the production of the drone is discussed in section 14.4.

14.1. Operations Plan

In order to make the drone available to as many hospitals as possible, a logistical concept for the operations of the drone is developed. This concept aims at providing this at the lowest possible cost, as well as minimal training involved for hospitals. For this, the drones are controlled from central control rooms, which can also monitor the performance and state of the drones. As there are many different connections these drones have to serve, it is not feasible for every hospital to operate their own drone. Furthermore, many hospitals will only need a drone a few times a week or month and thus cannot justify to buy a single drone for this. For these reasons, a network with drone airports is the most feasible option. A typical drone operation would consist of a flight to the first hospital to pick up the payload. It is then transported to the receiving hospital from where the drone would return to its base of operations where it can be refueled. Furthermore, these drone ports can be used to extend the range of drones for longer transports. Facilities, which send many payloads every day like blood banks can also operate their own drone port, which will speed up their operations. A visualization of this process is shown in Figure 14.1. It is good to note that the "logistics centre" mentioned in Figure 14.1 is something that actually already exists. An example would be "Eurotransplant"[1]. In the example of Eurotransplant, there is already dealt with the logistics between donating and receiving hospitals. The only thing different is that now they call the dispatch centre to inform them where and when the drone has to fly. Lastly it is also good to note that the production and delivery of the hydrogen is going to be outsourced to a third party [63].

14.2. Logistics Plan

Flight Plan

Before the drone departures the flight route is chosen and communicated with ATC. These flight routes are already pre-defined and made for transport between all hospitals. The flight plans are approved according to the EASA regulations, which means that the mission can be executed at any time and frequency desired [14]. These flight paths have to be as much removed from populated area as possible. Furthermore, due to noise, the flight paths have to conform to the guidelines about minimizing the nuisances to people and animals.

In the case of a mission failure the drone will send a signal to be able to be located. Another case when a drone arrives at the end of life stage is when it has reached its maximum amount of life cycles. In the case of end of life the drone is disposed, when disposing the drone it is important to do this in a sustainable manner. The end of life sustainability is elaborated upon in chapter 15.

Regulations

The regulations regarding drone use are renewed by EASA and were initially planned to become active in July 2020 [14], but will probably be postponed due to the corona crisis. Nevertheless, this regulations were taken into account for the design of the drone and the flight plan. As explained in the Baseline Report, there are three different

---
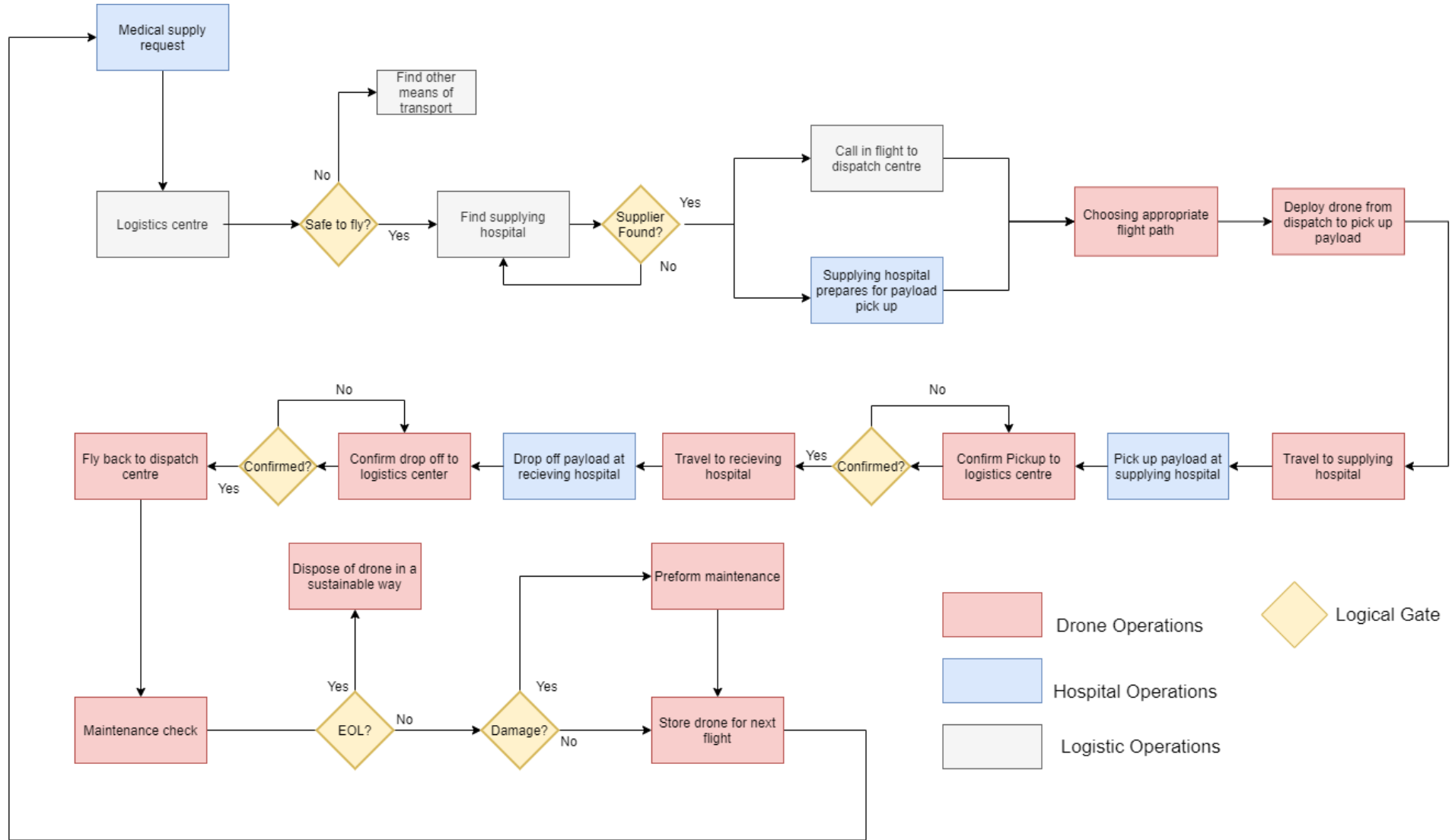
[1]https://www.eurotransplant.org/

Figure 14.1: Operational Flow

risk-based categories the drone could be in: open, specific and certified [62]. Since the drone operates BVLOS it is in either the specific or certified category. It is essential for the drone that it falls within the second (specific) category. That is because the certified category is for high risk drones that have an equivalent risk of a manned aircraft flying over dense populated areas. Due to this high risk, the drone would have to go through strict safety and reliability procedures. The gain and profit of the use of the drone do not weigh up to the time and cost consumed by these procedures.

There are certain rules that distinct the specific of the certified category for UAV's. According to Article 40 Regulation (EU) 2019/945 and Article 6 of UAS regulation 2019/947[[4], page 8]:

"

- Flying over assemblies of people with a UAS that has a characteristic dimension of less than 3 m may be in the 'specific' category unless the risk assessment concludes that it is in the 'certified' category.
- The transport of dangerous goods is in the 'certified' category if the payload is not in a crash-protected container, such that there is a high risk for third parties in the case of an accident.

"

It is thus clear that the drone should have a characteristic dimension of less than 3 [m]. The actual characteristic dimension is 2.98 [m], so the requirement is met. Next to that, the goods should be in a crash-protected container if they are dangerous. The medical drone will be transporting organs and blood packages for organ transplantation. These are only considered dangerous if it contains unchecked blood according to the International Air Transport Association. However, the blood samples come from a hospital and are meant for transfusion, which is always checked blood [2]. This means that the blood (same for organs) is not regarded as a dangerous good (IATA exception 3.6.2.2.3.7 [3]). Therefore there are no crash-protected containers necessary to comply with the specific category. Then there is the case of the hydrogen tanks. This is a relatively new concept for commercial drones and it is not mentioned in the new EASA rules. The risk from using the hydrogen tanks needs to be as low as possible. In order to confirm that the total risk is low enough for the specific category, the Specific Operations Risk Assessment needs to be performed [4][35]. This risk assessment covers all posible risk and the measures to mitigate them. The conclusion determines the relative risk category of the drone. This is something to do in future development of the drone in order to validate the placement in the specific category.

14.3. Reliability, Availability, Maintainability and Safety

The RAMS analysis is used to give a overview of the Reliability, Availability , Maintainability and safety of the Drone. In this chapter each of these subjects will be analyzed further.

Reliability & Safety

When looking at the reliability of the drone, the main method of ensuring reliability is by applying redundancy in all subsystems where possible. This redundancy ensures that in case of a system failure the drone can still function. Where applicable for each subsystem an example of redundancy will be elaborated on in the next section. Furthermore, the safety of the drone is analyzed for systems that don't have the necessary redundancy.

Stability and Control   In the subsystem stability and control redundancy is applied in many situations. An example is that the vertical tail has been sized for a situation where one engine is inoperative, this results in the fact that the drone can function normally when an engine fails. This can be seen as a form of redundancy. Furthermore, if a control surface fails there is also a form of redundancy, namely the rotors. The rotors can ensure control in all axes, although it is not as efficient it does introduce redundancy for the control of the drone. Lastly, each control surface has an extra servo to ensure redundancy.

Hydrogen subsystem   For the Hydrogen subsystem there are two main parts, namely the fuel cell and the hydrogen fuel. For the calculation of the fuel amount it was assumed that the drone flies with a 10 m/s headwind at all times, this means that there is a form of redundancy since flying with a constant headwind is highly unlikely. On top of that each motor is connected to two fuel cells, this means that in the case that a fuel cell fails there is always one that

---

[2] https://www.cdc.gov/bloodsafety/index.html

[3] https://www.iata.org/contentassets/b08040a138dc4442a4f066e6fb99fe2a/dgr-61-en-3.6.2.pdf

still provides power to the motor. Although the performance does decrease since there is less power the drone is still able to fly, just not at optimum conditions. These are two examples of how redundancy is applied in the Hydrogen subsystem.

Propulsion Subsystem   For the propulsion subsystem the motors used are to be acquired from a third party, these motors are known for their reliability and resistance to corrosion (see chapter 7). Furthermore the propulsion system also has the redundancy linked to the fuel cells mentioned earlier. As regards to safety, if the drone experiences a critical PCU failure there is a back up PCU, this PCU wont be able to fully replace the failed PCU but it will ensure that there is still enough power provided to the motors to provide a "controlled" crash landing.

Structures & Aerodynamics   These subsystems do not have a specific redundancy applied to them, all calculations have been performed with uncertainties and safety factors to ensure reliability during the mission. Therefore, when designing these subsystems safety factors are used to ensure that the drone can perform in case of unforeseen loads and circumstances. Furthermore, the structure surrounding the payload is reinforced in case of a high impact or crash, this is to preserve the payload.

Availability
When looking at the availability there are two parts that can be discussed. The availability of the technology and materials used within the drone and the availability for the use of the drone

Technological availability   In general the technology used in the drone is mostly standard and highly available, certain hardware and software are acquired from third parties which also implies a level of availability. The fuel cells are more interesting to look at, although the necessary fuel cells currently are available to be acquired from a third party, it could be important to note that the current development of these fuel cells is very rapid. Meaning that the technology is going to improve, this technology is not currently available but is expected to be so in the near future.

Drone Availability   Once the drone is fully functioning it can be used as soon as requested. The drones are all located in a "drone airport" (further explained in chapter 14). When the drone is needed it can be used as soon as possible. Furthermore, since the drone operates in all weather conditions (99% of all days), it is also available for 99% of the time. Finally, if all hospitals acquire one or more drones, they can be used multiple times a day since the flight duration is no longer than 2.29 hours. This results in a high availability of the drone

Maintainability
Maintenance is something that influences the availability and safety of the drone. It is desired that the drone goes through as little maintenance as possible but still ensuring the safety and reliability of the drone. The less the drone experiences maintenance the higher its availability. The maintenance and maintenance checks can be divided in 3 situations, pre-flight checks, post flight checks and periodic checks. If there is significant damage on the drone, maintenance is performed. In order to minimise the time to repair, a maintenance center is present within the drone airport. This ties in with the general theme of centralizing the operations of the drone.

Pre flight and Post flight checks   These checks are performed to find any surface damage as well as obvious damages or malfunctions. Before and after every flight the drone is checked by the operator. If there is nothing to report the drone is stored until its next flight. In the case of damage the drone is taken to the maintenance center of the "drone airport" where the necessary repairs are performed.

Periodic checks   Periodic checks are maintenance checks that are performed regardless if there is any damage seen or reported. The periodic check is performed every 10 flight hours as stated in the Baseline Report[62], here the drone is thoroughly checked internally and externally. Here the sensors are also checked to see if everything is still performing as desired.

14.4. Production Plan
Figure 14.2 shows the top level steps that need to be taken to actually produce the drone. The blue boxes show the first level, while in the following diagrams (Figure 14.3 and Figure 14.4) the orange boxes show the second level and the yellow boxes show the third level. First, all the components have to be made or bought. Then the three different groups of the drone need to be assembled and constructed: the wing, empennage and fuselage groups. This can be done in parallel, as the assembly of these groups does not depend on each other. Thereafter, the empennage will be

connected to the fuselage before the wing group is connected to the fuselage. This order is chosen, as the ducted propellers are very delicate and should be mounted onto the fuselage as late as possible. This production plan will not go into detail on the bolts, rivets and screws. The drone is not designed in enough detail yet to know what kind of and how much fasteners are needed. Therefore, this production plan only discusses the production of the main components.

The fuselage frames, wing structures, ducted propellers, tank and empennage are manufactured. The rest of the components, like the fuel cells, batteries, motors and wiring, are bought. This can all be bought in parallel, hence no diagram of this process is made. In Figure 14.3 the manufacturing of the components can be seen. Three types of materials are used: flax fiber composite, polyurethane foam and aluminium. All of these have their own manufacturing process. The flax fiber composite will be manufactured by injection moulding. Therefore, several moulds need to be made beforehand. Then, the injection moulding of all different parts can be done at the same time. Also, at the same time, the polyurethane foam is cut into the correct shape. This will be used in between two flax fiber composite layers in the ducts. It needs to be a thin layer, so this cutting needs to be done precisely. The aluminium part of the tank will be rubber formed as it has both a single-curved part as a double-curved part. Now that all parts are manufactured, a check needs to be performed on these parts. This is not shown in the diagram, but is done before the assembly of the groups. Blocks 1.8, 1.13 and 1.14 are done in order to make sure all the parts that are needed for a specific group are assembled together, such that the construction of the respective groups (blocks 3.0, 4.0 and 5.0 in Figure 14.2) can be started right away.
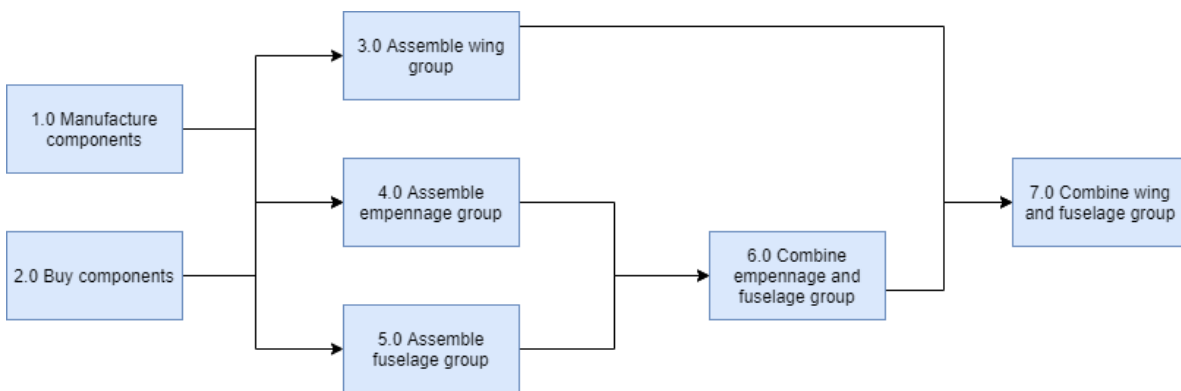

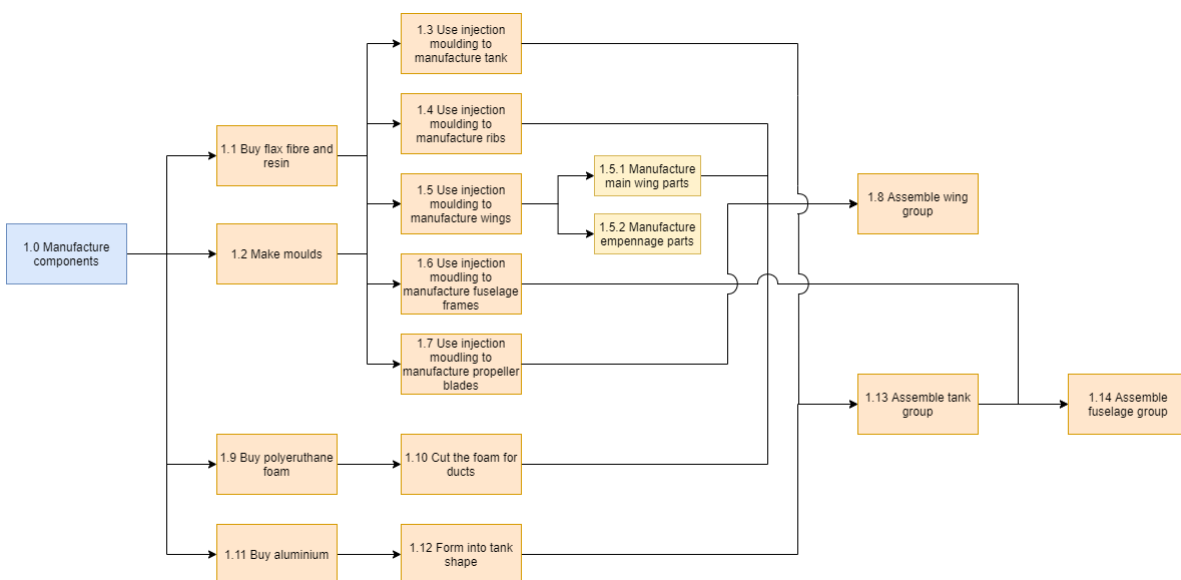Figure 14.2: Top level of the production plan diagram

Figure 14.3: Manufacturing the different parts

The assembly of all three groups is shown in Figure 14.4. First, the base structures for all three groups is constructed. For the wing group this consists of connecting all the ribs and the rectangular wing box to each other. Then, the

wiring used to connect the motor of the propellers to the power control unit is added. Then, the structure for the aileron is added. The aileron needs to be controlled, so the wiring to the actuators needs to be added. Now, the motor mounts can be mounted on the ducts. This is done as the last part, as this can be very delicate. Finally, the wing skin can be added. The wing skin consists of two parts: the top and the bottom part. The same sequence is used for the empennage group. First, the wing boxes and their ribs are connected to each other, then the control surfaces (rudder and elevator) are added and connected. Now, the horizontal and the vertical tail construction can be connected to each other. As the fuel tank will be used as tail arm, a robust connection from the tail surfaces to the fuel tank need to be made. Finally, the skin is added.

The assembly of the fuselage group consists of a lot of wiring. First, however, the base needs to be constructed and a connection to the fuel tank needs to be added. Then, all the electronics need to be considered. The power control unit (PCU) is the center. The fuel cells and battery need wiring to the PCU and the PCU has to be connected to the motors. Also, the fuel tank needs to be connected to the fuel cells. After this has been carefully done, the fuselage skin can be added, including the extra material on the belly to on which the drone will be landed.
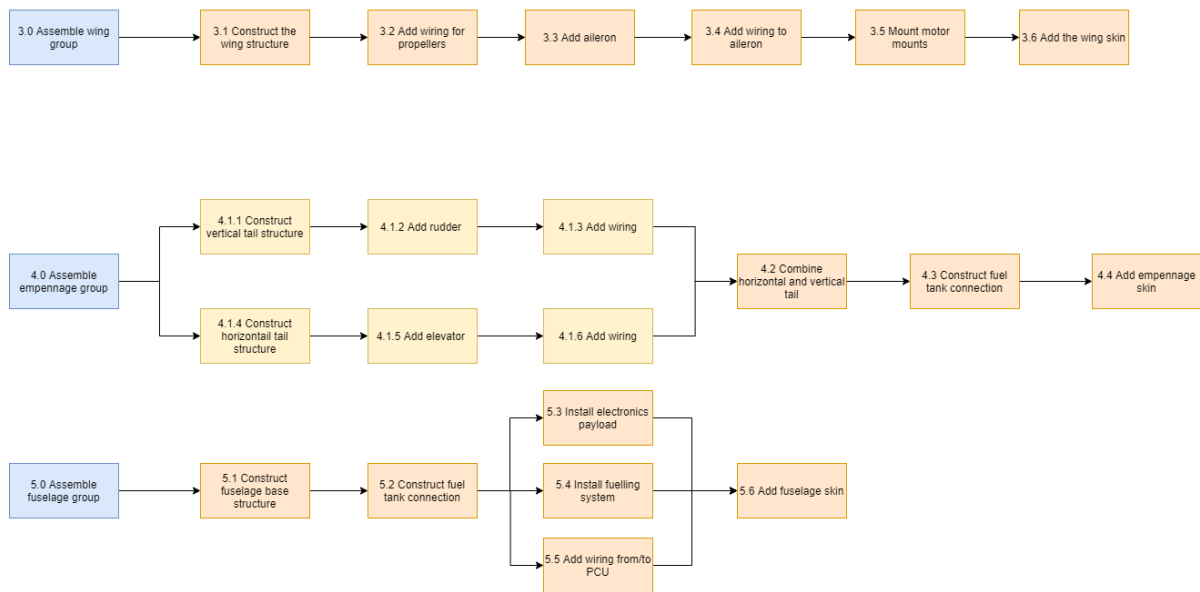

Figure 14.4: Second part of the production plan

The connection of all three groups is shown in Figure 14.5. The fuel tank is the connection between the empennage and the fuselage, so the fuel tank needs to be connected to both of these groups. Then, some wiring is needed from the control surfaces on the empennage to the controller in the fuselage. Finally, the wing group can be connected to the fuselage group. In this process, it is important that the motors are connected to the PCU.
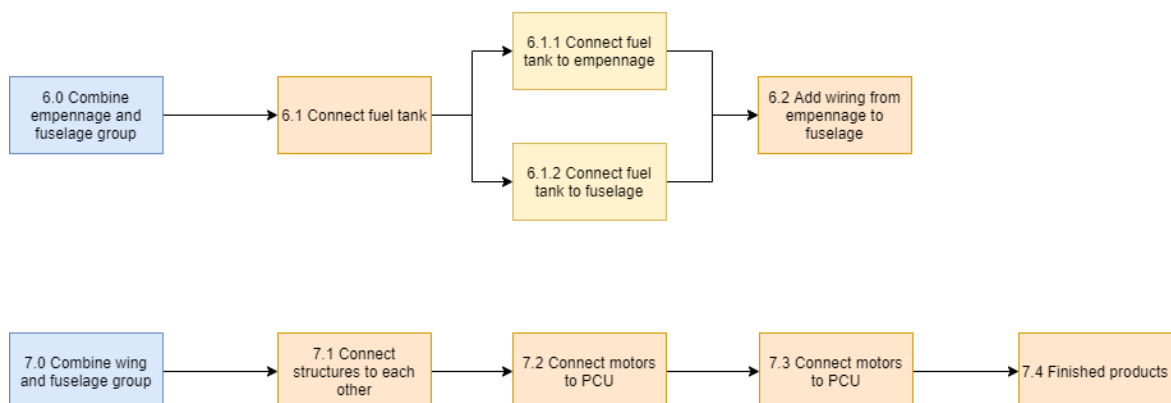

Figure 14.5: Second part of the production plan

15

Sustainability Development Strategy

A sustainable development is development that meets the needs of the present without compromising the ability of future generations to meet their own needs [41]. In the Baseline Report [62] the criteria with regards to this definition have been defined. In this chapter, the environmental sustainability criteria are elaborated. These include use of renewable energy, (toxic) emissions, recyclability, and responsible consumption. Furthermore since the drone needs to comply with MD-SYS18, the noise produced is also taken into account, which is more related to social sustainability. This chapter addresses the way sustainability is taken into account in the design by looking at each individual subsystem design and the design decisions that have been made based on the sustainability criteria that resulted in the current design. This can be found in section 15.1. Furthermore, the way and to what extent the drone contributes to sustainability is assessed in a life cycle assessment in section 15.2. Then in section 15.3 the drone requirements with regards to sustainability are analyzed followed by a recommendation chapter in section 15.4.

15.1. Subsystem Design

Besides designing for a drone to be as light as possible in order to save fuel consumption, each subsystem design has been designed with the sustainability criteria in mind. For each subsystem design choices have been made based upon making the drone circular and as sustainable as possible. These are based on the criteria set up in the Baseline Report [62].

Aerodynamics

In order to save fuel consumption, the L/D ratio is maximized as much as possible. An efficient aerodynamic design enhances the drag reduction, and thus saves unnecessary fuel consumption. This has been achieved by choosing the most suitable airfoil for the mission with its corresponding wing lay-out and low drag fuselage design. Furthermore, the rotors has been designed such that during both cruise and hover the least energy is required due to rotor pitch angle optimization for each flight phase.

Hydrogen

For the hydrogen subsystem, it is important to touch upon the sustainability of the hydrogen production, the fuel cells, batteries and the tank material.

For the hydrogen production, the energy that is used to make the hydrogen in the fueling station should be obtained in a renewable way. A possible way would be by means of electrolysis. Electrolysis uses an electric current that splits water into hydrogen and oxygen. When the energy that is used is renewable, thus for example wind- or solar- energy, there will be no emissions during the production of the hydrogen [1]. Another method that could be considered is the use of a reverse fuel cell.

The fuel cell produces water vapour as an output. Water vapour is an important greenhouse gas. Therefore, it is not sustainable to let the water vapour enter the environment. When the water vapour is condensated to small drops of water, it is no longer considered to be a greenhouse gas and thus can enter the air.

Next, the choice of insulation material of the tank will be discussed. Choosing MLI as the method of insulation reduces or even eliminates the use to adhesives, which improves recyclability. Also, the chosen *Lydall CRS Wrap*

---

[1] `https://www.energy.gov/eere/fuelcells/hydrogen-production-photoelectrochemical-water-splitting`

1303B is more environmental friendly than the average MLI insulation materials (or its original *CRS Wrap*), as it made from bio-soluble micro fiberglass, instead of carcinogenic fiberglass particles of respirable size. The chosen variant also does not require any personal protective equipment and has no particular hazard or precautionary statements, nor does it have any restrictions for disposal that have to be taken into account, unlike the original version [2].

The fuel cell is made of multiple materials. This includes metals, plastics, and composites. This makes it hard to recycle or dispose, as all of these materials have their own recycling process. As the specific information of the materials in the fuel cell of Intelligent Energy is confidential, it cannot be precisely determined how the recycling of the fuel cell can be done. However, Pieter Lantermans - who was interviewed during the design of the hydrogen subsystem, as mentioned in chapter 6- said that this is something that the company is looking into. Hence, it is expected that the recycling of such a fuel cell will be possible in the future.

For the batteries, it is assumed that lithium polymer (LiPo) batteries (or lithium-ion polymer) are supplied from the fuel cell manufacturer. Compared to the (liquid, non-polymer electrolyte) lithium-ion batteries, these are not that different. The most notable characteristics are that LiPo-batteries are able to have slightly higher specific energies[3]. Furthermore, it provides more possibilities regarding battery geometry/casing and LiPo batteries also have better performance in colder environments (below freezing point), all of which are advantages [3].

Propulsion

Noise is an important parameter in the sustainable design approach for aircraft. Aircraft noise has a significant effect on environment and people, which is why it has to be minimized as much as possible. This is also required by the EASA rules as to minimize the nuisances to people and animals [14].

Extensive noise calculations are extremely complicated and time consuming. Furthermore, there are no simple noise tools for a UAV of a comparable size or with ducted propellers. A very rough first estimate was performed to get a general idea of the noise production. More accurate estimations are beyond the scope of this project.

The propeller noise is estimated with Equation 15.1, which is based on experimental data [43].

$$SPL_{1,max} = 83.4 + 15.3 \cdot log(P_{br}) - 20 \cdot log(D) + 38.5 \cdot M_t - 3 \cdot (B-2) + 10 \cdot log(N_p) \tag{15.1}$$

$SPL_{1,max}$ is the sound pressure level in $[dB]$ at 1 $[m]$ from the source in the direction where it is maximal. P_{br} is the engine power in $[kW]$, B is the number of blades, N_p the number of propellers and M_t the tip mach number. For VTOL, the proprotors have a M_t of 0.113 according to the JBLADE program in chapter 5. The power used is 3.7 $[kW]$, with 2 blades and 2 propellers with 0.37 $[m]$ radius. This gives $SPL_{1,max} = 102.07$ $[dB]$. The back rotors have a radius of 0.135 $[m]$, a M_t of 0.073, 3 blades and 2 propellers using 1 $[kW]$ of power. This gives $SPL_{1,max} = 97.60$ $[dB]$. During cruise, only the proprotors are spinning. The M_t then is 0.083 with a power consumption of 4 $[kW]$, which yields $SPL_{1,max} = 101.43$ $[dB]$ As a rule of thumb, the noise reduces by 6 $[dB]$ by doubling the distance. Since this is at 1 meter from the source and the drone flies at 200 meter, the noise is reduced by at least 7*6=42 $[dB]$ (128 meter). This yields a noise of about 59.43 $[dB]$ for the ground level.

During cruise the drone is at a 200 $[m]$ altitude, which means the SPL is lower at the ground. Thus, the biggest noise problem is during VTOL. A noise level of over 100 $[dB]$ corresponds to the noise produced of a heavy truck or chipping hammer [43]. Since the drone has to land at hospitals in populated area, the noise should be as limited as possible. Even though there are no strict rules set by EASA for this drone category as of now, the noise levels need further attention in future stages of the design. The effect of the duct should also be analysed, which is a complicated aspect. Ducts do not necessarily reduce the noise of a propeller [43]. It should be noted that the calculated SPL's are not very accurate, as it is a simple formula based on statistics of larger propeller aircraft.

Stability and control

During cruise, control surfaces are used to control and passively stabilize the drone both longitudinally and laterally. The advantage of making use of these control surfaces over the use of differential thrust from the engines for control, is to save fuel. Power would only be needed for the deflection of the surfaces, but this requires far less energy compared to increasing or adjusting engine thrust. Furthermore, the horizontal and vertical tail are designed such

---

[2]https://www.lydallpm.com/products/low-temperature-insulation/crs-wrap-super-insulating-media/
safety-data-sheets/

[3]https://batteryuniversity.com/learn/article/the_li_polymer_battery_substance_or_hype

that it provides passive stability during cruise. This means that no active stability enhancement systems are required which safes energy and resources.

Structures

The choice of the materials used for the structure of the drone has a great influence on the sustainability of the drone and hence has been taken carefully into consideration during design. For the structures subsystem, the impact of the material selected and manufacturing process both need to be considered. The subsystem performs very well in both of these criteria. The composite used for most of the structure is a flax fiber composite with cellulose propionate (CP) resin. Both of these materials have little to no impact on the environment. The resin is a product of cellulose, meaning that it is bio-degradable and eco-friendly. Flax fibers are obtained from the linseed plant. Since more CO_2 is absorbed by the plant while it grows than is released during its processing, this material has a negative global warming indicator and acts as a form of carbon sequestration [32].

The process used to create the composite is injection moulding, which is a process that creates little to no waste. It also allows more complicated geometries, which limits the use of assembling tools on the structure, which further reduces the resources used.

15.2. Life Cycle Assessment

In the life cycle assessment (LCA) each phase in the lifetime of the drone is treated in order to show the way that the product contributes to sustainability and on which aspects it could be improved on. A systematic way to analyze the impact of the product on the environment throughout its life-cycle is to construct a so-called EcoDesign strategy wheel [4]. For the assessment the product is assumed to be a system. The environmental impacts of the drone are measured by considering the following aspects: use of materials (inputs), energy consumption (inputs) and (toxic) emissions (outputs). The life cycle has been divided into the following phases:

- Acquiring and consumption of materials

- Manufacturing techniques

- Operations and durability

- End of life (EoL)

The 'EcoDesign strategy wheel' visualizes strong and weak points of the drone with regards to environmental impact. This allows to show the extent to which the system contributes to sustainability and, if applicable, select suitable strategies to make the design even more sustainable in the future. Each dimension on the wheel represents a life cycle phase as defined above. For each phase the drone is assigned a score. In order to assign a score, an ordinal scale which ranges from 1 (lowest score) to 5 (highest score) are defined. With the scores defined, it is possible to discuss and analyze each life phase and assign a corresponding score to the drone. Note that with the emissions of CO_2 a positive global warming indicator is meant (thus producing more CO_2 than it is consumed in the complete process).

Acquiring and consumption of materials

- Score 1: The materials are not recyclable, toxic, and originate from non renewable sources. Harvesting and processing the materials require much energy and result in high CO_2 emissions.

- Score 2: The materials are somewhat recyclable, but toxic, and mostly originate from non renewable sources. Harvesting and processing the materials require an intermediate amount of energy and result in intermediate CO_2 emissions.

- Score 3: The materials/components are partly recyclable, non toxic, and partly originate from renewable sources. Harvesting and processing the materials require an intermediate amount of energy and result in intermediate CO_2 emissions.

- Score 4: The materials are mostly recyclable, non toxic, and partly originate from renewable sources. Harvesting and processing the materials require a intermediate amount of energy and result in low CO_2 emissions.

- Score 5: The materials are fully recyclable, non toxic, and fully originate from renewable sources. Harvesting and processing the materials require a low amount of energy and result in no CO_2 emissions (neutral or CO_2 negative contributor).

---

[4] `http://wikid.io.tudelft.nl/WikID/index.php/EcoDesign_strategy_wheel`

As explained in the previous section, flax fiber composites have a low environmental impact. The energy to produce raw material is much lower than of carbon or glass fiber. For the production, flax is mostly used as a shifting crop and no water is needed for extraction of the fibers [5]. The production of flax fibers, more CO_2 is absorbed by the plant than is released during its processing, making it a CO_2 negative contributor. Furthermore, the cellulose propionate resin is a product of cellulose, meaning that it is bio-degradable and eco-friendly. On top of this, it is possible to remelt the composite if no epoxy matrix is used, and hence can be used again in the injection moulding process. Flax fiber composites get a score 5 due to its recyclability, non toxicity and CO_2 negative contribution.

The fuel tank is made from aluminum. Aluminum is widely recycled which has the advantage that it is less energy intensive than creating new aluminum. Hence opting for a high use, or even complete use of recycled aluminum is more energy efficient, reducing its negative environmental footprint. Recycled aluminum receives a score of 4 due to its high recyclability, non-toxicity but low CO_2 emissions.

For the insulation of the tank, insulation material is used which consists of aluminum foil and bio-soluble microfiber glass. This material does not need any adhesive or adherent. Since the microfiber glass is bio-soluble and aluminum foil is used which can be recycled, the insulation material gets a score of 4.

Inside the structure of the ducts, polyurethane foam is used. The production of polyurethane foam results in CO_2 emissions and makes use of gases as blowing agent for the foam. The ones mostly used nowadays have a high global warming potential and remain in the atmosphere for a long time. However, these gases will be banned by 2023 and new techniques are developed which have a low global warming potential and are harmless to the ozone layer. Furthermore, technologies exist for the production of polyurethane from recycled material, hence for the selection of the polyurethane it is important to select a company which produces polyurethane from recycled materials. On top of this, polyurethane foam is used only for a small amount (less than a kilo) per drone. Polyurethane foam cannot be fully recycled. Part of it can be treated such that new raw material can be obtained for new production of polyurethane, the other non recyclable part cannot be used. Polyurethane scores a 2 due to the toxic emissions from the blowing agent and its low recyclability. If recycled material and non toxic blowing agents are used in the future, the score increases to 3.

The materials used for the construction of the batteries that are delivered with the fuel cells, include toxic chemicals to process the lithium (if LiPo batteries are used) and come from non-renewable sources. Taken into account that the provider of the fuel cells (and thus the batteries) does not use recycled materials for the construction of the batteries and fuel cells, at most a score of 2 can be assigned.

To conclude, since most parts of the drone will be made from flax fibers, around 10% aluminum and less than 1% polyurethane, for the material usage on average the drone scores around 4. But taken into account the materials necessary for the production of the batteries and fuel cells, the score of the drone results in an average of 3.5 [6].

Manufacturing Techniques
- Score 1: The manufacturing techniques used have a low efficiency, produce a high amount of non-recyclable waste, have a high energy consumption and make use of toxic lubricants, degreasers, or contaminants.

- Score 2: The manufacturing techniques used have a low efficiency, produce intermediate amount of non-recyclable waste, have a high energy consumption and make use of toxic lubricants, degreasers, or contaminants.

- Score 3: The manufacturing techniques used have an intermediate efficiency, produce a low amount of non-recyclable waste, have an intermediate energy consumption and do not make use of toxic lubricants, degreasers, or contaminants.

- Score 4: The manufacturing techniques used have an high efficiency, produce no or only recyclable waste, have an intermediate energy consumption and do not make use of toxic lubricants, degreasers, or contaminants.

---

[5] https://www.materialstoday.com/composite-processing/features/the-renaissance-of-flax-fibers/

[6] For the LCA, only the components of which the drone mainly consists of are taken into account. These include; the structure made out of flax fiber composite, the fuel cells and batteries, the aluminum tank and insulation and the foam for the ducts. The remaining components, for example; the cables, computer components, fasteners, etc. make up only 5-10% of the complete drone. Also, these components have a lifetime over 10 years, and thus are not per see the critical components in the assessment.

- Score 5: The manufacturing techniques used have a high efficiency, produce no or only recyclable waste, have a low energy consumption and do not make use of toxic lubricants, degreasers, or contaminants.

For part production of the drone, the following methods are used: injection moulding, cutting tools, and rubber forming. Injection moulding results in little to no waste. In order to make the resin flow, the material needs to be heated. Heating from the outside is not effective due to low heat conductivity of the composite. A common method for heating up the resin in order to make it flow is to provide the resin in granulate form. As a result of the rotating screw, the granulates compress each other and shear, which generates heat and results in a uniform heating method [58]. Power is required for rotating the screw and for applying pressure to the mould clamps (depending on the size of the mould). Furthermore, since most parts of the drone are produced from injection moulding, many moulds need to be constructed. If permanent moulds are used, they can be re-used and multiple parts can be obtained from the same mould. This increases its efficiency. Permanent moulds are expensive, thus if only a limited amount of drones are produced, it is better to use perishable moulds (for example lost wax casting). This, however, is less efficient. Furthermore injection moulding does not make use of any toxic fluids and hence it gets assigned a score of 4.

The polyurethane foam is cut via cutting machines. The machines itself do not require much energy, due to the low density of the foam. As a result, however, it is possible that some pieces of foam are cut off and not used, which is considered as non recyclable waste. It is therefore important when cutting the foam, all pieces of foam will be used in the product. Due to the possible waste the procedure is assigned a score of 3.

Another production technique is rubber forming, which is used for production of the tank. Rubber forming is widely used due to its low cost and efficiency. Many parts can be compressed at once. The same as in injection moulding, only one rigid die is needed to produce multiple of the same parts. However, high press forces and hence large machines are usually required. Also the soft tool that comes into contact with the material wears out over time but can be replaced. Rubber forming gets a score of 4.

For assembling, friction stir welding is used for the bonding of composite to composite and metal to metal. An advantage of friction stir welding is that the materials do not need to be heated, hence no flumes are generated. Furthermore it is energy efficient, but clamping forces are needed [58]. Hence a score of 4 is given.

To conclude, the largest contribution in part manufacturing technique is injection moulding and for assembling the friction stir welding. The cutting of the polyurethane is only a small part but attention should be paid that the waste should be limited. Hence a score of 3.8 for the manufacturing techniques has been found.

Operations and Durability
- Score 1: During operation there is an extreme amount of CO_2 emissions, the product is short-lived and not maintainable.

- Score 2: During operation there is a high amount of CO_2 emissions, the product has a low durability and low maintainability.

- Score 3: During operation there is an intermediate amount of CO_2 emissions, the product has a intermediate durability and low maintainability.

- Score 4: During operation there is a low amount of CO_2 emissions, the product has a intermediate durability and intermediate maintainability.

- Score 5: During operation there are no CO_2 emissions, the product has a high durability and high maintainability.

The operations and durability have three different aspects. These are green house gas emissions, the durability and the maintainability. The final grade of the phase is the weighted average of the three different aspects. The drone operates on hydrogen as fuel. Consequently, there are no CO_2 emissions during flight and the respective score for emissions is a 5.

Most of the structure consists of the flax fiber composite. Composites have a good life span and require less maintenance than competing materials [7]. Next to that, polyurethane and aluminum are used as well. Polyurethane

---

[7] http://compositeslab.com/

is very durable and can easily last for 15 years [8]. Aluminum is a durable material as well, due to its long lifetime and natural corrosion resistance. Furthermore, the fuel cells that are available on the market right now are used for only about 1000 flight hours (see chapter 6). This is not very durable but the expectation is that these fuel cells will drastically improve over the next few years, as they have done over the past years. The question then arises if only the fuel cells should be replaced after 1000 flight hours or the entire drone, because the fuel cells are by far the most expensive parts anyway. Due to the lack of durability of the fuel cells at this point in time, the drone scores a 3 for durability as of now. The batteries that come with the fuel cell, on the other hand, do not need to be replaced after those flight hours. The relative high score for durability is justified by fact that the fuel cells are the only limiting factor and are anticipated to improve significantly in the coming years.

For the maintainability aspect, the use of the tank as an integral part of the structure limits the maintainability of the tank. But, as described in subsection 6.2.2, this is solved by making the empennage detachable from the aft fuselage for ease of operations during maintenance and inspections. The other parts of the drone are easily accessible and maintainable except for the tilting mechanism of the engines which are located inside the wing, making it difficult to reach for inspection and maintenance. For these reasons the maintainability of the drone is scored at a 4. The final grade for this phase is thus a 4.

End of Life

- Score 1: At the end of life there are no recyclable parts and this phase consists of fully disposal of the material and components with CO_2 emission.

- Score 2: At the end of life there is a low amount of recyclable parts and this phase consists of partly disposal of the materials and components with CO_2 emission.

- Score 3: At the end of life there is a intermediate amount of recyclable parts and this phase consists of partly disposal of the materials and components but with no CO_2 emission.

- Score 4: At the end of life there is a high amount of recyclable parts and this phase consists of partly disposal of the materials and components and with no CO_2 emission.

- Score 5: At the end of life all parts can be recycled, no disposal of any material and components is needed, with no emission of CO_2.

The end of life phase is determined by the level to which the materials and components are recyclable or disposable. The materials in the drone are, as discussed earlier, polyurethane foam, the flax fiber composite and aluminum. In addition, the drone consists of bought products such as the fuel cells, batteries and motors. Polyurethane foam cannot be recycled yet, but it can be recovered as fuel at end of life. The flax fiber composite is biodegradable at end of life or can be recycled by remelting it and using it again in the injection moulding process [22]. The aluminum in the tank can technically be recycled. The problem however is that the tank is a complicated structure with an outer layer of aluminum, middle layer of insulation and then an inner layer of aluminum again. The insulation layer is bio-degradable which does not lead to emissions, but it can most likely not be recycled.

The fuel cells are not recyclable as a whole but can technically be recycled per individual part. This is however very cost inefficient and probably not worth doing as advised by Pieter Lantermans, who was previously mentioned in chapter 6. The selected motors are recyclable and reusable [9]. To conclude, The fuel cells and the tank are the limiting factors for the end of life sustainability, but are recyclable in parts. The other components, including the batteries, are well recyclable or disposable. This results in an overall score of 4.

EcoDesign Strategy Wheel

The scores of all different aspect can now be visualized in a radar plot as shown in Figure 15.1. The figure shows the strong and weak points of the drone with regard to environmental sustainability.
For acquiring and consumption of materials a score of 5 is set as the goal. However, due to the need for transportation of the goods, which often still occurs on the usage of fossil fuels, the goal for meeting a neutral or negative CO_2 contributor cannot be met yet. However, it is possible that the amount of CO_2 negative contributors cancels the CO_2 produced over the process. Furthermore, the use of polyurethane, for which recycling processes are still under development, does not guarantee a full recyclable material usage and toxic emissions might enter the atmosphere.

---

[8]http://polyurethanes.org/uploads/documents/sustainability
[9]http://www.designlife-cycle.com/lifecycles-of-brushless-motor

On top of this the materials needed for the production of the batteries and fuel cells include toxic chemicals. Hence dragging the average down to a score of 3.5.

For manufacturing techniques the goal is set at a score of 4. A total score of 3.8 has been obtained. The small shortage is due to the possibility of non recyclable waste from the polyurethane foam, which can be eliminated once techniques exist to recycle the foam or to make sure no materials is wasted.

For operations and durability the goal is set at a score of 4.5. This is because a small amount of CO_2 emission is allowed which might originate from for example transportation of maintenance equipment. As long as during flight it remains zero in order to meet MD-SYS29. But at the same time a high maintainability and durability is desired. The drone has assigned a score of 4, due to the relatively low life time of the fuel cells and difficulty with maintaining the tilting mechanism of the engines, making the drone less durable and maintainable.

For end of life the goal is set at a score of 4. This is because the drone does not have to be fully recyclable, as long as the parts that are disposed come from a renewable source and the disposals do not introduce any toxicity or CO_2 positive contributions. The drone scores a 4 mainly due to the limiting recyclability of the fuel cell system and the polyurethane foam but most of the parts are recyclable, or bio-degradable.
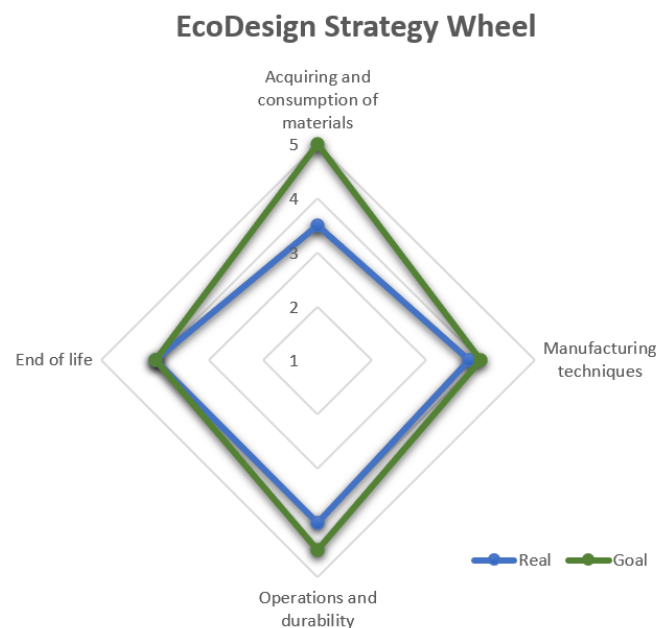

Figure 15.1: EcoDesign Strategy Wheel results

15.3. Requirements Compliance Matrix

With the knowledge from the subsystem designs and the life cycle assessment, the requirements with regards to sustainability of the drone can be analyzed. The sustainability requirements include the following:

MD-SYS27:   The hydrogen used to power the drone shall be produced in a sustainable way.
MD-SYS28:   The system shall be developed in a sustainable way.
MD-SYS29:   The drone shall have zero [CO_2] emissions during flight.
MD-SYS30:   The drone shall have a circular design.
MD-SYS31:   The drone shall be reusable for 40% of its components at its end of life.
MD-SYS32:   The components that are not reusable should have a lifetime of at least 10 years time.

The hydrogen used is assumed to be green hydrogen (thus produced from renewable energy sources) and the drone has been designed with the sustainability criteria in mind as described in the Baseline Report [62] and Midterm Report [63]. Furthermore, during flight the drone has zero CO_2 emissions due to its use of green hydrogen. The requirement on circularity is taken into account, however essential components such as the batteries and fuel cell have to be implemented in the design. Although these components do not comply fully with the circular design requirement, it is possible to select batteries which are produced from recycled parts as much as possible and possibilities for recycling fuel cells are under development as mentioned before. Since the drone mostly consists of recyclable components it is safe to say that the drone is for roughly 80% circular, which also applies to requirement MD-SYS31 on reusable components. The other 20% consists of the fuel cells, polyurethane foam, and small partly

non-recyclable components such as computer components, cabling, sensors, etc. The components that cannot be reused have a lifetime greater than 10 years, except for the fuel cell, for which recycling possibilities are under development. See Table 15.1 for the compliance matrix.

Table 15.1: Compliance matrix of the sustainability requirements

Requirement	Required	Actual	Fully met	Partially met	Not met	To be investigated
MD-SYS27:	n.a.	n.a.	✓			
MD-SYS28:	n.a.	n.a.	✓			
MD-SYS29:	n.a.	n.a.	✓			
MD-SYS30:	100%	> 80%		✓		✓
MD-SYS31:	40%	> 80%	✓			
MD-SYS32:	> 10 years	Fuel cells ≈ 1 year		✓		✓

15.4. Recommendations

The previous sections gave insights in the strengths and weaknesses in the sustainability of the design. From the weak points some recommendations for further improvement of the sustainability of the drone were established. The fuel cells, the batteries and the polyurethane foam are really restricting the overall good sustainability of the design. For improvement at the end of life, a proper solution has to be found for the recycle method of the fuel cells. Further investigation towards efficiently disposing or recycling of the fuel cells will have to be performed. Since the fuel cells also have a low durability, the performance of the drone with regards to durability can significantly improve with the use of better fuel cells. It is recommended to use the state of the art fuel cells, which are expected to grow substantially over the next few years. The lack of maintainability of the tilting mechanisms may cause problems in practice. Furthermore, the use of polyurethane foam makes the drone less recyclable and introduces some toxicity if the traditional way of production is used. It is worth investigating using different foams, or look into ways for production from recyclable parts. In order to improve the design with regards to material usage drastically, is to reconsider the usage of batteries. An option could be to make sure the batteries obtained are less toxic and making use of less non renewable sources.

16

Post DSE activities

After this project ends, a lot of designing, testing and building needs to be done still. This is all represented in this chapter. First, the project design and development logic for after this project are discussed in section 16.1. Then, a Gantt chart is provided showing all actions to be taken after this project. This is explained in section 16.2. Finally, all the costs that will come into play after this project are summarized and shown in section 16.3.

16.1. Project Design and Development Logic

Once the proposed design has been approved, its implementation can be started. This has been planned out to provide a clear structure. The Post DSE Project design and development logic is divided into four main sections. Firstly, it is required to have further research and development on the drone, as there are requirements that still require further investigation, it is necessary to research the options on fulfilling these requirements (more about the specific recommendations on this can be found in chapter 17). Furthermore, before having an actual prototype, the level of depth for the subsystems needs to be increased. After the level of depth is sufficient and the design has converged to below a certain error, the updated prototype design can be proposed.

Once the prototype design has been approved it needs to be built and tested. Before building the drone it necessary to find contractors willing to produce the necessary parts, and the further materials and tools need to be acquired. After this, the parts can be produced and assembled, then it enters its testing phase. This phase starts with ground testing, if it is found that it fails certain tests, this is a point where it reenters the research and development phase. Next, the flight test can begin where the all-weather conditions together with general flight performance can be tested. Once the testing phase is finished, it can enter the certification process, a more in depth explanation about the certification can be found in chapter 14.

Finally once the drone is certified, it can be mass produced. The production plan then needs to be updated according to the updates the design has experienced. Once this is done production and assembly can be performed and finally the drone can be delivered. During the life of the drone, customer feedback will be implemented as much as possible, and maintenance can be performed as specified in chapter 14. A visualization of this process is presented in Figure 16.1.

16.2. Gantt Chart

Combining the timeline with the logic diagram the Gantt chart is created. In the Gantt chart the different tasks can be seen in order and with their approximate duration. The Gantt chart can be seen in Figure 16.2. The process consists of four main parts: a research phase, the first prototype, a second research phase and finally the production. After starting production the final phase starts which is the life cycle management. This will continue indefinitely or as long as the drones are in circulation.

16.3. Cost Breakdown

For the financial budgetting of this post-DSE development, a preliminary cost breakdown has been made, which is shown in Table 16.1. In this table, the main branches of the post-DSE's Project Design and Development Logic have been used to estimate the cost throughout several phases, as can be seen in Figure 16.1. The origins of the cost have been discussed earlier in section 16.3 under the part 'Development Cost'.
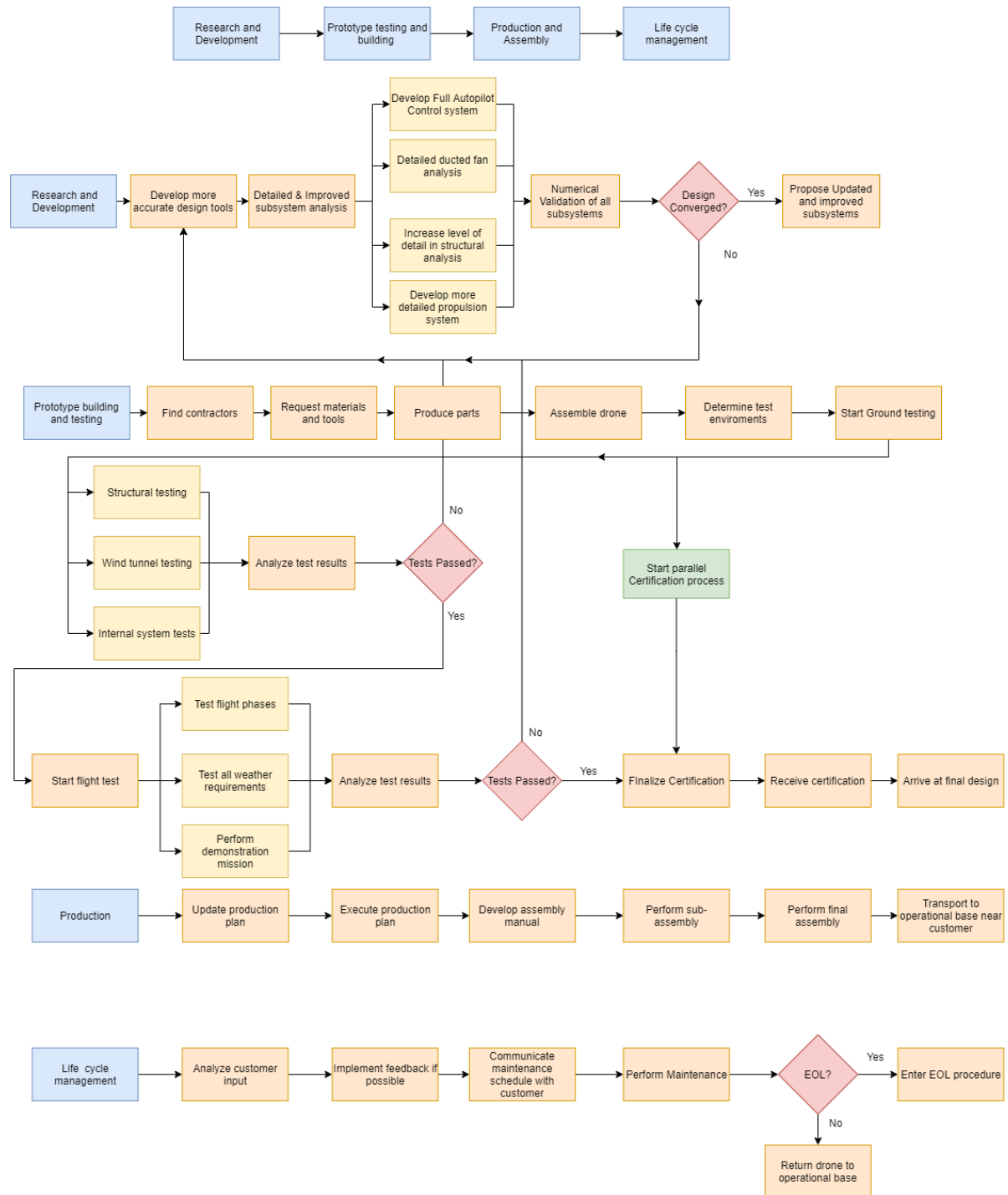
Figure 16.1: Post DSE Design and Development Logic Diagram

Table 16.1: Cost breakdown for Post-DSE phase

| Phase	Cost for	Amount	Remarks
Research and Development	First prototype (1 y) Second prototype (0.5 y)	€1.8M €0.9M	Average annual salary of €90k, for 20 engineers and scientists
Prototype Testing and Building	First prototype Certification	€0.1M €0.2M	Assumed to be similar to unit cost Assumed cost of €200K
Production and Assembly	Second prototype	€0.1M	Assumed to be similar to unit cost
Operations	Marketing and Finance Life Cycle Management	€0.3M	About 10% of total cost (idem)
(Development cost factor)		*€1.7M*	*Taken to be a factor of 1.5x*
Total		**€5.1M**	
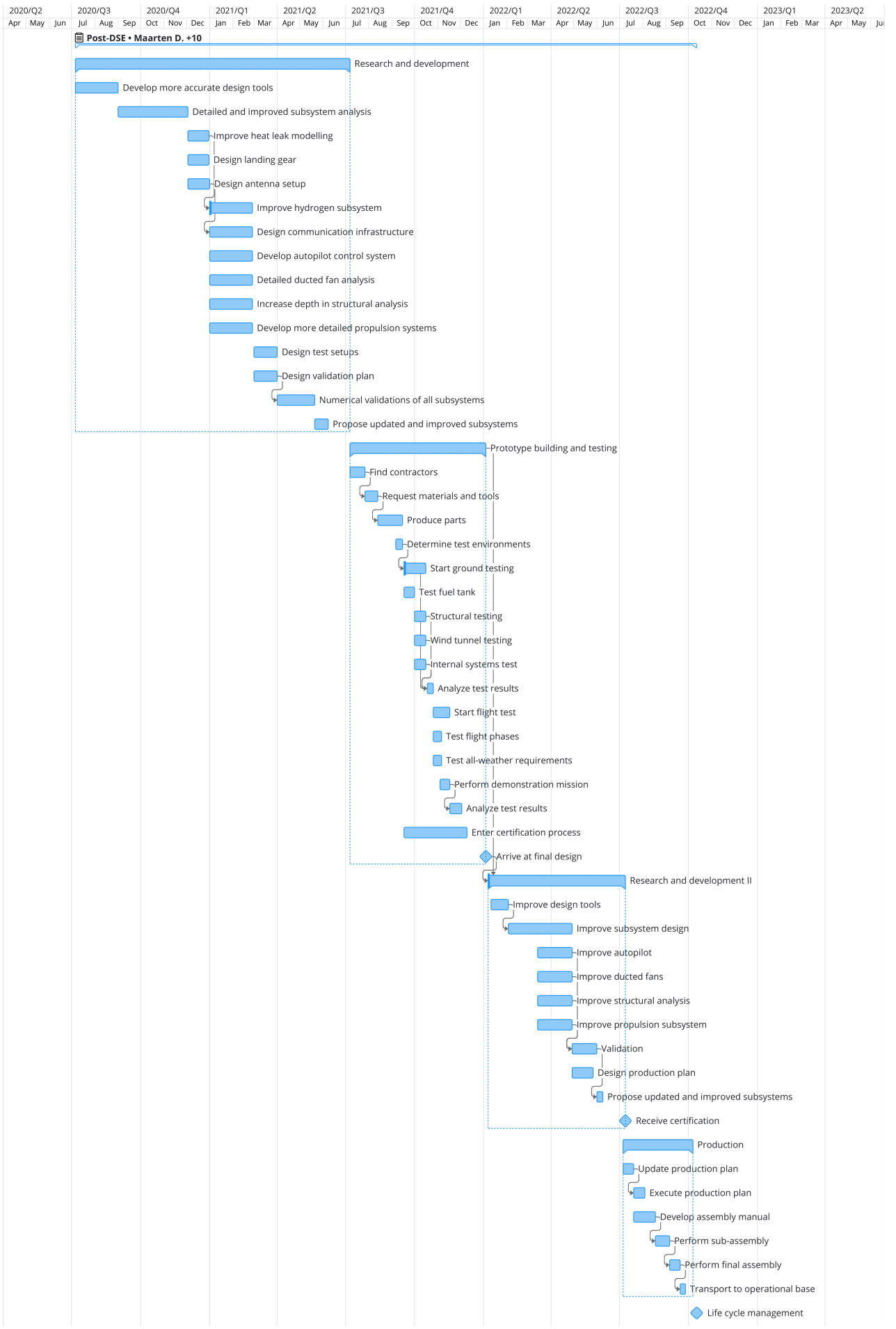
Figure 16.2: Post DSE Gantt chart

17

Conclusion and Recommendations

HEALR offers the solution to the problems faced by medical transport today. Transportation of organs, blood and tools will no longer be subjected to the uncertainties of travelling by car, including traffic, weather conditions and speed. The latter is of high importance for the transportation of transfusion blood samples. The goal of this report was to perform a detailed design of the chosen design concept in the Midterm Report [63]. This design concept is a winged drone system with tiltable thrust generators and its aim is to be the first transport drone that has a high payload capacity and high range.

The HEALR drone is an unmanned aerial vehicle that can be used for the transportation of medical goods such as organs, blood and vaccines. It has a Maximum Take-Off Weight of 36.03 $[kg]$ with a payload weight of 10 $[kg]$. The drone is hydrogen-powered, using a hydrogen fuel tank and fuel cells. The fuel cells are able to provide a total power of 4.2 $[kW]$. The drone can operate 99% of the days in a year, making medical goods more accessible. Furthermore the drone is able to complete a 100 $[nmi]$ (nautical miles) trip and return back to base. To make it easier to land and take-off in urban environments the drone is capable of preforming vertical take off and landing. In cruise the same rotors that supply power to the craft during VTOL can be tilted, such that they can be used in cruise. HEALR has a cruise speed of about 50 $[\frac{m}{s}]$, which is faster than the maximum speed an ambulance can reach. Furthermore the drone does not have to take into account traffic congestions and will therefore almost always be faster than an ambulance.

The operational cost of the drone are calculated to be 0.097 € $[/km/kg]$ payload and the unit cost will be around 83k €. For comparison, an ambulance car will cost around 125k € without any equipment [1]. This makes the drone a viable option for transporting medical payload.

For future work it is important to further investigate the integration of the payload in the fuselage and whether a cooling system is needed. The current holding mechanism might be too large to fit in the designed drone. The dampers and springs need to be sized by looking at the maximum acceleration the payload is allowed to take. The cooling system weight is assumed to be included in the weight of the payload, but this might change for different payloads. There is potential to use the heat from the payload for heating the liquid hydrogen, but this has not been thoroughly investigated yet. More detailed aerodynamic analysis is necessary. Models should be tested in wind tunnels to find its physical aerodynamic characteristics. Similarly, propeller tests will need to be done to validate its performance. It is also important to go into more detail with calculations and testing to find the noise created by the drone. The current estimation is not at a sufficient level of a detail to guarantee secure operation. It is also important to go into more detail with calculations and testing to find the noise created by the drone. The current estimation is not at a sufficient level of a detail to guarantee secure operation. The thrust delivered by two co-axial rotors also needs more research and testing. Until now, the transition phase has only been assessed for transition from take-off to cruise. The transition from cruise to landing configuration also needs to be evaluated.

For making the production of hydrogen more sustainable, power and cost efficient options need to be explored. The trade-off between using just one or multiple facilities also needs to be elaborated on. The future regulations regarding operation with hydrogen-power aircraft and on-board storage of liquid hydrogen fuel need to be complied with. Further research needs to be done to improve the modelling of heat leaks for the hydrogen tank, and validate

---

[1] shorturl.at/rtDF9

these models through experiments with cryogenic liquids and tanks.

More detailed dynamic models are to be made to evaluate the drone's stability during VTOL, transition and cruise. Furthermore, flight controllers in every degree of freedom are to be designed, as it has now been done for only the pitching motion. For the structure of the drone, the fuselage is still pending detailed analysis. More extensive validation with software and testing will also be necessary. The wing box can still be optimised for the shape of the wing. With a more optimised design, the weight of the structure can decrease, which has a positive effect on all the other subsystems.

The compliance with the all-weather operative requirement needs further investigation. For most subsystems it is assumed that the wind comes from one direction, while in reality it will switch unpredictably very often. This makes for example stability a lot harder to evaluate. For the structure of the drone, rain and hail have not been taken into consideration yet. Before the drone can fly in all-weather conditions it is of key importance these situations are looked at.

Bibliography

[1] XFLR5 Analysis of foils and wings operating at low Reynolds numbers. *Purdue University*, (October):1–71, 2009. URL `https://engineering.purdue.edu/~aerodyn/AAE333/FALL10/HOMEWORKS/HW13/XFLR5_v6.01_Beta_Win32(2)/Release/Guidelines.pdf`.

[2] Drone market outlook: Industry growth trends, market stats and forecast, March 2020. URL `https://www.businessinsider.com/drone-industry-analysis-market-trends-growth-forecasts?international=true&r=US&IR=T`.

[3] X. Li A. Rowe. Mathematical modeling of proton echange membrane fuel cells. *Elsevier*, December 2001. ISSN 4356–4362. URL `https://doi.org/10.1016/S0378-7753(01)00798-4`.

[4] European Union Aviation Safety Agency. Acceptable means of compliance (amc) and guidance material (gm) to commission implementing regulation (eu) 2019/947. 2019.

[5] Alex Ramirez-Serrano Ashraf M Kamal. Design methodology for hybrid (vtol + fixed wing) unmanned aerial vehicles. *Aeronautics and Aerospace Open Access Journal*, pages 1–12, 2018. ISSN 2576-4500. doi: https://doi.org/10.15406/aaoaj.2018.02.00047.

[6] Cooksey M. Wellwood-G. Goodes C. Brooks, G. Challenges in light metals production. *Transactions of the Institutions of Mining and Metallurgy, Section C: Mineral Processing and Extractive Metallurgy*, pages 25–33, 2007.

[7] B. Bensmann U. Krewer R. Hanke-Rauschenbach C. Winnefeld, T. Kadyk. Modelling and designing cryogenic hydrogen tanks for future aircraft applications. *Energies*, jan 2018. https://doi.org/10.3390/en11010105.

[8] Powis Rick Chelmins, David. Sampling and control circuit board for an inertial measurement unit. 2012. ISSN 20120009954.

[9] Vishnu Chipade, Abhishek Abhishek, Mangal Kothari, and Rushikesh Chaudhari. Systematic design methodology for development and flight testing of a variable pitch quadrotor biplane vtol uav for payload delivery. *Mechatronics*, 55:94–114, 01 2018. doi: 10.1016/j.mechatronics.2018.08.008.

[10] Toray Composite Materials America Inc. M35J High Modulus Carbon Fiber datasheet. 2018.

[11] B.H. da Silveira, P.R.C. Souza, and O. Almeida. Numerical Investigation of a Naca Air Intake for a Canard Type Aircraft. *International Journal of Advanced Engineering Research and Science*, 4(5):32–40, 2017. ISSN 23496495. doi: 10.22161/ijaers.4.5.7.

[12] Joshua Andrew Demoss. Drag measurements on an ellipsoidal body, 2007.

[13] EASA. COMMISSION IMPLEMENTING REGULATION on a high-level regulatory framework for the U-space, 2020.

[14] EASA. Easy access rules for unmanned aircraft systems (regulations (eu) 2019/947 and (eu) 2019/945). *European Union Aviation Safety Agency*, 2020.

[15] Electronic communication Committee. The European table of frequency allocations and application in the frequency range 9 kHz to 3000 GHz, 2011. URL `http://www.erodocdb.dk/Docs/doc98/official/pdf/ERCREP025.PDF`.

[16] Fischer A. Franklin and J. Anderson Plumer. *Lightning Protection of Aircraft*. NASA Lewis Research Center, 1977. ISBN NASA Reference Publication 1008.

[17] Charles W. Frick, Wallace F. Davis, Lauros M. Randall, and Emmet A. Mossman. An experimental investigation of naca submerged-duct entrances. *NACA ACR No. 5120*, 1945.

[18] Nikolajs Glīzde. Plotting the flight envelope of an unmanned aircraft system air vehicle. *Transport and Aerospace Engineering*, 4(1):80–87, Jan 2017. doi: 10.1515/tae-2017-0010.

[19] Albis Gmbh. Cellidor CP 400-10 datasheet. 2020.

[20] Will Graf, Jonathan Fleming, and Wing Ng. Improving ducted fan UAV aerodynamics in forward flight. *46th AIAA Aerospace Sciences Meeting and Exhibit*, (January):1–11, 2008. doi: 10.2514/6.2008-430.

[21] Dr. Michael Hirscher. *Handbook of Hydrogen Storage*. WILEY-VCH, 2010. ISBN: 978-3-527-32273-2.

[22] PlastiComp Inc. Complet LGF40-PA66 datasheet. 2018.

[23] J.C. van der Vaart E. de Weerdt C.C. de Visser A.C. in 't Veld E. Mooij J.A. Mulder, W.H.J.J van Staveren. AE3202 fight dynamics lecture slides. 2013.

[24] C. Jeffrey. *An Introduction to GNSS: GPS, GLONASS, Galileo and Other Global Navigation Satellite Systems*. NovAtel, 2010. ISBN 9780981375403.

[25] W. Johnson. *Helicopter Theory*. 02 1980.

[26] L. Drzal A. Mohanty Joshi, S.V. and S. Arora. Are natural fiber composites environmentally superior to glass fiber reinforced composites? *Composites Part A: Applied Science and Manufacturing*, pages 371–376, 2004.

[27] D. Fadeev K. Mikhaylov, J. Tervonen. Development of energy efficiency aware applications using commercial low power embedded systems. 2012.

[28] Istvan Kovacs, Rafhael Medeiros de Amorim, Huan Cong Nguyen, Jeroen Wigard, and Preben Elgaard Mogensen. Interference analysis for uav connectivity over lte using aerial radio measurements. September 2017. doi: 10.1109/VTCFall.2017.8287891. 2017 IEEE 86th Vehicular Technology Conference (VTC2017-Fall) ; Conference date: 24-09-2017 Through 27-09-2017.

[29] P. Adam & J. Leachman. Design of a reconfigurable liquid hydrogen fuel tank for use in the genii unmanned aerial vehicle. *AIP Conference Proceedings*, 1573(1):1299–1304, feb 2015. https://doi.org/10.1063/1.4860856.

[30] J. Leishman and Kenneth Rosen. Challenges in the aerodynamic optimization of high-efficiency proprotors. *Journal of the American Helicopter Society*, 56:12004–1, 01 2011. doi: 10.4050/JAHS.56.012004.

[31] D.Brent L.P Beland. Traffic congestion, transportation policies, and the performance of first responders. June 2018.

[32] Bcomp Ltd. ampliTex 5009 flax fabric datasheet. 2020.

[33] Hader M. Mapping autonomous urban air mobility's progress., March 2020. URL https://www.rolandberger.com/en/Point-of-View/Mapping-autonomous-urban-air-mobility's-progress.html.

[34] K. Akatsu M. Miyamasu. Efficiency comparison between brushless dc motor and brushless ac motor considering driving method and machine design. *Journal of Industry Applications*, 2, 2012.

[35] Lorenzo Murzilli. Jarus guidelines on specific operations risk assessment (sora). *Joint Authorities for Rulemaking of Unmanned Systems*, 2017.

[36] Abd. Rahim Abu Talib Nadiir Bheekhun and Mohd Roshdi Hassan. Aerogels in aerospace: An overview. Technical report, Universiti Putra Malaysia, nov 2013. doi.org/10.1155/2013/406065.

[37] E. D. Nicholas. Developments in the friction-stir welding of metals. *6th International Conference on Aluminium Alloys. Toyohashi, Japan.*, (October), 1998.

[38] M. Nita and D. Scholz. Estimating the Oswald Factor from Basic Aircraft Geometrical Parameters. *Deutscher Luft- und Raumfahrtkongress*, 281424:1–19, 2012.

[39] C.M. Lim M.J. Cho K.Y. Kim & J.H. Baik N.M. Garceau, S.Y. Kim. Comporottve study of types of vtol transport aircraft ducted fan design study of the vertodyne report r-80. July 1956. https://doi.org/10.1088/1757-899X/101/1/012130.

[40] C.M. Lim M.J. Cho K.Y. Kim & J.H. Baik N.M. Garceau, S.Y. Kim. Performance test of a 6 l liquid hydrogen fuel tank for unmanned aerial vehicles. *IOP Conference Series.: Mater. Sci. Eng.*, 101(1), nov 2015. https://doi.org/10.1088/1757-899X/101/1/012130.

[41] World Commission on Environment and Development. "our common future", 1987.

[42] Nicolas J. Pignier, Ciarán J. O'Reilly, and Susann Boij. Aerodynamic and aeroacoustic analyses of a submerged air inlet in a low-Mach-number flow. *Computers and Fluids*, 133:15–31, 2016. ISSN 00457930. doi: 10.1016/j. compfluid.2016.04.010.

[43] D.G. Prof. dr. Simons. *Introduction to Aircraft Noise*. Delft University of Technology, October 2019.

[44] Dr. Fabrizio Oliviero Prof. E. Gill. AE3211-l Systems Engineering and Aerospace Design lecture slides. 2020.

[45] B.T.C. Zandbergen R. Vos, J.A. Melkert. Aerospace design and systems engineering elements i-ae1222-ii, May 2020. TU Delft AE1222-II Course Lecture Slides.

[46] M. Ramasamy. Hover performance measurements toward understanding aerodynamic interference in coaxial, tandem, and tilt rotors. *Journal of the American Helicopter Society*, 2015.

[47] Daniel P. Raymer. *Aircraft Design: A Conceptual Approach*. American Institute of Aeronautics and Astronautics, Inc., 1992.

[48] Jonathan R. Southwick Richard O. Stroman, Michael W. Schuette. *Design Challenges and Modeling for an Efficient Liquid Hydrogen Storage Tank for Autonomous Systems*. AIChE International Congress on Energy 2011, jan 2011. URL: https://www.researchgate.net/publication/264543083.

[49] Karen Swider-Lyons Joseph A.Rodgers Daniel J.Edwards Richard O. Stroman, Michael W. Schuette. Liquid hydrogen fuel system design and demonstration in a small long endurance air vehicle. *International Journal of Hydrogen Energy*, 39(21):11279–11290, jul 2014. US Naval Research Laboratory, Sotera Defense Solutions Inc.; doi.org/10.1016/j.ijhydene.2014.05.065.

[50] A. Rigaldo. Aerodynamics gust response prediction, Jul 2011. URL https://www.diva-portal.org/smash/get/diva2:444284/FULLTEXT01.pdf.

[51] Dr.Jan Roskam. *Airplane Design Part IV: Preliminary Calculation of Aerodynamic,Thrust and Power Characteristics*. 2004.

[52] J. Roskam. *Airplane Aerodynamics and Performance*. DARcorporation, 1997.

[53] Jan Roskam. *Airplane Design -*. DARcorporation, 1985. ISBN 978-1-884-88550-1.

[54] Brian Roth. Control power design requirements for aircraft flying qualities. 2009.

[55] Robert T. Tornabene Brett A. Bednarcyk Lynn M. Powers Subodh K. Mital Lizalyn M. Smith Xiao-Yen J. Wang & James E. Hunter Roy M. Sullivan, Joseph L. Palko. Engineering analysis studies for preliminary design of lightweight cryogenic hydrogen tanks in uav applications. Technical Publication 2006-214094, NASA Scientific and Technical Information, may 2006. URL: https://ntrs.nasa.gov/search.jsp?R=20060021606.

[56] Mohammad H. Sadraey. *AIRCRAFT DESIGN A Systems Engineering Approach*. John Wiley & Sons, Ltd, 2013.

[57] P.M. Sforza. *Theory of Aerospace Propulsion (Second Edition)*. Elsevier, 2017. ISBN 978-0-12-809326-9.

[58] J. Sinke. AE3211-ll Production of Aerospace Systems lecture slides. 2020.

[59] J.R. Youn Song, Y.S. and T.G. Gutowski. Life cycle energy analysis of fiber-reinforced composites. *Composites Part A: Applied Science and Manufacturing*, pages 1257–1265, 2009.

[60] C. Stahlhut and J.G. Leishman. Aerodynamic design optimization of proprotors for convertible-rotor concepts. 1:593–616, 01 2012.

[61] Steven M. Arnold Roy M. Sullivan Jane M. Manderscheid & Pappu L.N. Murthy Subodh K. Mital, John Z. Gyekenyesi. Review of current state of the art and key design issues with potential solutions for liquid hydrogen cryogenic storage tank structures for aircraft applications. Technical Memorandum 214346, NASA, oct 2006. URL: https://ntrs.nasa.gov/archive/nasa/casi.ntrs.nasa.gov/20060056194.pdf.

[62] M. Dom M. Floriş A.V. Jadoenathmisier L.C. Kaffa F.H. Kuipers G.C.Y. Lieuw B.C. Ulyanov T.L.A. Vink-M. Wegener T. Bloem, F.M. van den Bogaard. Baseline report - all-weather hydrogen drone. *Delft University of Technology*, 2020.

[63] M. Dom M. Floriș A.V. Jadoenathmisier L.C. Kaffa F.H. Kuipers G.C.Y. Lieuw B.C. Ulyanov T.L.A. Vink-M. Wegener T. Bloem, F.M. van den Bogaard. Midterm report - all-weather hydrogen drone. 2020.

[64] M. Dom M. Floriș A.V. Jadoenathmisier L.C. Kaffa F.H. Kuipers G.C.Y. Lieuw B.C. Ulyanov T.L.A. Vink-M. Wegener T. Bloem, F.M. van den Bogaard. Project plan - all-weather hydrogen drone. *Delft University of Technology*, 2020.

[65] M.T. Todinov. *Risk-Based Reliability Analysis and Generic Principles for Risk Reduction*. Elsevier Science, Cranfield University, Cranfield, UK, 2007. ISBN 978-0-08-044728-5, https://doi.org/10.1016/B978-0-08-044728-5.X5000-8.

[66] Michael Felderhoff Ulrich Eberle and Ferdi Schüth. Chemical and physical solutions for hydrogen storage. *Angewandte Chemie International Edition*, 48, 2009. doi: 10.1002/anie.200806293.

[67] Th Van Holten and Melkert J.A. *Helicopter Performance, Stability and Control*. Delft University of Technology, November 2002.

[68] D. Verstraete. The potential of liquid hydrogen for long range aircraft propulsion, apr 2009. URL: http://hdl.handle.net/1826/4089.

[69] F. Berardino W. Spitz, R. Golaszewski. Development cycle time simulation for civil aircraft. January 2001.

[70] H.A. Wahl and D.T. Julian. Comparative study of types of vtol transport aircraft, ducted fan design study, 1956.

[71] J. Payet V. Michaud C. Ludwig Witik, R.A. and J.A.E. Månson. Assessing the life cycle costs and environmental performance of lightweight materials in automobile applications. *Composites Part A: Applied Science and Manufacturing*, pages 1694–1709, 2011.

[72] T. Zhang and G.N. Barakos. Review on ducted fans for compound rotorcraft. *The Aeronautical Journal*, (December 2019):1–34, 2020. ISSN 0001-9240. doi: 10.1017/aer.2019.164.

[73] Jiří Čečrdle. 2 - theoretical background of whirl flutter phenomenon. In Jiří Čečrdle, editor, *Whirl Flutter of Turboprop Aircraft Structures*, pages 13 – 31. Woodhead Publishing, Oxford, 2015. ISBN 978-1-78242-185-6. doi: https://doi.org/10.1533/9781782421863.13. URL http://www.sciencedirect.com/science/article/pii/B9781782421856500027.